

**PHASE-SPACE PERSPECTIVE OF  
PARTIALLY COHERENT IMAGING:  
APPLICATIONS TO BIOLOGICAL  
PHASE MICROSCOPY**

**MEHTA SHALIN BADRESH KUMAR**

(M.Tech.(Gold Medal), DA-IICT, India)

**PH.D. THESIS**

**NATIONAL UNIVERSITY OF  
SINGAPORE**

**2010**

**PHASE-SPACE PERSPECTIVE OF  
PARTIALLY COHERENT IMAGING:  
APPLICATIONS TO BIOLOGICAL  
PHASE MICROSCOPY**

by

**Mehta Shalin Badresh Kumar**

*(M.Tech. (Gold Medal), DA-IICT, India)*

**Thesis Advisor: Prof. Colin J. R. Sheppard**

**A THESIS SUBMITTED  
FOR THE DEGREE OF DOCTOR OF  
PHILOSOPHY OF NUS GRADUATE SCHOOL  
FOR INTEGRATIVE SCIENCES &  
ENGINEERING  
NATIONAL UNIVERSITY OF SINGAPORE**

**2010**

Copyright by  
Shalin B. Mehta  
2010

Published papers of the author are incorporated in this thesis, with permission of respective publishers who hold the copyright to the typeset version of the papers.

Ah Love! Could you and I with Fate conspire  
To grasp this sorry Scheme of Things entire,  
Would not we shatter it to bits – and then  
Re-mould it nearer to the Heart's Desire!

A translation of a *Rubaiyyat* by Omar Khayyam, which I first saw in the book “C Programming Language,” by Kernighan & Ritchie. I think this verse sums up the feeling that we often encounter during any scholarly pursuit.

# Acknowledgement

My Ph.D. has been an exciting journey, which has taken me across four laboratories, as many research projects, as well as five countries for scientific meetings and collaborations. This is an opportune moment of pause and of remembering my guides, companions, and supporters who made this journey possible and enjoyable.

I thank my Ph.D. advisor and mentor, Colin Sheppard, whose guidance and support made this journey adventurous and pleasant. Colin has been generous with his scientific insights, contagious enthusiasm, and support for research. I will treasure our impromptu discussions about things complex and simple, during which I had the pleasure of sampling his large sphere of interest and expertise. The Majority of the work presented in this thesis was initiated and has progressed due to these discussions. I have enjoyed a fine balance of independence and guidance from Colin, which has allowed me to explore interesting directions without getting lost. Despite bearing the responsibility of the head of the the division, Colin found ample time to sit down with his students to thrash out nagging questions. During these four years, I have learned from him, by instruction and by osmosis, what it means to be a good scientist, a good mentor, and a good friend.

I thank Rudolf Oldenbourg from Cellular Dynamics Program of Marine Biological Laboratory (MBL), my other mentor, in whose lab I spent two months during spring of 2010. During my relatively short interaction with him, I learned a lot about experimental phase microscopy from him. His experimental insights and openness in letting me pursue questions related to my thesis have been instrumental in timely completion of this thesis project. The main biological application presented in this thesis would not have been possible without the enthusiasm of Naoki, a fellow lab-mate at MBL, and Rudolf. While I was at MBL, Rudolf provided me with ample opportunities of interaction with diverse scientific community. I will fondly remember our walks to and snacks at the ‘Pie in the Sky’, during which we discussed issues ranging from the position of the diffraction orders in the back focal plane to the position of God in the universe.

I thank Martin Bastiaans from Eindhoven University of Technology, who gave us a crash course on phase-space optics while visiting NUS, and during whose lecture I had an ‘aha’ moment, which led us to develop the phase-space model of partially coherent imaging presented in this thesis.

Thanks to Caroline Lee from National Cancer Centre (NCC) of Singapore and Department of Biochemistry, NUS, in whose lab I received important training in biological research and biological lab techniques as part of the second lab-rotation of my Ph.D. This training forms the basis of some biological applications presented in the thesis. I thank her for providing me with the opportunity to present introductory talks and demonstrations to members of her lab. These talks and demonstrations not only fulfilled the teaching requirements of my Ph.D. scholarship, but also encouraged me to distill the essence of biological microscopy methods from the details. I thank Dr. Steve Oh from Bioprocessing Technology

Institute (BTI) and Dr. Ivan Reading from Singapore Institute of Manufacturing Technology (SIMTech) with whom I did my first experiments on confocal microscopy during my first lab rotation of Ph.D.

Naveen and Shakil are excellent sounding boards, good friends and helpful lab-mates. Their presence makes the lab an enjoyable place. I also benefited from collaboration with Shan Shan and discussions with Wai Teng. Jianwei, from NCC, was my patient teacher during the lab-rotation in Caroline's lab. I am thankful to Jianwei and all other lab-mates at NCC who happily put up with an excitable engineer with shaky hands. Their inputs during my microscopy talks at NCC made it abundantly clear that when one teaches, two learn. I thank Sounderya, Viveka, Viknish, Michelle, Grace, Jingbo, and Ma Kun for their friendship.

It has been very rewarding to collaborate with Naoki, my lab-mate at MBL, on the project of imaging of axoneme dynamics. His biological insights and willingness to try new microscopy approaches has made our collaboration highly enjoyable. His friendship and beautiful gift of sea-urchin skeletons are treasured. It was great to have met Amitabh Verma and Vithal Kudal at MBL at lunch and dinner tables. Chris Rieken and Rudi Rottenfusser, who are Zeiss experts looking after needs of MBL researchers, were ever ready with practical advice and indefinite loans of components. While participating in the mini-AQLM (Analytical & Quantitative Light Microscopy) course at MBL, I was amused and educated by insights and practical demonstrations of Shinya Inoué. During the same course, I enjoyed interacting with Rudolf, Michael Shribak, Amitabh Varma, Alex Valm, Grant Harris, Tomomi Tani, and Louie Kerr.

During informal seminars and at conferences, I have benefited from personal and email exchanges with Daniel Lubrich, Graham Wright, Nico Sturman, Nenad Amodaj, Arthur Adelstein, Karl Hoover, Laura Waller, George Barbastathis, Se Baek Oh, Lei Tian, Marc Levoy, Zhengyun Zhang, Rainer Heintzmann, Mats Gustaffson, Ramesh Raskar, Jerome Mertz, Sunney Xie, Kenji Yamazoe, Lu Fake, Chen Nanguang, Thorsten Wohland, Si Ke, Gong Wei, and Zheng Wei.

I thank the administration of NGS (NUS Graduate School for Integrative Sciences & Engineering), and in particular Irene, Marcus, Ivy, and Vivien, who have been patient and efficient with administrative issues at all stages of my graduate education. I have benefited from interactions with Justine Burley, former deputy director of NGS, who taught us a course on research ethics. I also thank current executive director of NGS, Li Baowen for his efforts at instilling a sense of community within NGS. I am thankful to administration at MBL and especially to Jane McNeil from Cellular Dynamics Program at MBL. Jane's expert support during processing of the US visa was instrumental in ensuring that I could visit Rudolf's group as planned. Her support at MBL helped me to settle down quickly and begin to focus on research.

My graduate scholarship was provided by NGS. NGS offers the flexibility of tailoring the Ph.D. program to the student's needs, which allowed me to pursue exciting directions. Funding from NGS enabled the collaborative visit to MBL and attendance at conferences, which has made positive impact on my thesis work. I was supported by MBL visiting research fellowship (Robert Day Allen Fellowship Fund and the Laura and Arthur Colwin Endowed Summer Research Fellowship Fund) during my collaboration with Rudolf's group. The research reported in this thesis has been supported by funding from Singapore Ministry of Education and intramural grants from NUS to Colin.

I have been nurtured by love and unwavering support of my family. I am indebted to my parents, who have lived thrifty lives to support our growth. Their patience and perseverance

have been examples for me to follow in my life. I thank my brother, friend and fellow lab-mate, Kalpesh, whose quiet support has helped me through several moments of transition and difficulty. I thank my better half, Naline, for her love and companionship. She has put up with my erratic schedule with a sense of humor. Her dedication to our welfare dwarfs my dedication to science. Due to her support, I could focus on research whenever the need arose. I am grateful for the presence of Shashvat, our little son, in our lives. He is even more dedicated to having fun and being naughty. His unconditional enthusiasm and exuberant explorations keep reminding me what is really important in life.

# Contents

<b>Acknowledgement</b>	<b>i</b>
<b>Contents</b>	<b>iv</b>
<b>Summary</b>	<b>vii</b>
<b>List of Tables</b>	<b>ix</b>
<b>List of Figures</b>	<b>x</b>
<b>Nomenclature</b>	<b>xi</b>
<b>1 Theme and background</b>	<b>1</b>
1.1 Quantitative phase microscopy . . . . .	1
1.2 Partially coherent imaging . . . . .	4
1.3 Phase-space perspective of partially coherent imaging . . . . .	10
1.4 Contributions and contents of the thesis . . . . .	15
1.4.1 Partially coherent imaging in DIC . . . . .	15
1.4.2 Novel partially coherent method for quantitative phase imaging . . .	16
1.4.3 Phase-space perspective of partially coherent imaging . . . . .	16
1.4.4 Biological applications of quantitative phase imaging . . . . .	16
1.5 Organization of the thesis . . . . .	17
1.5.1 Multimedia accompanying the thesis . . . . .	18
<b>2 Differential Interference Contrast</b>	<b>20</b>



2.1	Paper: Partially coherent image formation in differential interference contrast (DIC) microscope . . . . .	20
2.2	Paradoxical point spread function of DIC . . . . .	39
<b>3</b>	<b>Differential Phase Contrast</b>	<b>44</b>
3.1	Evolution of asymmetric-illumination based phase imaging methods . . . .	45
3.2	Paper: Quantitative phase-gradient imaging at high resolution with asymmetric illumination-based differential phase contrast . . . . .	46
3.3	Further discussion of imaging properties of AIDPC . . . . .	50
3.3.1	Effect of specimen absorption and birefringence . . . . .	50
3.3.2	Light throughput and signal to noise performance . . . . .	51
<b>4</b>	<b>Phase-space imager</b>	<b>54</b>
4.1	Paper: Phase-space representation of partially coherent imaging systems using the Cohen class distribution . . . . .	55
4.2	Phase-space imager in terms of the specimen's Wigner distribution and a system dependent kernel . . . . .	59
4.2.1	Marginals of the PSI and the PSI-kernel . . . . .	60
4.2.2	Interpretation of the PSI-kernel . . . . .	60
<b>5</b>	<b>Analysis using phase-space imager</b>	<b>65</b>
5.1	Paper: Using the phase-space imager to analyze partially coherent systems: bright-field, phase contrast, differential interference contrast, differential phase contrast, and spiral phase contrast . . . . .	65
<b>6</b>	<b>Quantitative biological microscopy</b>	<b>88</b>
6.1	Paper: Sample-less calibration of differential interference contrast microscope	89
6.2	Phase reconstruction from DIC and AIDPC images . . . . .	105
6.2.1	Efficient and robust registration of phase-gradient data measured with DIC and AIDPC . . . . .	108
6.3	Analysis of the dynamic beating of axoneme with dark-field microscope . .	112
6.3.1	Background and hypothesis . . . . .	112

6.3.2	Simulated images of axoneme under dark-field microscope . . . . .	115
6.3.3	Imaging of live specimens . . . . .	120
6.3.4	Measurement of bend propagation and intensity propagation along the length of the axoneme . . . . .	121
<b>7</b>	<b>Conclusion</b>	<b>125</b>
7.1	Summary of results . . . . .	126
7.1.1	Partially coherent methods of quantitative phase microscopy . . . .	126
7.1.2	Phase-space representation of partially coherent imaging . . . . .	126
7.1.3	High-resolution quantitative analysis of cellular morphology . . . . .	128
7.2	Future directions . . . . .	128
7.2.1	Partially coherent methods of quantitative phase microscopy . . . .	129
7.2.2	Phase-space representation of partially coherent imaging . . . . .	129
7.2.3	High-resolution quantitative analysis of cellular morphology . . . . .	130
	<b>Bibliography</b>	<b>131</b>

# Summary

Many specimens (particularly biological) are phase objects, i.e., they do not affect the intensity of light, but rather alter the phase of incident illumination. Imaging of phase specimens requires appropriate illumination and appropriate manipulation of scattered light to produce an image with phase contrast. The specimen may be illuminated from a single direction (e.g. using a laser, as in holography) or from a range of directions (e.g. using a halogen lamp with high-NA condenser, as in conventional microscopy). Methods that illuminate from a range of directions using an incoherent source (and hence give rise to partially coherent field at the specimen) provide high transverse and axial resolution, freedom from coherent speckle, and immunity against imperfections in the light-path. A popular example of the partially coherent method is differential interference contrast (DIC). While DIC has been used for qualitative microscopy since its inception, there is recent interest in using partially coherent phase methods (of which DIC is a special case) for high-resolution quantitative imaging of specimens. Since imaging is an inverse problem – of estimating the specimen’s properties from measured intensity – the forward problem of partially coherent imaging must be formulated in an elegant, computationally efficient and physically intuitive manner. Unlike fluorescence and coherent microscopy, partially coherent imaging is an inherently nonlinear process, which has impeded development of accurate forward analysis and useful inversion approaches.

This thesis reports four important advances in the direction of quantitative specimen analysis using partially coherent optical phase microscopy: 1) We provide an accurate model of image formation in the DIC microscope. Our results correct some incorrect assumptions held in the DIC community for three decades and elucidate the effects of key parameters of

the DIC microscope. 2) We discuss a novel wide-field imaging method, called Asymmetric Illumination-based Differential Phase Contrast (AIDPC), which overcomes key limitations of DIC (viz., corruption of DIC image due to specimen birefringence, low light-throughput, and non-linearity of information in DIC image). 3) We develop a phase-space (i.e., joint space-frequency) model, termed the phase-space imager (PSI). The PSI model provides an equivalent of the point-spread function model used in linear imaging. PSI elegantly captures non-linear image formation due to partial coherence, allows efficient computation of partially coherent images under a variety of methods and exploits an intuitive link with the Wigner representation used widely in signal processing literature. 4) We demonstrate biological applications based on above developments. In collaboration with Dr. Rudolf Oldenbourg and Dr. Naoki Noda (from Cellular Dynamics Program, Marine Biological Laboratory, Woods Hole, MA, USA), we analyze the dynamics of a highly-conserved molecular machine (called the axoneme) that powers flagella and cilia. We describe a new and robust registration algorithm required to reconstruct the specimen phase from images produced by DIC and AIDPC.

# List of Tables

1.1 Our published that are typeset verbatim in this thesis . . . . . 19

# List of Figures

1.1	Time-lapse images of a cancer cell that divides in three rather than two . . .	2
1.2	A general schematic of a partially coherent imaging system . . . . .	6
1.3	An experimental comparison of intensities in the image plane and the back focal plane between coherent and partially coherent illumination . . . . .	7
1.4	Point-spread function description of coherent imaging . . . . .	12
1.5	Phase-space description of transfer properties of coherent image formation .	13
2.1	Simulated and experimental images of a point assuming sheared point spread function (PSF) vs. assuming sheared specimen . . . . .	41
2.2	Improved schematic of the illumination path of the Nomarski-DIC microscope	43
3.1	Images of a highly birefringent specimen (potato starch) with AIDPC, DIC, Brightfield, and crossed-polarizers . . . . .	52
4.1	Description of partially coherent image formation in terms of the PSI-kernel	62
4.2	Comparison of the PSI-kernel and marginals at different coherence ratios. .	63
6.1	Direct reconstruction of specimen phase from DIC and AIDPC images . . .	107
6.2	Simulation of gradient phase-correlation method for registration of DIC and AIDPC data . . . . .	110
6.3	Registration of experimentally acquired DIC data with gradient phase-correlation algorithm . . . . .	111
6.4	Electron micrograph and schematic of the axoneme's structure . . . . .	113
6.5	Comparison of the supports of the mutual coherence produced by the dark-field annulus and the point spread function of the imaging objective . . . .	116
6.6	Computation of partially coherent dark-field images of the axoneme . . . .	119
6.7	Raw dark-field images of a beating axoneme . . . . .	121
6.8	Control experiment to verify the insensitivity of our image analysis software with respect to defocus . . . . .	122
6.9	A negative control (erratically beating axoneme) shows the lack of propagation of the flagellar bend and integrated intensity . . . . .	123
6.10	Analysis of the propagation of the bend and the scattering strength along the length of the beating axoneme . . . . .	124

# Nomenclature

$\mathcal{F}_x$	The operator that indicates Fourier transform over the variable $x$ . I use the kernel $e^{-2\pi i x m}$ for defining Fourier transform, i.e., $F(m) = \int f(x) e^{-2\pi i x m} dx$ .
$\mathcal{F}_m^{-1}$	The operator that indicates inverse Fourier transform over the variable $m$ . I use the kernel $e^{2\pi i x m}$ for defining Fourier transform, i.e., $f(x) = \int F(m) e^{2\pi i x m} dm$ .
$\lambda$	Wavelength of light
$\text{NA}_c$	Numerical aperture of the condenser
$\text{NA}_o$	Numerical aperture of the objective
$\otimes_x$	Convolution of two functions along <i>only</i> the $x$ dimensions, e.g., $W(\mathbf{m}, \mathbf{x}) \otimes_{\mathbf{x}} K(\mathbf{m}, \mathbf{x}) = \int W(\mathbf{m}, \mathbf{x}) K(\mathbf{m}, \mathbf{x} - \mathbf{x}_1) d\mathbf{x}_1$ .
$\Psi(\mathbf{m}, \mathbf{x})$	Phase-space imager
$K(\mathbf{m}, \mathbf{x})$	PSI-kernel of a partially coherent imaging system
$\xi$	Two dimensional vector representing pupil plane co-ordinates $(\xi, \eta)$ .
$\mathbf{m}$	Two dimensional vector representing spatial-frequencies along $(m, n)$ .
$\mathbf{x}$	Two dimensional vector representing spatial variables $(x, y)$ .
$C(\mathbf{m}, \mathbf{m}')$	PSI-window of a partially coherent imaging system
$P_c$	Condenser pupil: complex transmission at the front focal plane of the condenser. Due to incoherence, only the intensity of the pupil, $ P_c ^2$ , affects the image formation.
$P_o$	Objective pupil: complex transmission at the back focal plane of the objective.
$S$	Coherence ratio given as $\text{NA}_c/\text{NA}_o$ that quantifies the coherence of imaging system. Higher value of $S$ implies less coherent image formation.
$S_m(\mathbf{m}, \mathbf{m}')$	Mutual spectrum of the specimen defined as $T(\mathbf{m} + \frac{\mathbf{m}'}{2}) T^*(\mathbf{m} - \frac{\mathbf{m}'}{2})$
$T(\mathbf{m})$	Spectrum of the specimen transmission
$t(\mathbf{x})$	Transmission of the specimen
$W(\mathbf{m}, \mathbf{x})$	Wigner distribution
<b>AIDPC</b>	Asymmetric Illumination-based Differential Phase Contrast

**BFP** Objective Back Focal Plane

**Coherent imaging** Imaging with a source that is effectively a point (i.e., spatially coherent) such that the specimen is illuminated with a plane-wave in only one direction.

**DIC** Differential Interference Contrast

**DPC** Differential Phase Contrast

**FFP** Condenser Front Focal Plane

**Incoherent imaging** Imaging of a self-luminous specimen

**OPL** Optical Path Length

**OTF** Optical Transfer Function

**Partially coherent imaging** Imaging with an incoherent source and large illumination aperture such that the specimen is illuminated by several incoherent plane-waves over a range of directions.

**PSDIC** Phase-shifting DIC

**SNR** Signal to Noise Ratio

**TCC** Transmission cross-coefficient (a spatial-frequency domain partially coherent image formation model introduced by Hopkins)

**TIE** Transport of Intensity Equation



# Chapter 1

## Theme and background

In this chapter, I discuss which problems are being addressed and why they are interesting. The thesis addresses three related topics as elaborated upon in the sec. [1.1-1.3](#). Afterwards, I describe the main contributions of the thesis and how the thesis is organized.

### 1.1 Quantitative phase microscopy

A modern microscopist would reckon that quantitative imaging is said to furnish an indispensable instrument in the treatment of nearly every recondite question in modern biology (with apologies to Lord Kelvin, who reckoned that the Fourier's theorem is said to furnish an indispensable instrument in the treatment of nearly every recondite question in modern physics). In biological microscopy, fluorescence contrast is perhaps the most popular form of contrast. The reason for popularity of fluorescence is not only its molecular specificity, but the linear image formation model that applies to fluorescence imaging. Under several experimental conditions, the image produced by a fluorescence microscope is the linear convolution of the specimen's fluorophore density with the point spread function of the system. This linearity has allowed researchers to exert computational control over fluorescence imaging with methods such as deconvolution for 3D reconstruction, structured illumination for super-resolution, and adaptive optics for aberration compensation [[Pawley, 2006](#)].

There are several interesting applications where invasive fluorescent labeling need not be used, should not be used, or simply cannot be used. For such applications, measurement

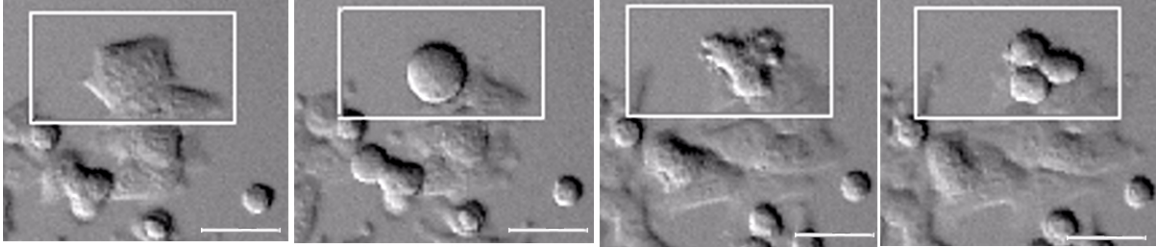


Figure 1.1: Snapshots from a time-lapse DIC images of FAT116 cells (HCT116 cells over-expressing FAT10) show that over-expression of FAT10 induces a single cell to divide into three rather than two. Scale-bar: 10  $\mu$ m. Collaborators: Jianwei Ren and Caroline Lee, National Cancer Center of Singapore. The raw image sequence is shown in media 1.1, in which ROI is marked with white rectangle.

of the intrinsic properties of phase (i.e., optical thickness) and birefringence (i.e., anisotropy in optical thickness) is required. The phase is a reliable measure of dry-mass, whereas the birefringence is a reliable measure of molecular order [Inoué and Spring, 1997]. Following are but a few examples of such applications.

- Fluorescent labeling need not be used for imaging gross errors in mitosis due to influence of certain genes: Long-term live cell imaging is often required in cancer research to estimate the effect of gene-of-interest on cell division, because cancer is essentially deregulated cell division. The large scale errors in cell division can be measured by imaging the condensed chromosomes and general cellular morphology, as illustrated by fig. 1.1. In this example, we noticed a surprising result that over-expression of a protein implicated of interfering with mitotic checkpoint machinery (FAT10) [Ren et al., 2006], caused a cell to divide in three rather than two. This observation was not made earlier with the same cell line in which the nuclear histone (H2B) was labeled with GFP. Thus, non-invasive phase microscopy can provide useful insights in long-term live imaging experiments.
- Fluorescent labeling should not be used for imaging soft-tissue with X-rays: X-ray absorption has been used mainly to image dense structures such as bone. To examine soft-tissues, sometimes X-ray contrast agents are used in the procedure called fluoroscopy. However, the contrast agents have detrimental effects on health. Therefore, in the field of X-ray imaging phase contrast that reveals the structure of soft-tissue

using either coherent synchrotron sources and incoherent laboratory sources has become interesting. In fact, several researchers believe that the ability to image phase (soft-tissue) with X-ray in medical settings could lead to ‘the biggest change in medical x-ray imaging since the invention of computed tomography’ [Lewis, 2004].

- Fluorescent labeling cannot be used for imaging an oocyte which is to be inseminated during the IVF (In-vitro fertilization) procedure: In the IVF procedure, clinicians need to assess the competence of the oocyte to increase the chances of successful fertilization and decrease the chances of multiple pregnancies incurred due to over-implantation. Clearly, such an analysis prohibits use of fluorescent labeling. It has been shown that the fertilization competence of the oocyte can be assessed by measuring the birefringence of its spindle of [Wang et al., 2001] with liquid crystal-based polarization microscope [Oldenbourg, 2005].

Biological microscopy received significant boost when Zernike invented [Zernike, 1955] phase contrast that allowed visualization of cellular processes within live cells. After his invention, several methods for visualization of phase information have been developed, of which Nomarski’s differential interference contrast (DIC) [Nomarski, 1960] and Hoffman’s modulation contrast [Hoffman and Gross, 1975] are but a couple of examples. Although methods of phase contrast and DIC have been available for six decades, accurate computation of the image of a known specimen and interpretation of the image of an unknown specimen have remained challenging due to lack of insightful forward analysis for these methods [Martin, 1966, Wilson and Sheppard, 1984, Singer et al., 2005]. Methods such as phase contrast, DIC, and Hoffman modulation contrast are designed for qualitative visualization rather than quantitative measurement and hence make it difficult to do objective analysis of biological processes. There is an emerging demand for an optical toolkit that allows quantitative measurement of phase, not just its visualization. To facilitate quantitative phase microscopy, we have developed an accurate, computationally efficient, and physically meaningful image formation model for phase imaging methods.

The connotation of the term ‘quantitative phase microscopy’ should be clarified at this stage. In biological applications, the term implies the ability to measure the biological

feature of interest (e.g., size of nucleus with respect to size of cytoplasm) without having to introduce any label, whereas in optical metrology, the same term implies the measurement of optical thickness of transmissive specimen or the surface profile of the reflective specimen. In several biological applications, one does not need to measure the optical thickness of the specimen, but rather an accurate *representation* of the optical thickness. By measuring the accurate representation of optical thickness, one can segment the features of interest. Segmentation is the typical starting point of most of the image-based biological analyses. Currently, fluorescent labeling is used even for non-molecular features such as the nucleus and cell membrane, to allow their automated segmentation. Having the perfect fluorescent labeling of such global features is difficult and more importantly, invasive. Applications that I discuss in this thesis are aimed at measuring phase-distribution at high resolution, high speed, and high signal to noise ratio. These measurements facilitate quantitative biological analyses as illustrated in Chapter 6. The phase retrieved by currently available partially coherent approaches (including those presented in this thesis) are affected by the filtering effects of the microscope. To make these methods quantitative in the sense of optical metrology, development of appropriate inversion algorithms is needed that account for filtering due to finite apertures of the microscope. The forward model presented in this thesis provides a useful framework to develop such inverse algorithms.

## 1.2 Partially coherent imaging

Imaging of the specimens that are not self-luminous may be broadly classified in two categories based on the type of illumination employed [Kou et al., 2010]:

- **Coherent phase imaging:** Methods that use spatially coherent illumination (e.g. laser) produce an amplitude in which the phase is linearly dependent on the optical path length (OPL) of the specimen, allowing measurement of phase information from which refractive index or thickness can be recovered. Although fast, direct single-shot holography has poor 3D imaging performance. Specifically, the spatial-frequency coverage of single-shot holography along the axial direction is inadequate to provide true 3D imaging [Kou and Sheppard, 2007]. One way to enhance 3D imaging is to

introduce tomography, through either object rotation or illumination scanning [Vertu et al., 2009, Kou and Sheppard, 2008, 2009]. Tomography enhances the 3D resolution by sequentially imaging the specimen from several directions. Coherent illumination is sensitive to imperfections in the light path, which exhibit themselves in the form of speckle noise and mottle. Moreover, the direct measurement of phase is wrapped and unwrapping procedure is sensitive to noise [Ghiglia and Pritt, 1998].

- **Partially coherent phase imaging:** On the other hand, performance of phase imaging systems can be improved by employing *simultaneous* illumination from a large range of directions. Such an illumination is engineered by using an incoherent source in conjunction with high-NA illumination optics, leading to partially coherent field at the specimen plane. Partially coherent methods, in contrast to coherent methods, produce an image which depends bi-linearly <sup>1</sup> on the specimens transmission [Hopkins, 1953, Sheppard and Choudhury, 1977, Wilson and Sheppard, 1984]. These methods can be designed to be sensitive to the gradient or curvature of the specimen phase, allowing retrieval of the phase via integration. Phase contrast, modulation contrast, and DIC are examples of partially coherent methods. Due to simultaneous illumination from several directions, a single partially coherent image provides better lateral resolution, axial resolution, and immunity to instrumental imperfections in comparison to a coherent image. Since partially coherent methods are sensitive to gradient or curvature of the phase, the problem of phase-wrapping faced in single-shot or tomographic coherent imaging is circumvented. Experimentally, partially coherent configurations are easier to setup as they use conventional sources such as halogen lamp, mercury-arc lamp, and light emitting diodes (LED). Thus, partially coherent imaging provides some experimental advantages of tomographic coherent imaging, without requiring several measurements. Nevertheless, the simultaneous illumination with several incoherent plane-waves breaks the linearity of image formation and makes it difficult to invert the imaging process to retrieve the specimen phase.

---

<sup>1</sup>The term ‘bi-linearity’ implies that the image at a given point in the image space depends on integral over pairs of points in the specimen space

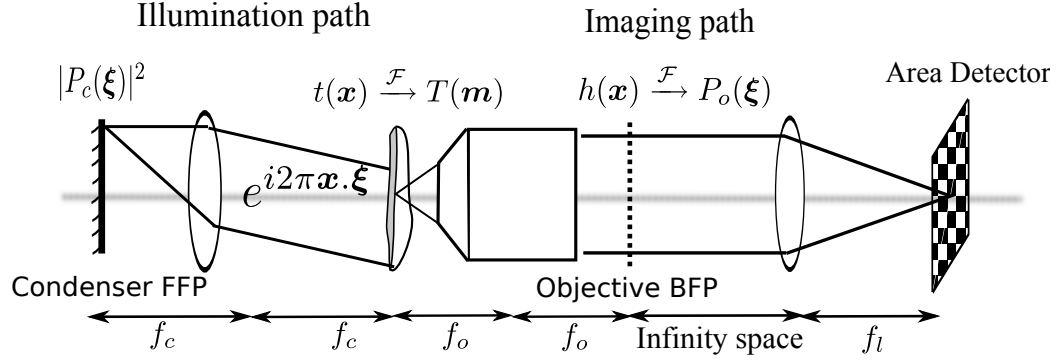


Figure 1.2: A general schematic of a partially coherent imaging system. The independent variables typeset in bold indicate two dimensional vectors.  $t(\mathbf{x})$  is the specimen's transmission,  $T(\mathbf{m})$  is the specimen's spectrum,  $P_c(\boldsymbol{\xi})$  is the pupil function of the condenser front focal plane (FFP),  $P_o(\boldsymbol{\xi})$  is the pupil function of the objective back focal plane (BFP), and  $\mathcal{F}$  indicates Fourier transform. Each point of the condenser located at  $\boldsymbol{\xi}$  illuminates the specimen with a plane-wave  $e^{i2\pi\mathbf{x}\cdot\boldsymbol{\xi}}$ .

Figure 1.2 shows a general schematic of a partially coherent imaging system. The performance of the imaging system is described by the intensity of the illumination pupil  $P_c$  and the amplitude of the objective pupil  $P_o$ . The so called coherence ratio  $S = NA_c/NA_o$  determines ‘how coherent’ the image formation is and critically affects the imaging properties. For the spatially coherent imaging system,  $S = 0$ . As  $S$  increases, the coherence of the field that illuminates the specimen reduces.

Figure 1.3 illustrates the effect of illumination with images of a stage micrometer taken with nearly coherent and partially coherent illumination along with corresponding intensity distributions in the objective back focal plane (BFP). As seen from images of the micrometer, the partially coherent image is drastically better in terms of resolution, and signal to noise ratio (SNR). In particular, the coherent noise in the form of the fringes produced by the imperfections in the light-path are observed in the coherent image, but not in partially coherent image.

It is instructive to compare the intensity distribution in the back focal plane between coherent and partially coherent illumination. In the coherent case, we clearly see the diffraction orders produced by the specimen in the back focal plane of the objective. Note that the objective aperture  $P_o(\boldsymbol{\xi})$  filters the diffraction orders that contribute to the image, and

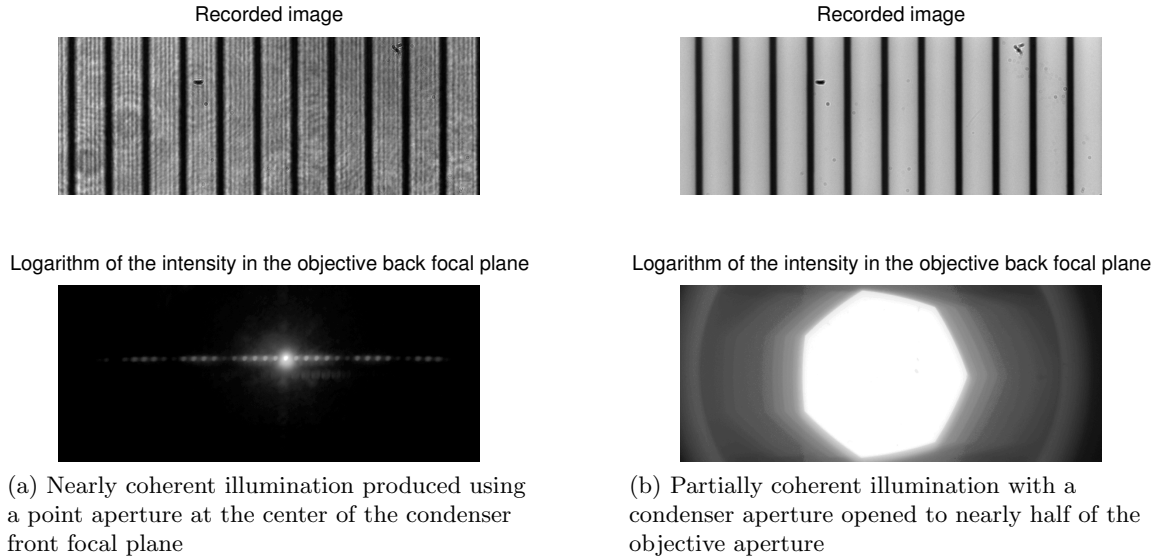


Figure 1.3: Intensity in the image plane (top row) and in the objective back focal plane (bottom row) with (a) almost coherent and (b) partially coherent illumination. The specimen is a stage micrometer with  $10\mu\text{m}$  spacing that is usually supplied with Zeiss microscopes. The spatially coherent illumination was created by placing a piece of paper with a hole at the center in the condenser turret. To avoid spectral blur of diffraction orders, the halogen lamp illumination was filtered through 546/10nm filter. I used 63X 1.4NA objective to capture the maximal number of diffraction orders. The observable dynamic range of intensities in the back focal plane was much higher than what could be recorded by the available 12-bit camera. Therefore, imaging of back focal plane was carried out at several exposures – starting with the lowest exposure which properly imaged the brightest, i.e., un-diffracted order, and increasing the exposure by a factor of 2 sequentially. The images acquired at different exposures (as shown in media 1.3) were combined into a single high dynamic range image. Note that increasing the exposure by a factor of 2 corresponds to acquiring additional 1-bit of dynamic information. The back focal plane images shown above are obtained by taking logarithm of the high dynamic range data. The experiment was carried out using Zeiss Axiovert 200M at Marine Biological Laboratory. Thanks to Rudolf Oldenbourg for suggesting the experiment.

hence acts as a low-pass filter. This intensity distribution is nothing but the filtered power spectrum,  $|T(\mathbf{m})P_o(\mathbf{m})|^2$ , of the specimen's transmission. Apart from the spectral peaks produced by the lines spaced apart at the distance of  $10\mu\text{m}$ , we also observe a broader variation (which follows the  $\text{sinc}^2$  pattern) due to finite width of the lines.

Unlike the coherent case, the diffraction orders produced by the grating overlap in the partially coherent case. The un-diffracted light (or zero spatial frequency of the specimen) produces the image of the condenser aperture, seen as the hexagonal shape at the center of the objective BFP in fig. 1.3b. Other spatial frequencies ( $\mathbf{m}$ ) of the specimen produce a shifted image of the condenser aperture,  $P_c(\xi - \mathbf{m})$  in the BFP, each of which appears as a shifted hexagon in fig. 1.3b. Taking an alternate view, one may say each point of the hexagonal condenser aperture  $P_c(\xi)$  produces a shifted version of the specimen's spectrum  $T(\mathbf{m} - \xi)$  in the objective BFP, because of the phase-ramp of  $e^{i2\pi\mathbf{x}\cdot\xi}$  that it imposes on the specimen. The filtered version of the shifted spectrum,  $T(\mathbf{m} - \xi)P_o(\mathbf{m})$  forms the image due to the point  $\xi$  in the condenser aperture. Since the image formation by each point of the condenser aperture is spatially coherent, the intensity at the image plane due to source point  $\xi$  can be written as,

$$\begin{aligned} I_\xi(\mathbf{x}) &= |\mathcal{F}_{\mathbf{m}}^{-1}[T(\mathbf{m} - \xi)P_o(\mathbf{m})]|^2 \\ &= \left| \int T(\mathbf{m} - \xi)P_o(\mathbf{m})e^{2\pi i\mathbf{m}\cdot\mathbf{x}}d\mathbf{m} \right|^2 \\ &= \iint T(\mathbf{m}_1 - \xi)T^*(\mathbf{m}_2 - \xi)P_o(\mathbf{m}_1)P_o^*(\mathbf{m}_2)e^{2\pi i(\mathbf{m}_1 - \mathbf{m}_2)\cdot\mathbf{x}}d\mathbf{m}_1d\mathbf{m}_2 \quad (1.1) \end{aligned}$$

In above equations, the amplitude spectrum of the image is linearly dependent on the amplitude spectrum of specimen. However, the intensity spectrum consists of *mixing* of pairs of spatial frequencies in the amplitude spectrum of the specimen. If above relationships are expressed in space domain (as shown in Ref. [Singer et al., 2005, Sec.21.3.1]), the intensity at each point in the image is seen to be dependent on pairs of points of the specimen amplitude. Such a dependence of the image intensity on amplitude of the specimen is called 'bi-linear' (i.e., linear in pairs) dependence.



In partially coherent imaging, mutual incoherence of the condenser points leads to the incoherent superposition of the intensity due to each point. Therefore, the total image intensity is given as,

$$I(\mathbf{x}) = \int |P_c(\boldsymbol{\xi})|^2 I_{\boldsymbol{\xi}}(\mathbf{x}) d\boldsymbol{\xi} \quad (1.2)$$

Due to superposition of intensities, the observed intensity is not linear in the specimen transmission. However, bi-linear dependence of the intensity on specimen transmission still holds as can be seen by substituting eq. 1.1 in eq. 1.2:

$$I(\mathbf{x}) = \int |P_c(\boldsymbol{\xi})|^2 \iint T(\mathbf{m}_1 - \boldsymbol{\xi}) T^*(\mathbf{m}_2 - \boldsymbol{\xi}) P_o(\mathbf{m}_1) P_o^*(\mathbf{m}_2) e^{2\pi i(\mathbf{m}_1 - \mathbf{m}_2) \cdot \mathbf{x}} d\mathbf{m}_1 d\mathbf{m}_2 d\boldsymbol{\xi} \quad (1.3)$$

The condenser points located far from the optical axes bring the information about the higher spatial frequencies of the specimen within the imaging pupil. Therefore, partially coherent imaging provides higher resolution (more information about the specimen) than does coherent illumination. In the above equations, the contributions of the specimen and the system are not separated. However, a change of variable  $\mathbf{m} - \boldsymbol{\xi} = \mathbf{m}'$  separates the contribution of the specimen spectrum and the system pupils, leading to the notion of the transmission cross-coefficient (TCC) introduced by Hopkins [Hopkins, 1953].

Due to experimental advantages of high resolution, high light throughput, high signal to noise ratio, and ease of setup, partially coherent methods such as DIC have been popular for wide range of biological applications in optical [Inoué and Spring, 1997, Inoué, 1999] microscopy. Recently, X-ray microscopy [von Hofsten et al., 2008, Olivo and Speller, 2007, Lewis, 2004] has also seen a surge of interest in partially coherent phase imaging with laboratory sources. In optical lithography, engineering of partially coherent illumination has long been pursued to push the finest feature size that can be etched [Schellenberg, 2004, Wong, 2001]. For all of these fields, it is attractive to develop *quantitative* imaging methods based on partially coherent illumination. However, due to the difficulty of working with bi-linear image formation, quantitative partially coherent approaches have emerged only recently.

In biological microscopy, current partially coherent approaches for retrieval of the specimen properties ignore full bi-linear image formation and use simplifying assumptions, chiefly the assumption of a slowly varying specimen [Lessor et al., 1979, Arnison et al., 2004, King et al., 2008, Pfeiffer et al., 2006, Mehta and Sheppard, 2009b]. I discuss these assumptions and their use for quantitative imaging in Chapter 6.

### 1.3 Phase-space perspective of partially coherent imaging

Phase-space or ‘joint’ representations, of which Wigner distribution is a well-known example, are widely used in signal analysis [Cohen, 1995] and optics [Testorf et al., 2006]. Phase-space representations originated in quantum physics to represent the probability of a particle possessing a position and momentum simultaneously [Wigner, 1932]. The idea was imported in the field of signal analysis by Gabor [Gabor, 1948] and Ville [Ville, 1958]. The motivation for using these ideas was provided by the need to analyze the change in the signal frequency as a function of time in applications where the representation in terms of time or frequency alone does not provide useful insights. The last sentence of the abstract of Ville’s paper [Ville, 1958] states: “These notions of instantaneous frequency and of the instantaneous spectrum are introduced to furnish a firm theoretical basis for studies of frequency modulation, ... , **and in a general way, of all problems for which classical harmonic analysis furnishes a description which departs too far from physical reality**”.

A phase-space distribution is a bi-linear function of the signal of interest and attempts to describe how the spectrum of the signal changes as a function of time (in signal analysis) or space (in most of the optical analysis). Unlike bi-linear representation in eq. 1.3, the pairs of points used in phase-space representations are related by center and difference coordinates. This can be appreciated from the definition of the Wigner distribution of the specimen transmission below:

$$\begin{aligned} W(\mathbf{m}, \mathbf{x}) &= \int t(\mathbf{x} + \frac{\mathbf{x}'}{2}) t^*(\mathbf{x} - \frac{\mathbf{x}'}{2}) e^{-2\pi i \mathbf{m} \cdot \mathbf{x}'} d\mathbf{x}' \\ &= \int T(\mathbf{m} + \frac{\mathbf{m}'}{2}) T^*(\mathbf{m} - \frac{\mathbf{m}'}{2}) e^{-2\pi i \mathbf{m}' \cdot \mathbf{x}} d\mathbf{m}'. \end{aligned} \quad (1.4)$$

Note the symmetry of the definition of the Wigner distribution in terms of the specimen transmission and its spectrum. In the above equation  $\mathbf{x}$  and  $\mathbf{m}$  are ‘central’ co-ordinates in space and spatial-frequency, respectively. Similarly,  $\mathbf{x}'$  and  $\mathbf{m}'$  are ‘difference’ co-ordinates.

The Wigner distribution possesses several fundamentally useful properties [Cohen, 1995], the chief among them is that the space and spatial-frequency marginals<sup>2</sup> of the Wigner distribution lead to the magnitude square of the signal and the power spectrum of the signal, respectively. The integration of the Wigner distribution along the frequency axis leads to a function of space which is called the space marginal (since it can be displayed in the margin along the space axis). Thus, the space marginal is defined as  $\int W(m, x) dm$  and the frequency marginal as  $\int W(m, x) dx$ . An additional useful property is that the Wigner distribution is shift invariant with respect to time and frequency shifts in the signal.

The phase-space perspective has led to significant insights in the study of the propagation and transformation of optical fields with any state of coherence [Bastiaans, 2009, 2008, Singer et al., 2005, Testorf et al., 2006, Lohmann et al., 2004]. However, an insightful and computationally efficient phase-space description of transfer properties of partially coherent systems was not available. This is the gap that we have attempted to fill with our model [Mehta and Sheppard, 2010a,c].

To illustrate the meaning of the phrase ‘description of transfer properties in phase-space,’ I describe a phase-space interpretation of coherent image formation. As discussed above, in the coherent imaging system, the image amplitude depends linearly on the specimen amplitude, but the image intensity depends bi-linearly on the specimen amplitude. Figure 1.4 simulates imaging of an amplitude grating which is illuminated by a plane-wave at 546nm wavelength and imaged with a 0.5 NA objective using the standard PSF model well as the line spread-function (LSF) model. The simulated specimen consists of a stretch of grating with  $2\mu\text{m}$  period and a stretch with  $1\mu\text{m}$  period. Note that I have plotted the quantities in the normalized units of  $\lambda/\text{NA}_o$ .

Since the illumination is coherent, the image amplitude is given as the convolution of the

---

<sup>2</sup>A marginal of a phase-space distribution is the integral projection along one of its dimension. For our purpose, the integral along the space (which is a function of the spatial frequency) is the spatial-frequency marginal. The integral along the spatial-frequency is the space marginal. The term ‘marginal’ reflects the fact that after the integration the result may be placed in the margin of the phase-space distribution.

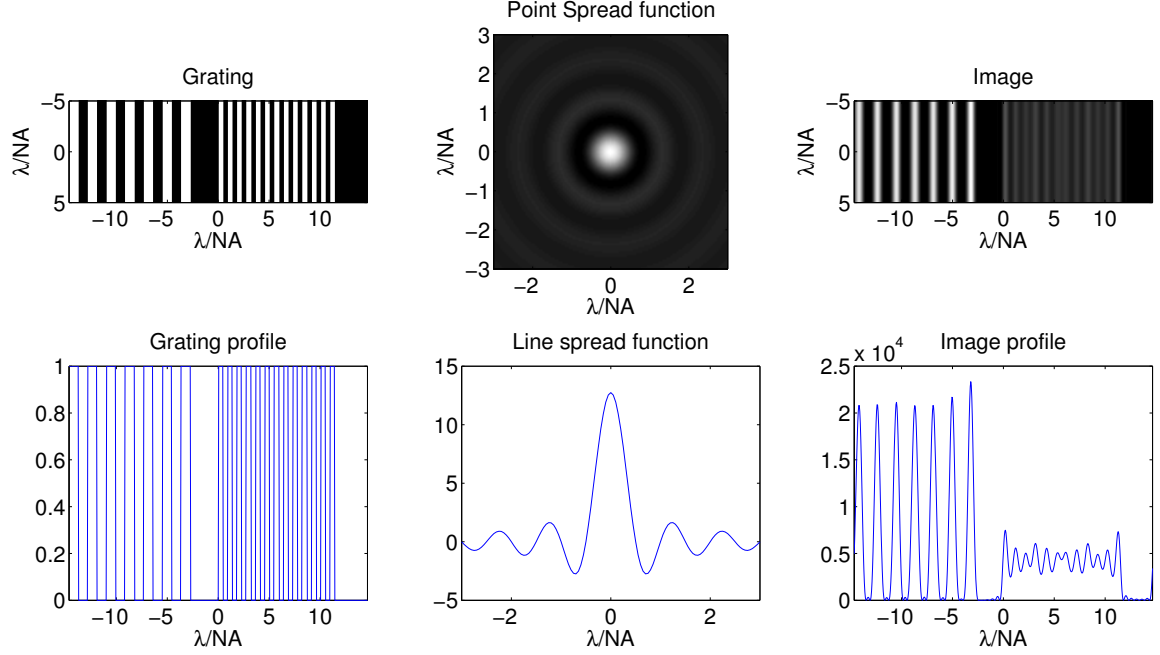


Figure 1.4: Imaging of 1D specimen using the point-spread function (top row) and line-spread function (bottom row) representations. Note that the left most column is the image intensity and not the image amplitude. All axes are expressed in the normalized units of  $\lambda/\text{NA}_o$ .

specimen with the PSF. The image intensity shown in the image is obtained as a magnitude square of the image amplitude. In terms of the PSF  $h(\mathbf{x})$ , the image  $I(\mathbf{x})$  is given by,

$$I(\mathbf{x}) = |i(\mathbf{x})|^2 = |t(\mathbf{x}) \otimes h(\mathbf{x})|^2. \quad (1.5)$$

For the one dimensional specimen used here, the image profile  $I(x)$  can be expressed as a convolution of the specimen profile  $t(x)$  and the LSF  $l(x)$  as follows.

$$I(x) = |i(x)|^2 = |t(x) \otimes l(x)|^2. \quad (1.6)$$

The LSF is the projection of the PSF along the direction in which the specimen is constant. I have deliberately chosen a one dimensional problem so that the two dimensional phase-space quantities can be plotted conveniently.

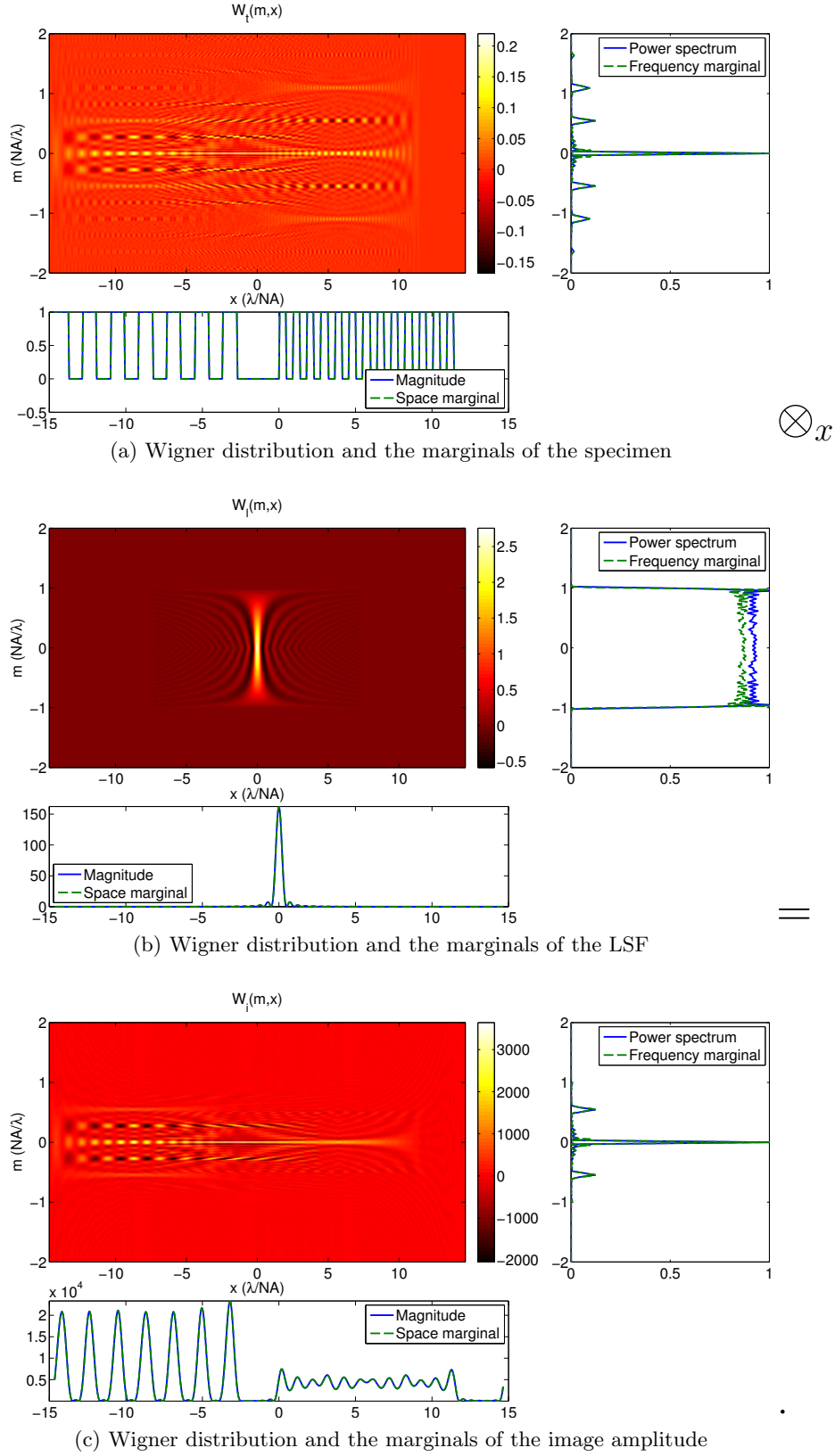


Figure 1.5: Phase-space description of transfer properties of coherent image formation shown in fig. 1.4. See the text for details.

If we express the convolution  $i(x) = t(x) \otimes l(x)$  using Wigner representation, we obtain,

$$W_i(m, x) = W_t(m, x) \otimes_x W_l(m, x), \quad (1.7)$$

where,  $W_*(m, x)$  indicates the Wigner distribution of the quantity  $*(x)$ . Note that the Wigner distribution of the image amplitude is related to the Wigner distribution of the specimen and the Wigner distribution of the LSF by the convolution along  $x$  dimension, but filtering along  $m$  dimension. Figure 1.5 simulates the image formation according to the above equation. The Wigner distribution of the specimen profile (fig. 1.5a) is blurred in  $x$  and filtered in  $m$  by the Wigner distribution of the system LSF (fig. 1.5b) to provide the Wigner distribution of the image amplitude (fig. 1.5c). For each of the Wigner distribution, the spatial marginal (plotted in lower margin of the distribution) provides the squared magnitude of the underlying quantity. Similarly, the frequency marginal (plotted in right margin of the distribution) provides the power spectrum of the underlying quantity. Thus, the recorded coherent image  $I(x)$  is obtained simply as the spatial marginal of the  $W_i(m, x)$ . To verify the accuracy of the Wigner distribution based computation of images, I have compared the marginals in fig. 1.5 with the corresponding magnitude squared quantity.

For partially coherent systems, Hopkins's TCC model provides a transfer function approach to image formation. The TCC accounts for both the imaging pupil and the illumination pupil, and determines how the specimen properties are affected by the system. Various discrete representations of TCC have been used widely in optical lithography for efficient image computation and optimization of mask and illumination [Yamazoe, 2008, Yamazoe et al., 2009b, Wong, 2001, Schellenberg, 2004, Yamazoe, 2010]. However, a phase-space model in the form of a 'kernel' that modifies the specimen's Wigner distribution (as illustrated for coherent case above) and captures the effects of both the imaging and the illumination pupil was not available. Due to bi-linearity of the Hopkins's TCC model (which does describe transfer properties) and phase-space representations, a connection between them had been anticipated for a long time. Our model, termed Phase-space Imager (PSI), presented in Chapters 4 and 5 establishes this connection and provides an equivalent of the point spread function for partially coherent imaging.

Figure 1.5 describes the linear image formation using a bilinear representation, which is mostly of instructional value. However, the partially coherent image formation is inherently bi-linear and hence a similar representation discussed in sec. 4.2 provides a non-redundant representation of image formation.

## 1.4 Contributions and contents of the thesis

Following are the main contributions of the thesis to the fields discussed above:

### 1.4.1 Partially coherent imaging in DIC

DIC is a polarization based shearing interferometer designed to allow interferometric imaging of the phase-gradient of the specimen with partially coherent illumination [Nomarski, 1960]. Diffraction effects due to imaging path of DIC have been studied for over three decades by assuming coherent illumination [Galbraith, 1982, Holmes and Levy, 1987, Lessor et al., 1979, Preza, 2000]. Some effort has also been put in understanding the role that the illumination plays in DIC [Nomarski, 1969, Sheppard and Wilson, 1980, Cogswell and Sheppard, 1992, Preza et al., 1999]. A widely accepted model of DIC due to Preza [Preza et al., 1999] assumes that illumination in DIC is the standard Köhler illumination. We have corrected this assumption by elucidating that the condenser-side prism alters the coherence of illumination in important manner. Our model provides an accurate description of diffraction effects due to both imaging and illumination in DIC. Our paper [Mehta and Sheppard, 2008] describing this study appears as sec. 2.1 in the thesis. In a similar vein, it has been assumed for three decades [Galbraith, 1982, Preza et al., 1999] that the image of a point in DIC is independent of coherence of illumination, because the point is always coherent with itself. However, we have shown that as a consequences of special coherence properties of DIC, the image of a point *does* depend on the illumination aperture. This surprising result is explained with help of experimental results and simulations based on our model in sec. 2.2.

### 1.4.2 Novel partially coherent method for quantitative phase imaging

To overcome shortcomings of DIC and phase-contrast, an attractive quantitative method of imaging phase-gradient called differential phase contrast (DPC) has been proposed in scanning electron and optical microscopy [Dekkers and de Lang, 1974, Hamilton and Sheppard, 1984, Hamilton et al., 1984]. By principle of reciprocity, we have developed a wide-field version of DPC using asymmetric illumination. The paper describing the method, called asymmetric illumination-based differential phase contrast (AIDPC), appears in sec. 3.2. I discuss imaging properties of AIDPC in light of additional experimental results in sec. 3.3.

### 1.4.3 Phase-space perspective of partially coherent imaging

To allow computation of partially coherent images and analysis of partially coherent systems in a physically meaningful way, we have developed a model called phase-space imager (PSI). The model can be considered a phase-space version of the TCC model and leads to an equivalent of the point spread function for partially coherent imaging. Our paper describing the development of the model from TCC model appears in sec. 4.1. Further development of the model described in sec. 4.2 leads to a phase-space description of partially coherent imaging that bears close resemblance to the description of coherent imaging provided in fig. 1.5. Our model allows study of imaging system of varying degrees of coherence given the knowledge of its imaging and illumination pupils. With help of the model, I have been able to compare the performance of five different partially coherent systems, that have originally been developed with different heuristic arguments. Our paper [Mehta and Sheppard, 2010c] describing this comparison appears in sec. 5.1. During the course of this research, I have developed a MATLAB toolbox for partially coherent image computation. The binary version of the toolbox is provided on DVD-ROM along with some example computations.

### 1.4.4 Biological applications of quantitative phase imaging

Due to the complexity of inverting a full bi-linear model, all partially coherent quantitative methods of biological microscopy employ simplifying assumptions. In chapter 6, I illustrate



applications of quantitative imaging with DIC and AIDPC in chapter with an assumption that the specimen is slowly varying.

Quantitative imaging requires calibration of experimental systems. The calibration of AIDPC involves only the knowledge of illumination wavelength, and the numerical apertures of the condenser and the objective. For calibrating a DIC system, we need to measure the shear and the bias in addition. We have found that the existing methods that use sub-resolution phase or fluorescent beads for calibrating a DIC microscope are either not accurate or too complex to use. We have developed a simple yet accurate method of measuring parameters of the DIC microscope from intensity measured in the BFP. The paper describing this calibration approach appears as sec. 6.1. We present a fast and robust algorithm of registering the phase-gradient images acquired with DIC and AIDPC in sec. 6.2.1. The registration is very important to obtain artifact free reconstruction of the specimen's optical path length. The experimental results demonstrating the phase-retrieval process are discussed shown in sec. 6.2.

In a unique quantitative biological study, I employ our bi-linear model for studying the dynamics of a near-resolution molecular machine called the axoneme, for which the assumption of a slowly varying specimen breaks down. Axoneme is a highly conserved molecular-machine with diameter of 250nm that consists of microtubules, dynein, and other supporting proteins. Axoneme powers the flagella and cilia of diverse cell types in diverse organisms, and observing the dynamic behaviour of axoneme has been a long-standing challenge. As presented in sec. 6.3, we analyzed the beating dynamics of axoneme by synergistic application of dark-field microscopy, simulations based on our PSI model, and quantitative image analysis.

The final chapter summarizes our results and also discusses future directions of the research enabled by our work.

## 1.5 Organization of the thesis

The content of the thesis is outlined in the previous section. Here, we note how the content is organized. Chapters 2-6 each mainly consist of one of our published papers. Each of these

chapters begins with a short summary, followed by the published paper, further followed by relevant unpublished results. Since the main content for the thesis is provided by our published papers, the introductory material is repeated to some degree, which the author hopes is not too distracting to the reader. An effort has been made so that chapters can be read independently. Nevertheless, the additional content and the papers are organized to bring out the connection of the papers to the overall theme of the thesis. Table 1.1 lists the published papers, their citation keys, and the sections in which they appear.

To facilitate easy reading, I use certain conventions to reference different components of the thesis. Each paper is typeset as a section within the chapter and is also paginated. Thus, the pages of the papers appear with the original page number as in the journal as well as the page number (within the thesis). For accessible referencing of figures, tables, and equations outside of the papers, their numbers are prefixed with the chapter number. Thus, the first figure of chapter 2 (not within the paper) is referred to as fig. 2.1, while the third equation in this chapter is referred to as eq. 1.3. To refer to the paper, we simply use the citation key of the paper mentioned in table 1.1. The symbols, abbreviations, and the frequently appearing terms are collected in the Nomenclature (page xii) for quick reference.

The multimedia files are referred to in the thesis as ‘media’. Instead of referring the media files by sequential numbers, I refer to them using the number of the figure to which they are associated.

### 1.5.1 Multimedia accompanying the thesis

Apart from the PDF copy of the thesis, quicktime movie files are uploaded in the electronic thesis database to allow access to the multimedia referred to in this thesis. These files should be viewable with free quicktime player on all platforms.

**Multimedia from published papers:** The media files from the published papers (typeset verbatim in the thesis) are not included with the thesis and can be accessed from the publisher’s website.

**Multimedia outside of published papers:** The media files referred to in the thesis outside of the papers are placed in a single folder. The names of the media files are

prefixed with the numbers of the figures with which they are associated. I refer to the media file with the same number as the corresponding figure. For example, media 1.3 is related to the fig. 1.3. These media files are collected into a folder named MediaOutsidePublishedPapers.

Published paper	Section	Key
S.B. Mehta and C.J.R. Sheppard, “Partially coherent image formation in differential interference contrast (DIC) microscope,” <i>Opt. Express</i> , vol. 16, 2008, pp. 19462-19479.	Sec. 2.1	[Mehta and Sheppard, 2008]
S.B. Mehta and C.J.R. Sheppard, “Quantitative phase-gradient imaging at high resolution with asymmetric illumination-based differential phase contrast,” <i>Optics Letters</i> , vol. 34, 2009, pp. 1924-1926.	Sec. 3.2	[Mehta and Sheppard, 2009b]
S.B. Mehta and C.J.R. Sheppard, “Phase-space representation of partially coherent imaging systems using the Cohen class distribution,” <i>Optics Letters</i> , vol. 35, Feb. 2010, pp. 348-350.	Sec. 4.1	[Mehta and Sheppard, 2010a]
S.B. Mehta and C.J.R. Sheppard, “Using the phase-space imager to analyze partially coherent imaging systems: brightfield, phase-contrast, differential interference contrast, differential phase contrast, and spiral phase contrast,” <i>Journal of Modern Optics</i> , vol. 57, 2010, pp. 718-739.	Sec. 5.1	[Mehta and Sheppard, 2010c]
S.B. Mehta and C.J.R. Sheppard, “Sample-less calibration of the differential interference contrast microscope,” <i>Applied optics</i> , vol. 49, 2009, pp. 2954-2968.	Sec. 6.1	[Mehta and Sheppard, 2010b]

Table 1.1: Our published papers that are typeset verbatim in this thesis and the sections in which they appear.

## Chapter 2

# Differential Interference Contrast

In this chapter, we present an accurate paraxial model for image formation in the differential interference contrast (DIC) microscope and a surprising but a real experimental observation that it leads to. Our paper [Mehta and Sheppard, 2008] that describes the image formation model is typeset as sec 2.1 in this chapter. The key contribution of our paper is the accurate modeling of effects of the illumination-side optics in DIC. With analytical, computational, and experimental results, we show that the existing DIC configurations may be classified according to how they illuminate the specimen. These configurations produce quite similar images when the coherence ratio ( $S = \text{NA}_c/\text{NA}_o$ ) is around 0.4. At higher coherence ratios, only the configuration due to Nomarski produces good image contrast. We clarify that a widely accepted diffraction model [Preza et al., 1999] makes wrong assumptions about how the illumination affects the image formation. Moreover, it has been assumed for three decades that the image of a point in DIC is not affected by the coherence of illumination [Galbraith, 1982, Preza et al., 1999]. This assumption appears valid because a bright point in an opaque background is always coherent with itself. However, in sec. 2.2 we show with experimental data and simulations (based on the model presented in our paper) that the image of a bright-point *does* depend on the illumination aperture. This result drives home the key point made by our image formation model.

### 2.1 Paper: Partially coherent image formation in differential interference contrast (DIC) microscope

# Partially coherent image formation in differential interference contrast (DIC) microscope

Shalin B. Mehta<sup>1,2,3,\*</sup> and Colin J. R. Sheppard<sup>1,2,4</sup>

<sup>1</sup>Optical Bioimaging Lab, Division of Bioengineering, National University of Singapore,  
7 Engineering Drive 1, Blk E3A 04-15, Singapore 117574

<sup>2</sup>Graduate Programme in Bioengineering, National University of Singapore,  
Singapore 117456

<sup>3</sup>Liver Cancer Functional Genomics Lab, Humphrey Oei Institute of Cancer Research,  
National Cancer Centre Singapore, Singapore 169610

<sup>4</sup>Department of Diagnostic Radiology, YLL School of Medicine,  
National University of Singapore, Singapore 119074

\* [shalin@nus.edu.sg](mailto:shalin@nus.edu.sg), [shalin.mehta@gmail.com](mailto:shalin.mehta@gmail.com)

**Abstract:** Some different image formation models have been proposed for Nomarski's differential interference contrast (DIC) microscope. However, the nature of coherence of illumination in DIC, of key importance in image formation, remains to be elucidated. We present a partially coherent image formation model for DIC and demonstrate that *DIC microscope images the coherent difference of shifted replicas of the specimen; but imaging of the each component is partially coherent*. Partially coherent transfer functions are presented for various DIC configurations. Plots of these transfer functions and experimental images provide quantitative comparison among various DIC configurations and elucidate their imaging properties. Approximations for weak or slowly varying specimens are also given. These improved models should be of great value in designing phase retrieval algorithms for DIC.

© 2008 Optical Society of America

**OCIS codes:** (110.2990) Image formation theory; (180.3170) Interference microscopy; (030.1670) Coherent optical effects; (050.1960) Diffraction theory

## References and links

1. F. Zernike, "How I discovered phase contrast," *Science* **121**, 345–349 (1955).
2. M. Françon and S. Mallick, *Polarization Interferometers: Applications in Microscopy and Macroscopy* (Wiley-Interscience, 1971).
3. M. Pluta, *Advanced Light Microscopy*, vol. 2 Specialized Methods (PWN-Polish Scientific Publishers, Warszawa, 1989).
4. R. D. Allen, G. B. David, and G. Nomarski, "The Zeiss-Nomarski differential interference equipment for transmitted-light microscopy," *Z. Wiss. Mikrosk.* **69**, 193–221 (1969).
5. R. D. Allen, J. L. Travis, N. S. Allen, and H. Yilmaz, "Video-enhanced contrast polarization (AVEC-POL) microscopy: a new method applied to the detection of birefringence in the motile reticulopodial network of *Allogromia laticollaris*," *Cell Motil.* **1**, 275–289 (1981).
6. C. J. R. Sheppard and T. Wilson, "Fourier imaging of phase information in scanning and conventional optical microscopes," *Phil. Trans. Roy. Soc. London, Series A* **295**, 513–536 (1980).
7. C. Cogswell and C. Sheppard, "Confocal differential interference contrast (DIC) microscopy: including a theoretical analysis of conventional and confocal DIC imaging," *J. Microsc.* **165**, 81–101 (1992).
8. C. Preza, D. L. Snyder, and J.-A. Conchello, "Theoretical development and experimental evaluation of imaging models for differential-interference-contrast microscopy," *J. Opt. Soc. Am. A* **16**, 2185–2199 (1999).

9. C. Preza, "Rotational-diversity phase estimation from differential-interference-contrast microscopy images," *J. Opt. Soc. Am. A* **17**, 415–424 (2000).
10. M. R. Arnison, C. J. Cogswell, N. I. Smith, P. W. Fekete, and K. G. Larkin, "Using the Hilbert transform for 3D visualization of differential interference contrast microscope images," *J. Microsc.* **199**, 79–84 (2000).
11. M. R. Arnison, K. G. Larkin, C. J. R. Sheppard, N. I. Smith, and C. J. Cogswell, "Linear phase imaging using differential interference contrast microscopy," *J. Microsc.* **214**, 7–12 (2004).
12. S. V. King, A. Libertun, R. Piestun, C. J. Cogswell, and C. Preza, "Quantitative phase microscopy through differential interference imaging," *J. Biomed. Opt.* **13**, 024020 (2008).
13. M. Shribak, J. LaFountain, D. Biggs, and S. Inoué, "Quantitative orientation-independent differential interference contrast (DIC) microscopy," *Proceedings of SPIE* **6441**, 64411L (2007).
14. J. A. O'Sullivan and C. Preza, "Alternating minimization algorithm for quantitative differential-interference contrast (DIC) microscopy," *Proceedings of SPIE* **6814**, 68140Y (2008).
15. Z. Kam, "Microscopic differential interference contrast image processing by line integration (LID) and deconvolution," *Bioimaging* **6**, 166–176 (1998).
16. M. Françon, *Optical Interferometry* (Academic Press, 1966).
17. O. von Hofsten, M. Bertilsson, and U. Vogt, "Theoretical development of a high-resolution differential-interference-contrast optic for x-ray microscopy," *Opt. Express* **16**, 1132–1141 (2008). <http://www.opticsexpress.org/abstract.cfm?URI=oe-16-2-1132>.
18. R. Danz, A. Vogelgsang, and R. Kathner, "PlasDIC - a useful modification of the differential interference contrast according to Smith/Nomarski in transmitted light arrangement," *Photonik* (2004). [www.zeiss.com/C1256F8500454979/0/366354E1E8BA8703C1256F8E003BBCB9/\\$file/plasdic\\_photonik\\_2004march\\_e.pdf](http://www.zeiss.com/C1256F8500454979/0/366354E1E8BA8703C1256F8E003BBCB9/$file/plasdic_photonik_2004march_e.pdf).
19. R. Danz, P. Dietrich, A. Soell, C. Hoyer, and M. Wägener, "Arrangement and method for polarization-optical interference contrast," (2006). US Patent No. 7046436.
20. M. Pluta, *Advanced Light Microscopy*, vol. 1 Principles and Basic Properties (PWN-Polish Scientific Publishers, Warszawa, 1988).
21. H. H. Hopkins, "On the diffraction theory of optical images," *Proc. R. Soc. Lond. A, Math. and Phys. Sci.* **217**, 408–432 (1953).
22. C. J. R. Sheppard and A. Choudhury, "Image formation in the scanning microscope," *J. Mod. Opt.* **24**, 1051–1073 (1977).
23. M. Born and E. Wolf, *Principles of Optics: Electromagnetic Theory of Propagation, Interference and Diffraction of Light*, 7th ed. (Cambridge University Press, Cambridge, 1999).
24. A. A. Lebedeff, "L'interféromètre à polarisation et ses applications," *Rev. d'Opt* **9**, 385–413 (1930). ("Polarization interferometer and its applications").
25. F. H. Smith, "Interference Microscope," (1952). US patent no. 2601175.
26. G. Nomarski, "Microinterféromètre différentiel à ondes polarisées," *J. Phys. Radium* **16**, 9–13 (1955). ("Differential microinterferometer with polarized waves").
27. M. Françon, "Polarization interference microscopes," *Appl. Opt.* **3**, 1033–1036 (1964).
28. P. Munro and P. Török, "Vectorial, high numerical aperture study of Nomarski's differential interference contrast microscope," *Opt. Express* **13**, 6833–6847 (2005). <http://www.opticsexpress.org/abstract.cfm?URI=oe-13-18-6833>.
29. J. W. Goodman, *Introduction to Fourier Optics*, 2nd ed. (McGraw-Hill, New York, 1996).
30. T. Wilson and C. J. R. Sheppard, "Coded apertures and detectors for optical differentiation," in *Int. Optical Computing Conference*, vol. 232, pp. 203–209 (Washington DC, 1980).
31. T. Wilson and C. J. R. Sheppard, *Theory and Practice of Scanning Optical Microscopy* (Academic Press, London, 1984).
32. B. Möller, "Imaging of a straight edge in partially coherent illumination in the presence of spherical aberrations," *J. Mod. Opt.* **15**, 223–236 (1968).
33. C. Preza, "Phase estimation using rotational diversity for differential interference contrast microscopy," Ph.D. thesis, Washington University (1998).

## 1. Introduction

Unstained biological specimens usually do not alter the amplitude of the incident light, i.e., they are phase specimens. Usually, detectors (eye, camera etc.) are sensitive only to the intensity. Hence, visualization of phase specimen requires some special method to convert phase information to intensity information. Zernike in 1930 realized that diffracted light from phase specimens is  $\lambda/4$  out of phase with the direct light [1]. He noted that to observe the phase information contained in the diffracted light "all one has to do is to throw the diffraction image on a coherent background. . .", which he created using narrow annular illumination that was delayed and attenuated suitably in the back focal plane of the objective. Whereas phase contrast restricts

the illumination and imaging apertures for producing an interference effect, Nomarski's Differential Interference Contrast (DIC) is a wavefront shearing interferometer [2, Ch. 6] [3, Ch. 7] that allows imaging with large illumination aperture. Larger condenser apertures result in higher lateral resolution and better depth discrimination which have contributed much to the popularity of Nomarski's DIC.

Currently, image formation models of DIC are of great interest as they are prerequisite to:

- accurate interpretation of DIC images in terms of specimen properties [4–8].
- quantitative retrieval of optical path length (i.e., phase) and absorption (i.e., amplitude) information from DIC images [9–13]
- improving DIC images by restoration [14, 15]

In Nomarski DIC transmission microscope, the polarization of the illumination is manipulated by a polarizer and a modified Wollaston prism to produce two orthogonally polarized, but spatially coherent, beams which have a minute angular split between them [4]. These beams, after being focused by the condenser, illuminate the specimen a small (sub-resolution) distance apart from one another. After these beams traverse the specimen and the objective, they are brought in spatial registration by another modified Wollaston prism, allowing them to interfere. Due to the spatial coherence, upon interference, a wave-field that depends on the phase difference between these two beams as well as their amplitudes is produced. The analyzer selects the interference term. Visibility of interference fringes (as defined by Young) is proportional to the spatial coherence between these two beams [16, Ch. 2, Ch. 7]. Effectively, the interference term represents subtraction of two laterally shifted and phase delayed replicas of the wavefront after the specimen [3, Sec. 7.2]. After being collected by the tube lens, the interference term results in an image that has phase-gradient contrast and hence a shadow-cast effect.

Although the requirement that the two beams need to be spatially coherent is well appreciated in geometric optics models of DIC, it is not always accounted for properly in diffraction based image formation models. For example, the most recent model for DIC that accounts for partially coherent illumination assumes that the coherence properties of Nomarski's DIC are the same as conventional brightfield imaging [8, Fig 7]. In this paper, we aim to elucidate the effects of coherence on the image formation properties of DIC microscope.

Interestingly, various DIC configurations differ in the coherence of the illumination employed. We model following DIC configurations in detail using scalar partially coherent image formation theory, whose lightpaths are shown schematically in Fig. 1:

- Nomarski's DIC with two Wollaston prisms (henceforth called Nomarski-DIC)
- A DIC microscope without a condenser-side Wollaston prism (henceforth called Köhler-DIC). Köhler-DIC configuration is not usually employed for visible light imaging, but a similar configuration has been developed as an X-ray DIC microscope [17].
- PlasDIC system developed by Zeiss [18, 19], which consists of a slit aperture in the condenser front focal plane (FFP) and a combination of polarizer, prism and analyzer inserted in objective back focal plane (BFP). As described in Sec. 3, PlasDIC can be modelled as a special design of the Köhler-DIC configuration.

In section 2, the coherence of various illumination methods and its effects on image formation are discussed. In the same section, the historical development of various DIC configurations is briefly reviewed to gain additional perspective of the relationship between various DIC configurations. In subsection 2.4, existing models of Nomarski-DIC are compared and their accuracy is considered. In section 3, we develop appropriate models for three DIC configurations in the

unifying framework of image formation in the spatial frequency domain. Complete partially coherent transfer functions are presented, for the first time to our knowledge, in sections 4 and 5 for various in-focus DIC configurations without assuming that object is either slowly varying or weak. Approximations for weak and slowly varying specimens are also given. Relationship between symmetry of the transfer functions and the contrast observed in the image is clarified with experimental images. The last section summarizes the results.

## 2. DIC configurations and existing image formation models

Image formation in DIC has usually been described by considering the propagation of light from the condenser FFP to the image plane. However, it is instructive to segregate the objective-side and the condenser-side light paths for various DIC configurations to illustrate effects of the coherence of illumination on image formation. Figure 1 depicts light paths for Köhler-DIC, Nomarski-DIC and PlasDIC configurations segmented in three key parts - illumination path, degree of coherence at the specimen plane, and imaging path. The figure also introduces the notation employed throughout the paper.

### 2.1. Objective-side light path

All three configuration share a similar objective-side light path. In all configurations, the objective-side Wollaston prism ( $W_o$ ), located in the BFP of the objective and sandwiched between crossed polarizers  $P_c$  and  $P_o$ , causes wavefront shear [20, Fig. 1.82]. Polarizer ( $P_c$ ) is employed before the FFP of the condenser in Köhler-DIC and Nomarski-DIC or just before objective BFP in PlasDIC. The prism  $W_o$  introduces angular shear of  $2\varepsilon$  in the wavefront, which corresponds to a lateral shear of  $2\Delta$  in the specimen plane, which is by design smaller than the resolution limit.

In effect, the prism  $W_o$  combines (appropriately) polarized wavefronts that arrive at the objective BFP at an angle  $2\varepsilon$  with respect to one another, i.e., it causes coherent vector addition of amplitudes that have propagated from points separated by  $2\Delta$  in the specimen plane. In Köhler-DIC and PlasDIC, these wavefronts (indicated by dashed and solid lines in Fig. 1(b) and 1(c)) are parallel polarized, whereas in Nomarski-DIC (Fig. 1(a)) such wavefronts are orthogonally polarized.

If the two wavefronts emerging from  $W_o$  (now polarized at  $0^\circ$  and  $90^\circ$  as shown in Fig. 1) have not experienced any relative phase shift, the resultant wavefront is linearly polarized. If the two component wavefronts have the same amplitude (which happens when  $P_c$  and  $P_o$  are set at extinction as is usual practice) the direction of polarization of the resultant wavefront is the same as the direction of the polarizer  $P_c$ . The specimen induced space-varying phase difference ( $\theta$ ) between these two wavefronts affects the ellipticity of polarization of the resultant wavefront. A constant phase difference ( $2\phi$ ) can be deliberately introduced as a bias to the phase difference induced by specimen. The analyzer ( $P_o$ ) which is crossed to  $P_c$  rejects the common term polarized in the direction of  $P_c$  and selects the interference term, increasing the contrast of the interference fringes. Note that the specimen induced phase difference  $\theta$  is proportional to the local phase gradient of the specimen because  $2\Delta$  is sub-resolution. In Nomarski-DIC, usually the bias is introduced by lateral movement of the prism  $W_o$ , and the same holds true for Köhler-DIC and PlasDIC.

### 2.2. Coherence of illumination

In full-field transmission systems, only the objective aperture performs imaging, whereas the condenser aperture controls the coherence of illumination and thus has an indirect effect on the imaging properties. The coherence of the imaging system varies with the coherence ratio,



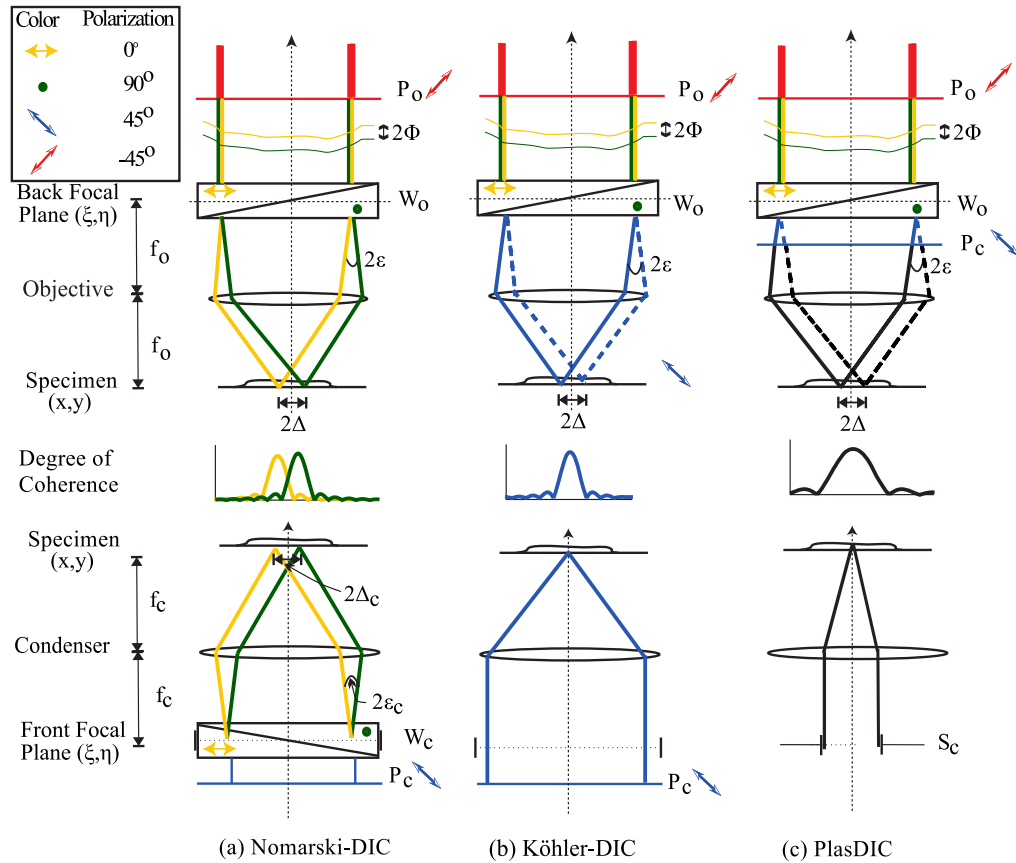


Fig. 1. Comparison of light paths in the direction of shear for three DIC configurations. Imaging in the orthogonal direction is conventional. For simplicity, Wollaston prisms are shown instead of modified Wollaston prisms employed in DIC. The direction of polarization of light in the plane normal to the optical axis is color coded as shown in the legend at top-left. Black line indicates un-polarized light. For all configurations, the light path has been segmented in three key components - the illumination path consisting of the condenser and optical elements in its FFP, the degree of coherence in specimen plane, and the imaging path consisting of the objective and optical elements beyond the objective including the tube-lens and the eyepiece (which are not shown here). Horizontal dimensions have been greatly exaggerated for depicting sub-resolution shear with clarity. Phase bias between two wavefronts coming out of  $W_o$  is assumed to be  $2\phi$ .

$S$  defined as ratio of the numerical aperture of the condenser to the numerical aperture of the objective and affects the transfer function of the imaging system [21, 22].

In all three configurations mentioned above, producing sufficient interference contrast when two sheared wavefronts spatially overlap in the objective BFP requires that the points from which they originate on the specimen plane are illuminated with sufficient degree of coherence. Two possible means of increasing the coherence of illumination are: 1) restricting the illumination aperture with a side effect that lateral resolution and depth sectioning are compromised, and 2) employing wavefront shear with large illumination apertures which preserves resolution and depth discrimination.

In Fig. 1(b), a Köhler-DIC configuration with condenser aperture of the same size as objective aperture is shown. As shown in Fig. 1(c), PlasDIC employs a slit ( $S_c$ ) to restrict the

illumination aperture in the direction of shear. In both of these cases, the degree of coherence in the specimen plane is related to the condenser aperture geometry via the Van-Cittert Zernike theorem [23]. When shear is of the order of the resolution, the coherence between points separated by  $2\Delta$  is not sufficient for producing detectable phase gradient contrast in Köhler-DIC, whereas in PlasDIC the degree of coherence is expanded sufficiently in the direction of shear by reducing the aperture size [18, Fig. 3]. It is interesting to note that, in the area of X-ray microscopy, von Hofsten et al. [17] have proposed a DIC microscope that uses a diffractive optical element (instead of polarizing components) as a shearing objective and a condenser aperture having size of roughly 0.5 times the objective aperture. Therefore, the image formation model of Köhler-DIC should be helpful in studying the properties of the X-ray DIC microscopes.

In contrast to the other two configurations, Nomarski-DIC employs wavefront shear to coherently illuminate points separated by  $2\Delta_c$ . It employs (Fig. 1(a)) a modified Wollaston prism ( $W_c$ ) in the FFP of condenser to produce orthogonally polarized beams that have angular shear of  $2\varepsilon_c$  between them. Two orthogonally polarized beams can be considered to be independent of each other, which implies that the specimen is illuminated by individual beams in a partially coherent manner. However, the wavefronts of these two beams are mutually spatially coherent at distances  $2\Delta_c$  in the specimen plane. This nature of coherence is shown schematically in Fig. 1(a). The coherence of each wavefront at the specimen can be computed by the Van-Cittert Zernike theorem.

Here, we have assumed that the light path from the condenser FFP to the objective BFP is free from spurious birefringence. The wavefront distortions in two orthogonally polarized beams induced by birefringent background (such as a plastic substrate on which specimen may be mounted) may mask the phase gradient information due to the specimen. In such situations, Nomarski-DIC fails to produce adequate interference contrast. Zeiss's PlasDIC alleviates this problem by placing all polarization sensitive components responsible for wavefront shear after the objective, albeit with a compromise that the condenser aperture has to be narrowed down in the direction of shear to achieve sufficient degree of coherence between points separated by the shear distance.

### 2.3. Evolution of DIC

Origins of DIC lie in the polarization based shearing interferometer designed by Lebedeff [4,24] [2, Ch. 6] in 1930, which has come to be known as Jamin-Lebedeff interferometer. Lebedeff's design employed calcite prisms cemented on top of the objective and condenser to produce an image duplication system with large shear. The large shear was employed to interfere the wavefront that has passed through the specimen with the (almost flat) wavefront that has passed through the surroundings. Smith [25] proposed an image duplication microscope which employed Wollaston prisms placed in the BFP of the objective and the FFP of the condenser to produce shear. Nomarski [26, 27] improved upon Smith's design by modifying the Wollaston prisms such that they can be placed beyond the focal planes of objective and condenser lenses. More importantly, he also employed sub-resolution shear providing contrast that is proportional to phase-gradient in the direction of shear rather than phase. All these methods employ matched birefringent prisms in illumination and imaging light paths so that rays separated by the shear distance in the specimen plane experience the same total optical path length (OPL) irrespective of the angle at which they illuminate the specimen (in the absence of intentionally introduced bias  $2\phi$ .) Such a matching of OPL is called compensation and is the same requirement as the requirement of coherence between the two beams.

Interestingly, Nomarski proposed a design in his paper [26, Fig 2] where slit illumination was employed to achieve sufficient coherence. Shearing was implemented by sandwiching a Wollaston prism between crossed polarizers placed in the BFP of objective as is done in PlasDIC.

Nomarski's original design with slit aperture was very similar to current PlasDIC configuration, except that PlasDIC employs a carefully computed width for the slit.

#### 2.4. Existing image formation models

Existing image formation models concern themselves with the problem of forward image calculation in Nomarski-DIC, as it is the almost exclusively used configuration in current biological research. We briefly review the most recent models and clarify the assumptions made by them that limit their utility to specific situations. We refer to earlier models only where necessary. Fuller discussion of earlier models can be found in the papers cited here.

Sheppard and Wilson [6] and Cogswell and Sheppard [7] provided the first detailed model based on transfer function theory for conventional and confocal Nomarski-DIC microscopes. In fact, Eq. (13) of Ref. [7] provides an accurate expression for the partially coherent transfer functions for conventional Nomarski DIC. In Ref. [7], the properties of the transfer function were considered along with effects of shear and bias settings for objects that are either weak or slowly varying. In sections 3-5, the transfer function theory reported in Ref. [7] is extended to objects that need not be weak or slowly varying.

Preza et al. [8] reported spatial and spatial frequency domain models for 2D and 3D imaging in Nomarski-DIC. The spatial domain models were employed for calculating images of known specimens, but frequency domain models were not discussed in detail. Equation (1) of Ref. [8] accounts for the effects of polarizer, analyzer and objective-side Wollaston prism by defining a point spread function (PSF) that is a linear combination of laterally-shifted and phase-shifted brightfield PSFs. However, the effect of the Wollaston prism on illumination side was not accounted for. As can be noticed from Eq. (3) and Fig. 7 in Ref. [8], the illumination was assumed to be standard Köhler illumination. In effect, Preza et al.'s model is for Köhler-DIC setup shown in Fig. 1(b). This difference between assumptions made in Ref. [7] and Ref. [8] led to an erroneous conclusion in Ref. [8] that Eq. (13) of Ref. [7] represents the transfer function of the Nomarski-DIC configuration *only in the coherent limit*. Preza et al.'s model has been successfully employed, albeit with assumption of small condenser aperture of up to 0.4 times the objective aperture, for computing images of known specimens [8] and designing phase-retrieval algorithms for uniformly absorbing [9, 12] and non-uniformly absorbing [14] specimens. As will be shown with the help of full partially coherent transfer functions and cell images in sections 3-5, Köhler-DIC and Nomarski-DIC have very similar imaging properties for condenser apertures smaller than around 0.4 times the objective aperture when the shear of around half the optical resolution is used. They behave identically when coherent illumination is employed. Thus, the imaging properties of Nomarski-DIC configuration with large condenser aperture have not been fully evaluated in [8], which we attempt to address in section 3.

Munro and Török have rigorously simulated imaging properties of Nomarski-DIC [28] under coherent illumination according to high NA, vectorial diffraction theory of Richards & Wolf. However, the spatial frequency domain approach has the distinct advantage of giving insight in how specimen's transmission spectrum gets affected by the imaging system.

### 3. Accurate models for various DIC configurations

In this section, we describe spatial frequency domain models for in-focus imaging with three DIC configurations under quasi-monochromatic illumination. For the sake of continuity of argument and to clarify assumptions, some previously published equations have been re-derived in this section.

### 3.1. Köhler-DIC and PlasDIC

PlasDIC is a special design of Köhler-DIC configuration in which a slit in the direction of shear is placed symmetrically with respect to the optical axis in the FFP of the condenser. Therefore, we derive the partially coherent transfer function only for Köhler-DIC.

Assume that the amplitude point spread function (PSF) of the objective is  $h_{BF}(x, y)$  in the bright-field configuration. Where,  $(x, y)$  are co-ordinates in the specimen plane (Fig. 1). Even without the condenser-side prism the polarizing components ( $W_o$ ,  $P_c$ , and  $P_o$ ) can introduce angular shear ( $2\epsilon$ ) and phase bias ( $2\phi$ ) to the wavefront in the objective BFP. Therefore, the PSF of the objective for Köhler-DIC can be given by,

$$h_K(x, y) = R[h_{BF}(x + \Delta, y) \exp(-i\phi)] - (1 - R)[h_{BF}(x - \Delta, y) \exp(i\phi)], \quad (1)$$

where,  $R$  determines the relative amplitude of the two wavefronts.  $R$  is adjusted by rotating polarizers  $P_c$  and  $P_o$  with respect to one another.  $2\Delta$  and  $2\phi$  are the shear and bias, respectively, and the shear azimuth is assumed to be in  $X$  direction.

Usually,  $P_c$  and  $P_o$  are crossed, leading to  $R = 0.5$ , i.e.,

$$h_K(x, y) = 0.5 [h_{BF}(x + \Delta, y) \exp(-i\phi) - h_{BF}(x - \Delta, y) \exp(i\phi)]. \quad (2)$$

We obtain the effective pupil of the objective, or coherent transfer function, as a 2D Fourier transform of the  $h_K(x, y)$ .

$$\begin{aligned} P_K(\xi, \eta) &= 0.5 \{ P_{BF}(\xi, \eta) \exp[i(2\pi\xi\Delta - \phi)] - P_{BF}(\xi, \eta) \exp[-i(2\pi\xi\Delta - \phi)] \} \\ &= iP_{BF}(\xi, \eta) \sin(2\pi\xi\Delta - \phi). \end{aligned} \quad (3)$$

$\xi$  and  $\eta$  are transverse co-ordinates in the pupil-planes (condenser FFP and objective BFP as illustrated in Fig. 1) normalized by the numerical aperture of the objective,  $NA_{obj}$ .  $P_{BF}(\xi, \eta)$  is the coherent transfer function of the brightfield microscope, which is simply a circle of radius equal to 1 [29]. Therefore, coherent transfer function for Köhler-DIC also has a normalized cutoff frequency of 1.

We emphasize that Eq. (2) and (3) describe imaging properties of the objective-side light path in the spatial and spatial frequency domains respectively. They provide a sufficient description of the imaging properties of Köhler-DIC if *coherent illumination, or point-illumination, is assumed*.

For partially coherent illumination, the partially coherent transfer function (also called transmission cross-coefficient) of the Köhler-DIC model can be written in terms of the objective pupil ( $P_K$ ) and the condenser pupil ( $P_{cond}$ ) as follows [21, 22]:

$$C_K(m, n; p, q) = \iint |P_{cond}(\xi, \eta)|^2 P_K(\xi - m, \eta - n) P_K^*(\xi - p, \eta - q) d\xi d\eta. \quad (4)$$

Limits of all integrals in this paper are from  $-\infty$  to  $\infty$ . In all equations presented in this paper,  $(m; p)$  and  $(n; q)$  are spatial frequency pairs in  $X$  and  $Y$  directions, respectively, normalized by the frequency variable,

$$m_0 = \frac{NA_{obj}}{\lambda}, \quad (5)$$

where  $\lambda$  is the wavelength of the quasi-monochromatic illumination.

The intensity image can be expressed in terms of the specimen spectrum,  $T(m, n)$ , and the partially coherent transfer function as,

$$I_K(x, y) = \iiint T(m, n) T^*(p, q) C_K(m, n; p, q) \exp\{2\pi i[(m - p)x + (n - q)y]\} dm dn dp dq. \quad (6)$$

The above equation illustrates that, in partially coherent imaging, the strength of the spatial frequencies produced in the image depends on pairs of spatial frequencies of the specimen, rather than individual frequencies.

Equations 4 and 6 describe the frequency transfer properties and the forward image calculation, respectively, for the Köhler-DIC configuration with a condenser aperture of any geometry.

### 3.2. Nomarski-DIC

Assuming the absence of spurious birefringence, as described in subsection 2.2, Nomarski-DIC employs two independent beams each having large aperture. We can calculate wavefronts produced by the two beams individually until they interfere in the back-focal plane of the objective.

If the specimen transmission is given by  $t(x, y)$ , two beams effectively image the transmission functions  $t(x + \Delta, y)$  and  $t(x - \Delta, y)$  because of the lateral shear. The effect of phase difference, i.e. bias of  $2\phi$ , between two beams can be modelled as equal and opposite phase offset added to the transmission functions. Therefore, the two beams can be considered to be imaging transmission functions  $t(x + \Delta, y) \exp(-i\phi)$  and  $t(x - \Delta, y) \exp(i\phi)$ , respectively.

The beams are spatially coherent to one another at distances  $2\Delta$  in the specimen plane, and  $W_o$  and  $P_o$  optically compute their coherent difference. Therefore, Nomarski-DIC microscope effectively images a difference of transmission functions seen by the two beams. We can write the specimen transmission function that is effectively imaged as,

$$t_N(x, y) = t(x + \Delta, y) \exp(-i\phi) - t(x - \Delta, y) \exp(i\phi). \quad (7)$$

Therefore, the Fourier spectrum of the imaged transmission function is given by,

$$\begin{aligned} T_N(m, n) &= T(m, n) \{ \exp[i(2\pi m\Delta - \phi)] - \exp[-i(2\pi m\Delta - \phi)] \} \\ &= 2iT(m, n) \sin(2\pi m\Delta - \phi). \end{aligned} \quad (8)$$

We have accounted for the effects of all polarizing components in the above equation. Hence, we can assume that the imaging performed by the rest of the components is brightfield. As the prism  $W_o$  is placed in the BFP of the objective, angular-split of  $2\varepsilon$  has no effect on aperture size as seen by the specimen. Therefore, both beams illuminate the specimen from an aperture of the same size. Thus, the transmission spectrum  $T_N$  is imaged in a partially coherent manner just as in a conventional bright-field microscope.

Therefore, the image in partially coherent Nomarski-DIC microscope is given by,

$$I(x, y) = \iiint T_N(m, n) T_N^*(p, q) C_{BF}(m, n; p, q) \exp\{2\pi i[(m - p)x + (n - q)y]\} dm dn dp dq \quad (9)$$

where,

$$C_{BF}(m, n; p, q) = \iint |P_{cond}(\xi, \eta)|^2 P_{BF}(\xi - m, \eta - n) P_{BF}^*(\xi - p, \eta - q) d\xi d\eta \quad (10)$$

is the partially coherent transfer function for brightfield imaging. By substituting  $T_N$  from Eq. (8) in Eq. (9), we can write an effective transfer function for Nomarski-DIC that images the original specimen spectrum  $T(m, n)$  as follows,

$$C_N(m, n; p, q) = 4C_{BF}(m, n; p, q) \sin(2\pi m\Delta - \phi) \sin(2\pi p\Delta - \phi). \quad (11)$$

This is the same expression as Eq. (13) in Ref. [7].

In this paper, the frequency variables  $(m, n; p, q)$  are normalized by the frequency  $m_0 = NA_{obj}/\lambda$  whereas in Ref. [7] they were normalized by the cutoff frequency  $2NA_{obj}/\lambda$ . This leads to cutoff of 2 for partially coherent transfer functions in this paper as opposed to cutoff of 1 as in Ref. [7].

### 3.3. Equivalence of Köhler-DIC and Nomarski-DIC in coherent limit

When the illumination is coherent, i.e. when condenser aperture is closed to a point, the transmission cross coefficient for Köhler-DIC configuration  $C_K$  in Eq. (4) reduces to the frequency response function [23, pp.601-605] which can be written as,

$$M_K(m, n; p, q) = P_K(m, n)P_K^*(p, q) = 4M_{BF} \sin(2\pi m\Delta - \phi) \sin(2\pi p\Delta - \phi) \quad (12)$$

where,  $M_{BF}(m, n; p, q) = P_{BF}(m, n)P_{BF}^*(p, q)$ .

$M_K$  relates the mutual intensity in the specimen plane to the mutual intensity in the image plane, whereas  $P_K$  relates complex amplitudes.  $M_K$  is sufficient description of imaging properties in coherent limit and is separable in  $P_K(m, n)$  and  $P_K(p, q)$ . Thus, transfer function that affects complex amplitude can be written for Köhler-DIC as,

$$C_K^{coh}(m, n) = P_K(m, n) = iP_{BF}(m, n) \sin(2\pi m\Delta - \phi) \quad (13)$$

For Nomarski-DIC, the brightfield transmission cross coefficient  $C_{BF}$  in Eq. (11) similarly reduces to coherent transfer function  $P_{BF}$ .  $P_{BF}$  can be considered to be imaging the complex amplitude spectrum  $T_N(m, n)$  (Eq. (8)). Therefore, the effective coherent transfer function (that images the original transmission spectrum  $T(m, n)$ ) for Nomarski-DIC is given by,

$$C_N^{coh}(m, n) = iP_{BF}(m, n) \sin(2\pi m\Delta - \phi) \quad (14)$$

Thus, both systems have the same transfer function in the coherent limit, and hence behave identically.

We note that Eq. (2), (3), (4), and (6) correspond to Eq. (1), (2), (14), and (15) in Ref. [8], respectively. Ref. [8] (which effectively models Köhler-DIC configuration) notes that the partially coherent transfer function of Eq. (4) reduces to frequency response function of Eq. (12) in the coherent limit [8, Eq.17]. The forms of Eq. (11) (which describes partially coherent image formation for Nomarski-DIC) and Eq. (12) (which describes coherent image formation for Köhler-DIC) are similar, but they describe two different quantities. Perhaps, this led to an erroneous conclusion in Ref. [8] that Eq. (13) of Ref. [7] (in fact, valid for partially coherent imaging in Nomarski-DIC) is applicable only to the coherent illumination.

## 4. Partially coherent transfer functions

### 4.1. Computation of transfer functions

As can be seen from Eq. (4) and (10), complete partially coherent transfer function can be computed as the area of overlap of the following three pupils: the squared magnitude of the condenser pupil, the objective pupil shifted by  $m$  and  $n$ , and the conjugate of the objective pupil shifted by  $p$  and  $q$  [22]. We have implemented an algorithm in MATLAB to compute the complete partial coherent transfer functions on the discrete 4D grid of  $(m, n; p, q)$  using this approach. The value of  $C(m, n; p, q)$  computed as an area of overlap of three pupils is normalized with area of the objective pupil making computed values independent of fineness of the grid. Note that for a brightfield system employing matched illumination, the partially coherent transfer function for the DC term of the specimen spectrum ( $C_{BF}(0, 0; 0, 0)$ ) is the same as area of the objective pupil. Therefore, when computed with our algorithm,  $C_{BF}(0, 0; 0, 0) = 1$ .

Pupil radii are normalized by the numerical aperture of the objective pupil ( $NA_{obj}$ ). Therefore, the objective pupil has radius of 1 and the condenser pupil has the radius equal to coherence ratio,  $S$ . As an example, pupils used for computing transfer functions of the three configurations with coherence ratio  $S = 0.7$ , shear  $2\Delta = 1/4m_0$  and bias  $2\phi = \pi/2$  are shown in Fig. 2. The frequency variables,  $(m, n; p, q)$ , are normalized by characteristic frequency,

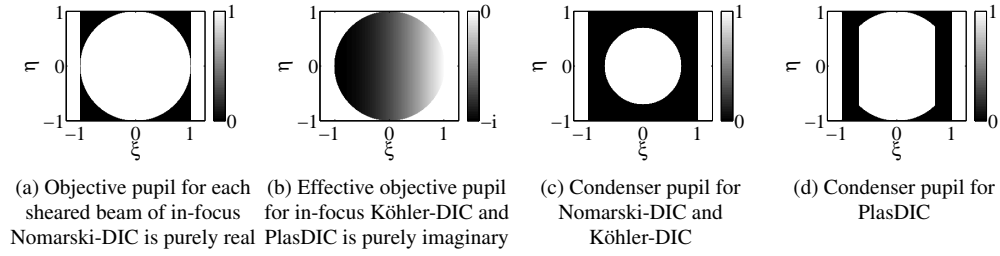


Fig. 2. Objective and condenser pupils used for computing transfer functions with  $S = 0.7$ , shear  $2\Delta = 1/4m_0$  and bias  $2\phi = \pi/2$ .

$m_o = NA_{obj}/\lambda$ . Correspondingly, the spatial variables such as shear are expressed as multiples of  $1/m_o = \lambda/NA_{obj}$ . We Note that in Ref. [7], the normalizing frequency variable ( $m_0$ ) is  $2NA_{obj}/\lambda$ . Therefore, normalized values of shear used in this paper correspond to half those reported in Ref. [7].

To compute transfer functions for Köhler-DIC and PlasDIC, we first compute the objective pupil as per Eq. (3). The condenser pupil for Köhler-DIC is a circle with radius of  $S$ . For PlasDIC, the condenser pupil is a slit and in our simulation we take coherence ratio,  $S$  to be the width of the slit. Then the partially coherent transfer function,  $C_K$ , is computed from Eq. (4).

To compute the partially coherent transfer function for Nomarski-DIC, we first compute  $C_{BF}$  from Eq. (10) with appropriate objective and condenser pupils.  $C_{BF}$  is modulated as shown in Eq. (11) to compute  $C_N$ .

Although it is possible to compute the image of a specimen having arbitrary 2D transmission using the four dimensional partially coherent transfer function, we assume a one dimensional specimen allowing a reduction to two dimensions. From Eq. (6) and (9), we can see that the image intensity along the  $X$ -direction depends only on the spatial frequency variable pairs ( $m; p$ ). Assuming a 1D specimen allows us to plot partially coherent transfer functions that describe imaging properties of a general one dimensional object and correlate their structure with contrast expected in the image.

As an example, Fig. 3 shows partially coherent transfer functions for one dimensional objects which have variations either parallel to the direction of shear or perpendicular to the direction of shear. Without loss of generality, shear azimuth is assumed to be in  $X$  direction.

#### 4.2. Symmetry of transfer function and contrast

Symmetry of the partially coherent transfer function determines the specimen information that gets transferred to intensity of the image [30, 31]. If the transfer function has even symmetry around  $m = -p$  axis, the resultant image has pure amplitude contrast, whereas odd symmetry of the transfer function around  $m = -p$  axis results in differential phase contrast.

As can be seen from Fig. 3(b), in the direction perpendicular to the shear, the partially coherent transfer function has even symmetry around  $m = -p$  axis. This observation holds true for all DIC configurations. Moreover, Fig. 3(b) has the same structure as for the brightfield microscope as reported in Ref. [32]. Thus, in all DIC configurations, imaging in the direction perpendicular to shear is similar to that in a brightfield microscope. Therefore, only amplitude information is expected to be imaged within the passband of the system. However, strong phase information that lies outside the passband of the system will affect the intensity of the image and in that sense a brightfield microscope does image phase information. This observations agrees with observation in Ref. [33, Appendix-1] that DIC microscope images specimens which have

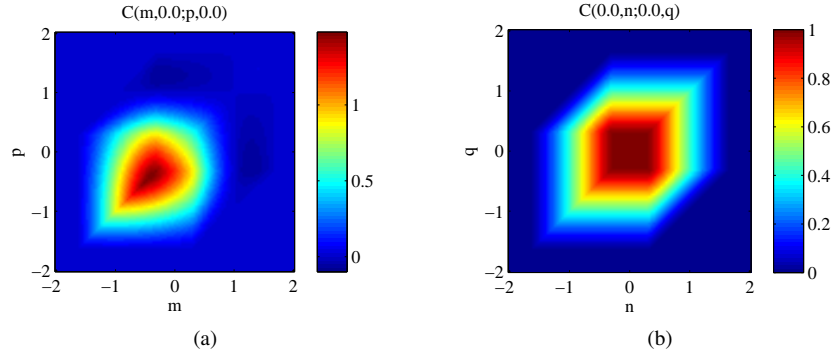


Fig. 3. Slices through the four dimensional partially coherent transfer function computed for a Nomarski-DIC system with  $S = 0.7$ , shear  $2\Delta = 1/4m_0$ , and bias  $2\phi = \pi/2$ . Shear azimuth is assumed to be in  $X$  direction.  $(m;p)$  denotes frequency variable pairs in the  $X$ -direction, whereas  $(n;q)$  denotes frequency variable pairs in the  $Y$ -direction. (a) An excerpt at  $n = q = 0$  from the image sequence (Media 1) showing 2D slices of the 4D transfer function along  $m$  and  $p$  with varying  $n$  and  $q$ . The slice at  $n = q = 0$  is a sufficient description for imaging of a specimen varying only in the  $X$  direction. (b) An excerpt at  $m = p = 0$  from the image sequence (Media 2) showing 2D slices of the 4D transfer function along  $n$  and  $q$  with varying  $m$  and  $p$ . The slice at  $m = p = 0$  is a sufficient description for imaging of a specimen varying only in the  $Y$  direction.

constant phase in the direction of shear but have ‘step-like’ phase in the perpendicular direction.

Having determined the structure of the transfer function in the direction perpendicular to shear in all DIC configurations, hereafter we only consider imaging in the direction of shear. Therefore, the transfer functions that we are concerned with are as follows:

For Nomarski-DIC,

$$C_N(m;p) = 4C_{BF}(m;p) \sin(2\pi m\Delta - \phi) \sin(2\pi p\Delta - \phi), \quad (15)$$

where,

$$C_{BF}(m;p) = \iint |P_{cond}(\xi, \eta)|^2 P_{BF}(\xi - m, \eta) P_{BF}^*(\xi - p, \eta) d\xi d\eta, \quad (16)$$

and for Köhler-DIC,

$$C_K(m;p) = \iint |P_{cond}(\xi, \eta)|^2 P_K(\xi - m, \eta) P_K^*(\xi - p, \eta) d\xi d\eta, \quad (17)$$

where  $P_K$  is defined by Eq. (3).

Although, the symmetry of the transfer function can provide information about the type of contrast present in the image, variations of the transfer function govern the strength with which different frequencies of the object are imaged. Frequency support of the transfer function determines resolution of the imaging system.

If the object is weak, a line  $C(m;0)$  through the 2D transfer function  $C(m;p)$  is sufficient description of imaging properties of the system and is called the weak object transfer function (WOTF). The even component of WOTF determines the strength with which amplitude is imaged and the odd component determines the strength with which phase gradient is imaged. If the object is slowly varying with respect to the resolution element, a line  $C(m;m)$  provides sufficient description of imaging properties and is called phase gradient transfer function (PGTF). The symmetry of PGTF shows how the imaging system behaves for increasing or decreasing slopes in optical path length of the object.



In the following section, we examine the structure of the partially coherent transfer functions in the direction of shear with respect to different values of coherence ratio and bias to investigate the resultant contrast and resolution. Contrast and resolution predicted by the structure of transfer function are evaluated with experimental images.

### 5. Imaging properties of three configurations

We first consider effects of the condenser aperture size, i.e., degree of coherence, on the imaging properties of Nomarski-DIC, Köhler-DIC, and PlasDIC in the direction of shear. A fixed shear of  $2\Delta = 0.25\lambda/NA_{obj}$  (i.e.,  $\Delta = 1/8m_0$ ) and bias of  $2\phi = \pi/2$  have been used in simulations as they are suitable for linear imaging of phase information in conventional DIC configuration with good contrast [7, pp.88-94].

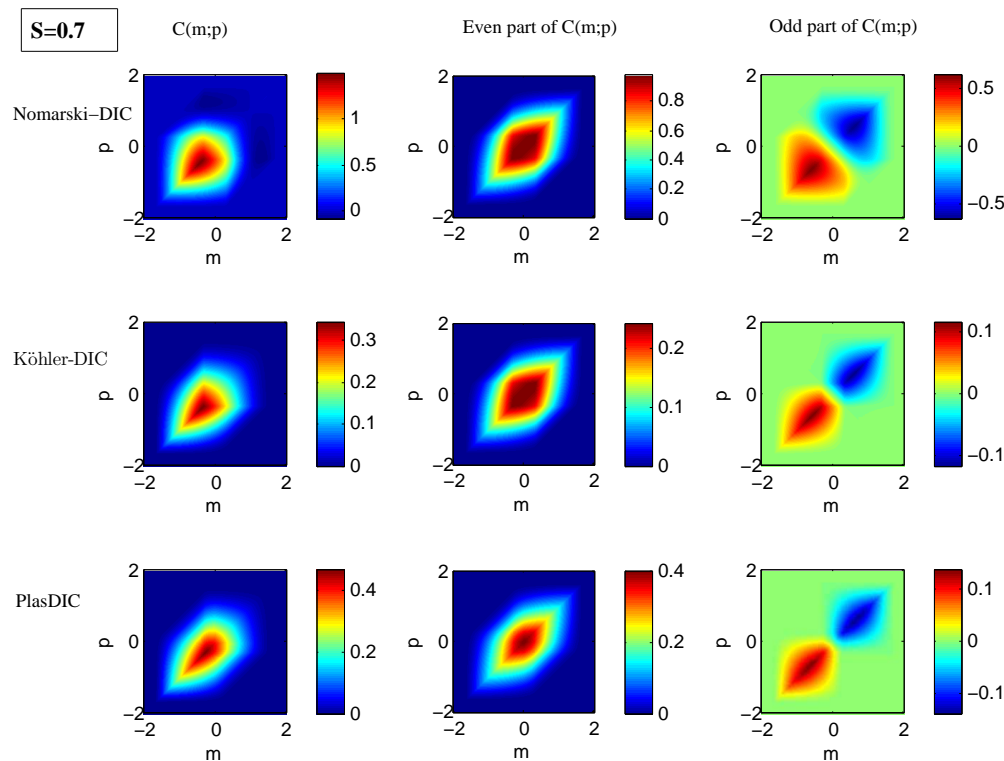


Fig. 4. An excerpt from the image sequence ([Media 3](#)) comparing partially coherent transfer functions for  $S = 1, \dots, 0.1$  for three configurations in the direction of shear. This is a snapshot at  $S = 0.7$ . The shear is assumed to be  $2\Delta = 1/4m_0$  and bias  $2\phi = \pi/2$ . Transfer functions are shown for Nomarski-DIC (top row), Köhler-DIC (middle row) and PlasDIC (bottom row). The transfer functions (left column) for all three configurations are separated into their even parts (middle column) and odd parts (right column). To allow clear visualization of frequency support and shape of the transfer function, the color look up table of each plot is stretched to the minimum and maximum values being displayed. Colorbar next to each plot allows comparison of relative strengths of the transfer functions at different values of  $S$  (for a given configuration).

Figure 4 ([Media 3](#)) is the image sequence showing transfer functions in the direction of shear computed for  $S = 1, \dots, 0.1$ . Comparing different features of transfer functions of three configurations as the coherence ratio ( $S$ ) decreases, one can quantitatively predict imaging properties

as the illumination becomes more coherent. We note that it is meaningful to compare minimum and maximum values of the transfer function as  $S$  changes only between PlasDIC and Köhler-DIC as they are described by the same imaging model. For interpretation of absolute values of plots, please see Sec. 4. Frequency support and shape of the transfer function provides information about resolution and fidelity, respectively, with which information is imaged. Relative strength with which amplitude and phase gradient information is imaged is governed by the relative strength of even and odd components of the transfer function.

Figure 5 shows the even and odd parts of the weak object transfer function and the phase gradient transfer functions for three configurations for  $S = 0.2, 0.4, 0.6, 0.8$  and 1.

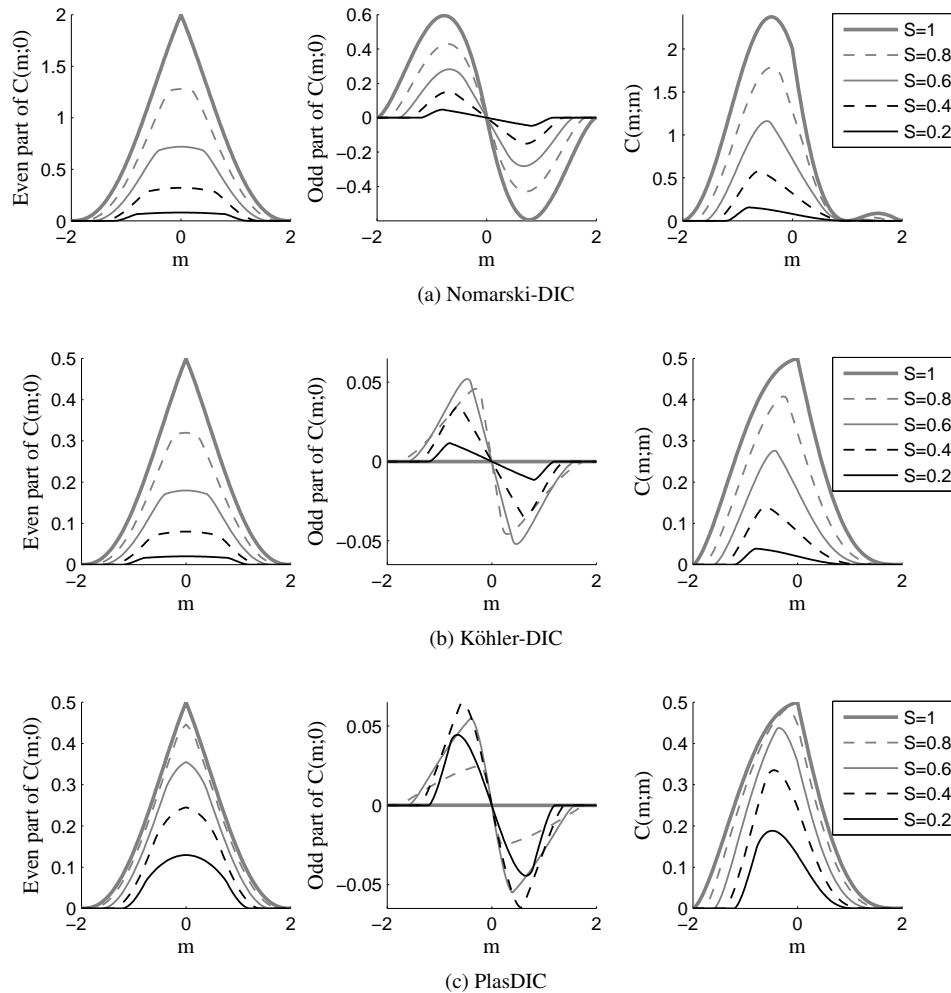


Fig. 5. Even part of weak object transfer function (left column), odd part of weak object transfer function (middle column) and phase gradient transfer functions (right column) for three DIC configurations.

From Fig. 4 ([Media 3](#)) and Fig. 5 we can make the following observations. In the following, we refer to the partially coherent transfer functions as  $C(m; p)$ , the weak object transfer function as  $C(m; 0)$  and the phase gradient transfer function as  $C(m; m)$ .

For all three configurations, the even part of  $C(m; p)$  is stronger than odd part of  $C(m; p)$  for

all values of  $S$ . Thus, the configurations considered here will not produce good phase contrast when the specimen contains strong amplitude information. However, as  $S$  reduces the odd part of  $C(m; p)$  becomes more similar in strength to the even part. Thus, smaller values of  $S$  lead to better phase gradient contrast.

Consider the case of matched illumination, i.e.,  $S = 1$ . The odd part of  $C(m; p)$  for Nomarski-DIC has broadest frequency support without zero crossings. Presence of zero crossings could lead to imaging of certain frequencies with reversed contrast and hence artifacts. For Köhler-DIC and PlasDIC, the odd part of  $C(m; p)$  does not transmit certain frequency pairs  $(m; p)$ . Therefore, when matched illumination is employed, the Nomarski-DIC configuration images phase gradient information with highest resolution and fidelity.

At  $S = 1$ , Köhler-DIC and PlasDIC are the same configuration. They cannot image weak phase information at all because the odd part of  $C(m; 0)$  is zero. However,  $C(m; m)$  for both is nonzero and therefore expected to image slowly varying phase information.  $C(m; m)$  for Nomarski-DIC has sharper changes with value of phase gradient. Therefore, a specimen which has both positive and negative gradients will have more pronounced shadow-casting and high-lighting in Nomarski-DIC rather than in Köhler-DIC. These effects can be observed in Fig. 8. We note that the curves for Nomarski-DIC for the even part of  $C(m; 0)$ , the odd part of  $C(m; 0)$  and  $C(m; m)$  are identical to those presented in Ref. [7] for the same shear and bias.

As condenser is stopped down to around  $S = 0.7$ , structures of  $C(m; 0)$  and  $C(m; m)$  for Nomarski-DIC and Köhler-DIC become slightly similar. Köhler-DIC and PlasDIC can now image weak phase information as  $C(m; 0)$  in both configurations have non-zero odd component. However,  $C(m; p)$  for Köhler-DIC and PlasDIC still do not transmit as wide a range of frequencies as for Nomarski-DIC.  $C(m; 0)$  for PlasDIC has a stronger even component than Köhler-DIC, which will lead to stronger imaging of amplitude of the weak object. PlasDIC also has stronger  $C(m; m)$  than Köhler-DIC, which leads to stronger imaging of slowly varying phase information.

As the value of  $S$  is reduced further, the transfer functions for all three configurations become rather similar. At  $S = 0.4$ , three configurations are characterized by similar  $C(m; p)$ ,  $C(m; 0)$  and  $C(m; m)$ . Therefore, when the condenser aperture size is around 40% of the objective aperture size, the use of condenser-side Wollaston prism is redundant. In such a situation, PlasDIC leads to a brighter image background than Köhler-DIC as its transfer functions are stronger at zero spatial frequency. We note that the value of  $S = 0.4$  is dependent on the assumption that shear is  $2\Delta = 1/4m_0$ . For bigger shear, the condenser will need to be stopped down further to expand the distance over which illumination is coherent. Conversely, systems employing smaller shear can work with a more open condenser. *This is the key conclusion about dependence of phase gradient contrast on degree of coherence of illumination.*

To verify whether Köhler-DIC and Nomarski-DIC behave as predicted above with change in  $S$ , we imaged  $16\mu\text{m}$  thick mouse intestine section (Invitrogen Fluocells prepared slide #4) with 20X 0.75 NA objective and 0.9 NA condenser. The value of  $S$  was changed with motorized condenser aperture. The microscope control software allowed calibrated change in the size of the motorized condenser aperture which was visually verified by looking at the objective back focal plane with a Bertrand lens. Using a condenser top lens of NA 0.9 allowed the maximum value of  $S$  to be 1.2. The smallest value of  $S$  was limited by the amount by which the aperture diaphragm could be closed. The bias was approximately set to  $\pi/4$  with a translatable modified Wollaston prism on objective side. The amount of shear employed by our microscope is not calibrated.

Figure 6 shows images for Nomarski-DIC and Köhler-DIC configurations for matched illumination and  $S = 0.4$ . It is evident that around  $S = 0.4$ , both Nomarski-DIC and Köhler-DIC produce similar phase gradient contrast. However, with matched illumination Köhler-DIC loses

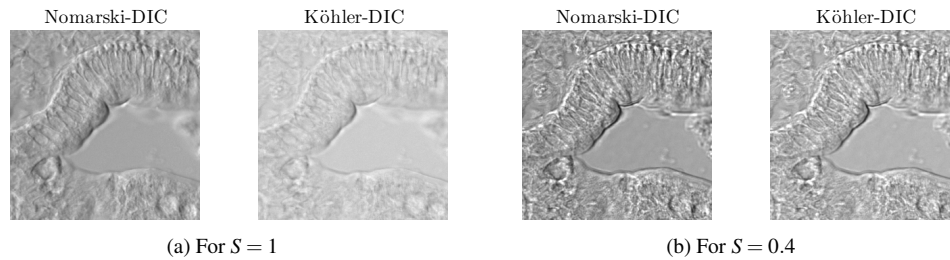


Fig. 6. Two excerpts from an image sequence (Media 4) showing variation in the phase gradient contrast with  $S$  in images of mouse intestine section (Invitrogen Fluocells prepared slide # 4) imaged with  $S = 0.3, \dots, 1.2$ . 20X 0.75 NA objective and 0.9NA condenser were used. Shear direction is horizontal. Quasi-monochromatic source of light was created by passing light from a Halogen lamp through a 550nm interference filter. Size of image is  $18.3\mu\text{m} \times 18.3\mu\text{m}$ . To be able to compare contrast in images, all images were taken with exposures such that they fill the camera's dynamic range almost equally. Further, all images have been converted to 32-bit floating point format and then pixel values were normalized to a maximum value of 1 before displaying.

phase gradient contrast especially for weak phase changes, while contrast in Nomarski-DIC is retained. Associated media Fig. 6 (Media 4) shows the variation in the image contrast as the value of  $S$  is increased from 0.3 to 1.2. It can be seen that as condenser aperture is opened, the role of the Wollaston prism in providing coherent illumination for two points separated by the shear becomes more important.

Next, we consider the effect of changing the bias in Köhler-DIC and Nomarski-DIC for two important condenser aperture sizes discussed above.

Figures 7 and 8 correlate the partially coherent transfer functions with the image of an optical fiber of diameter  $50\mu\text{m}$  under Nomarski-DIC and Köhler-DIC at bias values of  $2\phi = 0$  (left column),  $2\phi = \pi/2$  (center column), and  $2\phi = \pi$  (right column).

The optical fiber is a good approximation of a one dimensional slowly varying phase specimen except near the edges. Since the fiber was aligned with its axis perpendicular to the direction of shear, one can estimate the relative strengths with which phase gradients (along the direction of shear) are imaged by observing relative strength of the transfer function along line  $(m, m)$ . Therefore, this specimens' imaging can be described to good accuracy with a  $C(m, m)$  line through the transfer functions. As we move across fiber along the direction of shear, we first encounter a high positive phase gradient at one edge of the fiber which slowly reduces to zero at the center of the fiber, and then increases in opposite direction until we reach opposite edge of the fiber. It can be seen from Fig. 7 and 8 that for all cases, the variation in intensity in the image of fiber for different phase gradients follows closely the variation in  $C(m, m)$  for corresponding values of  $m$ .

It can be seen from Fig. 7 that for condenser aperture size of  $S = 0.4$ , both systems have almost the same transfer functions for all values of bias. The contrast observed in the images for the two systems is almost identical and correlates well with the structure of the transfer function. Transfer functions for  $2\phi = 0$  do not transmit low spatial frequencies and hence, both systems behave as dark-field imaging system. For bias of  $2\phi = \pi/2$ , both systems are seen to produce a typical shadow-cast effect and for  $2\phi = \pi$  both systems are seen to behave like brightfield systems with low cutoff.

However, when the condenser is opened to give matched illumination, we observe from Fig. 8 that Köhler-DIC does not image phase information very well. In particular, at  $2\phi = 0$  Köhler-

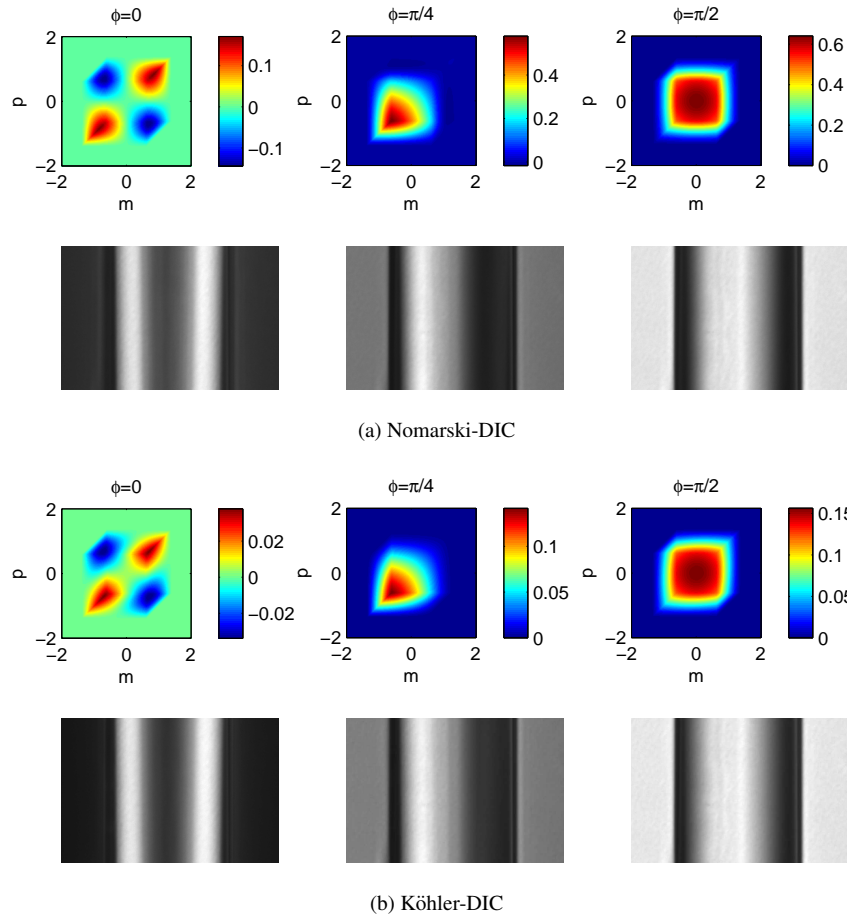
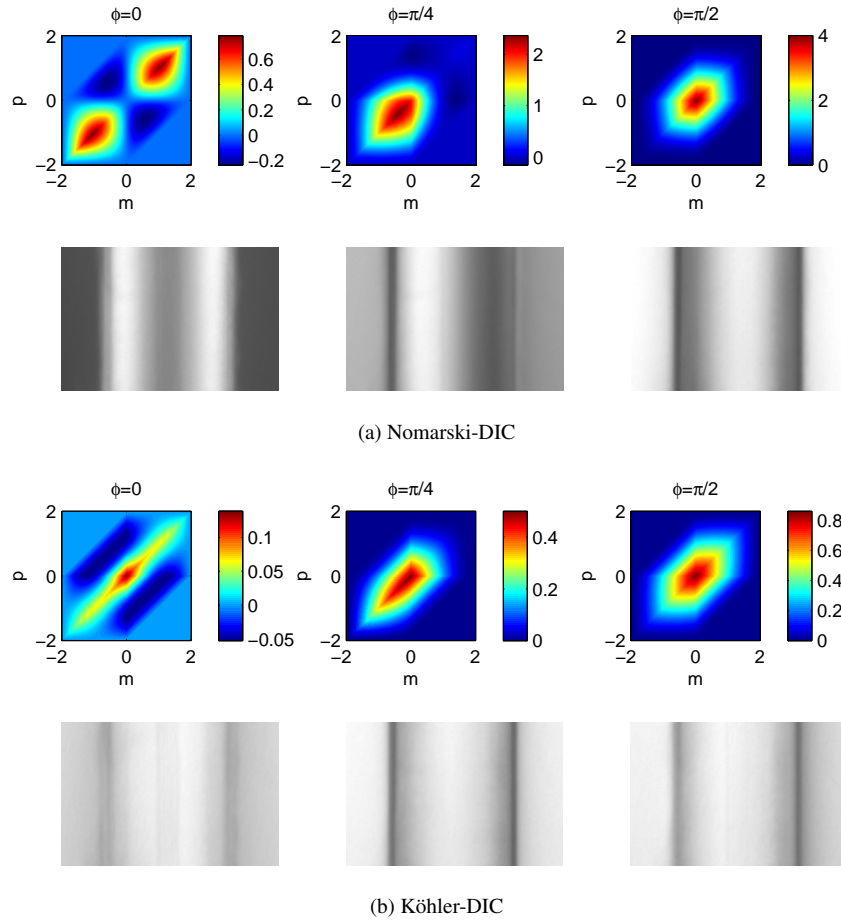


Fig. 7. Comparing partially coherent transfer functions  $C(m; p)$  at  $S = 0.4$  with images of an optical fiber in the direction of shear for (a) Nomarski-DIC and (b) Köhler-DIC for different values of bias. The optical fiber (core R.I.= 1.581, clad R.I.= 1.487, core diameter =  $10 \mu\text{m}$ , clad diameter=  $50 \mu\text{m}$ ) was aligned with its axis perpendicular to the direction of shear. Images were taken with a 40X 0.9 NA lens and 0.9NA condenser lens stopped down to  $S = 0.4$ . The fiber was immersed in water under a 0.17 mm glass coverslip, sealed with nailpolish, and imaged with quasi-monochromatic illumination as in Fig. 6.

DIC no longer behaves like a dark-field system whereas Nomarski-DIC does. Nomarski-DIC retains good shadow-cast imaging at  $2\phi = \pi/2$ , whereas Köhler-DIC does not. For  $2\phi = \pi$ , both systems behave almost like brightfield system with matched condenser.

## 6. Summary and conclusions

We have presented and verified an accurate model based on scalar diffraction theory for Nomarski's DIC. The model is summarized by Eqs. 11 and 9. This model accounts for effects of coherence of illumination due to the condenser-side Wollaston prism. Another means of achieving sufficient degree of coherence is to restrict the condenser pupil in the direction of shear. Zeiss has developed a DIC system, termed PlasDIC, based on this principle that allows imaging of phase gradient information for birefringent specimens. Properties of Nomarski-DIC and PlasDIC are examined alongwith a configuration, termed Köhler-DIC, that is similar

Fig. 8. Same as Fig. 7 but with  $S = 1$ .

to Nomarski-DIC but without the condenser-side prism. Imaging properties of PlasDIC and Köhler-DIC are described by Eqs. 4 and 6. It has been shown that when typical settings for shear and bias are employed, closing the condenser to approximately 0.4 times the objective aperture results in similar contrast for all three configurations. For wider condenser apertures, the second Wollaston prism is necessary to produce sufficient degree of coherence. Complete partially coherent transfer functions for one dimensional objects have been computed without assuming either a weak or a slowly varying object. The symmetry of the computed transfer functions has been discussed in light of the contrast seen in the image. Experimental images are in good agreement with predictions made from transfer functions (Fig. 6,7, and 8).

These accurate models for DIC configurations will enable accurate calculation of images of known specimen using the frequency domain approach. The models should be valuable in developing accurate phase retrieval algorithms from DIC images.

### Acknowledgment

C.J.R. Sheppard acknowledges support from the Singapore Ministry of Education Tier-1 funding (grants R397000022112 and R397000033112). S.B. Mehta acknowledges graduate scholarship from Graduate Programme in Bioengineering-NGS, National University of Singapore.

## 2.2 Paradoxical point spread function of DIC

An important conclusion of the paper presented in the previous section is that Nomarski's DIC configuration does not image a specimen with a sheared brightfield point spread function, but rather it images a sheared specimen transmission. The sheared-specimen is imaged with the brightfield partially coherent transfer function. We recently (two years after publishing our paper [Mehta and Sheppard, 2008]) discovered that in a short conference abstract published in 1969, Nomarski articulated the same observation [Nomarski, 1969]. However, from the short abstract it is difficult to assess if Nomarski pursued the full quantitative model.

In this section, we present a remarkable and surprising consequence of the above result. It is usually thought that if a bright-point in opaque background is imaged with *any* imaging system, its image (called, the point spread function) does not depend on how the point is illuminated, because the point is always coherent with itself. But, we show analytically and experimentally that the image of a point *does depend* on the illumination aperture in polarizing shearing interferometers. This result corrects the assumption held within DIC community for three decades [Galbraith, 1982, Preza et al., 1999] that imaging in DIC can be described using a 'point spread function' that does not vary with respect to the illumination. In the following equations, we denote two dimensional quantities by vectors typeset using bold-face characters as described in the Nomenclature.

The key components of the DIC microscope are Nomarski prisms, whose effects of introducing the spatial shear and phase bias can be accounted for using the following kernel,

$$\Delta_{DIC}(\mathbf{x}) = \delta(x + \Delta, y)e^{-i\phi} - \delta(x - \Delta, y)e^{i\phi}. \quad (2.1)$$

Galbraith [Galbraith, 1982] and Preza [Preza et al., 1999] assume that the image of a bright point on dark background, i.e., the so called *DIC point spread function (PSF)*, is given by a coherent difference (i.e., difference of complex amplitude) of shifted replicas of the bright-field point spread function. Therefore, the DIC image of a point, as per the

above assumption is given by,

$$I_c(\mathbf{x}) = |h_{BF}(\mathbf{x}) \otimes \Delta_{DIC}(\mathbf{x})|^2. \quad (2.2)$$

We call  $I_c(x, y)$  the *coherent point-image*. Note that the illumination does not appear in the above equation. In the paraxial approximation the brightfield PSF  $h_{BF}$  is given as,

$$h_{BF}(|\mathbf{x}|) = \frac{2J_1(|\mathbf{x}|)}{|\mathbf{x}|} e^{-iu|\mathbf{x}|^2}, \quad (2.3)$$

where  $|\mathbf{x}| = \sqrt{x^2 + y^2}$  is the transverse radial co-ordinate in the specimen plane expressed in units of  $\lambda/\text{NA}_0$ .  $u$  is the axial co-ordinate in the specimen plane expressed in units of  $\lambda/\text{NA}_0^2$ .

Fig. 2.1a shows  $I_c$  computed as per equation 2.2 with settings noted in the caption of the figure. It is seen that at bias 0,  $I_c$  will be exactly zero at  $(x, y) = (0, 0)$  because of even symmetry of the brightfield PSF around the origin. The coherent combination of brightfield PSFs leads to non-circular peaks in  $I_c$ . The nature of this computed PSF corresponds well with that presented by Galbraith [Galbraith, 1982], and Preza [Preza et al., 1999], but for different amount of shear. Note that both authors assume that the image of a point does not depend on the size of the illumination aperture.

Next, we draw attention to experimental images of a point shown in fig. 2.1b, acquired at  $S = 1, 0.5, 0.25$  respectively. These results were acquired by plating a glass-slide entirely with chrome and treating the tiny defects in plating process as point sources. Care was taken to image a sub-resolution feature. The in-focus images shown in fig. 2.1b required an exposure of 10s at  $S = 1$  to fill up the dynamic range of a sensitive CCD camera (Qimaging Retiga Exi) at halogen lamp setting of 5 V, which indicates that it was indeed a sub-resolution point. We notice that the measured image of a point does not approach zero at the center. More importantly, as we reduce the condenser aperture and approach  $S = 0.25$ , the experimental images approaches the coherent image of a point shown in fig. 2.1a. Thus, the experimental result does not match the assumption of coherent PSF. Note that this anomaly was observed, but was not accounted for, by Galbraith in context of Fig. 18 of



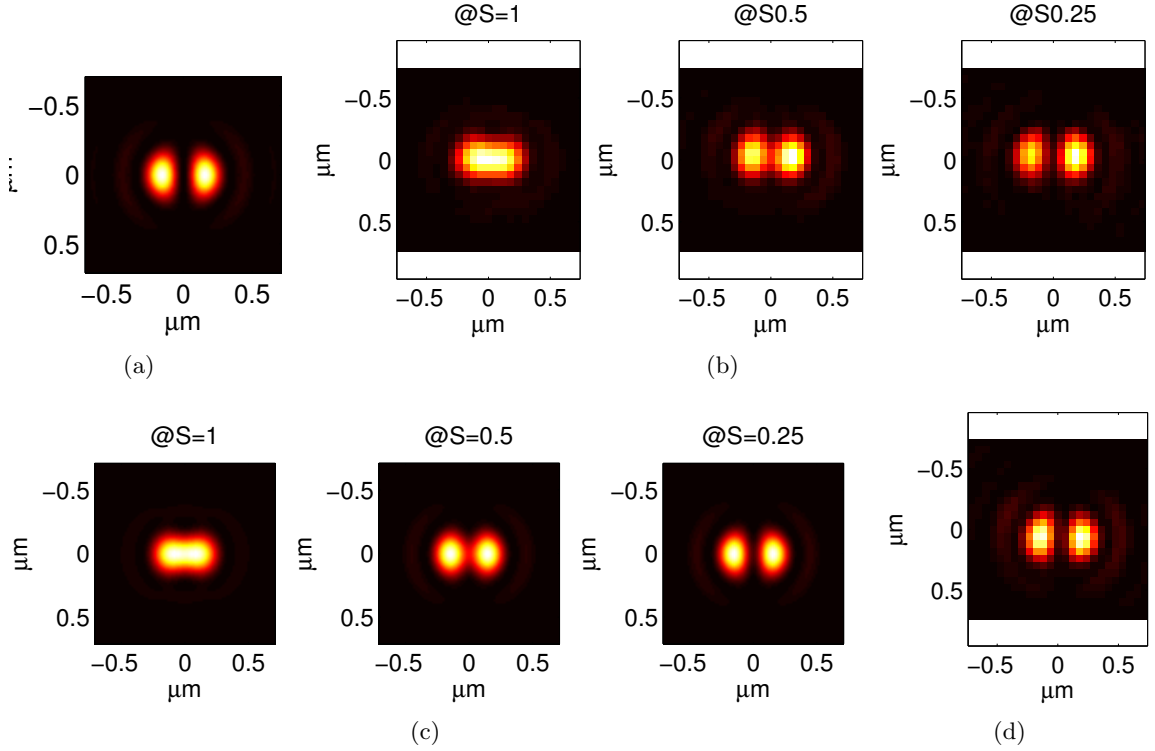


Figure 2.1: Simulated and experimental images of a point obtained by assuming a sheared point spread function (PSF) vs. assuming sheared specimen: (a) is the simulated image assuming sheared PSF model, (b) shows experimental images of a point at  $S = 1, 0.5, 0, 25$  under Nomarski-DIC configuration, (c) shows the simulated images of a point assuming sheared specimen model, and (d) are the experimental images of a point taken with matched illumination, but without the condenser-side prism. The experimental images were taken with Zeiss 100X1.3 NA objective in collaboration with Rudolf Oldenbourg at Marine Biological Laboratory. The shear of the corresponding prism was measured to be  $0.38\lambda/\text{NA}_0$  using the algorithm described in ref [Mehta and Sheppard, 2010b]. The bias was set to 0. The simulations were carried out at the above experimentally used settings.

Ref [Galbraith, 1982].

Next, we examine the image of a point using our partially coherent model. The point in space is represented by  $\delta(x, y)$  and in spatial-frequency by  $T(m, n) = 1$ . Substituting this constant specimen-spectrum in the model of Nomarski-DIC [Mehta and Sheppard, 2008, eq. 8], we see that the image of a point in DIC is given by,

$$I_D(x, y) = \iiint \sin(2\pi m\Delta - \phi) \sin(2\pi p\Delta - \phi) C_{BF}(m, n; p, q) e^{2\pi i[(m-p)x + (n-q)y]} dm dn dp dq, \quad (2.4)$$

where,  $C_{BF}$  is the transmission cross-coefficient of a brightfield system with the same parameters as the DIC system. The sinusoidal modulation of  $C_{BF}$  is due to the fact that DIC images a difference of shifted (in space and phase) replicas of the specimen transmission. Figure 2.1c shows  $I_D$  calculated as per above equation, which matches very well with experimental image of fig. 2.1b.

Finally, we examine an experimental image of the point by removing the condenser-side prism (i.e. Köhler-DIC configuration shown in [Mehta and Sheppard, 2008]) at  $S = 1$ . Note that even with matched illumination, the image obtained with Köhler-DIC agrees well with fig. 2.1a. When we changed the condenser aperture, the image in Köhler-DIC setup was not affected.

The results reveal that, in standard DIC configuration with two prisms, the image of a point depends on the size of condenser aperture. This surprising behavior is explained once we realize that DIC effectively images a specimen of the form  $t(x, y) = \delta(x + \Delta, y) - \delta(x - \Delta, y)$ . Thus, the effective specimen consists of two points rather than one, and image of two neighboring points *is* affected by coherence of illumination. When the condenser-side prism is removed, only one polarization is incident upon the specimen. Consequently, the two orthogonal polarizations produced by the shearing interferometer implemented by the objective-side prism originate from same scalar field and hence are coherent with respect to each other. Therefore, in Köhler-DIC setup, the image of a point does not depend on the condenser aperture. Above simulation (fig. 2.1a) and experimental (fig. 2.1d) results provide an experimental illustration of the fact that Preza's [Preza et al., 1999, Fig.4] partially coherent model fails to account for the condenser-side prism. The result can be

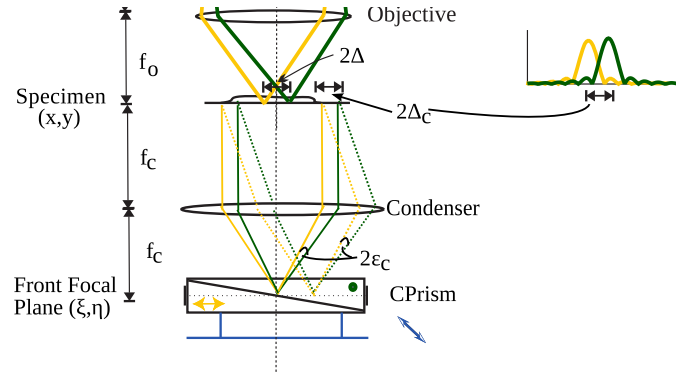


Figure 2.2: Improved schematic of the illumination path of the Nomarski-DIC microscope: The illumination system provides orthogonally polarized but spatially coherent radiation between points that are separated by a shear distance of  $2\Delta_c$ . All points of the condenser aperture illuminate the entire specimen due to the Köhler arrangement, but we have shown just two points for the sake of clarity. The condenser-side prism (CPrism) is designed to introduce identical angular shear of  $2\epsilon_c$  to wavefronts originating from each condenser point, which translates to spatial-shear of  $2\Delta_c$  at the specimen plane. The color-code used to indicate the polarization of the light is the same as in Ref [Mehta and Sheppard, 2008, Fig. 1].

explained from another point of view as well. The DIC configuration images *two replicas of the specimen using two orthogonal polarizations and hence the mutual coherence between these two polarization is important*. Careful thought shows that the mutual coherence between two polarizations at a given specimen point is affected by the size of the condenser aperture as depicted in fig. 2.2.

We have shown that the image of a point provides an insight into the behavior of spatial coherence when imaging with different configurations of DIC. Note that this effect is relevant to all polarization-based shearing interferometers and therefore, important in quantitative work performed with these devices.

The accurate diffraction model of image formation in DIC presented in this chapter is important for calibration of the experimental DIC system as presented in ref [Mehta and Sheppard, 2010b] and quantitative evaluation of the imaging properties of DIC as presented in ref [Mehta and Sheppard, 2010c].

## Chapter 3

# Asymmetric Illumination-based Differential Phase Contrast

The preceding chapter demonstrates that image formation in DIC is rather involved, because the contrast is generated by clever manipulation of polarization. As an alternative to DIC, a simpler method based on a split-detector has been proposed in the field of scanning microscopy. The method is called differential phase-contrast (DPC) [[Dekkers and de Lang, 1974](#), [Hamilton and Sheppard, 1984](#), [Hamilton et al., 1984](#)] and produces an image that has phase-gradient contrast. Although DPC produces an image that looks similar to DIC, it has different imaging properties and is more quantitative than DIC is. We have developed a full-field version of DPC based on the principle of reciprocity. The method is based on asymmetric illumination and hence called asymmetric illumination-based differential phase contrast (AIDPC). An introductory description of AIDPC is reported in ref. [[Mehta and Sheppard, 2009b](#)] that is typeset as sec. 3.2. Additional examples of experimental images obtained with AIDPC are shown in sec. 3.3. Before discussing AIDPC in detail, we review the use of asymmetric illumination for phase microscopy.

### 3.1 Evolution of asymmetric-illumination based phase imaging methods

The technique of visualizing the phase changes by oblique or asymmetric illumination is widely used as Schlieren (German for ‘striae’) photography in the field of fluid dynamics. Settles provides a thorough and entertaining history of Schlieren methods used for visualization of aerodynamics and fluid dynamics [Settles, 2001, Ch. 1], according to which Hooke did the first recorded experiments with oblique illumination.

We focus on the use of asymmetric illumination for phase microscopy during the late-20th century. Hoffman and Gross developed modulation contrast [Hoffman and Gross, 1975] by assuming the specimen to be consisting of small prisms. We call the same assumption ‘the slowly varying specimen assumption’ [Hamilton and Sheppard, 1984, Mehta and Sheppard, 2009b]. Hoffman’s modulation contrast uses a slit in the condenser FFP and an absorbing filter in the objective BFP. Hoffman made a point that the contrast mechanism employed by modulation contrast is not based on interference, in contrast to Zernike’s method <sup>1</sup>, but rather on refraction of direct light and its attenuation by the absorbing filter. Stewart [Stewart, 1976] pointed out, based on the principle of reciprocity, that a partially coherent system employing oblique illumination from a semicircular illumination aperture has the same imaging properties as a scanning system with a semicircular detector. He also suggested that the full-field system with two semicircular illumination apertures will have same imaging properties as a system with split detector, i.e., differential phase contrast <sup>2</sup>. Ellis used the idea of asymmetric illumination in the method of single side-band edge enhancement (SSEE) [Ellis, 1981] in conjunction with polarization optics. Ellis described the contrast mechanism of SSEE as the interference of direct light and only one ‘sideband’ from the light diffracted by a phase-grating. To describe quantitative performance of his method, Ellis computed ‘sideband capture’ curves, shown as Fig. 10 and 11 of Ellis’s patent [Ellis,

---

<sup>1</sup>Zernike developed phase-contrast based on the Abbe’s diffraction theory that decomposes an object as a sum of sinusoidal gratings. Zernike realized that the orders diffracted by a sinusoidal phase-grating are  $\lambda/4$  out of phase with respect to direct light. By changing the phase and the amplitude of the direct light, the *interference* of direct and diffracted light produces an image that represents specimen phase.

<sup>2</sup>Stewart’s paper was missed in our paper [Mehta and Sheppard, 2009b] because we discovered Stewart’s paper only when writing this thesis.

1981], as a function of spatial frequency of the grating. These curves are numerically the same as phase-gradient transfer functions discussed in our work. Kachar [Kachar, 1985] presented interesting biological results demonstrating the high-resolution and depth-sectioning properties of asymmetric illumination. Axelrod [Axelrod, 1981] and Piekos [Piekos, 1999] have pointed out experimental advantages of oblique illumination as compared to phase-contrast.

All of the above researchers, except for Stewart, have mainly discussed qualitative visualization using oblique illumination. Stewart computes images of phase-gratings with oblique detection in scanning system or equivalently oblique illumination in full-field system [Stewart, 1976, Sec II]. We have extended above research with experimental images and theoretical analysis of imaging of a general specimen. The preliminary analysis of AIDPC is carried out with slowly varying specimen assumption in ref [Mehta and Sheppard, 2009b] and more complete analysis with full partially coherent model is carried out in in ref [Mehta and Sheppard, 2010c, sec 5]. The image formation analysis performed by above researchers can be re-derived using our full partially coherent model and the corresponding assumptions.

### **3.2 Paper: Quantitative phase-gradient imaging at high resolution with asymmetric illumination-based differential phase contrast**

# Quantitative phase-gradient imaging at high resolution with asymmetric illumination-based differential phase contrast

Shalin B. Mehta<sup>1,2,4,\*</sup> and Colin J. R. Sheppard<sup>1,2,3</sup>

<sup>1</sup>Optical Bioimaging Lab, Division of Bioengineering, National University of Singapore, Block-E3A, #7-10, 7 Engineering Drive 1, Singapore 117574

<sup>2</sup>NUS Graduate School for Integrative Sciences and Engineering, 28 Medical Drive, Singapore 117456

<sup>3</sup>Department of Biological Sciences, National University of Singapore, 14 Science Drive, Singapore 117543

<sup>4</sup>shalin@nus.edu.sg

\*Corresponding author: shalin@nus.edu.sg

Received March 30, 2009; revised May 22, 2009; accepted May 24, 2009;  
posted May 27, 2009 (Doc. ID 109303); published June 18, 2009

We describe a full-field phase-gradient imaging method: asymmetric illumination-based differential phase contrast (AIDPC). Imaging properties of AIDPC are evaluated using the phase-gradient transfer-function approach and elucidated with experimental images of an optical fiber and a histochemical preparation of a skeletal muscle section. In comparison with full-field differential interference contrast, AIDPC does not require phase shifting for quantitative imaging of phase gradient, provides artifact-free images of birefringent specimens, requires shorter camera exposure, and has larger depth of focus. It is amenable to transfer-function engineering, simultaneous fluorescence imaging, and automated live cell imaging. © 2009 Optical Society of America

OCIS codes: 110.0180, 110.4850, 100.5070, 110.4980.

Imaging of biological specimens requires special optical processing to translate the optical thickness (i.e., phase) information to image intensity. Direct quantitative measurement of phase requires use of coherent illumination, leading to limited spatial resolution, lack of optical sectioning, and speckle from imperfections in the optical train. Phase-gradient imaging methods such as Nomarski's differential interference contrast (DIC) can accommodate large illumination apertures (i.e., partially coherent illumination), alleviating the above problems. In scanning optical microscopy, an intrinsically linear phase-gradient contrast method, termed differential phase contrast (DPC) has been evaluated [1–3]. In contrast to DPC, DIC images a complex mix of amplitude and phase-gradient information, necessitating approaches such as phase shifting (PSDIC) to establish a linear relationship between the image intensity and the specimen's phase gradient [4,5]. Linear measurement of phase gradient along two orthogonal directions allows retrieval of 2D phase distribution [4]. In this Letter, we demonstrate a wide-field equivalent of the scanning DPC microscope based on asymmetric illumination [6], termed asymmetric illumination-based differential phase contrast (AIDPC). Asymmetric illumination has long been used for high-resolution qualitative imaging of a phase specimen with shadow cast similar to DIC [7–9]. Tomographic approaches for measurement of phase distribution using coherent asymmetric illumination have been developed [10]. However, this seems to be the first report of quantitative phase imaging based on asymmetric illumination with a large aperture.

One can arrive at the wide-field equivalent of the scanning DPC system using the principle of reciprocity, as illustrated in Fig. 1. A scanning system with an incoherent detector has imaging properties iden-

tical to those of the full-field system with an incoherent source if two conditions are met [11]: (1) each system has the same objective apertures (i.e., pupil amplitude),  $P_o(\xi, \eta)$  and (2) the sensitivity distribution of the detector in the scanning system is the same as the intensity distribution of the condenser aperture,  $|P_c(\xi, \eta)|^2$ , in the full-field system. In scanning DPC, a split-detector or a quadrant diode is placed in the Fourier plane of the collector, and the image is formed by subtracting intensities recorded by two halves of the detector. A reciprocal wide-field DPC system has an antisymmetric condenser aperture with half of the aperture having negative effective intensity. We synthesize negative condenser intensity by subtracting two images acquired with semicircular condenser apertures in the direction of differentiation.

For experiments presented in this Letter, we simply placed semicircular pieces of opaque paper at two positions in the condenser turret. The paper blocks were adjusted to mask opposite halves of the con-

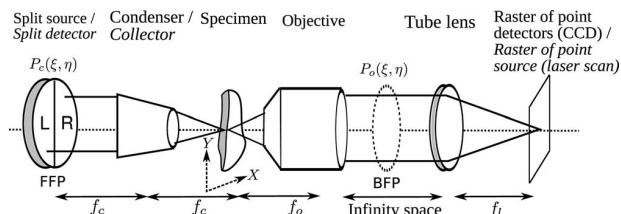


Fig. 1. Equivalence of a full-field system using a split source (AIDPC) and a scanning system with a split detector (scanning DPC). The light propagates from left to right in the full-field system and from right to left in the scanning system. Components of the scanning system are labeled in italics.  $f_c$ ,  $f_o$ , and  $f_t$  are focal lengths of the condenser/collector, objective, and tube lens, respectively. The phase differentiation is assumed to be along the  $X$  direction.



denser aperture, by looking at the front focal plane (FFP) of the condenser with a Bertrand lens. Precise placement of the aperture blocks at the FFP along the optical axis is necessary to achieve uniform illumination in the specimen plane. The image obtained with left half of the condenser aperture (say,  $I_L$ ) and the right half of the condenser aperture (say,  $I_R$ ) were used to compute average  $[(I_R + I_L)/2]$  and difference  $(I_R - I_L)$  images, which correspond to bright-field and the image considered to be DPC in scanning microscopy. Instead, we define the DPC image to be the ratio of difference and average images for reasons described later. Thus

$$I_{\text{DPC}} = 2 \frac{I_R - I_L}{I_R + I_L}. \quad (1)$$

In the following, the term DPC refers in general to scanning DPC and AIDPC.

When a slowly varying specimen (with respect to the spatial resolution) is assumed, the effects of finite illumination and imaging apertures used in DIC and DPC can be accounted for by using the phase-gradient transfer function (PGTF) [2]. With Köhler illumination, the phase gradient of  $m$  (normalized with respect to  $\text{NA}_{\text{obj}}/\lambda$ ) will image the condenser aperture displaced by  $m$  in the objective aperture. Thus the relative intensity with which that gradient is detected is equal to the area of overlap of the magnitudes of the condenser pupil and the objective pupil shifted by  $m$ . Hence, the PGTF of an imaging system can be computed as

$$C(m, n) = \iint |P_c(\xi, \eta)|^2 |P_o(\xi - m, \eta - n)|^2 d\xi d\eta, \quad (2)$$

where,  $m$  and  $n$  denote the specimen gradients along the  $X$  and  $Y$  directions. The same model can be arrived at by assuming a slowly varying specimen in full partially coherent transfer-function model of any full-field imaging system, e.g., for DIC [12,13]. Although it can be extracted from the partially coherent transfer function, PGTF is not a transfer function in the usual sense but relates the phase gradient and the image intensity in the sense of a look-up table. This leads to a useful property that the effective PGTF for the ratio of two images obtained with different apertures is the ratio of the corresponding PGTFs. Although the ratio in Eq. (1) normalizes in-focus absorption information, out-of-focus differential absorption that affects relative strengths of  $I_R$  and  $I_L$  can cause global bias in the DPC image.

Figure 2(a) shows the computed PGTFs in the direction of differentiation for different imaging modes, assuming matched illumination. PGTFs for  $I_L$  and  $I_R$  are computed by substituting semicircular  $P_c$  and circular  $P_o$  in Eq. (2). Pupils for the DIC configuration are simulated as shown in Fig. 2 of [13]. Notice that DIC configuration has nonlinear PGTF with prominent zero crossings, owing to finite aperture and finite shear. These zero crossings can lead to contrast reversals in the image and cause the linearization algorithms for DIC to fail, as they are also based on a

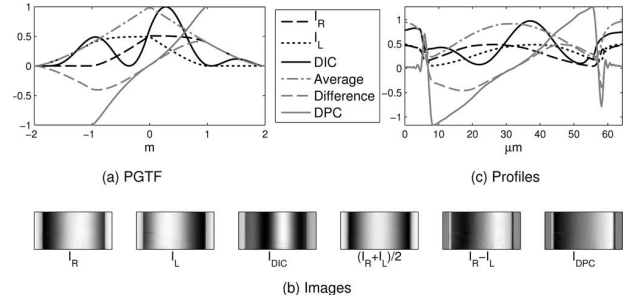


Fig. 2. Experimental comparison of computed PGTFs in (a) with contrast observed in images in (b) and line profiles in (c), for different imaging modes. In the orthogonal direction, imaging properties of all modes are the same as the bright field.

ratio of image intensities. With semicircular condenser apertures and matched illumination, the PGTF for DPC is nearly linear up to half the cutoff of the imaging system. However, optimization of the intensity variations in the condenser FFP using Eq. (2) allows synthesis of the PGTF of choice and consequently the desired phase-gradient contrast. An equivalent approach in scanning DPC is to use detectors of varying sensitivity distributions [2]. These AIDPC configurations can be constructed with a spatial light modulator placed at the FFP of the condenser acting as an effective source. Such an automated setup can be used for live-cell morphological imaging with AIDPC in transmission and fluorescence imaging in reflection without requiring mechanical movement. For *matched illumination*, we can achieve linear imaging of the phase gradient along a certain direction with linearly varying condenser intensity. This conclusion follows from the result  $2[\xi P(\xi, \eta) \otimes P(\xi, \eta)]_{(m,n)} = m[P(\xi, \eta) \otimes P(\xi, \eta)]_{(m,n)}$  [14], proven easily by taking the Fourier transform on both sides and using convolution and differentiation theorems.

For experimental verification, we used a 0.75 NA,  $20\times$  objective, matched condenser aperture, quasi-monochromatic illumination obtained with a  $\lambda = 550$  nm interference filter, an Olympus BX61 microscope equipped with strain-free optics, and a Peltier-cooled Olympus DP30BW monochrome camera. By observing the objective backfocal plane (BFP) with the Bertrand lens and counting the number of fringes that fit inside the BFP, the shear was estimated to be  $0.7\lambda/\text{NA}_{\text{obj}}$  according to the equation for the objective BFP (square of Eq. (3) in [13]). The bias was adjusted to  $\pi/2$  using a de Sénarmont compensator. Optical fiber is a good test specimen for verifying observations made with Fig. 2(a) and exhibits phase gradients from zero at center to very high at edges. When the fiber is aligned perpendicular to the direction of the shear, the intensity profile across its width should follow the shape of the PGTF in accordance with the phase gradient of the fiber. Figure 2(b) shows images of an optical fiber under different imaging modes taken from a light-guide bundle Edmund Optics #39366 (clad diameter  $50\ \mu\text{m}$ , core diameter unspecified, clad RI 1.487, core RI 1.581.) The fiber was immersed in water and mounted under a glass cover-



slip. The profiles across the width of the fiber in Fig. 2(c) are obtained by summing the pixels along the Y direction of images shown in Fig. 2(b). These profiles correspond well with the PGTFs presented in Fig. 2(a). The images of optical fiber in Fig. 2(b) corroborate the above prediction of contrast reversal in the DIC image. At the edges of the fiber, the phase gradient exceeds the cutoff of all imaging modes, refracting the entire cone of illumination out of the imaging aperture. At such high gradients quantitative relationship dictated by the PGTF fails.

Birefringence introduces different phase delays to orthogonally polarized beams of DIC, effectively causing local variations in the bias and disrupting the contrast mechanism of DIC. DPC does not rely on manipulation of polarization to achieve phase-gradient contrast and provides artifact-free images, even for strongly birefringent objects such as starch granules (images not shown). However, a strongly, birefringent region with its optic axis inclined with axis of the imaging system introduces a differential refractive index to left and right illumination half cones, compromising the quantitative nature of DPC. DPC can also be used to image samples grown on plastic [6]. In the absence of absorption information, either  $I_R$  or  $I_L$  provides qualitative phase-gradient contrast (see Fig. 1 of [15]). DIC can suppress some absorption information when used with low bias [12], but complete removal requires PSDIC. Figure 3 illustrates that DPC can visualize the morphology of a birefringent and absorbing specimen. Birefringent regions, appearing bright in Fig. 3(f), appear too dark or too bright in a PSDIC or DIC image at bias  $\pi/5$ . In absence of complimentary information, birefringent structures may be mistaken as absorbing in DIC, as seen in Fig. 3(c). The AIDPC image and the average image [Figs. 3(a) and 3(d)] show that DPC provides clearer separation of absorption and phase-gradient information. In conjunction with AIDPC, birefringence measurement by LC-Polscope [5] should provide

vide complementary information. The unmodified objective side-light path of AIDPC affords shorter exposure than possible with DIC or phase contrast. To fill up the dynamic range of the camera, the following exposure durations were required: 3.9 ms for  $I_R$  and  $I_L$  and 280 ms for the DIC image at bias  $\pi/5$ . In DIC, poor transmission of white light by polarizers and theoretical losses due to manipulation of polarization necessitate such long exposures.

We have experimentally noticed that AIDPC has around twice the depth of focus of DIC. A similar observation is made by Amos *et al.* [3] for scanning DPC. The PGTF of an imaging system depends only on the squared magnitude of the objective and condenser pupils [Eq. (2)] and hence predicts no effect from defocus or other aberrations. However, our algorithm for computing the full partially coherent transfer function of a general full-field imaging system [13] can be used to examine effects of defocus on imaging properties of DIC and DPC.

In conclusion, AIDPC allows linear imaging of phase-gradient information for a variety of specimens, easy engineering of the transfer function, artifact-free imaging of birefringent specimens, simultaneous high-resolution fluorescence imaging, shorter exposure, and automation for live-cell imaging. However, the quantitative nature is compromised when the specimen affects the left and right half cones of illumination with differential out-of-focus absorption or strong differential birefringence.

Support from the Singapore Ministry of Education Tier-1 grant (R397000033112) is acknowledged.

## References

1. D. K. Hamilton and C. J. R. Sheppard, *J. Microsc.* **133**, 27 (1984).
2. D. K. Hamilton, C. J. R. Sheppard, and T. Wilson, *J. Microsc.* **135**, 275 (1984).
3. W. B. Amos, S. Reichelt, D. M. Cattermole, and J. Laufer, *J. Microsc.* **210**, 166 (2003).
4. M. R. Arnison, K. G. Larkin, C. J. R. Sheppard, N. I. Smith, and C. J. Cogswell, *J. Microsc.* **214**, 7 (2004).
5. M. Shribak, J. LaFountain, D. Biggs, and S. Inoue, *J. Biomed. Opt.* **13**, 014011–10 (2008).
6. S. B. Mehta and C. J. R. Sheppard, presented at Focus on Microscopy 2008, April 13–16, 2008, Awaji, Japan. [www.focusonmicroscopy.org/2008/PDF/089.pdf](http://www.focusonmicroscopy.org/2008/PDF/089.pdf).
7. G. W. Ellis, "Edge enhancement of phase phenomena," U.S. patent 4,255,014 (March 10, 1981).
8. B. Kachar, *Science* **227**, 766 (1985).
9. R. Yi, K. K. Chu, and J. Mertz, *Opt. Express* **14**, 5191 (2006).
10. T. Noda, S. Kawata, and S. Minami, *Appl. Opt.* **31**, 670 (1992).
11. C. J. R. Sheppard and T. Wilson, *J. Opt. Soc. Am. A* **3**, 755 (1986).
12. C. J. Cogswell and C. J. R. Sheppard, *J. Microsc.* **165**, 81 (1992).
13. S. B. Mehta and C. J. R. Sheppard, *Opt. Express* **16**, 19462 (2008).
14. T. Wilson and C. J. R. Sheppard, *Proc. SPIE* **232**, 203 (1980).
15. S. B. Mehta and C. J. R. Sheppard, presented at Focus on Microscopy 2009, April 5–8, 2009, Krakow, Poland. [www.focusonmicroscopy.org/2009/PDF/396\\_Mehta.pdf](http://www.focusonmicroscopy.org/2009/PDF/396_Mehta.pdf).

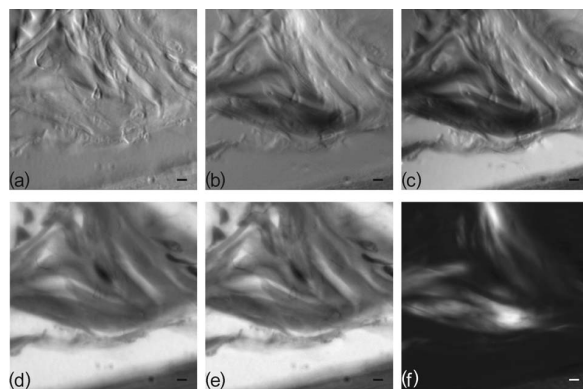


Fig. 3. AIDPC segregates absorption and phase-gradient information in a birefringent specimen. Images of H&E-stained skeletal muscle section (Carolina biological #313256) with different imaging modes: (a) AIDPC, (b) PSDIC (according to the four-frame algorithm of [4]), (c) DIC image with bias  $\pi/5$ , (d) average  $(I_R + I_L)/2$ , (e) bright field, and (f) crossed polarizers. Images were acquired using 0.9 NA, 40 $\times$  objective, matched illumination, and white light from a halogen lamp set at 7 V. Scale bar, 2.5  $\mu$ m.

### 3.3 Further discussion of imaging properties of AIDPC

In this section, we elaborate upon the effects of the specimen's birefringence and absorption on phase-gradient contrast produced by AIDPC. We also compare the light throughput and background in AIDPC and DIC.

#### 3.3.1 Effect of specimen absorption and birefringence

DIC image is a mixture of phase, absorption, and birefringence information, and therefore difficult to interpret for specimens that have all of the above features. The birefringence of the specimen or of the optical path degrades the DIC image significantly, because birefringence disrupts the precise manipulation of the polarization employed to produce the phase-gradient contrast. In contrast, (AI)DPC does not rely on polarization manipulation to produce the phase-gradient contrast and hence provides artifact-free images of birefringent specimens. Moreover, (AI)DPC also separates the amplitude and the phase information much more clearly.

The ratiometric nature of AIDPC in effect normalizes for absorption in the plane of focus. However, two half-apertures used in AIDPC would give rise to an intensity gradient in the image in the presence of differential absorption out of focus. This intensity gradient may be interpreted as arising from the phase gradient in the specimen. This behaviour occurs because  $I_R$  and  $I_L$  illumination cones (seen by a single camera pixel) are relatively well-separated in space everywhere but at the plane of focus, unlike DIC. Therefore, if an out-of-focus plane contained more absorbers on the right hand side of the sample than on the left, there would be a global bias in the AIDPC image. In the context of imaging unstained biological specimens this is a rare enough difficulty, and would not significantly impede the potential usefulness of the technique.

It has been shown that oblique illumination in a polarized light microscope produces an image sensitive to the component of the specimen birefringence *along the central ray of the illuminating aperture* [Shribak and Oldenbourg, 2004]. Therefore, one may think that AIDPC image may contain artifacts when a birefringent specimen with strong component along the central ray of one of the semicircular aperture is imaged. For the sake of illustra-

tion, let us consider a calcite crystal with its optic axis aligned parallel to the central ray of one of the semicircular aperture (say, left-half) used in AIDPC. Therefore, the central ray from the left-half aperture will experience a refractive index of 1.66 and the central ray from the right-half aperture will experience a refractive index of close to 1.49. However, image formation in AIDPC is partially coherent and not just the central ray but the entire aperture contributes to contrast. Therefore, the effect of the specimen birefringence is negligible. To illustrate this point, we compare images of potato starch granules taken with DIC, AIDPC, brightfield, and crossed polarizers in fig. 3.1. Starch granules have radially oriented regions which are alternately crystalline and semi-crystalline [Gallant et al., 1997, pp. 188]. The crystalline regions act as a positive uniaxial crystal and are responsible for the maltese cross seen under polarized light as seen in fig. 3.1. Starch granules present nearly all possible inclinations of the birefringence axes to the imaging system like the re-constituted aster mentioned in ref [Shribak and Oldenbourg, 2004]. From fig. 3.1, we notice that AIDPC image does not show observable artifacts due to specimen birefringence.

### 3.3.2 Light throughput and signal to noise performance

First, we elaborate upon the significantly different exposure values reported in [Mehta and Sheppard, 2009b, fig 3] when imaging with AIDPC and DIC. The exposure values mentioned in the [Mehta and Sheppard, 2009b, fig 3] take into account the entire optical path from the source to the detector. The images were taken without an interference filter after the source. In AIDPC, we lose 50% of the light to half-aperture. Ideally in DIC, we lose 50% of the light to polarizer (as the source was a halogen lamp in our case). Since a bias of  $\pi/2$  gives rise to nearly circularly polarized wavefront just before the analyzer, we lose another 50% upon transmission through the analyzer. Therefore, the theoretical transmittance of DIC system at bias  $\pi/2$  would be 25%. However, optical components in light-path further reduce the transmission. We made rough measurements of transmittance of the optical components by inserting them in the bright-field light-path (without an interference filter) and noticing the reduction in pixel values at fixed exposure. Values are as follows: polarizer's transmittance under unpolarized light 27%; analyzer's transmission for light polarized along its transmission axis 33%; combined transmittance of quarter wave plate

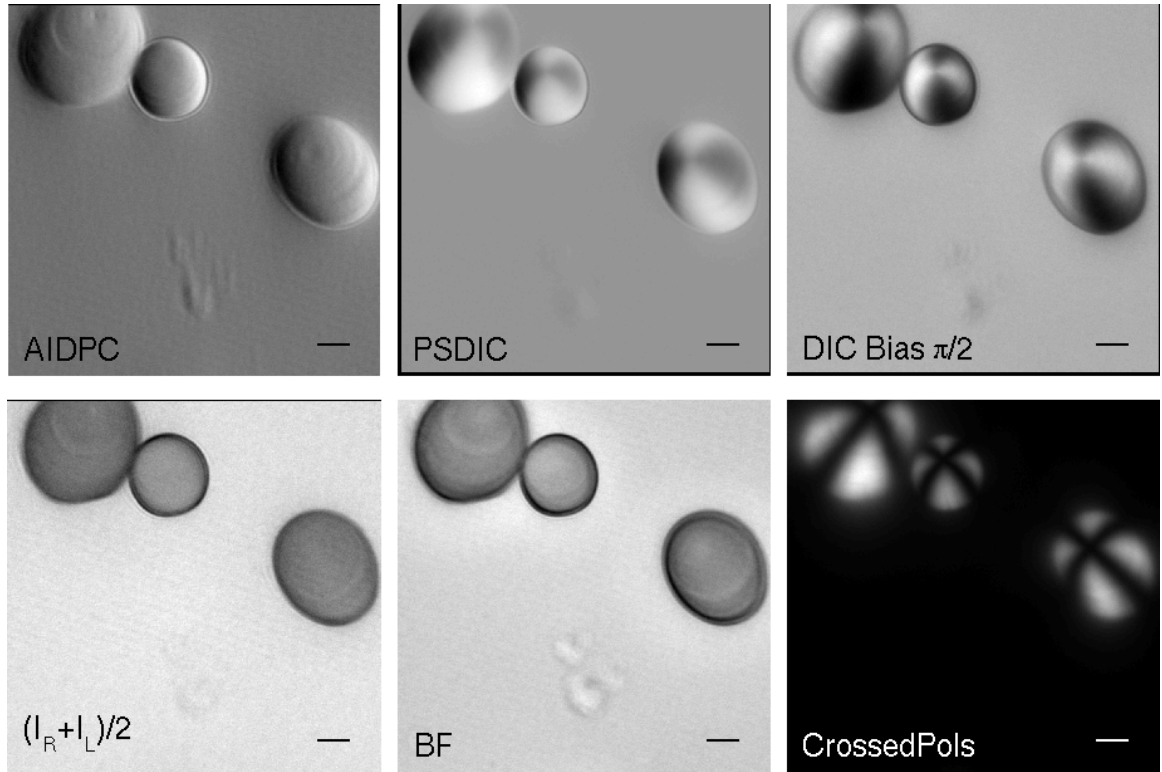


Figure 3.1: Images of potato starch granules with AIDPC, phase-shifting DIC (PSDIC), DIC at bias  $\pi/2$ , average of left and right oblique illumination images  $((I_L + I_R)/2)$ , brightfield (BF), and crossed polarizers (CrossedPols): The image taken with crossed polarizers reveal the arrangement of birefringent domains within the starch granules. The regions whose birefringence axes is at an angle other than  $0^\circ$  or  $90^\circ$  appear bright between crossed polarizers. DIC and PSDIC images show birefringence contrast, whereas the AIDPC images has phase-gradient contrast. The average image from left and right half apertures is the same as brightfield image.

(used for de Senarmont compensation) and prisms in unpolarized light - 90%. Thus, the effective transmittance of the light-path is  $0.27 * 0.33 * 0.9 * 0.5 = 4\%$  - the last factor of 0.5 being due to the bias of  $\pi/2$ . Thus, overall transmission of AIDPC in our experimental setup is 50% whereas that of DIC at bias  $\pi/2$ , at which highest transmission is expected, is 4%. Therefore, exposure values noted in [Mehta and Sheppard, 2009b, fig 3] at bias  $\pi/5$  are expected. We should note that the high-losses noted above for polarizers are due to the broadband nature of the illumination.

Imaging in AIDPC is not limited by shot noise but rather the background such as mottle and specimen absorption. We acquire all images to fill up the dynamic range of the camera pixels. Consequently, in each image, the brightest pixel receives roughly the same number of photons. Therefore, each asymmetric image will have nearly the same shot noise contribution as either brightfield or single DIC image. It is known that for weak phase specimens, mottle is a much severe problem than shot-noise [Allen and Allen, 1983]. If shot-noise is indeed found to be a problem, the short exposure afforded by AIDPC can be used for taking multiple images and averaging them. The phase gradient information reinforces upon subtraction of the images but the unwanted amplitude information tends to cancel.

## Chapter 4

# Phase-space imager

From the previous two chapters, it is evident that image formation in phase-microscopy methods such as DIC, oblique illumination or DPC has been *described* with different approaches. Some image formation models turned out to be inaccurate due to incorrect assumptions, as was shown to be the case in Chap 2 for some existing models of DIC [Preza et al., 1999]. The development of different interpretations of image formation, based on different assumptions about the specimen (e.g., periodic, weak, or slowly varying) or the system (e.g., coherent illumination), is due to the inherent bi-linearity of partially coherent imaging. The above mentioned assumptions are aimed at interpreting the image formation in ‘linear terms’ so that physical intuition can be derived and images of known specimens can be computed.

In this chapter, we report our attempt at overcoming the above assumptions, but nevertheless achieving the physical insight and the ability to compute images of known specimens. A well-established and often-used bi-linear model of partially coherent image formation is Hopkins’s transmission cross coefficient (TCC) model [Hopkins, 1953]. The TCC model has been used to understand image formation in full-field and scanning microscopy methods [Sheppard and Choudhury, 1977, Wilson and Sheppard, 1984], and for image computation in optical lithography systems [Schellenberg, 2004, Yamazoe, 2008, 2010]. Nevertheless, there is a general demand for development of a more intuitive and computationally efficient model of partially coherent imaging [Martin, 1966, Singer et al., 2005]. Since the phase-space representations (briefly described in sec. 1.3) and the TCC model both are bi-linear, a

phase-space ‘link’ to the TCC model has long been anticipated but never quite established. We establish this link by describing the image formation in partially coherent system using a windowed-Wigner distribution. We describe the basic features of the model and illustrate its use in our paper [Mehta and Sheppard, 2010a] that is typeset as sec. 4.1. We thank Dr. Martin Bastiaans (Eindhoven University of Technology, Netherlands) for his crash-course on phase-space optics during his visit to Singapore. During one of his lectures, we came upon the idea that windowed-Wigner distribution may lead us to a useful phase-space model from the TCC model.

Instead of describing wave propagation (the goal of majority of current phase-space representations in optics), our phase-space representation offers a ‘systems’ view of partially coherent imaging in a similar vein as the representation of linear imaging in terms of the point spread function or the optical transfer function. Our representation, named phase-space imager (PSI), expresses the output of the imaging system (i.e., image) as a linear operation between the input (i.e., mutual spectrum or Wigner distribution of the specimen’s transmission) and a system dependent function. Cohen has shown [Cohen, 1966, 1995] that all bi-linear phase-space distributions can be expressed as windowing of the input signal’s mutual spectrum<sup>1</sup> or the convolution by a suitable kernel of the input signal’s Wigner distribution. All such phase-space representations are said to constitute the Cohen class of signal representation. Our model, called *phase-space imager*, also is a member of Cohen class. In our paper (sec 4.1), we develop the PSI model starting from the TCC model in which image formation is described as filtering of the mutual spectrum of the specimen. In sec 4.2, we describe the PSI model as a convolution of the specimen’s Wigner distribution and the kernel (called PSI-kernel).

## 4.1 Paper: Phase-space representation of partially coherent imaging systems using the Cohen class distribution

---

<sup>1</sup>See the entry for  $S_m(\mathbf{m}, \mathbf{m}')$  in the nomenclature for a definition of the mutual spectrum.



# Phase-space representation of partially coherent imaging systems using the Cohen class distribution

Shalin B. Mehta<sup>1,2,\*</sup> and Colin J. R. Sheppard<sup>1,2,3</sup>

<sup>1</sup>Optical Bioimaging Laboratory, Division of Bioengineering, National University of Singapore, Block-E3A, #7-10, 7 Engineering Drive 1, Singapore 118431

<sup>2</sup>NUS Graduate School for Integrative Sciences and Engineering, 28 Medical Drive, Singapore 117456

<sup>3</sup>Department of Biological Sciences, National University of Singapore, 14 Science Drive, Singapore 117543

\*Corresponding author: shalin.mehta@gmail.com

Received August 28, 2009; revised December 17, 2009; accepted December 21, 2009;  
posted December 23, 2009 (Doc. ID 116357); published January 26, 2010

We develop a phase-space representation (termed *phase-space imager*) suitable for analysis and design of imaging systems that use large illumination apertures (partially coherent illumination). The representation, developed from the transmission cross-coefficient model, falls in the general Cohen class of distributions and elegantly captures the bilinear nature of image formation in partially coherent systems. It uses only the requisite number of dimensions and leads to an efficient algorithm for calculating images. Computed partially coherent images of a double slit and a two-dimensional sinusoidal spoke are presented. © 2010 Optical Society of America

OCIS codes: 050.5082, 110.4980, 110.4850.

Partially coherent illumination has the desirable properties of higher lateral resolution, depth sectioning, and immunity against speckle noise, in comparison to coherent illumination. Hence, there is recent interest in quantitative imaging with partially coherent systems, which necessitates accurate models.

Figure 1 schematically shows typical partially coherent imaging systems that can be implemented either in scanning or in wide-field mode. The imaging system is characterized by the intensity distribution of the incoherent condenser/collector pupil  $|P_c(\xi)|^2$  and complex transmission of the objective pupil,  $P_o(\xi)$ . Both modes provide identical images provided the specimen is reciprocal. The specimen is assumed to be modeled by a transparency  $t(x)$ . Aberrations of the imaging system are accounted for by using a complex objective pupil, and the aberrations at the condenser aperture are unimportant owing to its incoherence. Coherence of imaging is controlled by the ratio of the condenser NA to the imaging NA,  $S = NA_c/NA_o$ , which is called the coherence ratio. In this Letter, for brevity's sake, 2D independent variables are represented by vectors and indicated by boldface characters. All integrals over vector coordinates signify two-dimensional integrals and range from  $-\infty$  to  $\infty$ . Throughout the Letter, the space variables are expressed in normalized units of  $\lambda/NA_o$ , where  $\lambda$  is the mean wavelength of quasi-monochromatic illumination. The pupil and spatial frequency variables are expressed in normalized units of  $NA_o/\lambda$ . The kernel used to Fourier transform  $\mathbf{x}$  variable to  $\mathbf{m}$  variable is  $e^{-2\pi i \mathbf{x} \cdot \mathbf{m}}$ , where  $\mathbf{x} \cdot \mathbf{m}$  is the inner product of vectors. Fourier transform over vector variable  $\mathbf{x}$  is represented by  $\mathcal{F}_{\mathbf{x}}$ .

Imaging properties of the partially coherent systems have to be described using a bilinear model [1,2]. A well-established model for partially coherent imaging is based on the concept of the transmission cross-coefficient (TCC) that arises when image formation is described in the spatial-frequency domain

[1,2]. In the TCC model, bilinearity appears in the form of dependence of a spatial frequency of the image on the pairs of spatial frequencies of the specimen. Wigner distribution and other phase-space representations (whose kernels do not depend on the signal) are also bilinear [3]. Phase-space representations express “pairs” in terms of their center and difference coordinates, as evident from the spatial-frequency definitions of the Wigner distribution of the specimen's transmission given by

$$W_t(\mathbf{m}, \mathbf{x}) = \int T\left(\mathbf{m} + \frac{\mathbf{m}'}{2}\right) T^*\left(\mathbf{m} - \frac{\mathbf{m}'}{2}\right) e^{2\pi i \mathbf{m}' \cdot \mathbf{x}} d\mathbf{m}', \quad (1)$$

where,  $T(\mathbf{m}) = \mathcal{F}_{\mathbf{x}}[t(\mathbf{x})]$ . The projection of the Wigner distribution along the spatial-frequency dimension,  $\int W d\mathbf{m}$ , is called the *spatial marginal* and is equal to the squared magnitude of the specimen transmission,  $|t(\mathbf{x})|^2$ . Analogously, the *spatial-frequency marginal* of the Wigner distribution is the squared magnitude of the spectrum,  $|T(\mathbf{m})|^2$ .

Since phase-space representations lead to better physical insight and computational algorithms [3,4], it is attractive to study bilinear image formation in phase-space. Significant progress has been made in

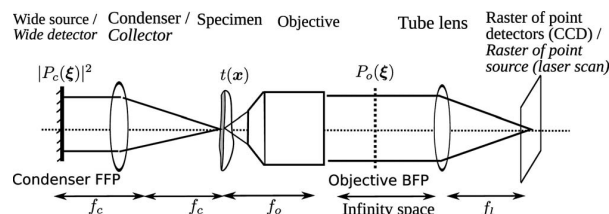


Fig. 1. A scanning-based (light propagation from right to left) or wide-field (light propagation from left to right) partially coherent imaging system is described by intensity distribution in the condenser pupil and amplitude distribution in the objective pupil. Labels in italics indicate terms used for the scanning microscope.



the description of partially coherent signals and their propagation through linear optical system in phase space [4]. However, only a few attempts have been made to derive phase-space descriptions of the overall transfer properties of a partially coherent system. Ojeda-Castañeda [5] described imaging of a 2D specimen using a projection of 8D bilinear ray-spread function, which is a generalization of 4D coherent ray-spread function proposed by Bastiaans [4]. The bilinear ray-spread function is not determinable from the pupils of the imaging system. Castañeda [6] derived a phase-space representation by considering transfer of spatial coherence wavelets but did not describe efficient computation of images. In this Letter, for the first time to our knowledge, a nonredundant phase-space representation of transfer properties of partially coherent imaging systems is derived. The model allows improved interpretation of the TCC model, can be used for analysis and design of partially coherent imaging methods, and leads to an efficient algorithm for computing images.

As per the TCC model, the image intensity can be written in terms of the specimen spectrum  $T(\mathbf{m})$  and the system pupils in the following form [1]:

$$I(\mathbf{x}) = \int \int T(\mathbf{m}_1) T^*(\mathbf{m}_2) C(\mathbf{m}_1, \mathbf{m}_2) \times e^{2\pi i(\mathbf{m}_1 - \mathbf{m}_2) \cdot \mathbf{x}} d\mathbf{m}_1 d\mathbf{m}_2. \quad (2)$$

In the above,

$$C(\mathbf{m}_1, \mathbf{m}_2) = \int |P_c(\xi)|^2 P_o(\mathbf{m}_1 + \xi) P_o^*(\mathbf{m}_2 + \xi) d\xi$$

is the TCC of the imaging system. Interpreting graphically, the TCC is an area of overlap of three pupils—the condenser pupil situated at the center, the objective pupil shifted by  $\mathbf{m}_1$  and the conjugate objective pupil shifted by  $\mathbf{m}_2$ . When computing images of multiple specimens under the given imaging system, and vice versa, the separation of  $T(\mathbf{m}_1) T^*(\mathbf{m}_2)$  and the TCC allows efficient computation. The TCC describes the strengths with which pairs of the specimen spatial frequencies,  $(\mathbf{m}_1, \mathbf{m}_2)$ , are transferred to the image.

We arrive at a phase-space model by substituting the frequency pair  $(\mathbf{m}_1, \mathbf{m}_2)$  by center and difference frequency variables,  $\mathbf{m} = \frac{1}{2}(\mathbf{m}_1 + \mathbf{m}_2)$  and  $\mathbf{m}' = \mathbf{m}_1 - \mathbf{m}_2$ . Noting that the Jacobian of the transformation is unity the intensity can be expressed as

$$I(\mathbf{x}) = \int \int T\left(\mathbf{m} + \frac{\mathbf{m}'}{2}\right) T^*\left(\mathbf{m} - \frac{\mathbf{m}'}{2}\right) C(\mathbf{m}, \mathbf{m}') \times e^{2\pi i \mathbf{m}' \cdot \mathbf{x}} d\mathbf{m} d\mathbf{m}'. \quad (3)$$

Upon integrating over  $\mathbf{m}'$ , we notice that the image intensity is a spatial marginal of a particular phase-space distribution as follows:

$$I(\mathbf{x}) = \int \Psi(\mathbf{m}, \mathbf{x}; C) d\mathbf{m}, \quad (4)$$

where

$$\Psi(\mathbf{m}, \mathbf{x}; C) = \int T\left(\mathbf{m} + \frac{\mathbf{m}'}{2}\right) T^*\left(\mathbf{m} - \frac{\mathbf{m}'}{2}\right) C(\mathbf{m}, \mathbf{m}') \times e^{2\pi i \mathbf{m}' \cdot \mathbf{x}} d\mathbf{m}' \quad (5)$$

is the windowed Wigner distribution [3] of the specimen transmission. We call this distribution the phase-space imager (PSI), which describes transfer of specimen transmission to the image intensity when imaged with a system of arbitrary coherence. The above derivation uses the definition of the Wigner distribution based on the spectrum of the specimen [Eq. (1)]. The distribution in Eq. (5) falls in the general Cohen class of bilinear distributions whose windows do not depend on the signal. ([3], Sec. 9.3).

The quantity being windowed,  $T(\mathbf{m} + \mathbf{m}'/2) T^*(\mathbf{m} - \mathbf{m}'/2)$ , can be called the *mutual specimen spectrum* as it is a function of pairs of frequencies. The window in this case is  $C(\mathbf{m}, \mathbf{m}')$ , which is termed the *PSI-window* and is given by

$$C(\mathbf{m}, \mathbf{m}') = \int |P_c(\xi)|^2 P_o\left(\mathbf{m} + \frac{\mathbf{m}'}{2} + \xi\right) \times P_o^*\left(\mathbf{m} - \frac{\mathbf{m}'}{2} + \xi\right) d\xi. \quad (6)$$

Equations (4)–(6) provide an insightful interpretation of the behavior of partially coherent systems. The imaging system can be said to filter the mutual specimen spectrum, the filter being the PSI-window (which depends on the pupils of the imaging system). The symmetry of the PSI-window determines the contrast produced by the imaging system, whereas the support of the PSI-window determines the resolution. The PSI model connects image formation with extensive literature on windowed phase-space distributions [3]. Deeper understanding of partially coherent image formation can be gained by exploring this signal processing view further.

Analogous to TCC, the PSI-window is computed as the area of overlap in the  $\xi$  plane, but by shifting both objective pupils by  $\mathbf{m}$ , and from that point shifting the  $P_o$  by  $\mathbf{m}'/2$  and the  $P_o^*$  by  $-\mathbf{m}'/2$ . We notice that  $C(\mathbf{m}, -\mathbf{m}') = C^*(\mathbf{m}, \mathbf{m}')$ , i.e., the PSI window is Hermitian symmetric along the  $\mathbf{m}'$  dimension, which ensures positive intensity. We adapted our previous algorithm of computing the TCC as an area of overlap of shifted pupils [7] for computation of PSI-window. In normalized units mentioned at the beginning, the radii of  $P_o$  and  $P_c$  are 1 and  $S$ , respectively. Since  $\mathbf{m}$  represents the distance between  $P_o(\xi)$  and  $P_c(\xi)$ , the PSI-window cuts-off at  $m_0 = 1 + S$ , along that dimension.  $\mathbf{m}'$  represents the distance between  $P_o(\xi)$  and  $P_o^*(\xi)$  and hence PSI-window cutoffs at  $m'_0 = 2$ . The cutoffs of PSI-window along  $\mathbf{m}$  and  $\mathbf{m}'$  for various coherence ratios can be observed from Media 1 related to Fig. 2.

A transparent line is the simplest 1D object whose image is influenced (albeit not significantly) by the coherence of illumination (i.e.,  $S$ ) ([1], Sec. 6). Even for the line, image cannot be expressed in closed form

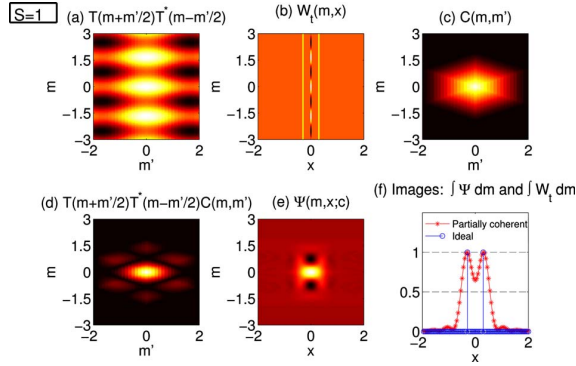


Fig. 2. (Color online) Simulating the effects of coherence of illumination on resolvability of a double slit: a snapshot from [Media 1](#) (2.6 MB) at  $S=1$ . See the text for details.

for all values of  $S$ . We illustrate and verify our algorithm by simulating image of a double slit. Goodbody [8] presented numerically computed images of a double slit for general value of  $S$ . Transmission of a double slit is given by  $t(x, y) = \delta(x + x_s/2) + \delta(x - x_s/2)$ , and hence the spectrum by  $T(m, n) = \cos(2\pi m x_s/2) \delta(n)$ , where  $x_s$  is the separation between two infinitesimal slits and  $(m, n)$  are spatial frequencies along  $(x, y)$ . Figure 2 and the associated image sequence ([Media 1](#)) show computation of the ideal and partially coherent images of a double slit (with  $x_s = 0.6\lambda/\text{NA}_0$ ) under the bright-field microscope.

The ideal system has infinitely large imaging and illumination apertures, leading to  $C(\mathbf{m}, \mathbf{m}') = 1$ . From Eq. (5), we see that  $\Psi(\mathbf{m}, \mathbf{x}; c)$  reduces to the usual Wigner distribution of the specimen transmission, whose spatial marginal from Eq. (4) is  $|t(\mathbf{x})|^2$ . Thus the ideal imaging system leads to the specimen magnitude as expected. Figures 2(a), 2(b), and 2(f) show calculated mutual specimen spectrum, Wigner distribution, and the ideal image (i.e., spatial marginal of the Wigner distribution), respectively, for the double slit. To calculate a partially coherent image, we first compute the PSI-window along  $X$  dimension as per Eq. (6) as shown in Fig. 2(c). Now, the image of any specimen can be computed by evaluating Eqs. (5) and (4) in following steps: (1) multiply the mutual specimen spectrum with the PSI-window as shown in Fig. 2(d), (2) Fourier transform the product along  $\mathbf{m}'$  to obtain the PSI as shown in Fig. 2(e), and (3) project the PSI along  $\mathbf{m}$  to obtain the image intensity. The associated image sequence ([Media 1](#)) shows above quantities calculated at  $S=0.1 \dots 2$ . These coherence ratios cover the range from quite coherent to nearly incoherent illumination and demonstrate remarkably the effects of the coherence on the resolution of the closely spaced double slit. In particular, it is seen that the resolvability of the slits improves as  $S$  approaches the value of 1.3 and then reduces again as  $S$  approaches the value of 2. These oscillations in “two-line” resolution are akin to oscillations in two-point resolution [9]. The images that we compute are in good agreement with those presented by Goodbody.

Our model can be used for computing partially coherent images of even 2D specimens with complex

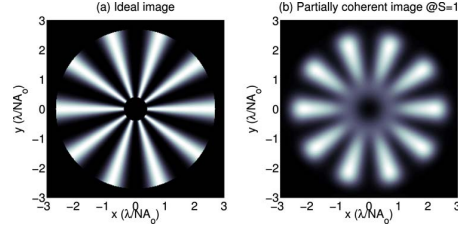


Fig. 3. (Color online) Computed images of a sinusoidal spoke target under bright field microscope: (a) ideal image, (b) a snapshot from a sequence ([Media 2](#)) (914 KB) of partially coherent images computed for different condenser sizes.

transmissions, as illustrated by images of a sinusoidal spoke target shown in Fig. 3 and [Media 2](#). We employed 4D phase-space computation to simulate above images, which is perhaps the first result of its kind. The PSI facilitates use of FFT algorithm for implementation of key steps in computation, thus allowing us to compute a  $201 \times 201$  pixel image in  $\sim 5$  min on our quad-core computer. The transmission of the simulated specimen in cylindrical coordinates is,  $t(r, \theta) = \cos(2\pi 10 \theta)$ ,  $0.4 \leq r \leq 2.7$ . The ideal image is computed as  $|t(x, y)|^2$  and the partially coherent images are computed using the algorithm outlined for Fig. 2. Spoke target presents higher spatial frequencies near the center, which are better resolved as  $S$  is increased.

In conclusion, we have shown that the image produced by a partially coherent imaging system is given by the spatial marginal of a windowed Wigner distribution, termed PSI, of the specimen’s transmission. The window, termed the PSI-window, is computable from the pupils of the imaging system and provides an equivalent of transfer function for partially coherent imaging. We believe that this model paves the way for an exciting signal processing perspective of partially coherent imaging. We have presented, for the first time, phase-space-based computed images of a complex 2D diffracting structure under bright field microscope with varying coherence ratio.

The authors thank M. J. Bastiaans, Eindhoven University for stimulating discussions.

## References

1. H. H. Hopkins, Proc. R. Soc. London Ser A **217**, 408 (1953).
2. C. J. R. Sheppard and A. Choudhury, J. Mod. Opt. **24**, 1051 (1977).
3. L. Cohen, *Time-Frequency Analysis* (Prentice Hall, 1995).
4. M. J. Bastiaans, in *Advances in Information Optics and Photonics*, A. T. Friberg and R. Dändliker, eds. (SPIE Press, 2008), vol. PM183, pp. 27–56.
5. J. Ojeda-Castañeda and E. E. Sicre, J. Mod. Opt. **31**, 255 (1984).
6. R. Castañeda, Appl. Opt. **47**, E53 (2008).
7. S. B. Mehta and C. J. R. Sheppard, Opt. Express **16**, 19462 (2008).
8. A. M. Goodbody, Proc. Phys. Soc. London Sect. B **70**, 361 (1957).
9. H. H. Hopkins and P. M. Barham, Proc. Phys. Soc. London Sect. B **63**, 737 (1950).

## 4.2 Phase-space imager in terms of the specimen's Wigner distribution and a system dependent kernel

The representation of the phase-space imager (PSI) in terms of the PSI-window that filters the specimen's mutual spectrum provides an efficient method of image computation and a direct link with the TCC model. In this section, we develop an alternative description of the PSI that may lead to deeper physical insight. This new description of partially coherent imaging is in terms of a system dependent 'kernel' that is convolved along the space dimension with the Wigner distribution of the specimen. This description is the partially coherent generalization of the Wigner representation of coherent image formation shown in fig. 1.5.

The expression for PSI shown as eq.5 in ref. [Mehta and Sheppard, 2010a] implies that the PSI is an inverse Fourier transform (along the  $\mathbf{m}'$  dimension) of the filtered mutual spectrum. The filter is the PSI-window. Writing symbolically,

$$\Psi(\mathbf{m}, \mathbf{x}) = \mathcal{F}_{\mathbf{m}'}^{-1} [S_m(\mathbf{m}, \mathbf{m}') C(\mathbf{m}, \mathbf{m}')] . \quad (4.1)$$

In the above equation  $S_m(\mathbf{m}, \mathbf{m}') = T(\mathbf{m} + \frac{\mathbf{m}'}{2}) T^*(\mathbf{m} - \frac{\mathbf{m}'}{2})$  is the mutual spectrum of the specimen and  $C(\mathbf{m}, \mathbf{m}')$  is the system's PSI-window. After transforming the above quantities according to the inverse Fourier operator that appears above, we have

$$\Psi(\mathbf{m}, \mathbf{x}) = W_t(\mathbf{m}, \mathbf{x}) \otimes_{\mathbf{x}} K(\mathbf{m}, \mathbf{x}). \quad (4.2)$$

In the above equation, we have used the definition of the Wigner distribution  $W_t(\mathbf{m}, \mathbf{x})$  in terms of the specimen's mutual spectrum as in eq. 1.4.

The above equation describes partially coherent image formation as a linear operation between bi-linear quantities. The equation exhibits the same 'modus operandi' as eq. 1.7, except that the kernel that modifies the Wigner distribution of the specimen is  $K(\mathbf{m}, \mathbf{x}) = \mathcal{F}_{\mathbf{m}'}^{-1} C(\mathbf{m}, \mathbf{m}')$  rather than the Wigner distribution of the coherent spread function. We call the quantity  $K(\mathbf{m}, \mathbf{x})$ , the *PSI-kernel*.

### 4.2.1 Marginals of the PSI and the PSI-kernel

Since both the PSI and the PSI-kernel are bi-linear distributions, their marginals are expected to provide interesting information about the imaging process.

As we have discussed, the spatial marginal of the PSI is the partially coherent image. We obtain the frequency marginal of the PSI along the space as follows.

$$\begin{aligned}
 \int \Psi(\mathbf{m}, \mathbf{x}) d\mathbf{x} &= \int \mathcal{F}_{\mathbf{m}'}^{-1} [S_m(\mathbf{m}, \mathbf{m}') C(\mathbf{m}, \mathbf{m}')] d\mathbf{x} && \text{From eq. 4.1} \\
 &= S_m(\mathbf{m}, 0) C(\mathbf{m}, 0) && \text{Projection along } \mathbf{x} \text{ is slice along } \mathbf{m}' \\
 &= |T(\mathbf{m})|^2 [|P_o(\mathbf{m})|^2 \otimes |P_c(\mathbf{m})|^2]. && (4.3)
 \end{aligned}$$

Thus, the frequency marginal of the PSI is  $|T(\mathbf{m})|^2 C(\mathbf{m}, 0)$ .  $C(\mathbf{m}, 0)$  is the convolution of the magnitude of the imaging and illumination pupils. The above marginal informs us about the spatial frequencies *of the specimen* transferred to the image. Note that the spectrum of the image (i.e., the Fourier transform of the spatial marginal of the PSI) is going to be different from the specimen's spatial frequencies that contribute to the image (i.e., the frequency marginal of the PSI).

As can be appreciated from the eq. 4.2, the PSI reduces to the PSI-kernel when the specimen is a point, i.e.,  $t(x) = \delta(x)$ ,  $T(m) = 1$ , and  $W_t(m, x) = \delta(x)$ . Therefore, the frequency marginal of the PSI-kernel is  $C(m, 0)$  and the spatial marginal of the PSI-kernel is the partially coherent image of a point (for 4D phase-space) or of a line (for 2D phase-space). In fact, we have computed the images of a point in the DIC microscope (shown in fig. 2.1 and represented by eq. 2.4) as a spatial marginal of the 4D PSI-kernel of the DIC configurations.

Thus, the PSI-kernel representation is a physically meaningful distribution with physically meaningful marginals.

### 4.2.2 Interpretation of the PSI-kernel

We illustrate the above interpretation of the partially coherent image formation in fig. 4.1. Figure 4.1 and associated media 4.1b and media 4.1c show the process of computation of

partially coherent images of an amplitude grating under brightfield microscope as the size of the condenser aperture is decreased. The parameters of the grating and the imaging system are the same as noted for fig. 1.4 and 1.5. PSI-kernels shown in fig. 4.1 can be computed by first computing the PSI-window as illustrated in ref. [Mehta and Sheppard, 2010c] and then applying the inverse FFT along the  $\mathbf{m}'$  dimension.

We notice that as the coherence ratio  $S$  is reduced, the PSI-kernel approaches the Wigner distribution of the coherent line spread function shown in fig. 1.5.

More insight can be gained in the nature of the PSI-kernel by deriving its relationship with the Wigner distribution of the imaging pupil. The relationship between the Wigner distribution of the imaging pupil and the PSI-kernel can be obtained by taking the inverse Fourier transform of the expression of the PSI-window shown in eq.6 of ref. [Mehta and Sheppard, 2010a].

$$\begin{aligned}
 K(\mathbf{m}, \mathbf{x}) &= \mathcal{F}_{\mathbf{m}'}^{-1} \left[ \int |P_c(\boldsymbol{\xi})|^2 P_o \left( \mathbf{m} + \boldsymbol{\xi} + \frac{\mathbf{m}'}{2} \right) P_o^* \left( \mathbf{m} + \boldsymbol{\xi} - \frac{\mathbf{m}'}{2} \right) d\boldsymbol{\xi} \right] \\
 &= \int |P_c(\boldsymbol{\xi})|^2 W_h(\mathbf{m} + \boldsymbol{\xi}, \mathbf{x}) d\boldsymbol{\xi} \\
 &= W_h(\mathbf{m}, \mathbf{x}) \otimes_{\mathbf{m}} |P_c(-\mathbf{m})|^2
 \end{aligned} \tag{4.4}$$

In the above equation,  $W_h$  is the Wigner distribution of the point spread function of the imaging path expressed in terms of the mutual spectrum of the objective pupil. Note that  $W_h$  is the four dimensional version of the Wigner distribution of the line-spread function  $W_l$  described in eq. 1.7. The above equation reveals that the intensity of the condenser pupil *blurs* the Wigner distribution of the imaging pupil along the frequency dimension to give rise to the PSI-kernel. The PSI-kernel in turn blurs the Wigner distribution of the specimen (eq. 4.2) to give rise to PSI, whose spatial marginal is the image.

It is instructive to examine the effect of reducing the condenser aperture (i.e., the effect of gradually increasing the coherence of illumination) as illustrated in fig. 4.2. Media 4.1b shows the PSI-kernel as the value of  $S$  reduces from 1 to 0.1, whereas media 4.1c shows the PSI for the same values of  $S$ . As the support of the condenser aperture reduces, the support of the PSI-kernel reduces along the frequency axis, whereas the support along the

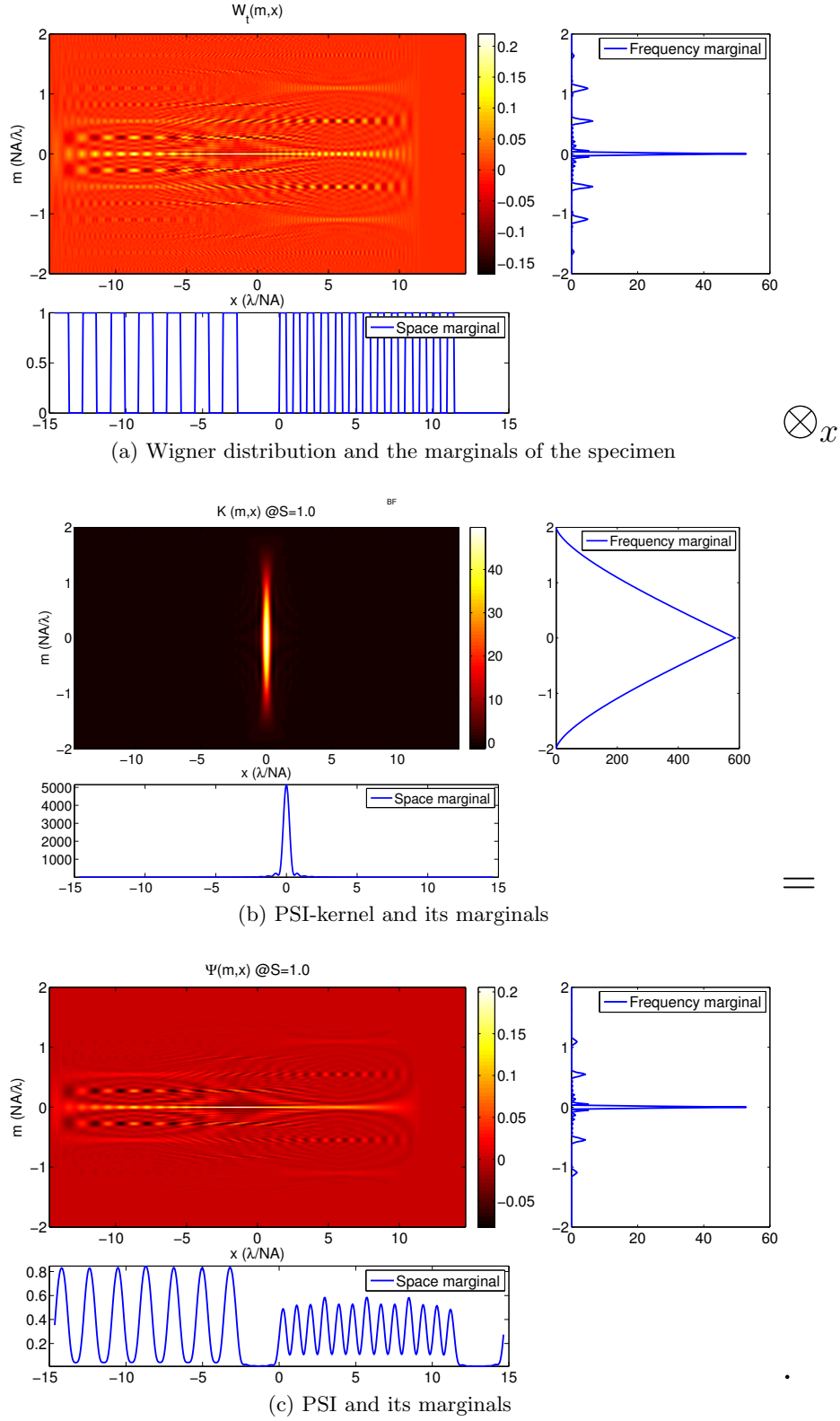


Figure 4.1: Description of partially coherent image formation in terms of the PSI-kernel. See the text for the details.

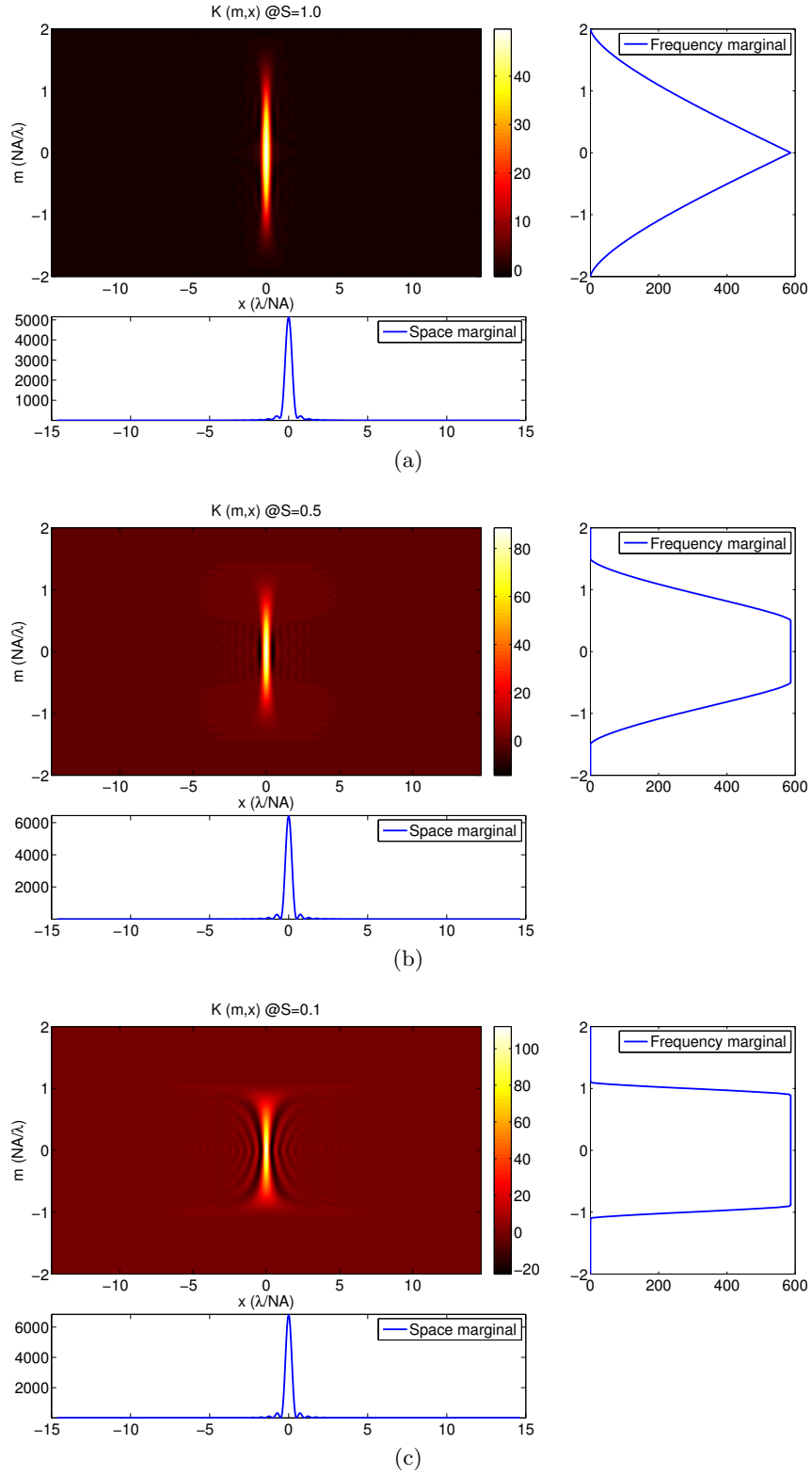


Figure 4.2: Comparison of the PSI-kernel and marginals at different coherence ratios.



spatial axis increases. Moreover, as the condenser aperture is stopped down, the PSI-kernel becomes less smooth. The increase in support along  $x$  and the decrease in support along  $m$  of the PSI-kernel as the coherence of illumination is increased accounts for the reduction in resolution. From the spatial marginal of the PSI shown in media 4.1c, we can see that increased coherence leads to reduction in the strength of the image of the  $1\mu\text{m}$  grating.

When the condenser aperture is reduced to a point (i.e.,  $P_c(\mathbf{m}) = \delta(\mathbf{m})$ ), the PSI-kernel reduces to the Wigner distribution of the point/line-spread function and the image formation described by eq. 4.2 reduces to coherent image formation described by eq. 1.7.

Thus, the PSI-kernel provides a bi-linear equivalent of the point spread function or optical transfer function for partially coherent imaging system.



## Chapter 5

# Analysis using phase-space imager

In the previous chapter, we derived the phase-space imager model and discussed its basic properties. In this chapter, we make use of the model for analysis of the various phase imaging methods. We compare image formation and imaging properties of five different phase microscopy methods, each of which was originally developed with different approximate models. Using the general frame-work of the phase-space imager, we show how the assumptions made in the development of a given method affect the method's performance in terms of resolution and contrast. To compare different imaging systems, we have used the PSI-window representation of the phase-space imager. The comparison has been published in ref [Mehta and Sheppard, 2010c], which is typeset as sec. 5.1 and constitutes the entire chapter. One may use the PSI-kernel representation of the phase-space imager to arrive at the same comparison.

### 5.1 Paper: Using the phase-space imager to analyze partially coherent systems: bright-field, phase contrast, differential interference contrast, differential phase contrast, and spiral phase contrast

## Using the phase-space imager to analyze partially coherent imaging systems: bright-field, phase contrast, differential interference contrast, differential phase contrast, and spiral phase contrast

Shalin B. Mehta<sup>a,b,\*</sup> and Colin J.R. Sheppard<sup>a,b,c</sup>

<sup>a</sup>Optical Bioimaging Lab, Division of Bioengineering, National University of Singapore, Block-E3A, #7-10, 7 Engineering Drive 1, Singapore 118431; <sup>b</sup>NUS Graduate School for Integrative Sciences and Engineering, 28 Medical Drive, Singapore 117456; <sup>c</sup>Department of Biological Sciences, National University of Singapore, 14 Science Drive, Singapore 117543

(Received 1 November 2009; final version received 16 March 2010)

Various methods that use large illumination aperture (i.e. *partially coherent illumination*) have been developed for making transparent (i.e. phase) specimens visible. These methods were developed to provide qualitative contrast rather than quantitative measurement – coherent illumination has been relied upon for quantitative phase analysis. Partially coherent illumination has some important advantages over coherent illumination and can be used for measurement of the specimen's phase distribution. However, quantitative analysis and image computation in partially coherent systems have not been explored fully due to the lack of a general, physically insightful and computationally efficient model of image formation. We have developed a phase-space model that satisfies these requirements. In this paper, we employ this model (called the *phase-space imager*) to elucidate five different partially coherent systems mentioned in the title. We compute images of an optical fiber under these systems and verify some of them with experimental images. These results and simulated images of a general phase profile are used to compare the contrast and the resolution of the imaging systems. We show that, for quantitative phase imaging of a thin specimen with matched illumination, differential phase contrast offers linear transfer of specimen information to the image. We also show that the edge enhancement properties of spiral phase contrast are compromised significantly as the coherence of illumination is reduced. The results demonstrate that the phase-space imager model provides a useful framework for analysis, calibration, and design of partially coherent imaging methods.

**Keywords:** phase-space imager; partially coherent imaging; image formation; differential interference contrast; differential phase contrast; spiral phase contrast

### 1. Introduction and background

#### 1.1. Phase imaging with partially coherent illumination

In the history of optical microscopy methods, the second Nobel prize related to microscopy was awarded to Frits Zernike in 1953 for the development of the phase-contrast [1], which allowed visualization of optically transparent specimens. Development of the phase-contrast was due to an insight that Zernike gained in the coherence properties of light, while studying behavior of light reflected from phase-gratings [2]. Since then, several optical contrast methods that use large illumination aperture have been developed to better visualize, and recently, to quantify morphology without having to label the specimens. Some of these methods are: differential interference contrast (DIC) [3], asymmetric illumination contrast [4], scanning differential phase contrast

(DPC) and asymmetric illumination-based differential phase contrast (AIDPC) [5,6], single sideband edge enhancement [7], Hoffman modulation contrast [8], and transport of intensity [9]. The methods mentioned above illuminate the specimen with an incoherent source of finite size using a large illumination aperture, which leads to partially coherent illumination at the specimen. As described in the next subsection, large illumination aperture leads to non-linear image formation, which makes it difficult to obtain quantitative measurements of the specimen from measured images. Despite of advantages provided by partially coherent illumination, spatially coherent illumination has been preferred for quantitative measurement of phase information – due to the linear model applicable to such methods. A classic example of coherent imaging method that provides quantitative phase information is holography (see [10], Chapter 9). An example of

\*Corresponding author. Email: shalin@nus.edu.sg; shalin.mehta@gmail.com

coherent imaging method whose partially coherent version is evaluated in this paper is spiral-phase contrast (SPC) [11–13].

In the field of X-ray microscopy, phase sensitive methods have drawn attention relatively recently. Nevertheless, they are already expected to provide ‘a generational improvement in diagnostic capabilities of X-ray imaging’ (see [14] and references therein). The reason for excitement around X-ray phase-methods is that they provide much higher visibility of anatomical structures in comparison to the conventional absorption based X-ray imaging. The initial phase-contrast methods to be adopted in X-ray regime were based on coherent illumination, which requires use of expensive synchrotron sources. The results obtained with coherent X-ray phase imaging provided promising diagnostic capabilities, but the need for synchrotron sources has prevented their mainstream clinical use. Recently, partially coherent X-ray phase microscopy methods that use laboratory X-ray sources have been investigated in greater detail and shown to be diagnostically valuable [15].

Although coherent imaging (using laser in optical regime or using synchrotron radiation in X-ray regime) provides quantitative information, it has some serious drawbacks – namely, lack of depth sectioning, half the lateral resolution than possible with partially coherent methods, and speckle noise. Therefore, it is attractive to develop quantitative partially coherent imaging systems that provide measurement of the distribution of phase – not just its visualization at high resolution. It is sometimes advantageous to obtain quantitative phase-distribution (where relative phase is accurately measured but not the absolute value) with partially coherent illumination to overcome disadvantages of coherent illumination mentioned above. One such application is analysis of biological processes (e.g. cell division) by computer-assisted processing of cellular morphology. Partially coherent methods are also simpler to setup, robust against environmental factors, and immune to impurities in the optical path. With appropriate calibration, these methods can lead to quantitative measurement of the absolute optical thickness of the specimen. An example is provided by measurement of the refractive index profile of optical fibers using differential interference contrast [16].

Alongside optical contrast methods mentioned previously, fluorescence microscopy has seen tremendous development in the optical regime. Apart from the fact that fluorescent labels provide molecular information, a linear image formation applicable to fluorescence microscopy is a major contributor to its success. This linearity allows digital removal of the blurring introduced by the optics of the microscope using fast deconvolution algorithms. It also allows

development of new mechanisms of extending instrument resolution (e.g. using structured illumination, or adaptive optics [17]). For design of quantitative schemes comprising partially coherent imaging and digital deblurring, it is imperative to have a computationally efficient model that accurately captures physical properties of the system. In the field of optical microscopy, however, the literature on full partially coherent image computation has been limited – see for example [18–20]. It is worth noting that in the field of photo-lithography, software tools have been developed for simulation of partially coherent imaging of masks [21]. These tools, although computationally expensive, are being used for optimization of mask structure and illumination structure to achieve desired pattern of light on the photoresist. As of now, the optimization tools employ rather inefficient search, and therefore could benefit from intelligent optimization afforded by a physically intuitive and a computationally efficient image formation model.

We have developed an accurate model for a widely used partially coherent method of differential interference contrast (DIC) [22,23] based on the transmission cross-coefficient (TCC) model [24]. The TCC model is briefly reviewed in Section 2. As an alternative to the rather complex image formation process of DIC, a simple and more linear method of differential phase contrast (DPC) – based on the split detector – has been developed [5] in scanning optical microscopy. We have developed a full-field version of DPC, termed the asymmetric illumination-based differential phase contrast (AIDPC) [6]. With the help of calibrated test specimens, we have shown that AIDPC provides quantitative measurement of a thin specimen’s phase gradient [25,26]. We have applied the TCC based model to compute transfer properties of phase contrast and Hoffman modulation contrast [27]. To provide a physically insightful and computationally efficient approach, we have recently derived a phase-space model for partially coherent imaging from the TCC model [28]. The model, called, the *phase-space imager*, expresses the image intensity in terms of the specimen’s Wigner distribution and a ‘window’ dependent on the system’s structure. Using the phase-space imager, we have analyzed the image of a double-slit produced by the bright-field microscope. Using the phase-space imager, we have also been able to compute images of general test-specimens (e.g. spoke target) [28]. In this paper, we use the phase-space imager to quantitatively analyze image formation in five partially coherent systems – bright-field (BF), Zernike’s phase contrast (PC), differential interference contrast (DIC), differential phase contrast (DPC), and spiral phase contrast (SPC). The phase-sensitive methods noted above have

720

S.B. Mehta and C.J.R. Sheppard

been designed with different principles and this is one of the few studies comparing their transfer properties in a unified quantitative framework. The phase-space models for description and propagation of partially coherent light have been investigated extensively [29] (see also [19], Chapters 22–24), but the unique aspect of our approach is that we describe the *transfer properties of the system* in the phase-space.

### 1.2. Image formation in partially coherent systems

Figure 1 shows a general schematic applicable to a microscope using any form of partially coherent radiation (optical, X-ray or electron). The imaging system consists of an illumination path that brings radiation from a quasi-monochromatic and spatially incoherent source to the specimen, the specimen itself, and the imaging path that forms an image of the specimen on the detector. The imaging system is characterized by the intensity distribution of the incoherent condenser pupil  $|P_c(\xi)|^2$  and complex transmission of the objective pupil,  $P_o(\xi)$ . Various contrast methods essentially differ in choice of structure of  $|P_c(\xi)|^2$  and  $P_o(\xi)$ . These two pupils fully characterize the imaging system. In this paper, we have employed the paraxial approximation to allow simpler calculations. The specimen is assumed to be modelled by a transparency  $t(x)$ . Aberrations of the imaging system are accounted for using a complex objective pupil. The aberrations of the condenser aperture do not affect the image due to its incoherence. Throughout the paper, 2D independent variables are represented by vectors and indicated by bold-face characters.

Let us write a model for the system shown in Figure 1 from the first principles. The image intensity can be written by noting that image formation by each point of the condenser is spatially coherent and the image produced by the entire condenser is the sum of the intensities due to individual condenser points.

This leads us to the *space-domain model* of partially coherent systems as follows:

$$\begin{aligned} I(x) &= \int |P_c(\xi)|^2 |\exp(2\pi i \xi \cdot x) t(x) \otimes h(x)|^2 d\xi \\ &= \iiint |P_c(\xi)|^2 t(x_1) t^*(x_2) h(x - x_1) h^*(x - x_2) \\ &\quad \times \exp[2\pi i \xi \cdot (x_1 - x_2)] dx_1 dx_2 d\xi, \end{aligned} \quad (1)$$

where  $|P_c(\xi)|^2$  is the intensity distribution of the condenser aperture and  $h(x)$  is the amplitude point spread function (PSF) of the imaging path.  $\exp(2\pi i \xi \cdot x)$  is the oblique plane-wave illumination produced by the condenser's point located at  $\xi$ . All integrals range from  $-\infty$  to  $\infty$  unless otherwise noted.

The size of the condenser aperture ( $\text{NA}_{\text{con}}$ ) relative to the objective aperture ( $\text{NA}_{\text{obj}}$ ) determines the coherence of illumination. As the size of the condenser aperture increases, more incoherent point-sources contribute to image formation and reduce coherence at the specimen. A factor, called the coherence ratio,  $S = \text{NA}_{\text{con}}/\text{NA}_{\text{obj}}$  is useful in specifying the coherence of illumination and is used throughout the paper.

The above equation shows that partially coherent imaging is inherently nonlinear (precisely, bi-linear) due to the presence of a large illumination aperture. The bi-linearity of the image formation is manifested as dependence of the image intensity at a given point on the *pairs of specimen-points* ( $x_1$  and  $x_2$ ), rather than individual specimen points. Due to the bi-linearity of the model, even for simple specimens, image calculation requires numerical computation – e.g. computation of an image of a single slit under general bright-field system requires numerical evaluation (see [24], Section VI). On most occasions, simplifying assumptions about the specimen are employed to linearize the model – the most common assumption being that the specimen is weak [30–32]. Less common but a useful assumption is that the specimen is slowly varying [26,33]. An accurate model that does not make above

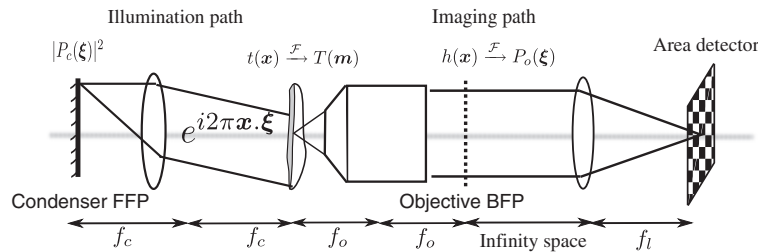


Figure 1. A general model of a partially coherent imaging system. The imaging system is characterized by the intensity distribution in the condenser front focal plane (FFP) and the complex amplitude distribution in the objective back focal plane (BFP). The symbol  $\mathcal{F}$  is used to denote Fourier transform relationship between two quantities.  $f_c$ ,  $f_o$ , and  $f_l$  are focal lengths of the condenser, the objective, and the tube-lens, respectively.

assumptions and captures the bi-linear behavior in an elegant and physically intuitive manner is required to research partially coherent systems. Such a model should also be computationally efficient to allow fast computation of images in forward direction and reconstruction of phase information using inverse algorithms. We believe that the *phase-space imager* provides such a model and attempt to demonstrate this by analyzing five different phase-imaging methods using the model.

### 1.3. Organization of the paper

The rest of the paper is organized as follows: Section 2 uses the bright-field system as a running example to illustrate how image formation is described using the phase-space imager. For the sake of continuity and self-sufficiency, we discuss key aspects of the phase-space imager described in our recent work [28]. We use an optical fiber as a test specimen for computation of images and their experimental verification. Subsequently, using the same approach we compare image formation in PC (Section 3), DIC (Section 4), DPC (Section 5) and SPC (Section 6). For SPC, we examine how coherence of illumination affects image formation and consequently image contrast. We note that SPC has originally been developed as a coherent imaging method and in this paper we are investigating how much departure from perfect spatial-coherence can be tolerated. In Section 7, we compare computed and experimental images for bright-field, DIC, and DPC. In the same section, images of a hypothetical general phase profile are computed to illustrate the resolution and the contrast afforded by different imaging systems. Subsequently, we compare above imaging methods in terms of their suitability for quantitative imaging with partially coherent illumination. Section 8 discusses the directions of further investigation and concludes the paper with a summary of presented results.

Throughout the paper, we use a 20X 0.75NA Olympus UPlanSApo objective, 0.75 NA dry condenser, and the halogen light filtered through  $\lambda = 550$  nm bandpass interference filter. All computation is carried out in normalized units of  $\lambda/\text{NA}_{\text{obj}}$  for space and  $\text{NA}_{\text{obj}}/\lambda$  for spatial frequencies. Thus, all space and spatial-frequency quantities in the paper were computed in units of  $0.73 \mu\text{m}$  and  $1.37 \mu\text{m}^{-1}$ , respectively. However, spatial dimensions are plotted in  $\mu\text{m}$  and spatial-frequency dimensions are plotted in  $\mu\text{m}^{-1}$  by scaling the axes.

To be able to plot the phase-space quantities, we have limited our attention to one dimensional (1D) specimens – which have constant transmission along

the  $Y$ -direction and variable transmission along the  $X$  dimension. Therefore, when interpreting the results, one can assume that the 2D co-ordinates (represented by bold-face characters in the equations) are scalar co-ordinates. In plots, the specimen is represented by a 1D signal whereas all 2D phase-space quantities are plotted as images.

An example of computed images of a general 2D amplitude specimen using the 4D phase-space imager can be found in [28].

## 2. The phase-space imager model illustrated using bright-field system

The key to efficient computation of partially coherent images is to express the image formation in a domain that allows fast computation and physical interpretation. Such an example is provided by computation of convolution using the FFT algorithm. In this section, we derive the phase-space imager from Equation (1) via the TCC model and demonstrate the process by computing an image of an optical fiber under a bright-field system with matched illumination (i.e.  $S = 1$ ).

For other key characteristics of the model and details of its relationship with other phase-space models of partially coherent systems, the reader is referred to [28].

### 2.1. Spatial-frequency model

In Equation (1), we substitute the convolution  $[\exp(2\pi i \xi \cdot x) t(x)] \otimes h(x)$ , by the product of the shifted version of the specimen spectrum,  $T(\mathbf{m}) = \mathcal{F}[t(x)]$ , and the pupil function,  $P(\xi) = \mathcal{F}[h(x)]$ . The shift in the specimen spectrum is due to oblique illumination from points of the condenser. We use kernel of the form  $\exp(-2\pi i \mathbf{x} \cdot \mathbf{m})$  throughout the paper for calculating the forward Fourier transform. This leads to

$$\begin{aligned} I(\mathbf{x}) &= \frac{1}{C_N} \int |P_c(\xi)|^2 \left| \int T(\mathbf{m} - \xi) P_o(\mathbf{m}) \exp(2\pi i \mathbf{m} \cdot \mathbf{x}) d\mathbf{m} \right|^2 d\xi \\ &= \frac{1}{C_N} \iint |P_c(\xi)|^2 T(\mathbf{m}_1 - \xi) P_o(\mathbf{m}_1) \\ &\quad \times \exp(2\pi i \mathbf{m}_1 \cdot \mathbf{x}) T^*(\mathbf{m}_2 - \xi) P_o^*(\mathbf{m}_2) \\ &\quad \times \exp(-2\pi i \mathbf{m}_2 \cdot \mathbf{x}) d\mathbf{m}_1 d\mathbf{m}_2 d\xi \\ &= \frac{1}{C_N} \iint T(\mathbf{m}_1) T^*(\mathbf{m}_2) \left[ \int |P_c(\xi)|^2 P_o(\mathbf{m}_1 + \xi) P_o^*(\mathbf{m}_2 + \xi) d\xi \right] \\ &\quad \times \exp[2\pi i (\mathbf{m}_1 - \mathbf{m}_2) \cdot \mathbf{x}] d\mathbf{m}_1 d\mathbf{m}_2 \\ &= \iint T(\mathbf{m}_1) T^*(\mathbf{m}_2) C(\mathbf{m}_1, \mathbf{m}_2) \exp[2\pi i (\mathbf{m}_1 - \mathbf{m}_2) \cdot \mathbf{x}] d\mathbf{m}_1 d\mathbf{m}_2. \end{aligned} \quad (2)$$

In the above,  $C(\mathbf{m}_1, \mathbf{m}_2) = (1/C_N) \int |P_c(\xi)|^2 P_o(\mathbf{m}_1 + \xi) P_o^*(\mathbf{m}_2 + \xi) d\xi$  is the normalized transmission



cross-coefficient (TCC) of the imaging system. The TCC is also called partially coherent transfer function (PCTF) or bi-linear transfer function. Interpreting geometrically, the TCC is the area of overlap of three pupils – the condenser pupil assumed to be situated at the center, the objective pupil shifted by  $\mathbf{m}_1$  and the conjugate objective pupil shifted by  $\mathbf{m}_2$  [34]. Figure 2(a) illustrates how we compute area of overlap of three pupils as a function of spatial frequency pairs  $(\mathbf{m}_1, \mathbf{m}_2)$ . As recommended by Martin ([18], Chapter 8), to compare different imaging systems, we normalize the TCC such that the image of a perfectly transmitting specimen ( $t(x)=1$ ) is unity. Substituting  $T(\mathbf{m})=\delta(\mathbf{m})$  in Equation (2) we see that the proper value of normalizing factor  $C_N$  in the above equations should be  $\int |P_c(\xi)|^2 |P_o(\xi)|^2 d\xi$ .

In the frequency domain model, the bi-linear nature of image formation is manifested as the dependence of the image's spatial frequency on pairs of the specimen spatial frequencies. The TCC describes the strength with which such pairs of specimen spatial-frequencies are transferred to the image.

We notice that the TCC model separates the contribution of the specimen (in the form of  $T(\mathbf{m}_1)T^*(\mathbf{m}_2)$ ) and the system (in the form of  $C(\mathbf{m}_1, \mathbf{m}_2)$ ) to the image. This separation allows study of the system's properties in terms of the structure of TCC. The separation also saves time when computing images of the same specimen under different imaging systems and vice versa. We call the quantity  $T(\mathbf{m}_1)T^*(\mathbf{m}_2)$  the *bi-linear spectrum* of the specimen.

Throughout this paper, we use a sheathless optical fiber immersed in water as a specimen for computation and experiments. The fiber was taken from a light-guide bundle available from Edmund optics # 39366 (clad dia. 50  $\mu\text{m}$ , core dia. unspecified, clad RI 1.487, core RI 1.581.) Since the core diameter of the fiber is not specified by the manufacturer, we use the clad RI to model the entire fiber's RI. The simulated transmission, spectrum and bi-linear spectrum of the fiber are shown in Figure 3.

Some comments about the choice of the specimen are in order. The optical fiber is a 1D specimen, whose phase-space representation (as we see later) is intuitive to interpret and possible to plot in 2D. Since theoretical analysis assumes a thin specimen, we decided to choose as thin a fiber as we could. Widely available fibers (e.g. SMF28) have clad diameter of 250  $\mu\text{m}$ , and hence we chose this fiber from a light-guide bundle which is five times thinner. Still, the chosen sample is not really thin with respect to the focal depth, leading to some discrepancy between computed and experimental images, as discussed in Section 7.1.

Next, we show the computation of the system's TCC. Throughout the paper, we employ normalized units of  $\lambda/\text{NA}_{\text{obj}}$  for space and  $\text{NA}_{\text{obj}}/\lambda$  for spatial-frequency quantities during computation, but use real units ( $\mu\text{m}$  and  $\mu\text{m}^{-1}$ , respectively) for plotting the results. In normalized units, the objective pupil  $P_o(\xi)$  is a circle of radius 1, and is the same as the coherent transfer function of the imaging path. If the illumination were coherent (i.e. the condenser aperture was reduced to a point along the optical axis), the objective pupil defines the transfer properties of the system which is now linear. Since we use matched illumination, the condenser pupil,  $|P_c(\xi)|^2$  also has radius of 1 in normalized units. Therefore, the TCC cuts off at 2 along  $m_1$  and  $m_2$  co-ordinates. Along  $m_1=m_2$ , the cut-off is determined by the area of overlap of the condenser and the objective pupil. Therefore, the cut-off along the  $m_1=m_2$  axis is  $1+S$ . Along the  $m_1=-m_2$  axis, the cut-off is determined by the area of overlap of two shifted objective pupils and is therefore equal to 2 in normalized units, irrespective of the coherence of illumination. We employed the algorithm discussed in Section 4 of [23], to compute the full TCC (where it is referred to as PCTF) from pupils of the system. Figure 4 shows computation of the TCC and the filtered bi-linear spectrum. We display only those parts of the bi-linear spectrum which are transmitted by the system. Due to the cut-offs noted above, the TCC has a support resembling a

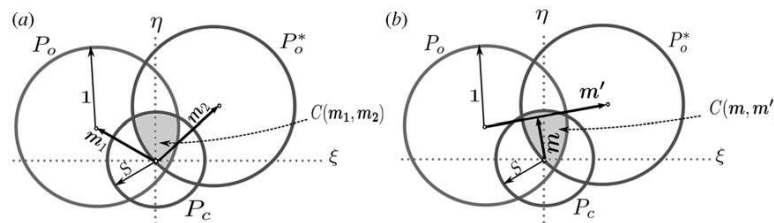


Figure 2. (a) Transmission cross-coefficient (TCC) and (b) the phase-space imager window (PSI-window) both are computed as an area of overlap of shifted pupils of the system. Note that in this illustration, we have assumed the condenser aperture to be 0.7 times the objective aperture, i.e.  $S=0.7$ .

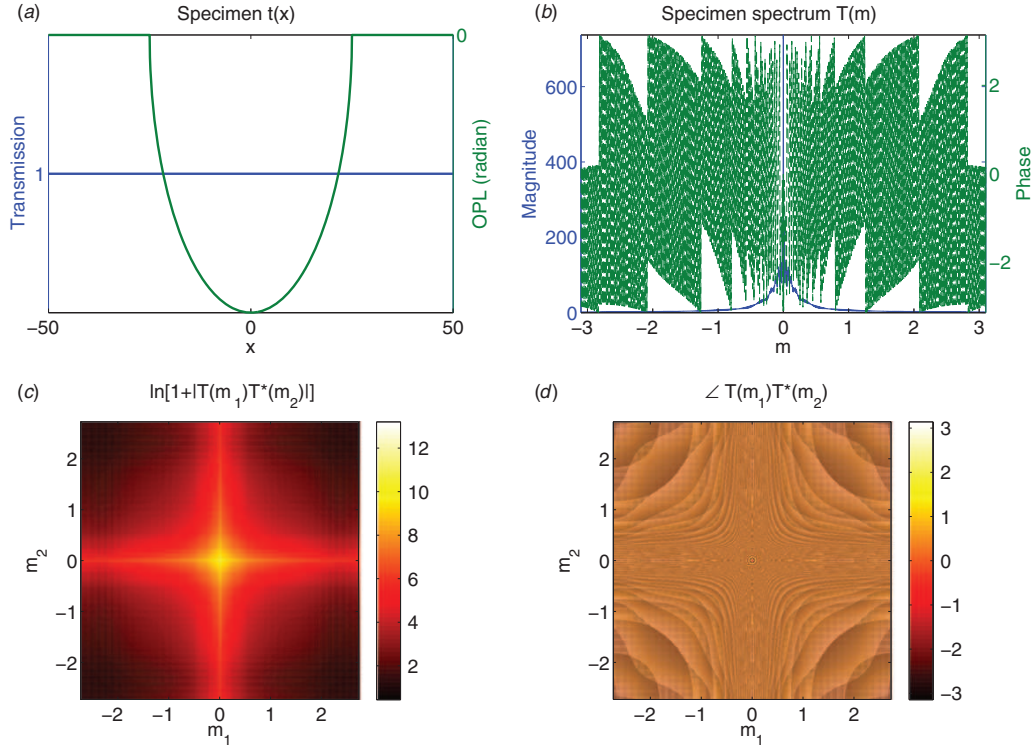


Figure 3. Simulated properties of an optical fiber: (a) the transmission and the optical path length, (b) its spectrum, (c) log-magnitude of the bi-linear spectrum, and (d) phase of the bi-linear spectrum. Note that we use natural logarithm to calculate log-magnitude. The simulated specimen is an optical fiber having diameter  $50\mu\text{m}$  and RI 1.487 immersed in water (RI 1.33). The wavelength of  $0.55\mu\text{m}$  is used. On both sides of the fiber,  $12.5\mu\text{m}$  long background is simulated to capture effects at the edge of the fiber. Spatial quantities are plotted in  $\mu\text{m}$  and the spatial-frequency quantities in  $\mu\text{m}^{-1}$ . (The color version of this figure is included in the online version of the journal.)

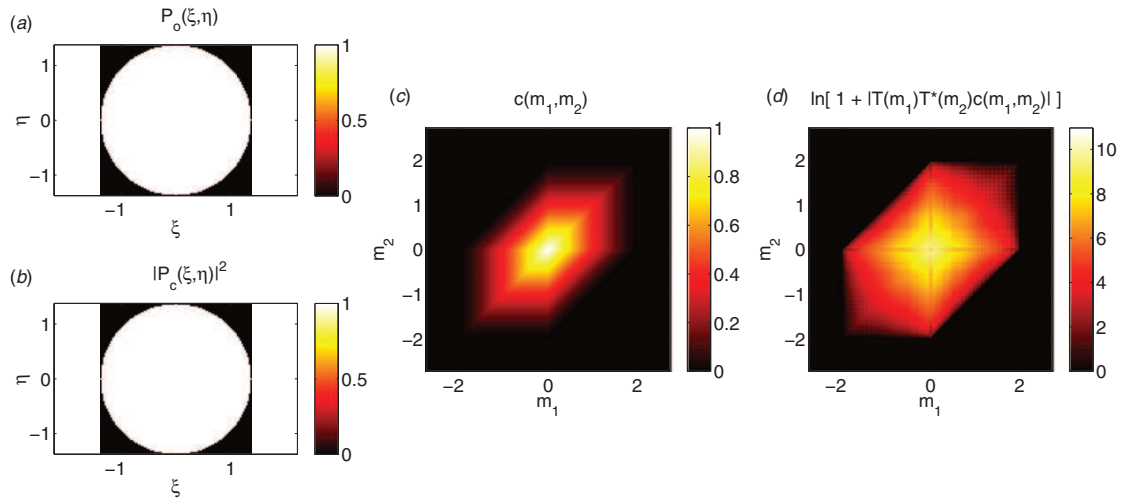


Figure 4. Transmission cross-coefficient for a matched-illumination ( $S=1$ ) bright-field system (c), computed using the objective pupil (a) and the condenser pupil (b). Log-magnitude of the bi-linear spectrum filtered by the TCC is also shown (d). When interpreting the TCC and the PSI-windows plotted in subsequent figures, it is important to note that the axes of 2D plots ((c) and (d) in this figure) represent spatial frequencies in the  $X$ -direction only. (The color version of this figure is included in the online version of the journal.)

724

S.B. Mehta and C.J.R. Sheppard

stretched hexagon rotated by  $45^\circ$ . Our computed TCC shown in Figure 4(c) matches very well with supports of TCC discussed in several other works [18,34,35].

To compute the partially coherent image, one should multiply the filtered bi-linear spectrum by phase-factor  $\exp(2\pi i(\mathbf{m}_1 - \mathbf{m}_2) \cdot \mathbf{x})$  and evaluate the integral of Equation (2) numerically.

## 2.2. Phase-space imager: derivation and computation

The description of image formation in terms of pairs of points or pairs of spatial frequencies of the specimen is not very intuitive. In signal analysis, Wigner distribution and other phase-space distributions are used which have bi-linear dependence on the signal. They are designed to approximately represent instantaneous spectrum of the signal, and hence are closer to physical intuition [36]. In all phase-space distributions, the ‘pairs’ in the space or spatial-frequency domain are expressed using the center and difference co-ordinates. As we show now, the phase-space imager is a transform of the specimen transmission which elegantly captures bi-linear nature of image formation and key effects of the imaging system.

Substituting the frequency variables  $\mathbf{m}_1$  and  $\mathbf{m}_2$  in Equation (2) by the center and difference frequency variables,  $\mathbf{m} = \frac{1}{2}(\mathbf{m}_1 + \mathbf{m}_2)$  and  $\mathbf{m}' = \mathbf{m}_1 - \mathbf{m}_2$ , and noting that the Jacobian of the transformation is unity,

$$I(\mathbf{x}) = \iint T\left(\mathbf{m} + \frac{\mathbf{m}'}{2}\right) T^*\left(\mathbf{m} - \frac{\mathbf{m}'}{2}\right) C(\mathbf{m}, \mathbf{m}') \times \exp(2\pi i \mathbf{m}' \cdot \mathbf{x}) d\mathbf{m} d\mathbf{m}'. \quad (3)$$

It should be noted that the above change of variables represents rotation of the  $(\mathbf{m}_1, \mathbf{m}_2)$  space followed by linear scaling.

We call the quantity  $T(\mathbf{m} + (\mathbf{m}'/2))T^*(\mathbf{m} - (\mathbf{m}'/2))$  the *mutual spectrum* of the specimen, which we henceforth denote by  $S_m(\mathbf{m}, \mathbf{m}')$ . When the mutual spectrum is integrated along the center co-ordinate  $\mathbf{m}$ , we obtain the autocorrelation of the spectrum. The specimen’s Wigner distribution can be computed from the mutual spectrum by taking the inverse Fourier transform along the delay dimension  $(\mathbf{m}')$  as follows:

$$W_t(\mathbf{m}, \mathbf{x}) = \int S_m(\mathbf{m}, \mathbf{m}') \exp(2\pi i \mathbf{m}' \cdot \mathbf{x}) d\mathbf{m}'. \quad (4)$$

The projections of the Wigner distribution along the space and spatial frequency axes represent the densities of the signal along spatial frequency and space, respectively. The projection along space is called the *spatial-frequency marginal* and is equal to magnitude-squared spectrum. The projection along spatial frequency is called the *spatial-marginal* and is equal to the magnitude-squared specimen.

From Equation (3), we see that the image intensity is the spatial marginal of a certain distribution (denoted  $\Psi$ ). Thus,

$$I(\mathbf{x}) = \int \Psi(\mathbf{m}, \mathbf{x}; C) d\mathbf{m}, \quad (5)$$

where

$$\Psi(\mathbf{m}, \mathbf{x}; C) = \int S_m(\mathbf{m}, \mathbf{m}') C(\mathbf{m}, \mathbf{m}') \exp(2\pi i \mathbf{m}' \cdot \mathbf{x}) d\mathbf{m}', \quad (6)$$

is the *windowed Wigner distribution of the specimen transmission*. This distribution is the phase-space imager. The window in this case is the  $C(\mathbf{m}, \mathbf{m}')$ , which we call *phase-space imager window (PSI-window)* and is given by

$$C(\mathbf{m}, \mathbf{m}') = \frac{1}{C_N} \int |P_c(\xi)|^2 P_o\left(\mathbf{m} + \frac{\mathbf{m}'}{2} + \xi\right) P_o^*\left(\mathbf{m} - \frac{\mathbf{m}'}{2} + \xi\right) d\xi. \quad (7)$$

To compute the PSI-window, we shift both objective pupils by  $\mathbf{m}$ , and from that point the objective pupil is shifted by  $\mathbf{m}'/2$  and the conjugate objective pupil by  $-\mathbf{m}'/2$ , as illustrated in Figure 2(b). The area of overlap of three pupils (after normalization by the factor  $C_N$ ) is the value of PSI-window at  $(\mathbf{m}, \mathbf{m}')$ . We adapted our previously published algorithm for computing the TCC [23] to compute PSI-window. Since  $\mathbf{m}'$  is the distance between the objective and the conjugate objective pupil, the PSI-window cuts off at 2 in normalized units of  $\text{NA}_{\text{obj}}/\lambda$ , along the  $\mathbf{m}'$  axes.  $\mathbf{m}$ , on the other hand, represents the distance between the objective and the condenser pupils and therefore PSI-window is zero beyond  $1 + S$  along that axis. The effect of the coherence on the cut-off and shape of the PSI-window can be appreciated from the movie associated with Figure 11, Section 6. We have shown that the PSI is a special distribution of a general Cohen class of distributions with interesting properties [28,36].

Now we examine computation of the Wigner distribution of the fiber. The mutual spectrum of the specimen as shown in Figure 5, is computed from the specimen’s spectrum. The Wigner distribution of the specimen is obtained by the inverse Fourier transforming the mutual spectrum along  $\mathbf{m}'$  dimension as per Equation (4). The calculations are verified to be correct by comparing the marginals with the magnitudes of the specimen and its spectrum. In temporal signal analysis, the central co-ordinate of the instantaneous frequency (i.e. the first moment of the instantaneous spectrum at each time point) represents instantaneous frequency, which is given by the derivative of the phase of an analytic signal (see [36], Chapter 6). Analogously, in spatial signal



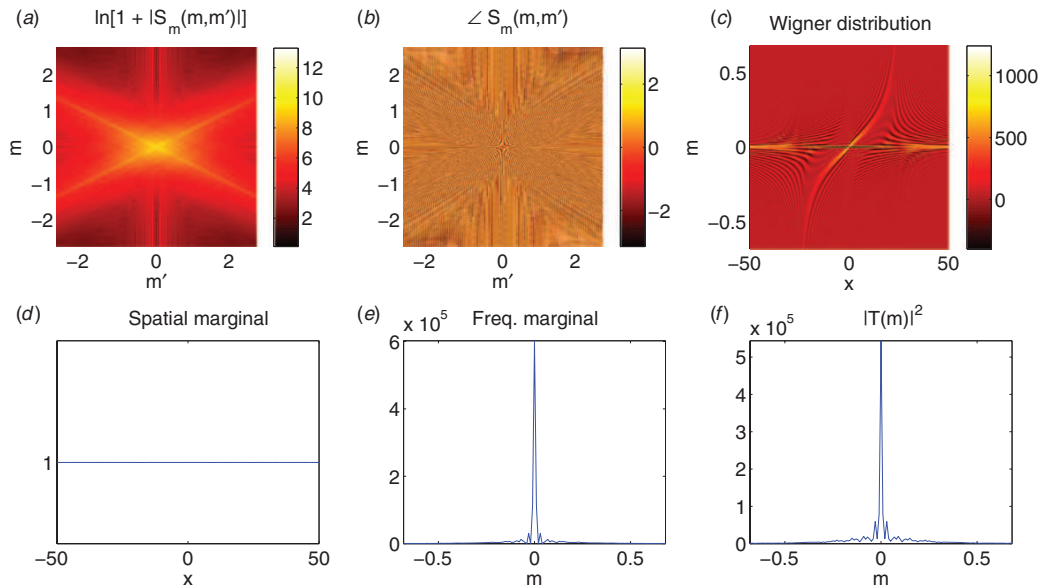


Figure 5. Computation of the Wigner distribution of the fiber which is described in Figure 3: (a) and (b) show log-magnitude and phase of the mutual spectrum, which when inverse Fourier transformed along delay dimension, gives the Wigner distribution of the specimen as shown in (c). The spatial-marginal of the distribution (d) is the same as the square of the transmission of the specimen. The spatial-frequency marginal of the distribution (e) is compared against the magnitude-squared spectrum ( $|T(m)|^2$ ) of the specimen (f). The correctness of marginals indicates that the computation of the Wigner distribution is correct. Notice that the Wigner distribution is concentrated around the phase gradient of the specimen – a quantity equivalent to the instantaneous frequency in temporal signal analysis. (The color version of this figure is included in the online version of the journal.)

analysis, the Wigner distribution shows the variations in the phase gradient of the specimen, which is evident from the Wigner distribution of the fiber. Since an optical fiber's phase gradient is easy to visualize, it is a good specimen to study the effects of the imaging system on the specimen's Wigner distribution.

Figure 6 shows the computation of the image of the fiber under the same imaging conditions as described in Figure 4. Computation was done in following manner:

- Calculate the PSI-window,  $C(m, m')$ , from system's pupils.
- Filter the specimen's mutual spectrum,  $S_m(m, m')$ , with PSI-window.
- Calculate the PSI,  $\Psi(m, x)$ , by inverse Fourier transforming the filtered mutual spectrum along the  $m'$  dimension.
- Obtain the partially coherent image as a spatial-marginal of the PSI.

For simulations presented in this paper, we used MATLAB<sup>TM</sup> software's object oriented capabilities. The general imaging model was implemented as a parent class, from which specific imaging systems were derived by specifying pupils. We implemented the approach described as type-IV Wigner distribution in [37] to compute phase-space quantities from discretized

sequence. The 'type-IV' Wigner distribution is essentially equivalent to the discrete Fourier transform in that both the space and spatial-frequency domains are assumed to be discrete and periodic. It has been shown that the important properties of the Wigner distribution are preserved *only when* the discretized signal has an odd number of samples [37]. The computation of mutual-spectrum can be vectorized and is therefore very fast. To produce results of good fidelity, we sampled the profile of the specimen at 10 times the Nyquist rate dictated by the cut-off of the imaging system along the  $m'$  dimension. The computational bottle-neck is encountered when computing the PSI-window. Since the computation of the PSI-window at each  $(m, m')$  can be carried out independently, we use a parallel computation algorithm. With our implementation, computing an image of the specimen profile having 1241 samples required approximately one minute on our Intel i7 processor based quad-core computer. When implementing the above computation in MATLAB, we encountered a MATLAB-specific question – how to correctly use MATLAB's FFT routines so that one obtains a real inverse Fourier transform (i.e. PSI) from a Hermitian quantity (mutual spectrum)? The solution follows when one realizes that the FFT algorithm assumes the origin to be the first

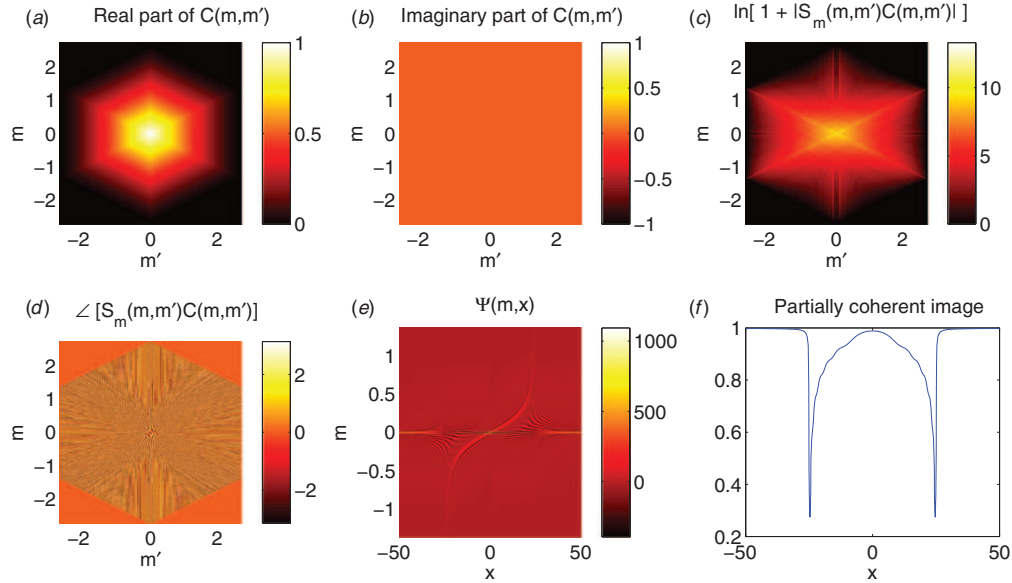


Figure 6. Computation of the partially coherent image of the fiber under bright-field setup. The imaging conditions are the same as in Figure 4. Parts (a) and (b) show real and imaginary parts, respectively, of the PSI-window of the system computed from the pupils. Parts (c) and (d) show the log-magnitude and phase, respectively, of the filtered mutual spectrum. Phase-space imager is shown in (e) whose spatial-marginal gives the partially coherent image shown in (f). For clarity, only the region of the mutual spectrum which is transferred to the image by PSI-window is displayed. The PSI is zoomed along the  $m$  axis to display the region which has observable variation. (The color version of this figure is included in the online version of the journal.)

value of the discrete signal, whereas in our model the origin is at the center.<sup>1</sup>

The simulated bright-field image shows that image intensity is the same as the background (at  $S=1$ ) near the center of the fiber, but drops sharply at the edge of the fiber. This observation conforms with the fact that the bright-field microscope mainly images amplitude information. However, the phase information that is beyond the cut-off of the imaging system causes drop in image intensity.

In Sections 3–6, we follow the method of computing partially coherent images mentioned above to analyze various contrast mechanisms.

### 3. Phase contrast

Phase contrast was primarily designed as a coherent method. Zernike found that the coherent light diffracted from phase-gratings is  $\lambda/4$  out of phase with respect to the incident light, which corresponds to the phase difference of  $\pi/2$ . The interference of strong incident light and weak diffracted light at this phase difference does not produce appreciable contrast. He devised a scheme of imposing additional  $\pm\lambda/4$  delay and some absorption on the direct light to

provide a coherent background on which diffracted light produces sufficient contrast.

To avoid disadvantages of coherent illumination, in practice, phase-contrast is used as a partially coherent system in which the specimen is illuminated with an annulus in the condenser FFP and direct light is modified by a semi-absorbent phase-ring (which matches the dimensions of the annulus) in the objective BFP. Figure 7 simulates a typical phase-contrast setup. In practice, the objective phase-ring is kept slightly larger than the condenser annulus to capture all of the direct light. Due to slightly larger phase-ring, not only the direct light but diffracted light produced by low spatial frequencies of the specimen are filtered. Additionally, the diffracted light originating from adjacent points on the condenser annulus also passes through the phase-ring.

The loss of lower spatial frequencies and precise extent of it are clearly visible from the plots of the real and imaginary parts of the PSI-window in Figures 7(d) and (e), respectively. This unavoidable modification of lower spatial frequencies (stemming from the fact that the annulus and phase-ring cannot be made infinitesimally small) leads to halo, i.e. oscillations at the phase edges [38], and shade-off, i.e. drop in intensity away from the edges of an extended smooth phase object, artifacts. The halo artifact can be noticed at the edge

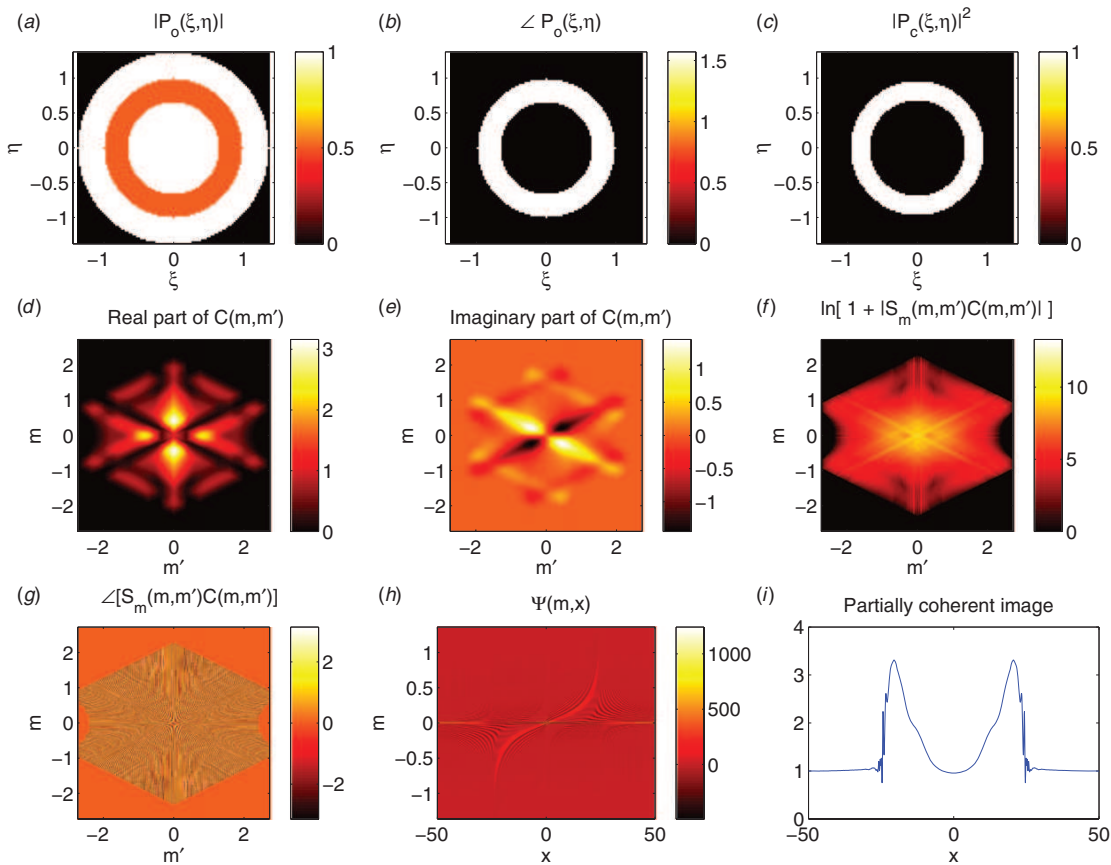


Figure 7. Computation of the partially coherent image of the fiber under phase-contrast. The system parameters are the same as noted in Figure 4 with addition of phase-contrast components. The condenser annulus spans the numerical aperture range of 0.375–0.525, whereas the objective phase-ring spans the numerical aperture range of 0.36–0.54. The phase-ring is assumed to have transmission of half and the phase-delay of  $\pi/2$  at the wavelength of illumination. Parts (a) and (b) are magnitude and the phase of the objective pupil, respectively. Part (c) denotes the intensity of the condenser pupil. Note that the pupil variables and frequency variables are expressed in units of  $\mu\text{m}^{-1}$ . These real axes were obtained by scaling the normalized frequency (and pupil) axes by  $\text{NA}_{\text{obj}}/\lambda$ . Parts (d) and (e) show real and imaginary parts of the PSI-window, respectively. Parts (f) and (g) are the log-magnitude and phase of the filtered mutual spectrum, respectively. Parts (h) and (i) are the phase-space imager and partially coherent image (obtained as a spatial marginal of the phase-space imager), respectively. (The color version of this figure is included in the online version of the journal.)

and the shade-off artifact is prominent at the center of the simulated images of the fiber as shown in Figure 7(i) and Figure 12(b), Section 7. There have been attempts at overcoming these artifacts by use of apodized phase-rings [39]. A recent approach uses randomly distributed source-points and matching phase-delays implemented using two SLMs (spatial light modulators) placed at the condenser FFP and objective BFP [40]. Although the approach based on two SLMs appears to use of full aperture, one still needs to use an illumination from a sparse set of points within the illumination aperture to avoid unwanted filtering of diffracted light. Thus, the entire aperture (or even a significant fraction, say 50%, of the aperture) cannot be used with phase-contrast without

consequent halo and shade-off artifacts. Some authors have investigated the theoretical basis of optimizing parameters of the phase-ring [41] by assuming a periodic specimen. Such theoretical analysis and optimization of various phase-contrast configurations can be greatly facilitated with the phase-space imager approach – without requiring any assumptions except for a thin specimen.

#### 4. Differential interference contrast (DIC)

DIC is a wavefront shearing interferometer that allows imaging with large illumination aperture [42]. It consists of polarizing components (two modified

Wollaston prisms that sandwich the specimen, and are themselves sandwiched between crossed polarizers) that shear the partially coherent illumination beam in two orthogonal polarizations, which are focused a sub-resolution distance apart at the specimen plane. The sheared beams, after traversing the specimen, are combined again with a user-controllable phase delay (called, bias) between the two beams. Each beam is individually partially coherent but both beams are mutually coherent since they were derived from the same beam originally. Due to this coherence, upon recombination, these two beams produce an interference contrast that represents the specimen's phase gradient.

Although DIC is used with partially coherent illumination, initial models have assumed coherent illumination to study the effects of shear and bias on properties of the imaging path [43,44]. Recently, partially coherent models have been developed that account for properties of the illumination as well [22,23,45]. Cogswell and Sheppard [22] assumed matched illumination ( $S=1$ ) and accounted for the effects of both the condenser-side and the objective-side prisms. Preza et al. [45] accounted for an arbitrary illumination aperture, but did not account for the effects of the condenser-side prism and assumed standard Köhler illumination. We elucidated the effects of both the condenser geometry and the condenser-side prism on coherence of illumination to develop a more complete model of imaging in various configurations of DIC [23]. We termed the standard DIC setup, Nomarski-DIC, and the DIC setup lacking the condenser-side prism (as simulated by Preza et al.), Köhler-DIC (see [23], figure 1). We have shown with simulations of TCC and experimental images that the role of condenser-side prism is to illuminate the points that are separated by the distance equal to shear in a spatially coherent manner. The shearing interferometry, per se, is performed entirely by the objective-side light path. In this section, we compute full partially coherent images of an optical fiber under both types of configurations using the phase-space imager. In the following analysis, we assume that the shear is along the  $x$ -direction and that the fiber is aligned with its width along the direction of the shear. If the shear and bias employed by the DIC microscope are  $2\Delta$  and  $2\phi$ , let us define a kernel

$$\Delta_{\text{DIC}}(\mathbf{x}) = \delta(x + \Delta, y) \exp(-i\phi) - \delta(x - \Delta, y) \exp(i\phi), \quad (8)$$

which accounts for the spatial shift and the phase shift introduced by the DIC components. Note the use of scalar space variables  $(x, y)$  and the scalar spatial

frequency  $m$  along the  $x$ -direction. The effect of shear is only along the  $x$ -direction, and the imaging in the  $y$ -direction remains the same as in the bright-field setup.

#### 4.1. Nomarski-DIC

In the Nomarski-DIC configuration, both prisms employ the same shear and effectively image the following transmission function of the specimen (see [23], equation 7):

$$t_N(\mathbf{x}) = t(\mathbf{x}) \otimes \Delta_{\text{DIC}}(\mathbf{x}). \quad (9)$$

In the frequency domain above convolution leads to the modification of the specimen spectrum by factor  $2i \sin(2\pi m\Delta - \phi)$ . The modification of the specimen spectrum can be accounted for by modifying the bright-field TCC (see [23], equation 11), and equivalently by modifying the bright-field PSI-window. Therefore, the PSI-window for Nomarski-DIC is

$$C_{\text{ndic}}(\mathbf{m}, \mathbf{m}') = C(\mathbf{m}, \mathbf{m}') \sin \left[ 2\pi \left( m + \frac{m'}{2} \right) \Delta - \phi \right] \sin \left[ 2\pi \left( m - \frac{m'}{2} \right) \Delta - \phi \right], \quad (10)$$

where  $m$  and  $m'$  are center and difference spatial frequencies along the  $x$ -direction. Figure 8 illustrates the process of computation of the image of the fiber under the Nomarski-DIC system. The shear noted in the caption of the figure is estimated by making measurements at the back focal plane of the objective [46]. Note that the PSI-window shown in Figure 8(d) was computed by first computing the bright-field PSI-window using pupils shown in Figures 8(a)–(c), followed by modulation as per Equation (10).

#### 4.2. Köhler-DIC

Preza et al. [45] assumed that the illumination is of the form  $\exp(2\pi i \xi \cdot \mathbf{x})$  in the DIC microscope and that the effects of shear and bias are entirely accounted for by a modified PSF. This assumption ignores the fact that the condenser-side prism causes the points separated by shear to be illuminated coherently. The effect of shear in the imaging path was accounted for by the PSF of the form

$$h_{\text{kdic}}(\mathbf{x}) = h(\mathbf{x}) \otimes \Delta_{\text{DIC}}(\mathbf{x}). \quad (11)$$

Therefore, the objective pupil (which is the Fourier transform of  $h_{\text{kdic}}$ ) is given by

$$P_{\text{kdic}}(\xi) = 2i \sin(2\pi \xi \Delta - \phi), \quad (12)$$

where  $\xi$  denotes the pupil variable along the  $x$ -direction.

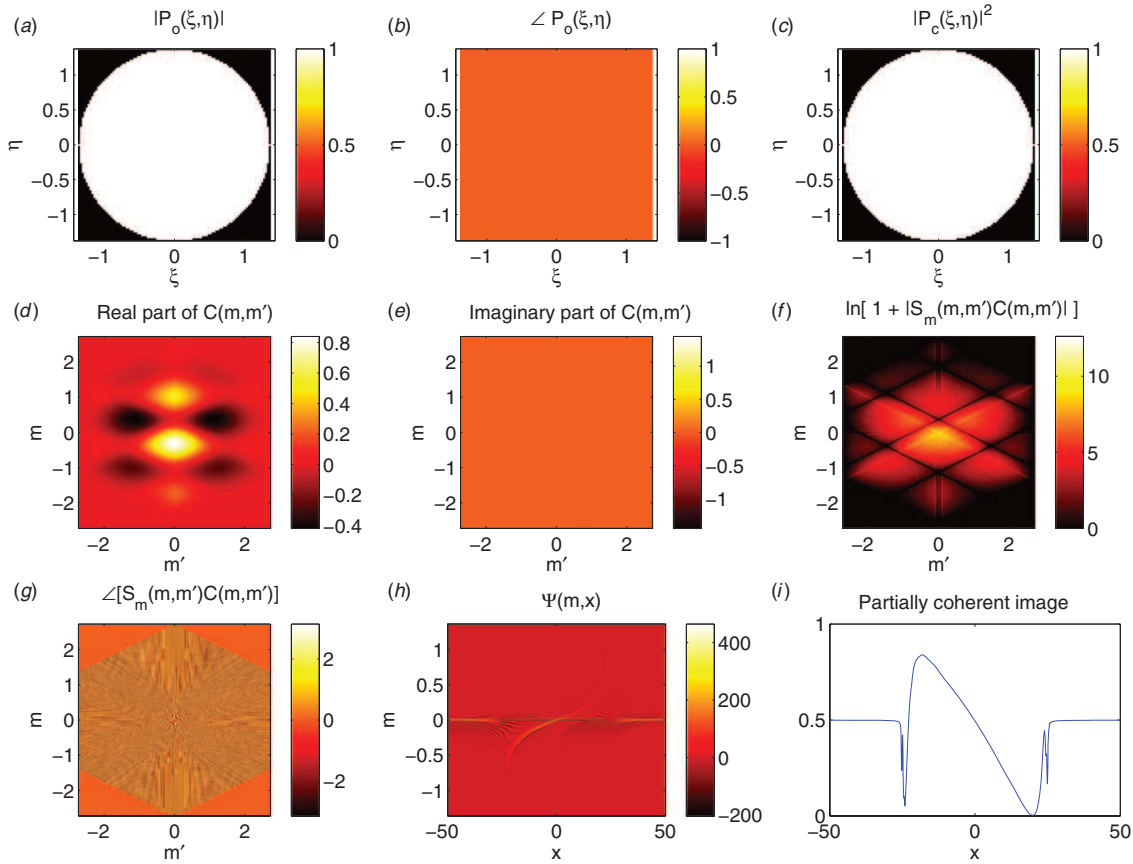


Figure 8. Computation of the partially coherent image of the fiber under Nomarski-DIC: imaging system parameters are the same as in Figure 4 with addition of the DIC components that provide shear  $2\Delta = 0.91 \lambda / \text{NA}_{\text{obj}}$  and bias  $2\phi = \pi/2$ . The arrangement of this figure is the same as Figure 7. (The color version of this figure is included in the online version of the journal.)

We use the above pupil in the phase-space imager model to compute the image of the optical fiber under Köhler-DIC as illustrated in Figure 9.

The PSI-window of the Nomarski-DIC (Figure 8(d)) has sinusoidal modulation, which gives rise to differential weighting of the spatial-frequency components in the specimen mutual spectrum, leading to enhancement of certain phase gradients as observed in the PSI for Nomarski-DIC (Figure 8(h)). Thus, the Nomarski-DIC model predicts the typical shadow-cast image observed under the DIC microscope. The simulated profile and image of the fiber under Nomarski-DIC are shown in Figure 8(i) and in Figure 12(c) (Section 7), with the experimentally measured image shown in Figure 13(b), Section 7.

The structure of the PSI-window (Figure 9(d)) for the Köhler-DIC configuration is closer to bright-field setup. The effects of the sinusoidal modulation of the objective pupil as given by Equation (12) are smoothed

out when it is used for computation of the PSI-window. This is equivalent to stating that when typical partially coherent illumination is employed, the coherence at the specimen is not sufficient for the shearing interferometer on the objective side to provide useful contrast. This leads to the simulated images shown in Figures 9(i) and 12(d). For comparison, an experimental image is shown in Figure 13(c).

These computed and experimental images demonstrate the useful role played by the condenser-side prism, and more generally, the need for accounting of the coherence properties of the illumination in the image formation process.

## 5. Differential phase contrast (DPC)

As is evident from discussion in the previous section, DIC has a rather complex image formation that



730

S.B. Mehta and C.J.R. Sheppard

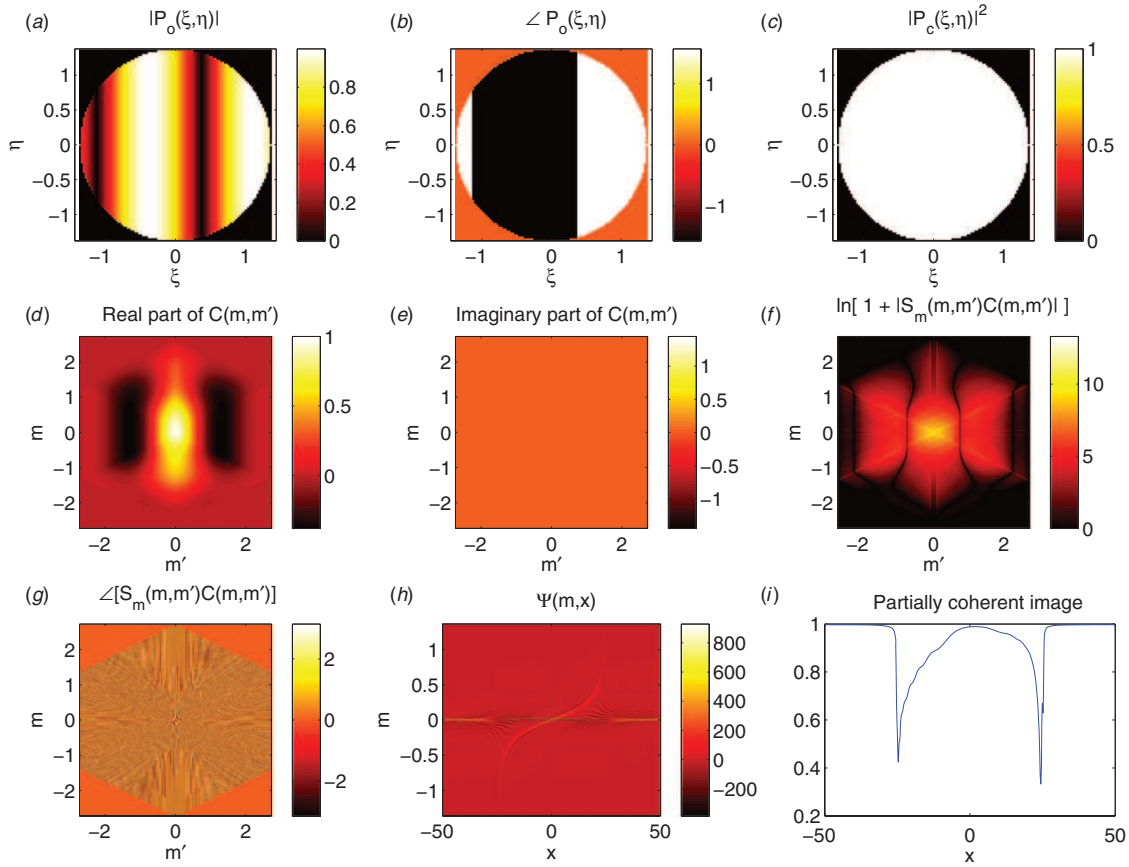


Figure 9. Computation of the partially coherent image of the fiber under Köhler-DIC. Parameters of the imaging system are the same as described in Figure 8, except that the condenser-side prism is not used. The arrangement of this figure is the same as Figure 7. (The color version of this figure is included in the online version of the journal.)

depends on the shear, the bias and the system's pupils. Because of this complexity, the DIC image does not linearly represent the specimen's phase gradient. Therefore, quantitative imaging with DIC necessitates use of approaches such as phase-shifting, which require acquisition of multiple images at different bias values [47]. As a simpler and more quantitative alternative, DPC was developed using a split-detector in scanning optical microscopy [5]. The image in the scanning DPC system is obtained by subtracting the signals obtained from opposite halves of the split-detector. Scanning DPC is sensitive to small changes in the specimen's phase gradients and is inherently more quantitative. We developed a reciprocal equivalent of the DPC system that uses a 'split-source' – which is positive in one half and negative in the other. The negative half of the split-source is synthesized by acquiring two images by blocking opposite halves of the condenser aperture and then taking their difference.

Since this method uses asymmetric illumination (from halves of the condenser aperture), we call it asymmetric illumination-based differential phase contrast [6]. Since both methods are reciprocal to one another, their imaging properties are identical. AIDPC differs from the Schlieren-type imaging methods, e.g. Hoffman modulation contrast [8] and asymmetric illumination contrast [4], in terms of the synthesized negative condenser-aperture that allows quantitative imaging of the phase gradient.

Simulated image formation in AIDPC is shown in Figure 10. From Figure 10(d) we notice that the PSI-window of AIDPC has a simple structure which is odd along the instantaneous spectrum ( $m$ ). This odd symmetry results in sensitivity of AIDPC to phase gradient information as is evident from the PSI shown in Figure 10(h) and simulated images shown in Figures 10(i) and 12(e). Thus, AIDPC provides nearly linear measurement of the directional

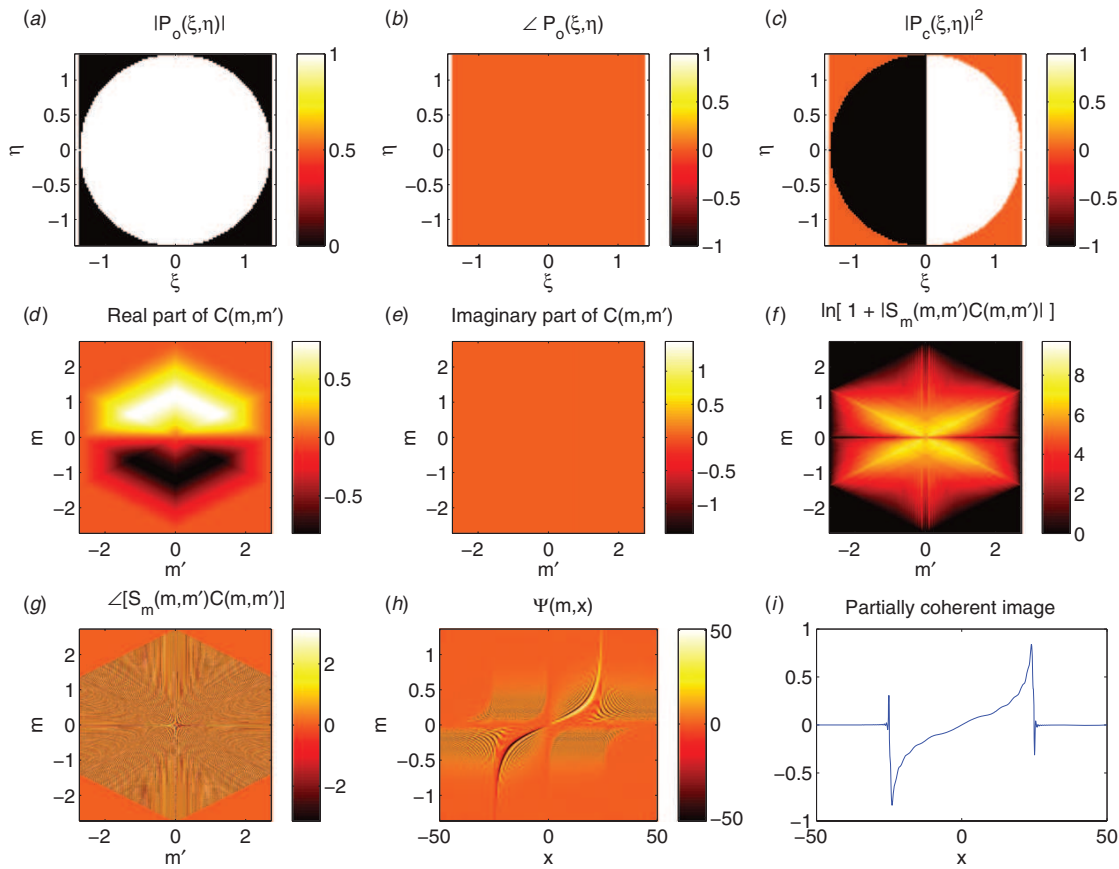


Figure 10. Computation of the partially coherent image of the fiber under AIDPC. The system parameters are the same as described in Figure 4, with addition of a split condenser aperture. Note that the negative intensity in the condenser aperture was synthesized by subtracting two images obtained with opposite halves of the aperture closed. The arrangement of this figure is the same as Figure 7. AIDPC is seen to be sensitive and linearly dependent on the gradient of the specimen. (The color version of this figure is included in the online version of the journal.)

gradient of the specimen and is simple to implement (no modification on the objective-side light path is required).

## 6. Spiral phase contrast (SPC)

The last imaging system that we examine is SPC. SPC is a coherent method that has been shown to provide isotropic edge enhancement for amplitude and phase specimens [12]. SPC involves use of a spiral phase modulation in the back focal plane of the objective. It is interesting to investigate the amount of partially coherent which can be tolerated with SPC such that its edge enhancement abilities are preserved.

Figure 11 shows the computation of the image with matched illumination. The associated image sequence shows the computation of the image using the PSI for

coherence ratios,  $S=0.2, 0.4, 0.8$ , and  $1$ . It is observed that up to  $S=0.4$ , spiral phase contrast images the entire fiber with a constant intensity, except at the edge. Thus, as long as the condenser aperture is smaller than 40% of the objective aperture, one does not need to use a coherent source. We hypothesize that such a setup can provide partially coherent imaging that retains the isotropic edge enhancement capabilities of the spiral phase microscope, albeit accompanied by loss of contrast. Note that such a partially coherent system may need to be implemented with a physical phase-plate rather than a spatial light modulator (SLM), as the SLMs usually have a narrow range of acceptance angles. These observations match with the experimental results obtained using a physical spiral phase-plate in [13]. In Section 7, with the help of simulated images of a general phase profile, we show that the contrast produced by the spiral phase

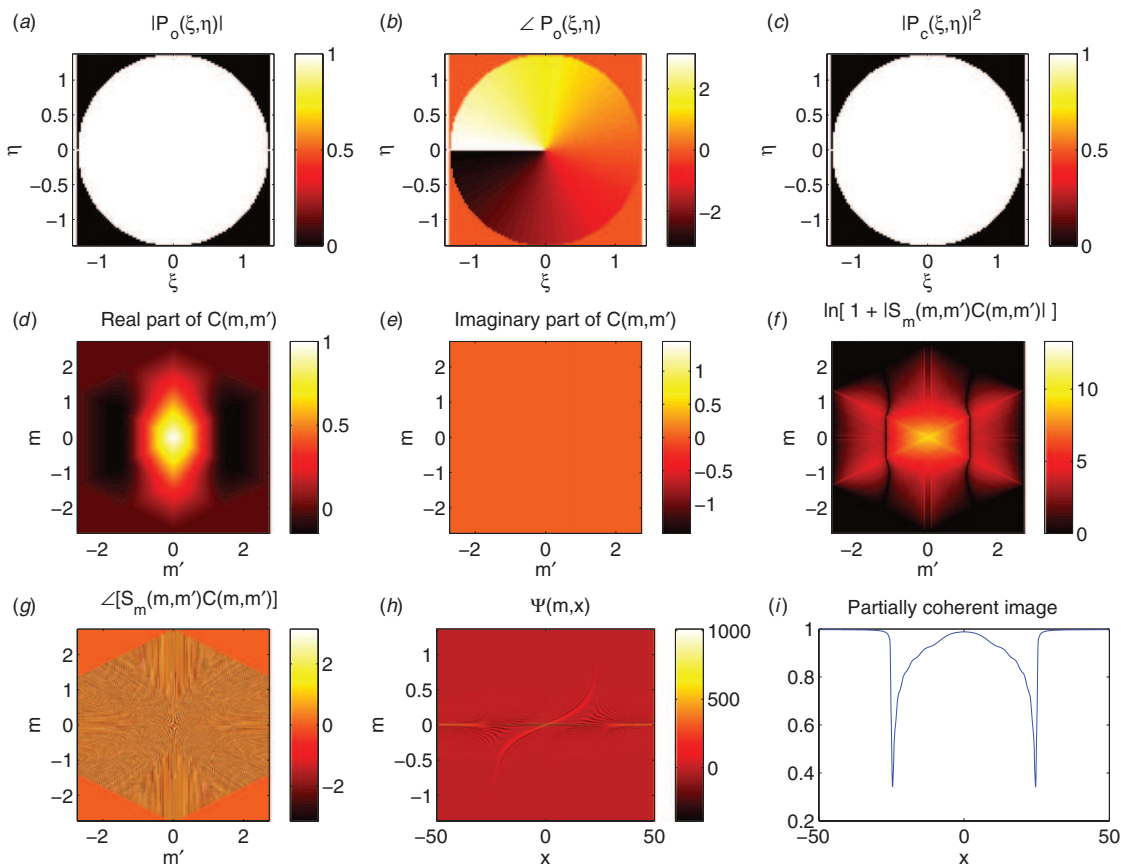


Figure 11. Computation of partially coherent image of the fiber under partially coherent spiral-phase setup. The parameters of the imaging system are the same as described in Figure 4, except for the presence of a spiral phase-plate at the objective BFP. The arrangement of this figure is the same as Figure 7. The image computed at  $S=1$  as shown here appears very similar to the bright-field image. The associated image sequence (movie 1) shows the above computation for increasing size of the condenser at  $S=0.2, 0.4, 0.6, 0.8$ , and  $1$ . (The color version of this figure is included in the online version of the journal.)

microscope changes significantly as we open the condenser aperture. This behaviour is expected, since only the on-axis point of the condenser aperture is imaged onto the phase-singularity of the spiral phase in the objective BFP. Thus, only the light originating from the central condenser point experiences right manipulation that gives rise to isotropic edge enhancement.

## 7. Comparison of contrast methods

In this section, we compare computed images of the fiber from Sections 2–5 with experimentally acquired images. We also compare computed images of a hypothetical 1D phase-variation consisting of sharp and smooth features at matched illumination ( $S=1$ ) and nearly coherent illumination ( $S=0.05$ ). These

comparisons allow us to illustrate the contrast and resolution properties of different phase imaging methods.

### 7.1. Experimental images of the fiber

Figure 12 shows the profiles computed in previous sections extended in the vertical direction to simulate images of the fiber under different imaging systems. It is seen that the images have expected appearances and features.

We compare the simulation results obtained for four imaging systems (bright-field, Nomarski-DIC, Köhler-DIC, and DPC) with experimentally measured images. The experimental setup as described in the figures was constructed. We used an Olympus BX61 motorized microscope that was equipped with



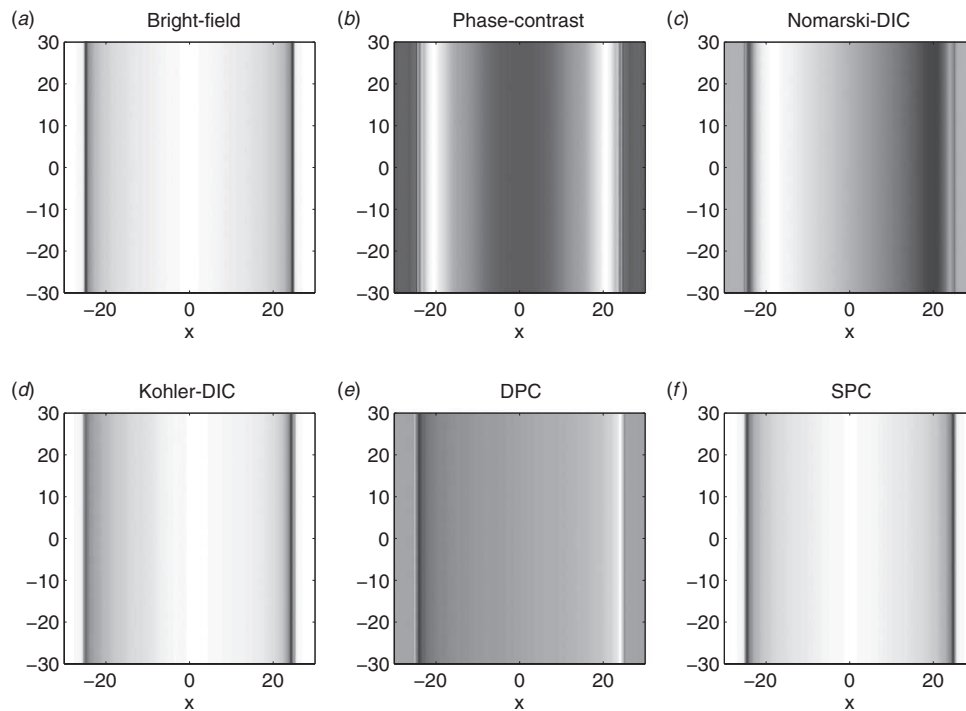


Figure 12. A comparison of images of the fiber computed under different imaging systems described in Sections 3–6.

Qimaging Retiga Exi monochrome cooled CCD camera. The motorized parts of the microscope and the camera were controlled using the open-source acquisition software, micro-manager.<sup>2</sup> Although there is some mismatch between computed and measured intensity profiles, all key features match. As mentioned previously, one of the reasons for the mismatch is the fact that the specimen is much thicker than the depth of focus of the imaging systems, whereas a thin specimen is assumed in the model.

## 7.2. Computed images of a general phase-profile

Simulated and experimental images of the optical fiber already allow useful comparison of the contrast produced by different imaging methods. We see from Figures 12 and 13 that at matched illumination ( $S = 1$ ), bright-field, Köhler-DIC, and SPC provide nearly the same contrast when a fiber is imaged. These three methods image only the high-frequency phase information. Nomarski-DIC and DPC, on the other hand, provide a phase-gradient contrast, with DPC providing an image that is more linearly related to the specimen phase gradient. It is instructive to consider imaging of a general phase profile to compare the resolution in addition to contrast.

### 7.2.1. With matched illumination

Figure 14 shows the computed image of a hypothetical phase variation consisting of smooth features (such as triangular, sinusoidal, square variation each spanning the distance of  $5\mu\text{m}$ ) and a sharp feature (a phase ‘double-slit’ in between the square feature). These images are computed at matched illumination, using the settings and PSI-windows discussed in Sections 2–6. To allow proper comparison, all computed images are normalized so that maximum value in the image is 1. The results appear somewhat different from the usually expected ones – because the filtering effects due to finite aperture come into play apart from the contrast effects.

The following interesting observations can be made from Figure 14.

- Bright-field, Köhler-DIC, and SPC fail to image the smooth variations of triangle, sinusoid, and square. They show moderate decrease in intensity due to medium spatial frequencies introduced by these features. They show significant decrease in intensity at the edges of the square feature as high spatial frequencies are filtered due to the finite aperture. The double-slit remains unresolved in these three systems and gives rise to the

734

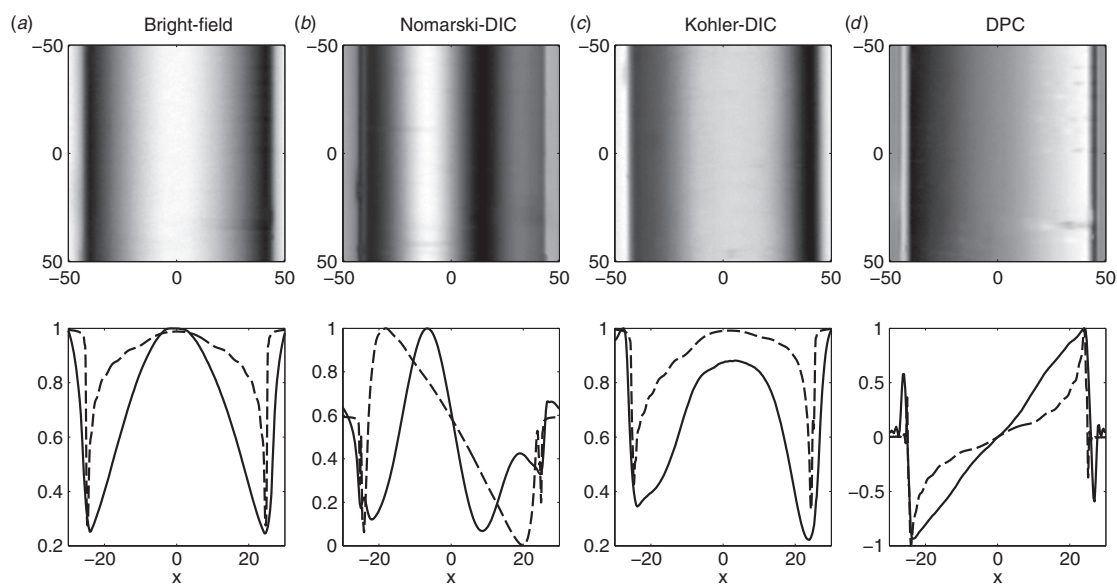
*S.B. Mehta and C.J.R. Sheppard*

Figure 13. A comparison of experimental images (top row) and experimental and simulated intensity profiles (bottom row) for different imaging systems. To reduce effects of noise, the experimental intensity profiles were obtained by averaging the image along vertical dimension. It is seen that all key features predicted by the simulated results are observed in the experimental images.

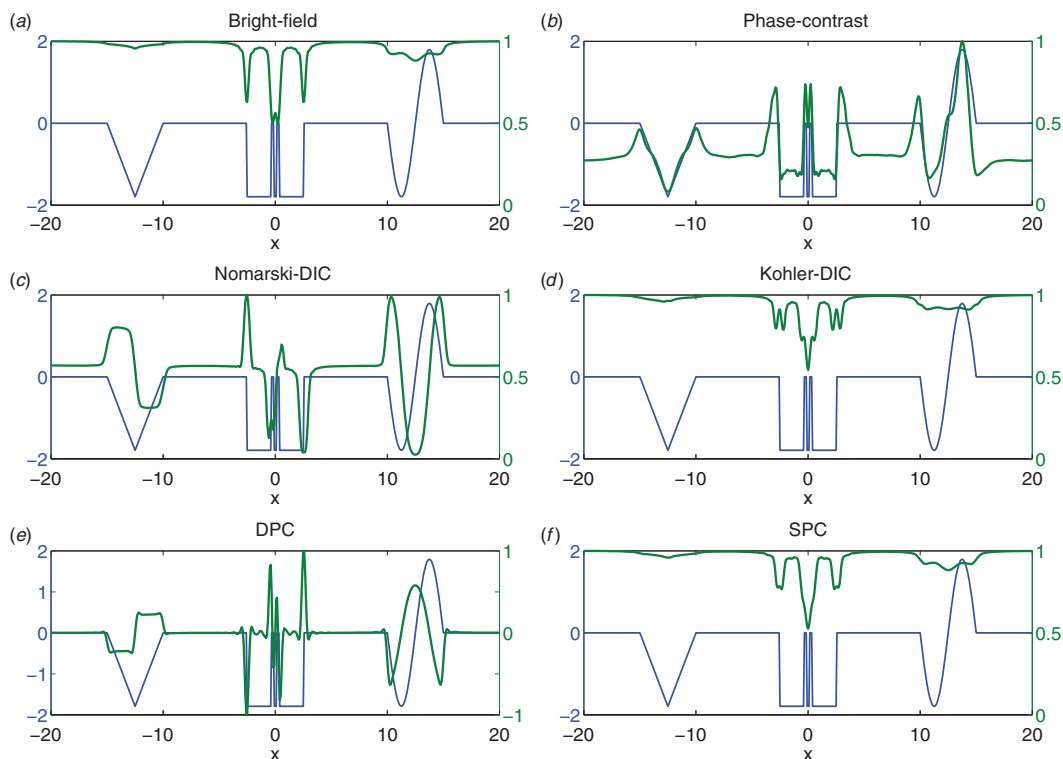


Figure 14. Partially coherent images ( $S=1$ ) of a general phase profile consisting of sharp and smooth features: the blue line in all the plots shows the phase of the specimen, whereas the green line shows the computed (and normalized) image. The parameters of different imaging systems are the same as noted in Sections 3–6. The  $x$ -axis is expressed in  $\mu\text{m}$ . (The color version of this figure is included in the online version of the journal.)

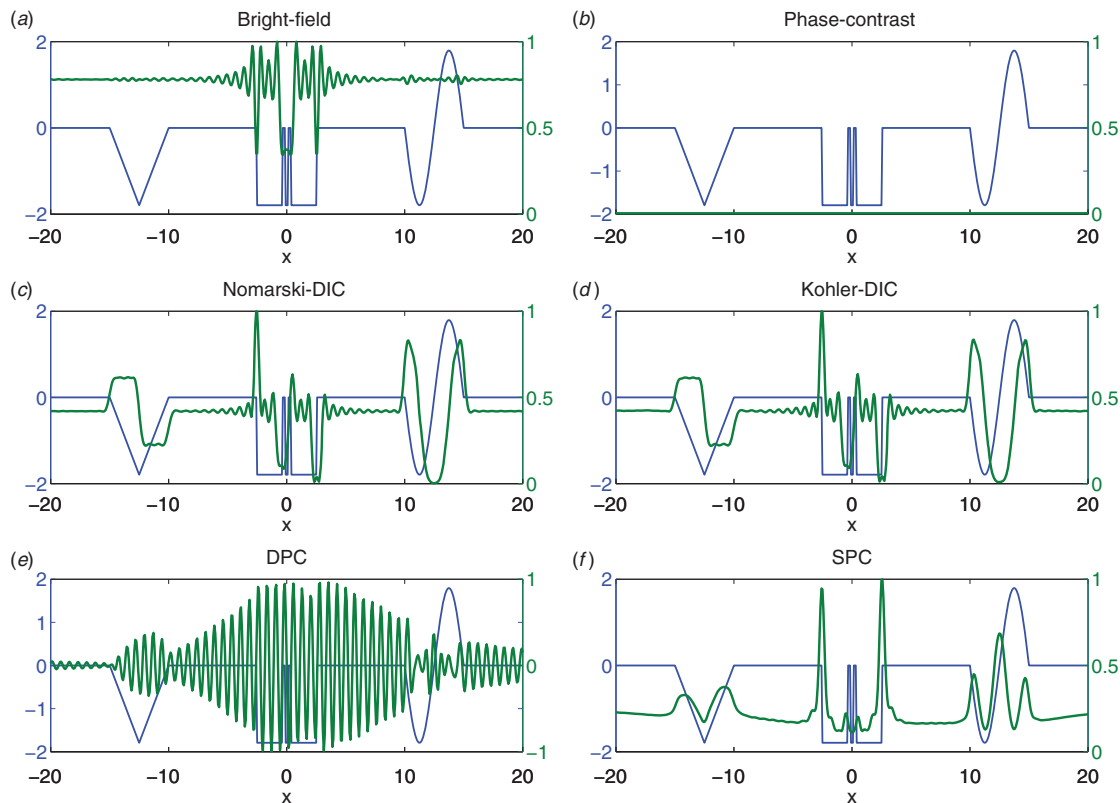


Figure 15. Nearly coherent images ( $S=0.05$ ) of a general phase profile consisting of sharp and smooth features: the blue line in all the plots shows the phase of the specimen, whereas the green line shows the computed (and normalized) image. The parameters of different imaging systems are the same as noted in the corresponding figures in Sections 3–6, except that the condenser NA is assumed to be 0.15. The  $x$ -axis is expressed in  $\mu\text{m}$ . (The color version of this figure is included in the online version of the journal.)

most prominent decrease in intensity due to the removal of the high spatial frequencies out of the broad spectrum they present to the imaging systems.

- At matched illumination, the SPC fails to image edges of the specimen with high intensity. Thus, SPC's contrast mechanism fails and filtering effects due to finite aperture dominate.
- Phase contrast produces an image that represents the phase, albeit not linearly. The halo artifact is visible around each phase discontinuity. The shade-off artifact is visible as a drop in image intensity where the phase is constant.
- Nomarski-DIC at bias  $\pi/2$  does image phase gradient of the specimen, but shows some non-linearity and spatial shift with respect to the gradient of the phase. To obtain the image that linearly represents phase gradient of the

specimen from a DIC microscope, one needs to use the phase-shifting procedure [47].

- Differential phase contrast provides an image that most linearly represents the phase gradient of the specimen at matched illumination. However, the double-slit is imaged with smaller intensity variation than the edges of the square feature – a consequence of filtering due to the finite aperture. Thus, DPC is a particularly suitable method for quantitative imaging of phase information, when partially coherent illumination is used. The absolute phase profile can be obtained by combining phase gradients measured in the  $X$ - and  $Y$ -directions.

### 7.2.2. With nearly coherent illumination

Next, we discuss computed images (Figure 15) and PSI-windows (Figure 16) at nearly coherent

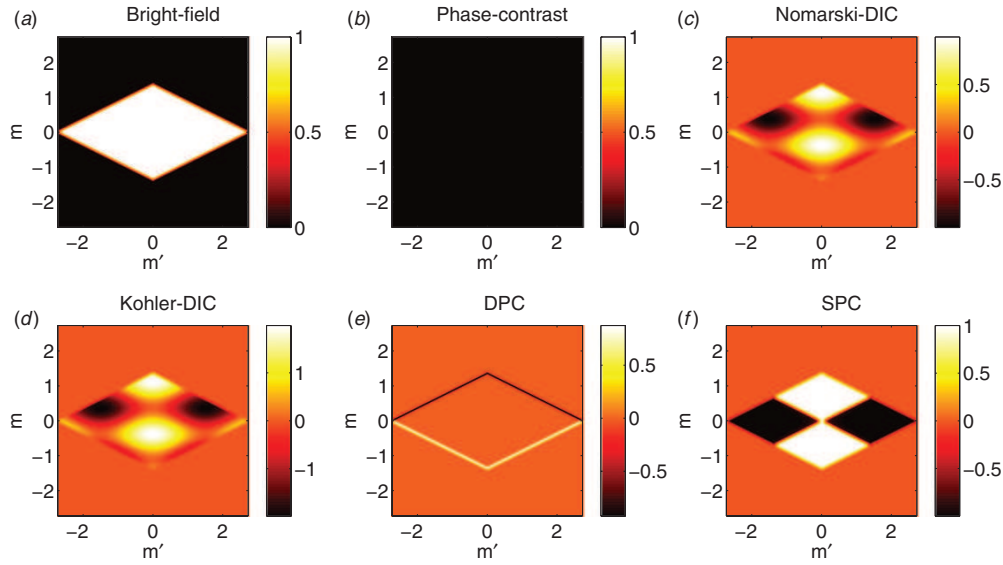


Figure 16. Computed PSI-windows for different imaging systems at  $S=0.05$ . The other settings are as noted in Figure 15. (The color version of this figure is included in the online version of the journal.)

illumination ( $S=0.05$ ). In Figure 17, we compare the images under bright-field, Nomarski-DIC, and SPC using fully coherent illumination with images computed at  $S=0.05$ . Since the specimen is constant along the  $Y$ -direction, its spectrum is given by a Dirac-delta along the  $Y$ -direction. Therefore, to compute fully coherent images shown in Figure 17, we filtered the spectrum of the specimen with a one-dimensional slice of the objective pupil along the  $X$ -direction. The intensity image was computed as a squared magnitude of the image amplitude (i.e. inverse Fourier transform of the filtered spectrum).

As expected, the images differ greatly in comparison to the partially coherent case presented in previous figures. The important observations follow:

- The bright-field image (Figure 15(a)) shows the edges (of square feature and double-slit) with the same drop in intensity as they now become indistinguishable due to reduced cut-off of the system. Spatial frequencies due to the triangle and sinusoidal feature are not imaged appreciably. The PSI-window for the bright-field system (Figure 16(a)) transfers the lower part of the specimen's mutual spectrum without much modification. The cut-offs of all the systems are the same as the bright-field system, but the structure of the PSI-window differs. The coherent image computed under the bright-field setup (Figure 17(a)) matches very well with the nearly coherent image at  $S=0.05$ .
- For phase-contrast, the condenser size is so small that no light (direct or diffracted) passes through the phase-ring (parameters noted in Figure 7). Consequently, the PSI-window (Figure 16(b)) and the image (Figure 15(b)) both are zero.
- The PSI-windows (Figures 16(c) and (d)) and images (Figures 15(c) and (d)) produced by the Nomarski-DIC and Köhler-DIC systems are identical. This result corroborates the result obtained in [23] that when coherent illumination is employed the condenser-side prism (used in Nomarski-DIC) is redundant. As seen in Figure 17(b) DIC images computed assuming fully coherent illumination match excellently with the nearly coherent image at  $S=0.05$ .
- The PSI-window of DPC (Figure 16(e)) transmits only a minute region of the mutual spectrum of the specimen when a very small condenser aperture is employed. Therefore, the image (Figure 15(e)) exhibits only sinusoidal variations corresponding to the passband of the system.
- The SPC provides an interesting case to analyze at nearly coherent illumination. Its PSI-window (Figure 16(f)) transmits the lower region of the mutual spectrum with modulation that has the same symmetry as observed for DIC systems. Consequently, SPC 'regains' its ability to image phase edges. However, we notice that unlike DIC, SPC

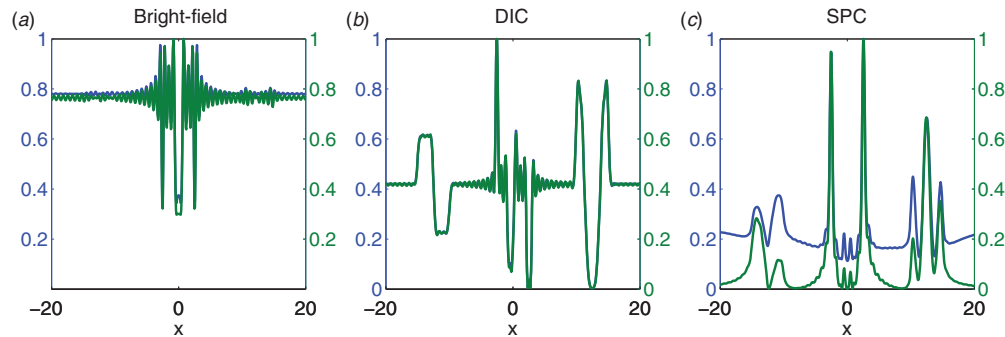


Figure 17. Comparison of images computed under fully coherent condition (green lines) at  $S=0$ , with images computed under nearly coherent (blue lines) condition at  $S=0.05$ . (The color version of this figure is included in the online version of the journal.)

transmits a zero spatial frequency pair (DC term) from the mutual spectrum. Thus, even slight partial coherence of the source leads to a DC bias in the image. The comparison of a nearly coherent and a fully coherent image under SPC shown in Figure 17(c) shows this DC bias clearly. This property of the PSI-window of SPC follows from the fact that only the central point in the condenser aperture is imaged onto the phase singularity of the spiral phase in the objective BFP.

The computed image at  $S=0.05$  (Figure 15(f)) shows that unlike the partially coherent case, the nearly coherent system images the edges of the square feature with high intensity. However, the finite aperture still causes the double-slit to be imaged with low intensity. This same behavior is observed when the nearly coherent and fully coherent images under SPC are compared in Figure 17(c). Moreover, imaging of triangular and sinusoidal features under nearly coherent illumination is improved but not much as when fully coherent illumination is used. With our simulation at  $S=0.2$  and  $0.4$ , we observed that the DC bias in SPC increases rapidly and contrast for non-edge features reduces fast as the condenser aperture is opened. While the fact that the edges are imaged with high intensity by SPC is widely appreciated, the filtering effects on features such as a double-slit, sinusoidal and triangular phase feature are perhaps not.

We note that above comparison for different imaging systems is carried out for the first time. Some of the above observations corroborate with earlier research, whereas certain new observations are made.

## 8. Discussion and conclusion

It will be useful to overcome some of the inherent assumptions in the existing model. DIC and DPC

typically use high-NA illumination and imaging. Therefore, extending the PSI model to account for effects of high-NA is interesting. The assumption of a thick specimen will require a description of the image formation in three dimensions. Owing to the bi-linear nature of partially coherent imaging, the partially coherent model would be six-dimensional.

Nevertheless, in its current form, the model can be used to design new imaging systems. One such application is to design illumination patterns for AIDPC that provide more linear imaging and control over depth sectioning of the system. These illumination patterns can be easily implemented using a spatial light modulator.

It will be fruitful to study fundamental relationships between the structure of the PSI-window and contrast observable in the imaging system. It is worth noting that the symmetry of the TCC dictates the type of contrast observable in the image [35]. In the signal processing community, there is a large amount of literature on the windowed Wigner distribution. PSI is in some sense a special instance of the windowed Wigner distribution. We should note that PSI being a 'real' distribution, does not conform to some of the guidelines laid out for ideal phase-space distributions, e.g. it does not possess marginals that are Fourier pairs. The examination of signal-processing properties of the phase-space imager will enhance the physical intuition that can be derived from the model.

In conclusion, we have illustrated a phase-space model that elegantly captures the bi-linear nature of image formation in partially coherent systems. The model is general and the only assumptions involved in its development are quasi-monochromatic illumination, a transparency-like specimen and a paraxial imaging system. As per this model, the image in a partially coherent system is given as a spatial-marginal of the phase-space imager. The phase-space imager is related to the specimen and the system by the



specimen's mutual spectrum and the system's PSI-window that modifies the mutual spectrum. We have discussed five different imaging methods originally designed for different purposes. We have shown analysis of a standard phase-contrast setup. We demonstrated the important role played by the condenser-side prism in the DIC setup. It was shown that DPC provides the most linear transfer of the specimen's phase-gradient information among the methods considered, when matched illumination is used. We found that the spiral phase contrast method need not use coherent illumination for edge enhancement. For the purpose of edge enhancement, SPC can be used with partially coherent illumination ( $S < 0.4$ ), but the contrast for non-edge features drops significantly as the coherence of illumination reduces. Among these methods, DIC and DPC have been shown to provide quantitative information under partially coherent illumination. DIC has complex image formation and requires use of phase-shifting to obtain an image that is linearly dependent on the specimen's phase gradient. DPC, on the other hand, is inherently more linear and is simple to implement. The simulated and experimental images (Figures 12–14) obtained with DIC and DPC confirm this observation.

This study demonstrates that the phase-space imager model is valuable for unified analysis of partially imaging systems that have been developed with disparate principles in mind. It will also be useful for design of new quantitative partially coherent systems that synergize optical acquisition and digital reconstruction.

### Acknowledgements

SBM thanks the development team (particularly, Arthur Edelstein, Nico Stuurman, and Nenad Amodaj) of the micro-manager – an open-source microscopy acquisition software – for help with development of the hardware driver<sup>3</sup> for the Olympus BX61 microscope. The authors also thank the anonymous reviewer for critically analyzing the manuscript and helping us improve the readability of the results.

### Notes

1. A discussion about this can be found on the web page: <http://shalin.wordpress.com/2009/12/06/fftiff/>
2. <http://www.micro-manager.org/>
3. <http://valelab.ucsf.edu/~nico/MMwiki/index.php/OlympusIX81/BX61>

### References

- [1] Microscopes: Time Line. [http://nobelprize.org/educational\\_games/physics/microscopes/timeline/index.html](http://nobelprize.org/educational_games/physics/microscopes/timeline/index.html)
- [2] Zernike, F. *Science* **1955**, *121*, 345–349.
- [3] Nomarski, G. Interference Polarizing Device for Study of Phase Objects. US Patent 2924142, 1960.
- [4] Kachar, B. *Science* **1985**, *227*, 766–768.
- [5] Hamilton, D.; Sheppard, C.J.R. *J. Microsc.* **1984**, *133*, 27–39.
- [6] Mehta, S.B.; Sheppard, C.J.R. *Opt. Lett.* **2009**, *34*, 1924–1926.
- [7] Ellis, G.W. Edge Enhancement of Phase Phenomena. US Patent 4255014, 1981.
- [8] Hoffman, R.; Gross, L. *Appl. Opt.* **1975**, *14*, 1169–1176.
- [9] Teague, M.R. *J. Opt. Soc. Am.* **1983**, *73*, 1434–1441.
- [10] Goodman, J.W. *Introduction to Fourier Optics*, 2nd ed.; McGraw-Hill: New York, 1996.
- [11] Bernet, S.; Jesacher, A.; Fürhapter, S.; Maurer, C.; Ritsch-Marte, M. *Opt. Express* **2006**, *14*, 3792–3805.
- [12] Fürhapter, S.; Jesacher, A.; Bernet, S.; Ritsch-Marte, M. *Opt. Express* **2005**, *13*, 689–694.
- [13] Maurer, C.; Jesacher, A.; Fürhapter, S.; Bernet, S.; Ritsch-Marte, M. *J. Microsc.* **2008**, *230*, 134–142.
- [14] Lewis, R.A. *Phys. Med. Biol.* **2004**, *49*, 3573–3583.
- [15] Olivo, A.; Arvanitis, C.D.; Bohndiek, S.E.; Clark, A.T.; Prydderch, M.; Turchetta, R.; Speller, R.D. *Nucl. Inst. Methods Phys. Res. A* **2007**, *581*, 776–782.
- [16] Kouskousis, B.; Kitcher, D.J.; Collins, S.; Roberts, A.; Baxter, G.W. *Appl. Opt.* **2008**, *47*, 5182–5189.
- [17] Pawley, J.B. *Handbook of Biological Confocal Microscopy*, 3rd ed.; Springer: New York, 2006.
- [18] Martin, L.C. *The Theory of the Microscope*; Blackie: Glasgow, 1966.
- [19] Singer, W.; Totzeck, M.; Gross, H. *Handbook of Optical Systems, Vol. 2, Physical Image Formation*; Wiley-VCH: Germany, 2005.
- [20] Saleh, B.; Rabbani, M. *Appl. Opt.* **1982**, *21*, 2770–2777.
- [21] Schellenberg, F.M. Resolution Enhancement Techniques in Optical Lithography. In *Resolution Enhancement Techniques in Optical Lithography*; SPIE Milestone Series; SPIE Press: Bellingham, WA, 2004; Vol. MS178.
- [22] Cogswell, C.; Sheppard, C. *J. Microsc.* **1992**, *165*, 81–101.
- [23] Mehta, S.B.; Sheppard, C.J.R. *Opt. Express* **2008**, *16*, 19462–19479.
- [24] Hopkins, H.H. *Proc. R. Soc. Lond. A* **1953**, *217*, 408–432.
- [25] Mehta, S.B.; Sheppard, C.J.R. Full-field Phase-gradient Contrast Methods for Label-free Quantitative Imaging of Cellular Morphology: AIDPC and DICFocus on Microscopy Conference Series, Krakow, Poland, April 5–8, 2009. [http://www.focusonmicroscopy.org/2009/PDF/396\\_Mehta.pdf](http://www.focusonmicroscopy.org/2009/PDF/396_Mehta.pdf).
- [26] Mehta, S.B.; Sheppard, C.J.R. Asymmetric Illumination Based Differential Phase Contrast (AI-DPC) for Full-field Transmission Imaging of Phase Information in Biological Specimens. Focus on Microscopy Conference Series, Osaka-Awaji, Japan, April 13–16, 2008. [www.focusonmicroscopy.org/2008/PDF/089\\_Mehta.pdf](http://www.focusonmicroscopy.org/2008/PDF/089_Mehta.pdf)
- [27] Mehta, S.B.; Sheppard, C.J.R. Transfer Function Analysis of Partially Coherent Phase Imaging Methods and Evaluation for Quantitative Imaging, *OSA*

- Technical Digest*; Frontiers in Optics, San Jose, CA, Oct 11–15, 2009; Optical Society of America: Washington, DC, 2009; FMK6.
- [28] Mehta, S.B.; Sheppard, C.J.R. *Opt. Lett.* **2010**, *35*, 348–350.
- [29] Bastiaans, M.J. Applications of the Wigner Distribution to Partially Coherent Light Beams. In *Advances in Information Optics and Photonics*; Friberg, A.T., Dändliker, R., Eds.; SPIE Press: Bellingham, WA, 2008; Vol. PM183, pp 27–56.
- [30] Sheppard, C.J.R.; Wilson, T. *Phil. Trans. Roy. Soc. Lond. A* **1980**, *295*, 513–536.
- [31] Streibl, N. *J. Opt. Soc. Am. A* **1985**, *2*, 121–127.
- [32] Nugent, K.A.; Arhatari, B.D.; Peele, A.G. *Ultramicroscopy* **2008**, *108*, 937–945.
- [33] Sheppard, C.J.R.; Hamilton, D.K.; Cox, I.J. *Proc. R. Soc. Lond. A* **1983**, *387*, 171–186.
- [34] Born, M.; Wolf, E. *Principles of Optics: Electromagnetic Theory of Propagation, Interference and Diffraction of Light*, 7th expanded ed.; Cambridge University Press: Cambridge, UK, 1999.
- [35] Wilson, T.; Sheppard, C.J.R. *Theory and Practice of Scanning Optical Microscope*; Academic Press: London, 1984.
- [36] Cohen, L. *Time-frequency Analysis: Theory and Applications*; Prentice Hall PTR: Englewood Cliffs, NJ, 1995.
- [37] O'Neill, J.C.; Flandrin, P.; Williams, W.J. *IEEE Signal Process. Lett.* **1999**, *6*, 304–306.
- [38] Wilson, T.; Sheppard, C.J.R. *Optik* **1981**, *59*, 19–23.
- [39] Otaki, T. *Opt. Rev.* **2000**, *7*, 119–122.
- [40] Maurer, C.; Jesacher, A.; Bernet, S.; Ritsch-Marte, M. *Opt. Express* **2008**, *16*, 19821–19829.
- [41] Som, S.C.; Mondal, P.K. *J. Mod. Opt.* **1967**, *14*, 259–268.
- [42] Pluta, M. *Advanced Light Microscopy Specialized Methods*; Elsevier PWN: Warszawa, 1989; Vol. 2.
- [43] Galbraith, W. *Microscopica Acta* **1982**, *85*, 233–254.
- [44] Holmes, T.J.; Levy, W.J. *Appl. Opt.* **1987**, *26*, 3929.
- [45] Preza, C.; Snyder, D.L.; Conchello, J. *J. Opt. Soc. Am. A* **1999**, *16*, 2185–2199.
- [46] Mehta, S.B.; Sheppard, C.J.R. Sample-less Calibration of the Differential Interference Contrast Microscope. *Appl. Opt.* [Online early access]. Published Online: Apr 12, 2010. <http://www.opticsinfobase.org/abstract.cfm?msid=122175>.
- [47] Cogswell, C.J.; Smith, N.I.; Larkin, K.G.; Hariharan, P. *Proc. SPIE* **1997**, *2984*, 72–81.

## Chapter 6

# Quantitative phase microscopy for biological applications

In this chapter, we report biological applications of partially coherent phase microscopy methods of DIC, AIDPC, and dark-field. We describe how we reconstruct the phase information from DIC and AIDPC images and how we analyze dark-field images of a beating sperm flagellum to sense the dynamic changes in its internal structure. The chapter mainly consists of image analysis algorithms developed for various tasks involved in quantitative biological imaging, viz., calibration of experimental microscope, registration of acquired images, reconstruction of phase, and feature extraction.

When using experimental systems for quantitative analysis, one must calibrate the essential parameters of the system. For the majority of partially coherent systems (like bright-field, AIDPC, and dark-field), knowledge of the geometry of the objective and the condenser apertures and the wavelength of quasi-monochromatic illumination are required. While the wavelength of illumination is under control of the experimenter, the aperture geometries can be measured without much difficulty by imaging the back focal plane of the objective after the microscope has been aligned for Köhler illumination. The calibration of DIC, however, requires knowledge of shear and bias as well. Several authors have proposed approaches for calibration of shear and bias based on known specimens – mainly sub-resolution phase and fluorescent beads. By using accurate image analysis, we found that these approaches



are inaccurate. We present our sample-less and accurate approach [Mehta and Sheppard, 2010b] of calibrating the shear in sec. 6.1.

In sec. 6.2, we present algorithms for registration of DIC and AIDPC images and their use for reconstruction of the optical path length of the specimen. Since inversion of complete bilinear partially coherent model is difficult at this moment, we use the assumption of a slowly varying specimen (with respect to the resolution of given partially coherent system) in our reconstruction process. We incorporate a heuristic deconvolution step to account for the fast varying phase information within the specimen. These algorithms are useful in obtaining quantitative maps of the optical thickness of the specimen that corresponds to the dry mass of the biological specimen. Quantitative measurement of morphology is useful for analyzing biological processes with long-term live imaging experiments.

In sec. 6.3, we present algorithms for quantitative analysis of the beating pattern of a sperm flagellum from dark-field time-lapse images. The analysis reveals important aspects of a highly conserved biological machinery called the axoneme [Greek axōn, axis + Greek nēma, thread] that powers the flagella and cilia of the majority of the eukaryotic cells. The imaging and analysis of axoneme dynamics was carried out in collaboration with Dr. Rudolf Oldenbourg and Dr. Naoki Noda at Marine Biological Laboratory (MBL), Woods Hole, USA during my collaborative visit to MBL.

## **6.1 Paper: Sample-less calibration of differential interference contrast microscope**

# Sample-less calibration of the differential interference contrast microscope

Shalin B. Mehta<sup>1,2,\*</sup> and Colin J. R. Sheppard<sup>1,2,3</sup>

<sup>1</sup>Optical Bioimaging Lab, Division of Bioengineering, National University of Singapore, Block-E3A, #7-10, 7 Engineering Drive 1, Singapore 117574

<sup>2</sup>Graduate School for Integrative Sciences & Engineering, National University of Singapore, Singapore 117456

<sup>3</sup>Department of Biological Sciences, National University of Singapore, Singapore 117543

\*Corresponding author: shalin.mehta@gmail.com

Received 11 January 2010; revised 8 April 2010; accepted 9 April 2010;  
posted 12 April 2010 (Doc. ID 122175); published 19 May 2010

Analysis of image formation in a differential interference contrast (DIC) microscope and retrieval of the specimen's properties require calibration of its key parameters, viz. shear and bias. We present a method of measuring the shear and the bias of a DIC microscope from the interference fringes produced in the back focal plane of the objective. Previous approaches, which use calibrated specimens such as polystyrene or fluorescent beads, provide rather approximate measurements of shear or require a complex optical setup. The method presented is accurate, relies on simple image analysis, and does not require a specimen. We provide a succinct and accurate description of properties of Nomarski prisms to explain the rationale behind the method. © 2010 Optical Society of America

OCIS codes: 180.3170, 110.2960, 110.2990, 110.4980.

## 1. Introduction

A differential interference contrast (DIC) microscope is a polarization-based wavefront-shearing interferometer that allows use of a large illumination aperture for imaging transparent specimens [1,2]. In contrast to spatially coherent phase imaging methods, large illumination aperture (i.e., *partially coherent illumination*) leads to high lateral resolution, depth sectioning, and lack of speckle noise. Although DIC was developed as a qualitative imaging method, it has been extended to provide semiquantitative and quantitative information about the phase distribution (i.e., optical path length) of the specimen [3–7]. Quantitative analysis with DIC necessitates development of its image formation model and methods of calibrating experimental systems. In this paper, we develop an accurate calibration procedure that relies on intensity measurements performed in the

back focal plane of the objective. To explain the rationale of the method, we review the properties of the Nomarski prism, which is a key component of the DIC microscope.

DIC's optical train, in the configuration due to Nomarski, employs four polarization-sensitive components: two Nomarski prisms that sandwich the specimen, which are in turn sandwiched by a pair of crossed polarizers. The schematic layout of the DIC microscope can be found in several references [1,2]. The discussion in this paper is based on the schematic presented in Fig. 1(a) of Ref. [8] and related description of image formation in DIC. The following abbreviations are used to refer to different components of a DIC microscope:

- OPrism: objective-side Nomarski prism.
- CPrism: condenser-side Nomarski prism.
- BFP: objective back focal plane where the fringes produced by OPrism are effectively localized.

The concept of fringe localization is reviewed in Appendix A.

- FFP: condenser front focal plane where the fringes produced by CPrism are effectively localized.

Also, we use the terms point source, spatially coherent source, and coherent illumination interchangeably to imply a condenser FFP closed down to a point on the optical axis. The term partially coherent illumination/partially coherent source refers to a source of finite size consisting of individually incoherent point sources. Unless specified, the term partial coherence should not be confused to imply a source having large emission bandwidth, i.e., partial temporal coherence.

The key parameters of the DIC microscope and the symbols that we use to represent them are as follows:

- Objective shear ( $2\Delta$ ): the separation in the specimen plane between foci of the sheared imaging beams in the specimen plane.
- Condenser shear ( $2\Delta_c$ ): the separation in the specimen plane between points that are illuminated coherently.
- Bias ( $2\phi$ ): constant relative phase shift introduced between sheared beams.
- Numerical aperture (NA) of imaging path ( $\text{NA}_{\text{obj}}$ ).
- Numerical aperture of illumination path  $\text{NA}_{\text{con}}$ . The coherence ratio,  $S = \text{NA}_{\text{con}}/\text{NA}_{\text{obj}}$ , determines coherence of the imaging system, and a higher value of  $S$  implies reduced coherence in the specimen plane.
- Average wavelength of quasi-monochromatic illumination ( $\lambda$ ).
- Relative strengths of sheared beams determined by the angle between transmission axes of the polarizers. In this paper, we assume that the polarizers are crossed, which leads to beams of equal strength.

To facilitate quantitative analysis, a quasi-monochromatic source is assumed throughout the paper and experimentally created by placing an interference filter (Olympus IF 550) between the halogen lamp and the condenser.

The effects of shear, bias, imaging NA, and relative strength of beams have been studied by various researchers over the past three decades [9–12], *assuming coherent illumination*. Assumption of coherent illumination allows use of mathematically tractable linear image formation models, but ignores the fact that DIC employs a large illumination NA and an incoherent source. An illumination from an incoherent source through a large NA leads to partially coherent illumination at the specimen. While coherent image is related linearly to the specimen transmission, a partially coherent image depends bilinearly [13,14] on the specimen transmission. By bilinear dependence, we imply that the image intensity at any given point is a function of the specimen transmission at *pairs of points*. Equivalently, spatial frequencies observed in the image depend not only on the specimen

spatial frequencies but also on mixing of pairs of specimen spatial frequencies. Owing to the complexity of the partially-coherent model, the role of the illumination path in DIC has been clarified relatively recently. Sheppard and Wilson, and Cogswell and Sheppard [15,16], proposed a DIC model assuming equal  $\text{NA}_{\text{con}}$  and  $\text{NA}_{\text{obj}}$ , but took into account shearing due to both prisms. Preza [17] studied effects of illumination geometry assuming that the specimen is imaged with a point-spread function, which is a coherent difference of spatially and phase-shifted replicas of the bright-field point-spread function. However, as explained in Ref. [8], Preza's model failed to take into account the role of CPrism ([17], figure 3). Mehta and Sheppard [8] corrected this assumption to take into account effects of both prisms as well as general illumination geometry (e.g., slit and varying  $\text{NA}_{\text{con}}$ ).

Our model elucidated that the DIC microscope with both prisms images an effective transmission that is the coherent difference of spatially and phase-shifted replicas of the *specimen's transmission*. In contrast, Preza's model shears the PSF of the imaging path, which amounts to modeling the so called Köhler-DIC setup noted in Ref. [8]. We have developed a general phase-space model, termed a phase-space imager (PSI) that allows efficient computation [18] of partially coherent images. With help of a phase-space imager we have compared resolution and contrast in five phase microscopy methods [19].

Employing any of the above image formation models for image calculation, instrument design, or reconstruction requires measurement of the key parameters mentioned earlier.  $\text{NA}_{\text{obj}}$ ,  $\text{NA}_{\text{con}}$ , and  $\lambda$  are usually specified. If bias is introduced by translation of either prism and not by a calibrated method such as de Sénarmont compensation, it needs to be measured. Shear introduced by the OPrism is usually not specified by manufacturers and has to be measured. A few approaches have been proposed for measurement of shear of OPrism using a calibrated specimen [11,20]. These approaches either do not provide accurate measure of shear or require complex experimental procedure (as discussed in Section 4). Moreover, they do not allow estimation of bias or the shear of CPrism.

Since the Nomarski prisms lead to interference fringes in the objective BFP, there should be a way of measuring shear and bias *without a specimen*. In this paper, we present such an approach based on image analysis of the intensity pattern in the BFP, evaluate its accuracy, and discuss the effects of noise and systemic errors.

The rest of the paper is organized as follows. Section 2 and the related Appendix A provide a succinct and accurate review of properties of Nomarski prisms used in DIC. Section 3 provides a description of the experimental setup used in this paper. The same section discusses the measurement of shear with a carefully constructed benchtop setup, which provides a benchmark for measurements performed

with our relatively simple approach. Section 4 discusses accuracy of approaches for measurement of shear that use either a subresolution phase or a subresolution fluorescent specimen. Section 6 then describes our acquisition and image processing algorithm for measuring shear (in normalized units of  $\lambda/\text{NA}_{\text{obj}}$ ) and bias. Evaluation of the accuracy of the specimen based methods and our method is carried out in Section 7. The same section also discusses effects of various sources of noise and systemic errors. Section 8 concludes the paper with a discussion of effects of dispersion, alternative approaches that we tried, and a summary of results.

## 2. Basic Properties of the Nomarski Prism

It is useful to recall the basic features of the Nomarski prism in order to appreciate the calibration procedures described in this paper. DIC setups that use a coherent source can be implemented with the help of a grating [1,21] or spatial light modulator [22]. Special properties of the Nomarski prism bestow the DIC setup with the capability of high-contrast shearing interferometry even with a source that is spatially partially coherent (i.e., a source of finite physical extent) and temporally partially coherent (i.e., a source having a large emission spectrum or a white-light source). The reader is referred to Appendix A for an explanation of how the coherence of the source affects the interference fringes produced by the Nomarski prism. The key observations drawn from the appendix are the following: (1) With a partially coherent source, the fringes produced by the OPrism are localized in the objective BFP. Therefore one should carefully focus at BFP when measuring the fringe intensity. (2) In absence of dispersion, the prism introduces constant angular shear to all wavelengths, resulting in fringes whose period varies linearly with the wavelength. Consequently, the contrast of fringes recorded with a white-light source is lower than the fringes recorded with a quasi-monochromatic light. Therefore, use of quasi-monochromatic illumination is important for recording the fringes.

Using a *collimated beam of monochromatic light*, the shear introduced by the Nomarski prism (or any other birefringent angular beam splitter) can be determined by measuring the period of the interference fringes with respect to the wavelength (see figure 1.79 of [23]) with a benchtop optical setup as per the following relationships.

As discussed in Appendix A, the relationship between the period of the fringe ( $P$ ) and the angular shear ( $2\epsilon$ ) caused by the prism is

$$P = \frac{\lambda/2}{\tan(\epsilon)} \simeq \frac{\lambda}{2\epsilon}. \quad (1)$$

Typically, the shear angles used by Nomarski prisms are so small that even though wavelengths are of the order of hundreds of nanometers, the fringe periods are of the order of a few millimeters.

It is worth noting that only the OPrism causes shearing interferometry, and the CPrism provides coherent illumination required to achieve good contrast ([8], figures 1 and 6). This fact can be easily verified by acquiring images of small beads with either OPrism or CPrism inserted in the bright-field light path. As shown in Fig. 1, only the OPrism causes blurring of the bright-field image of beads due to shear. Therefore one should measure the shear of OPrism for use in image calculation or phase retrieval. On our microscope, we found that the fringes of the CPrism imaged in the BFP were slightly narrower than those produced by OPrism but do not cause significant reduction in image contrast.

When OPrism is placed in the BFP, we achieve shear of  $2\Delta$  in the specimen plane. Angular and lateral half-shears are related by

$$\Delta = \tan(\epsilon)f_o = \frac{\lambda f_o}{2P}, \quad (2)$$

where  $f_o$  is the focal length of the objective.

However, with partially coherent illumination and imaging, the *relative size of shear and the imaging aperture* becomes important. As evident from forward image formation analysis in [8,16], one needs to know the amount of shear normalized with respect to  $\lambda/\text{NA}_{\text{obj}}$ . The algorithm presented in this paper measures this quantity. Once the shear is measured in this normalized unit, physical shear can be determined for a given wavelength and objective. In the following, we use the term “shear” to refer to both full-shear  $2\Delta$  and half-shear  $\Delta$  both, with the meaning implied by the context.

## 3. Experimental Setup and Benchmark for Measurements

We have used an Olympus BX61 motorized microscope equipped with strain-free optics and a Qimaging Retiga Exi cooled-CCD camera with a dynamic range of 12 bits. To image the BFP, a Bertrand lens attachment available from Olympus (U-CPA) is used. The motorized parts of the microscope and the

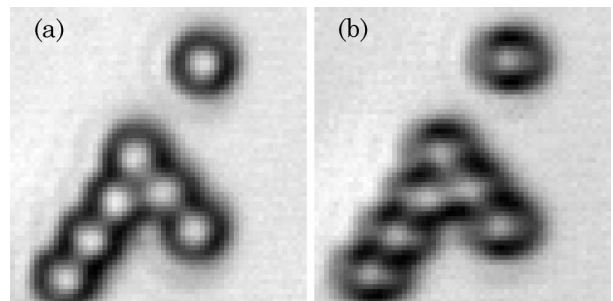


Fig. 1. Only with the OPrism does one observe blurring effect of the shear on bright-field images of beads: images of 780 nm diameter polystyrene beads from Micro-particles GmbH (courtesy Bai Jianhao from National University of Singapore), obtained with (a) only the CPrism or (b) only the OPrism in the bright-field light path. Neither polarizer was inserted in the light path. Direction of shear is along the horizontal.



camera are controlled with open-source image acquisition package  $\mu$ manager (<http://www.micro-manager.org>). We developed the driver software for the BX61 microscope controller in collaboration with the  $\mu$ manager development team using the documentation provided by Olympus, Inc. The driver is available with the  $\mu$ manager package. For results presented in this paper, we have used three strain-free objectives from the Olympus UPlanSApo series:  $20 \times 0.75$  NA,  $40 \times 0.9$  NA, and  $40 \times 0.6$  NA. We use an Olympus universal condenser (UCD8) with a motorized aperture stop and a dry top-lens (U-TLD) that provides illumination NA in the range of 0.3–0.9. When acquiring the images of the BFP, we always use matched illumination (i.e., the condenser aperture stop opened so as to match the objective aperture). Our microscope uses a single prism with moderate amount of shear (U-DICTS) as OPrism. The system employs different CPrisms placed in the condenser turret tailored to the spatial-shear produced by the fixed OPrism and changing focal length of the objective. To adjust the bias, de Sénarmont compensation [24] was employed by placing a quarter wavelength plate between the OPrism and a rotatable analyzer. The rotatable analyzer carries accurate markings to allow calibrated adjustment of the bias. For image processing and data analysis, MATLAB (version 2008a) is used. In the following text, typewriter font indicates MATLAB functions used for specific tasks. For experimental evaluation of the phase-specimen or fluorescent-specimen based methods of measuring shear described in Section 4, we used beads of 175 nm diameter (PS-Speck fluorescent point source kit, Invitrogen). We chose bright fluorescent beads so that they are easier to locate with fluorescence contrast. We chose the beads that fluoresce in the blue region so that green (550 nm) illumination used for transmission imaging does not excite fluorophores. The beads were difficult to image with DIC when immersed in an index matching mounting medium, and hence were immersed in water after carefully drying on a coverslip. Even after that, the contrast in the DIC image of the beads was rather poor, and noise from the camera made it difficult to distinguish the intensity variation. Therefore, we averaged 100 images acquired with burst mode of the camera to achieve better signal to noise ratio (SNR). Note that earlier researchers have used larger beads [5,17] because of the difficulty of imaging very small beads.

The magnification provided by the objective is  $M = f_l/f_o$ , where  $f_l$  and  $f_o$  are focal lengths of the tube lens and the objective, respectively. Substituting for  $f_o$  in Eq. (2), angular shear can be calculated as

$$\varepsilon = \arctan\left(\Delta \frac{M}{f_l}\right) = \arctan\left(\Delta_n \frac{\lambda}{\text{NA}_{\text{obj}}} \times \frac{M}{f_l}\right), \quad (3)$$

where  $\Delta_n$  is the shear in normalized units of  $\lambda/\text{NA}_{\text{obj}}$ .  $\Delta_n$  is the quantity that we measure. Olympus micro-

scopes with infinity-corrected optics use  $f_l = 180$  mm. For results presented in Sections 6 and 7, we use quasi-monochromatic illumination with  $\lambda = 550$  nm. Substituting for  $\lambda$  and  $f_l$  in Eq. (3), we obtain an expression for angular shear in terms of the magnification and NA of the objective for our Olympus microscope:

$$\varepsilon = 3.056 \times 10^{-6} \Delta_n \frac{M}{\text{NA}_{\text{obj}}}. \quad (4)$$

#### A. Measurement of Angular Shear with Benchtop Setup

To provide an independent benchmark for shear measured on the microscope, we measured the angular shear with normally incident monochromatic light using the benchtop setup shown in Fig. 2(a). Light produced by laser diode (Edmund Optics NT59-088) with emission wavelength of 650 nm was focused with a 30 mm focal-length lens and spatially filtered with a pinhole. The sidelobes of the beam expanding from the pinhole still retained inhomogeneities and hence were cropped using a beam stop. The lens (focal length 300 mm) placed 300 mm away from the pinhole was followed by a beam expander (Thorlabs BE10M) to eventually provide a normally incident plane wave. The optical axes of the cemented birefringent wedges in the Nomarski prism were carefully oriented toward horizontal and vertical. The transmission axes of the polarizer and the analyzer were set at  $45^\circ$  to the horizontal and were mutually crossed. The above directions are in the plane normal to the direction of propagation of the light. A camera (Qimaging Retiga Exi) with a pixel size of  $6.45 \mu\text{m}$  and sensor geometry of  $1360 \times 1036$  pixels was placed right after the analyzer to record the interference fringes.

The recorded fringes are shown in Fig. 2(b), which contain high-frequency coherent noise due to scattering from dust and imperfections in the light path. The log spectrum of the recorded fringe shows a bright circular feature corresponding to the highest spatial frequencies recorded. The horizontal fringe gives rise to the bright line in the log spectrum along the horizontal. We know *a priori* that the fringes produced by the OPrism have low frequency along the horizontal and are constant along the vertical. Most of the energy of the fringes is concentrated at bright pixels at the center of the spectrum. We filter the spectrum with a low-pass rectangular mask, shown by a black line in Fig. 2(c). Inverse Fourier transforming the filtered spectrum gives smooth fringes shown in Fig. 2(d). We average the image shown in Fig. 2(d) along the vertical to obtain a profile shown in Fig. 2(e) that represents average shear introduced by the OPrism. The averaged data is normalized to unity and then fit to a squared sinusoid using MATLAB's nonlinear least squares curve-fitting tools (using the function `fit`). The expression to which the data were fit is as follows:

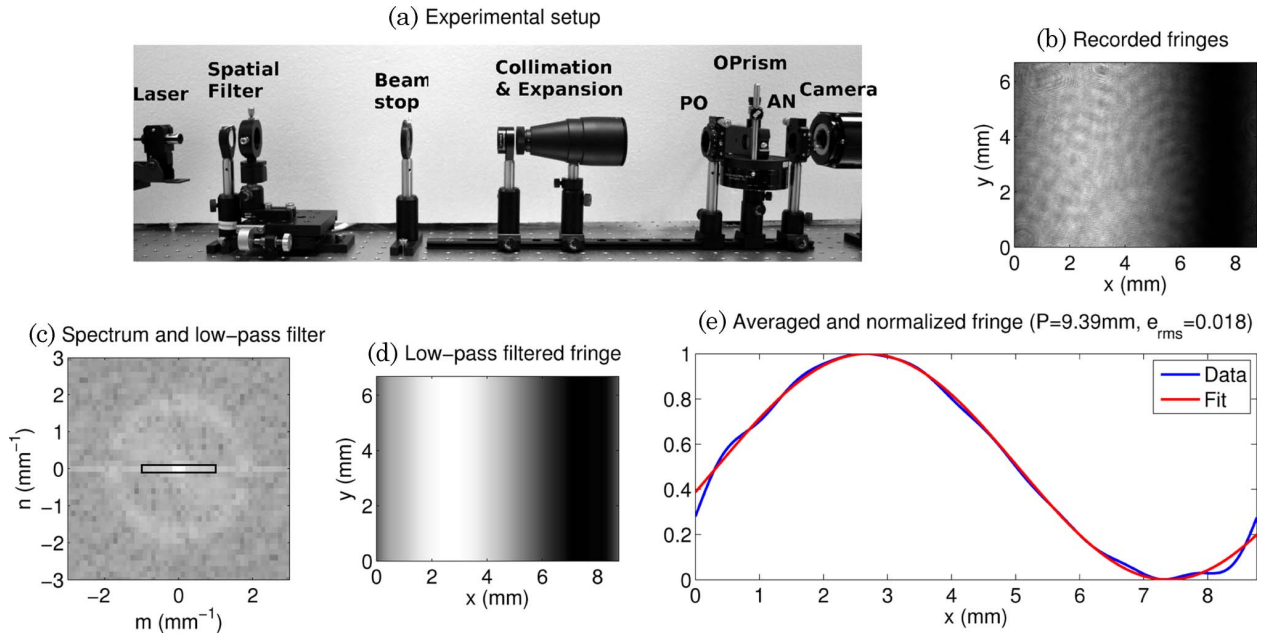


Fig. 2. (Color online) Measurement of angular shear of our DIC prism using monochromatic illumination with a carefully aligned benchtop setup. PO is the polarizer and AN is the analyzer.

$$f(x) = \frac{1}{2} \left[ 1 + \cos \left( 2\pi \frac{x}{P} - \alpha \right) \right]. \quad (5)$$

The variable  $x$  represents the spatial distance on the CCD chip, and the parameter  $\alpha$  allows the fitting routine to translate the sinusoid to match the experimental data.  $P$  is the period of the fringe that we need to estimate. As noted in Fig. 2(e) the period was measured to be 9.39 mm. The rms error ( $e_{\text{rms}}$ ) of the fit was 1.8% only. Substituting  $\lambda = 0.65 \mu\text{m}$  and  $P = 9.39 \times 10^3 \mu\text{m}$  in Eq. (1), we obtain the following value of the angular half-shear,

$$\varepsilon_r = 3.46 \times 10^{-5}. \quad (6)$$

While the benchtop setup requires an effort of constructing a properly aligned light path, our approach makes use of the prealigned light path present in the microscope. Additionally, our approach employs a partially coherent source, which provides immunity against coherent noise introduced by imperfections in the light path.

Since our Olympus setup employs a single OPPrism for all objectives, the angular shear computed from different measurements must be the same. Conversely, once the angular shear of the OPPrism is measured, one should be able to compute the spatial shear for any objective from its focal length. We use this fact to verify that the presented method measures the shear correctly. Note that the shear measurements carried out in the rest of the paper are at 550 nm wavelength. It is expected that the dispersion of the components causes slightly different angular shear at 550 nm in comparison to 650 nm.

#### 4. Evaluation of Specimen-based Methods

van Munster [11] suggested that the image of a small bead (a subresolution phase specimen) will have bright and dark peaks separated approximately by the shear at a bias of  $2\phi = \pi/2$ . This method has been used by quite a few researchers to estimate shear [5,17]. However, this method is inaccurate, because the location of peaks in the DIC image of a subresolution phase specimen is affected by factors other than shear. This behavior is explained below with help of a simulation presented in Fig. 3 and related Media 1, as well as experimental results of Figs. 4 and 5.

A DIC microscope with two prisms effectively images a coherent difference of shifted (in space and phase) replicas of the specimen's transmission ([8], equation (7)). Assuming the specimen transmission to be  $t(x,y)$ , the DIC microscope images an effective transmission given by

$$t_D(x,y) = t(x + \Delta, y)e^{-i\phi} - t(x - \Delta, y)e^{i\phi}. \quad (7)$$

The bead, being a phase specimen, is described by a complex transmission function  $t(x,y)$ , whose phase is the optical path length of the bead. We assume a subresolution bead (smaller than  $0.61\lambda/\text{NA}_{\text{obj}}$ ) whose effective transmission is shown in Figs. 3(a) and 3(b). The parameters of the bead and imaging system are noted in the figure caption. It is worth noting that, for any bias, the separation between the maxima and minima of the phase of the  $t_D(x,y)$  is  $2\Delta$  only if  $2\Delta \geq R$ , where  $R$  is the radius of the bead.

Each point of the condenser,  $P_c(\xi, \eta)$ , illuminates the specimen by an oblique plane wave, expressed by  $e^{i2\pi(\xi x + \eta y)}$ . Thus, off-axis points, i.e.,  $(\xi, \eta) \neq (0, 0)$ ,

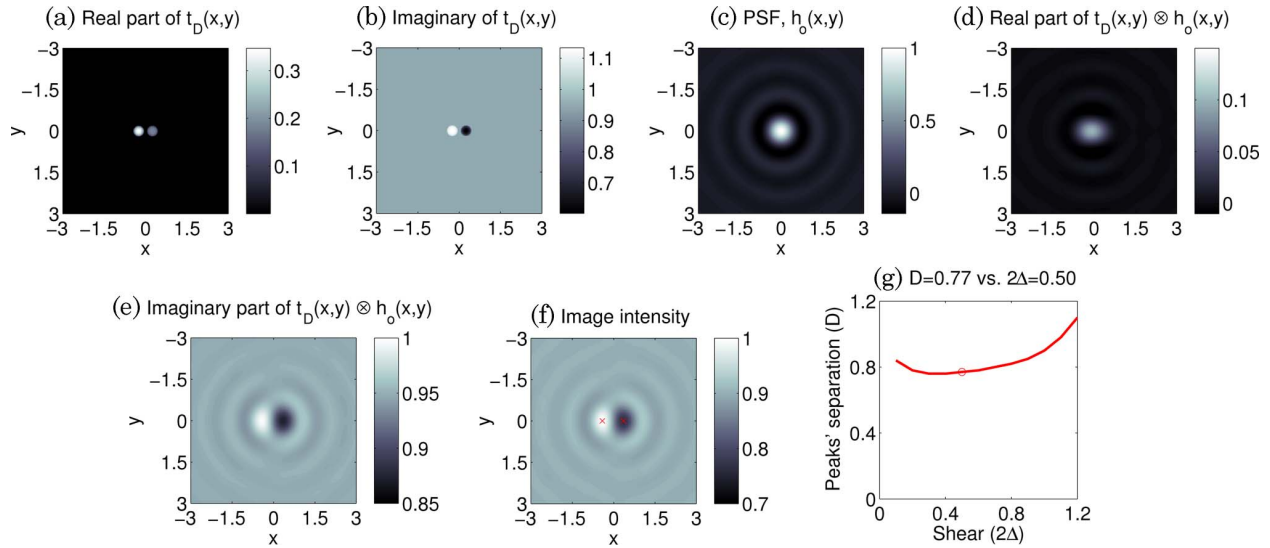


Fig. 3. (Color online) DIC image of a bead due to the central point of the condenser aperture: a snapshot from an image sequence (Media 1) showing computed images and their peaks at different shears. All coordinates are in the normalized units of  $\lambda/\text{NA}_{\text{obj}}$ . The bead is assumed to have a diameter of 0.4, RI of 1.59, and is immersed in water (RI 1.33). For the purpose of calculating the optical path length of the bead, the wavelength is assumed to be  $0.55 \mu\text{m}$ ; (a) and (b) are real and imaginary parts of the effective transmission  $t_D(x,y)$ , (c) is the amplitude PSF of the aberration-free system (i.e., jinc function), (d) and (e) are real and imaginary parts of the amplitude image produced by convolution of the transmission and the PSF, (f) is the image intensity, and (g) is the plot of shear versus distance between peaks in the image. The markers in (f) identify the peaks of the image. The bias is assumed to be  $\pi/2$  at all shears. Note that the color maps of the different plots are adjusted to allow clear display of data. In particular, the imaginary part of the image is an order of magnitude stronger than the real part.

of the condenser aperture contribute a phase slope of  $e^{i2\pi(\xi x + \eta y)}$  to the effective transmission. The effective transmission due to each condenser point, given by  $e^{i2\pi(\xi x + \eta y)} t_D(x,y)$ , is convolved with the amplitude PSF of the imaging light path,  $h_o(x,y)$ . The intensity image produced by each condenser point is therefore given by

$$I_{(\xi,\eta)} = |e^{i2\pi(\xi x + \eta y)} t_D(x,y) \otimes h_o(x,y)|^2. \quad (8)$$

Note that the peaks of the magnitude of the above convolution are not necessarily located at peaks of the phase of  $t_D(x,y)$ . The phase slope due to off-axis illumination and the convolution by the imaging PSF, when combined, can result in peaks not being separated by the shear distance in the image of the bead produced by each condenser point. In Fig. 3, we assume coherent illumination, and consequently the effective transmission is simply  $t_D(x,y)$ . Figure 3(c) shows the amplitude PSF of the bright-field setup whose radial profile is given by  $2J_1(v)/v$ , where  $v = 2\pi x \lambda / \text{NA}_{\text{obj}}$  is the normalized optical coordinate. The real and imaginary parts of the amplitude image,  $t_D(x,y) \otimes h_o(x,y)$ , are shown in Figs. 3(d) and 3(e), respectively. The intensity image (magnitude square of the amplitude) is shown in Fig. 3(f).

We compute the intensity image for varying shear, results of which are shown in Media 1 for shears ranging from 0.1 to 1.2. The distance ( $D$ ) between peaks in the intensity image is plotted against the shear  $2\Delta$  in Fig. 3(g). As can be clearly seen from

Media 1, the peak separation in the DIC image is usually larger than the shear when small shears typical of experimental DIC setups are used. Due to complex image formation, the peak separation is nonlinearly dependent on shear. This explains a surprising observation from Fig. 3(g) that peak separation may reduce when shear is increased, when coherent illumination is used.

The true DIC image of the bead is the sum of images produced due to all condenser points. Thus, a partially coherent DIC image is given by

$$I_{\text{DIC}}(x,y) = \iint |P_c(\xi,\eta)|^2 I_{(\xi,\eta)}(x,y) d\xi d\eta. \quad (9)$$

The results of Fig. 3 were computed assuming coherent illumination for the sake of computational efficiency. Nevertheless, they illustrate that the distance between peaks in a DIC image is not a proper measure of the shear, since image formation of a phase specimen is related in a complex manner with settings of the imaging system. A valid but rather complex approach of estimating the shear would be to compute a partially coherent 2D image at different shears and design an appropriate surface fitting algorithm to fit the experimental data. Partially coherent image computation for DIC is discussed in section 4 of [19].

We corroborate the above analysis with two experimental results. First, when imaging a subresolution phase specimen, changing the condenser aperture introduces an easily visible change in the size of and

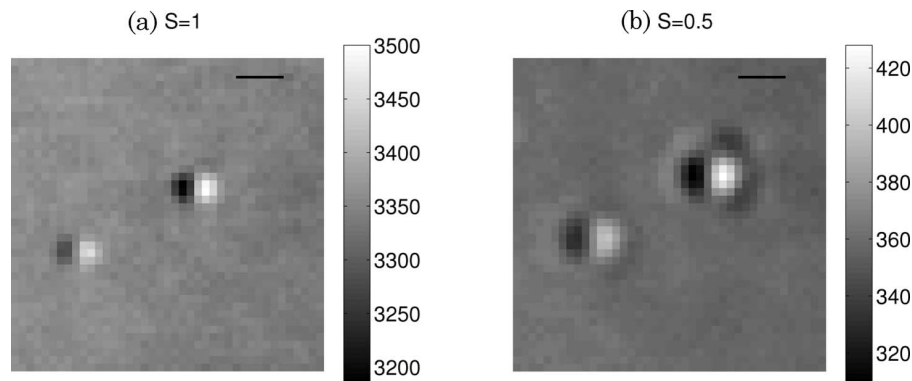


Fig. 4. Distance between peaks in the image of a subresolution phase specimen is dependent on the size of the illumination aperture: DIC images of  $170\text{ }\mu\text{m}$  diameter PS-Speck beads acquired with quasi-monochromatic light of  $550\text{ nm}$  wavelength using a  $40\times 0.6$  NA objective,  $\pi/2$  bias, and (a)  $S = 1$  as well as (b)  $S = 0.5$ . Since the specimen had weak phase information, we averaged 100 images acquired in burst mode to obtain a good SNR. The scale bar is  $1\text{ }\mu\text{m}$ .

distance between peaks as shown in Fig. 4. The second but less visible effect is that the distance between the peaks remains nearly the same across a range of biases, since a subresolution bead is a weak specimen. A corresponding experimental result is presented in Fig. 5. We observe that distance between peaks at all three biases is nearly the same, and the contrast of the image reduces as bias is increased. These experimental results (as well as theoretical analysis in [16]) show that for a specimen having a small range of phase variation, small bias suffices for linear imaging of the gradient. Therefore the notion that bias ( $2\phi$ ) of  $\pi/2$  has to be used is not really valid, because better contrast is obtained for smaller bias values for weak phase specimens. From images of Fig. 5, we find that distance between peaks is  $0.49\text{ }\mu\text{m}$ . In normalized unit, shear  $2\Delta$  is  $0.53\lambda/\text{NA}_{\text{obj}}$ . According to Eq. (4),  $\Delta_n = 0.265$  leads to angular shear of  $\varepsilon = 5.4 \times 10^{-5}$ , which is 56% larger than direct measurement of Eq. (6). Thus, experimental data corroborate the above analysis that the peak distance typically overestimates the shear.

Since the complex interaction of the phase specimen and partially coherent imaging system confounds the distance between peaks, it is tempting to investigate the possibility of measuring the shear

by estimating peak distance in the image of a *subresolution fluorescent bead*. Since fluorescence imaging is incoherent and described by a linear model, analysis of acquired data is simpler. We imaged the PS-Speck beads described earlier by inserting only the OPrism in the light path with three objectives of interest. The images are shown in Fig. 6. Note that both illumination and emission are sheared by the OPrism. The role of illumination is to provide uniform intensity at the specimen plane, which is not affected by the shear. The fluorescence emitted by the bead is unpolarized. In the imaging path, the OPrism splits the fluorescence in two orthogonal polarizations that match its crystal axes; however, both of these beams are mutually incoherent. This gives rise to an *incoherent sum of the shifted images of the bead* due to shear of the OPrism. The image is effectively the same as that produced by two closely spaced fluorescent beads separated by the distance equal to the shear of the OPrism. Therefore small shears cannot produce two separate peaks as seen for the  $40\times 0.6$  NA objective in Fig. 6(c). This point is explained by simulating DIC images of a subresolution fluorescent specimen at different shears. Figure 7 and associated Media 2 show how the distance between peaks observed in the DIC image of a

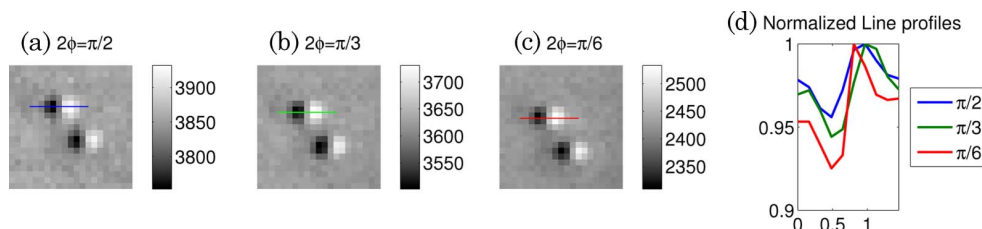


Fig. 5. (Color online) Distance between peaks in the image of a subresolution phase specimen is nearly independent of the bias: (a), (b), and (c) are raw images of PS-Speck beads acquired with a  $40\times 0.6$  NA objective and matched illumination at bias ( $2\phi$ ) of  $\pi/2$ ,  $\pi/3$ , and  $\pi/6$ , respectively. The color bar next to images shows that, while the image shape does not change much, contrast reduces at larger bias values. (d) shows normalized line profiles through the center of beads and clarifies the previous point. Pixel width is  $6.45/40\text{ }\mu\text{m}$ . The distance between peaks in all images is  $0.49\text{ }\mu\text{m}$ . Since the specimen had weak phase information, we averaged 100 images acquired in burst mode to obtain good SNR.



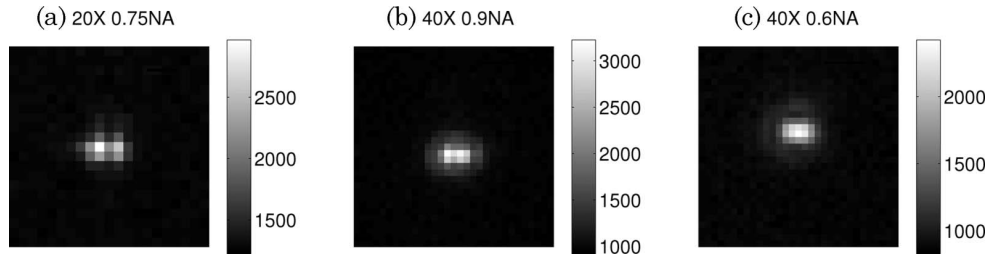


Fig. 6. Images of fluorophores under (a)  $20 \times 0.75$  NA, (b)  $40 \times 0.9$  NA, and (c)  $40 \times 0.6$  NA objectives obtained with only the OPrism inserted in the light path.

subresolution fluorescent specimen changes as the shear is changed. To compute the image shown in Fig. 7(a), we simply took a sum of two Airy disks separated by shear. Up to the shear of  $2\Delta = 0.45\lambda/\text{NA}_{\text{obj}}$ , the image does not have separate peaks. Even when two peaks are detected, incoherent imaging of a fluorescent specimen leads to an overestimate of the shear, when the shear is below Rayleigh resolution limit, i.e.,  $2\Delta < 0.61\lambda/\text{NA}_{\text{obj}}$ .

The curves of Figs. 3(g) and 7, which show peak separation at varying shears, appear surprisingly different. However, they are expected to be very different due to the type of specimen imaged and different coherence of the imaging process. It is known that a phase specimen imaged coherently behaves very differently from an incoherently imaged self-luminous specimen [25].

Recently, a relatively precise but complex approach based on dual-focus fluorescence correlation spectroscopy (2fFCS) has been demonstrated [20]. In this method, the Nomarski prism is used to produce two overlapping focal volumes for an FCS measurement. The diffusion coefficient of calibrated monodisperse fluorescent beads measured with 2fFCS is compared to that measured by dynamic light scattering (DLS). This comparison allows measurement of shear in the sample plane at a given wavelength. This approach requires recourse to a precisely calibrated specimen and a complex experimental setup to characterize the Nomarski prism.

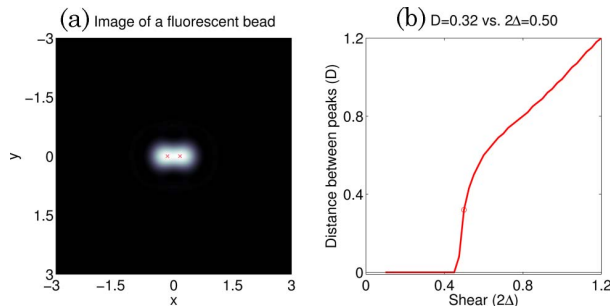


Fig. 7. (Color online) Snapshot from an image sequence (Media 2, 1.5 MB) shows (a) the computed image of a subresolution fluorescent bead under the DIC microscope at shear of  $2\Delta = 0.5$  and (b) the relationship between the distance between peaks in the image and the shear. The markers in (a) identify the peaks of the image.

## 5. Image of the Objective Back Focal Plane

In contrast to the above methods, the approach presented in this paper does not use any specimen and is based on the model of the fringes produced by the Nomarski prism within the BFP. Moreover, methods described in Section 4 are not useful in calibration of the bias. Dana has shown that when a sliding Wollaston prism is used to adjust the bias, it is possible to calibrate the position of the prism in terms of the bias by measuring the variation in intensity of background (i.e., the region of uniform optical path length) ([26], subsection 3.1.3). The method presented in this paper allows direct estimation of shear and bias from images acquired at the BFP.

The key idea behind our image analysis algorithm is that the normalized shear can be calculated by measuring the period of the interference fringes relative to the size of the BFP. The algorithm consists of (a) imaging the objective BFP with and without the interference fringes produced by the OPrism, (b) estimating the size (in pixels) of the BFP, and (c) estimating the shear by fitting the equation of the image of the BFP to measured data.

When only the OPrism is in the light path between crossed polarizers (configuration called Köhler-DIC in [8]), it introduces an optical path difference varying linearly across the BFP between the two orthogonally polarized beams it produces. When these beams pass through analyzer, the sinusoidal fringes are produced in the BFP. However, when both prisms are inserted in the light path, the CPrism compensates the optical path differences and the BFP appears dark, except for the Maltese cross caused by depolarization due to focusing of light [23].

As discussed in Appendix A, the fringes produced due to different condenser points are nearly the same in the BFP, i.e., plane of localization. When one focuses away from the BFP using a Bertrand lens under partially coherent illumination, one can observe the blurring of the fringes. Thus, the intensity recorded at BFP has the same profile irrespective of the coherence of illumination. Next, we model the fringe profile assuming coherent illumination. In the Köhler-DIC setup with coherent illumination, the amplitude produced in the objective BFP is given as [[8], equation (3)]

$$P_{\text{DIC}}(\xi, \eta) = iP_{\text{BF}}(\xi, \eta) \sin(2\pi\xi\Delta - \phi). \quad (10)$$

Therefore the intensity recorded in the BFP is given by

$$|P_{\text{DIC}}(\xi, \eta)|^2 = |P_{\text{BF}}(\xi, \eta)|^2 \sin^2(2\pi\xi\Delta - \phi), \quad (11)$$

where  $\xi$  and  $\eta$  are pupil variables expressed in units of  $\text{NA}_{\text{obj}}/\lambda$ , which represents the coherent spatial-frequency cutoff of the imaging system. In this normalized unit, the radius of the objective pupil is 1. Since the source is imaged at the back-focal plane, the bright-field pupil may have variations that affect the fringes. Therefore one should normalize the image of the BFP obtained with OPrism with an image of the bright-field BFP to retrieve the interference fringes,

$$\begin{aligned} \sin^2(2\pi\xi\Delta - \phi) &= \frac{1}{2} [1 - \cos(4\pi\xi\Delta - 2\phi)] \\ &= \frac{|P_{\text{DIC}}(\xi, \eta)|^2}{|P_{\text{BF}}(\xi, \eta)|^2}. \end{aligned} \quad (12)$$

From Eq. (12), we notice that the frequency of the recorded fringes is  $2\Delta$  in normalized  $(\xi, \eta)$  coordinates, e.g., if  $2\Delta = 0.5\lambda/\text{NA}_{\text{obj}}$ , exactly one period of the interference fringes will fit inside the BFP since the BFP has the normalized diameter of 2.

## 6. Algorithm for Estimating the Shear and Bias

We describe the acquisition and analysis algorithm in four stages, labeled (a)–(d) in the following discussion. Each subfigure of Fig. 8, also labeled (a)–(d), shows results obtained at a given stage of the algorithm.

### A. Acquisition of BFP Images, $|P_{\text{BF}}|^2$ and $|P_{\text{DIC}}|^2$

As bias is changed, different parts of the fringe appear in the BFP as observed in Media 3. Figure 8(a) shows a snapshot at  $2\phi = 0$ . Since the peak of the fringe is observable in the BFP at  $2\phi = \pi$ , we set camera exposure at that setting to fill the dynamic range of the camera. We acquire  $|P_{\text{DIC}}|^2$  at this exposure using bias values at an interval of  $\pi/6$  in the range 0 to  $2\pi$ .  $|P_{\text{BF}}|^2$  is acquired separately to fill up the dynamic range of the camera. As can be seen from the  $|P_{\text{BF}}|^2$  image, the illumination aperture is not of uniform intensity. A magnified image of a filament of the halogen lamp is projected in the FFP, which is perceivable as bright region oriented at  $45^\circ$ . Additionally, stronger Fresnel reflections near the periphery of the lenses cause a drop in intensity at the periphery of FFP.

### B. Preprocessing and Registration of $|P_{\text{BF}}|^2$ and $|P_{\text{DIC}}|^2$

We encountered two experimental difficulties in retrieving normalized fringes: presence of debris [which causes spurious contrast when  $|P_{\text{DIC}}|^2$  is divided by  $|P_{\text{BF}}|^2$  as per Eq. (12)] and slight translation

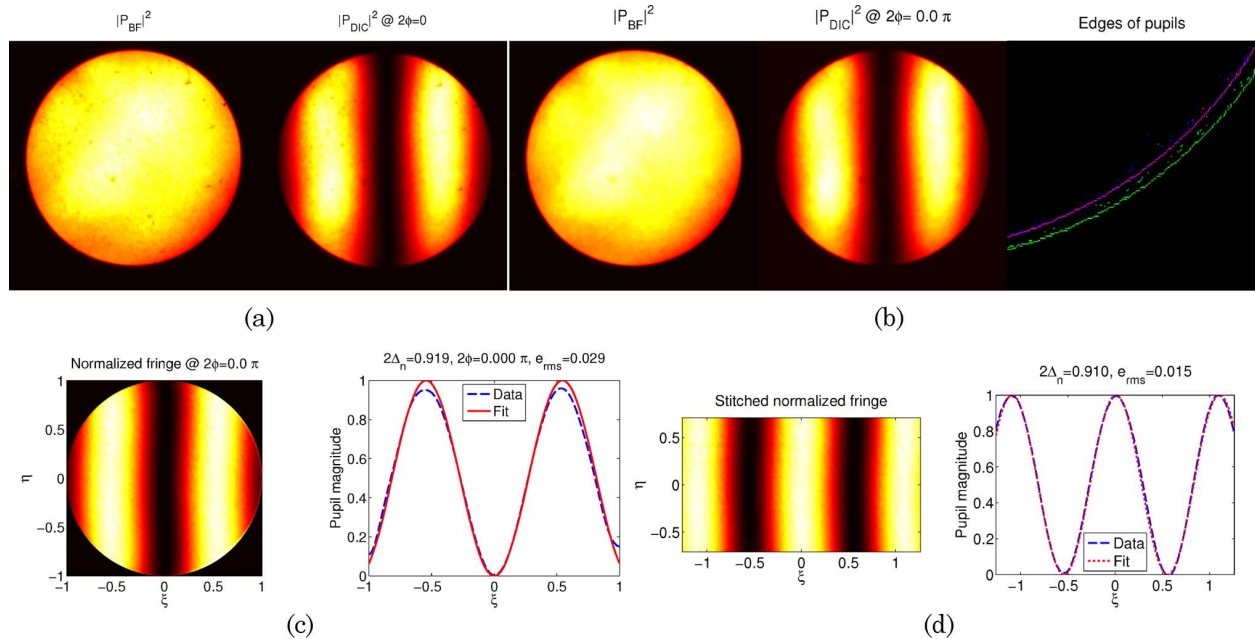


Fig. 8. (Color online) Steps involved in accurate estimation of the shear and bias of OPrism by processing the images acquired at the BFP: (a)  $|P_{\text{BF}}|^2$  is the recorded intensity of bright-field BFP,  $|P_{\text{DIC}}|^2$ , a snapshot from an image sequence (Media 3, 748 KB) is the recorded intensity of the fringes produced due to OPrism at given bias. (b) Snapshot from an image sequence (Media 4, 1233 KB) shows preprocessing steps to remove the artifacts due to debris and to register  $|P_{\text{DIC}}|^2$  with  $|P_{\text{DIC}}|^2$ . The red, green, and blue pixels in the rightmost panel show the edges of  $|P_{\text{BF}}|^2$ , acquired  $|P_{\text{DIC}}|^2$ , registered  $|P_{\text{DIC}}|^2$ , respectively. (c) Snapshot from a sequence (Media 5, 1389 KB) shows (left panel) the normalized fringe obtained at zero bias and (right panel) an estimate of normalized shear ( $2\Delta_n$ ) and bias  $2\phi$ . (d) By stitching the normalized fringes obtained at different bias, a more accurate estimate of the shear is obtained. In (c) and (d),  $e_{\text{rms}}$  is the root-mean-square error between the experimental data and the fitted data.

of the  $|P_{\text{DIC}}|^2$  image as bias is changed. The translation is due to the slightly tilted analyzer used by the manufacturer (as an additional antireflection mechanism) in our setup. This translation is observable in Media 3. This hardware problem could not be remedied, as the rotatable analyzer is an integrated product. We instead register the  $|P_{\text{DIC}}|^2$  image acquired at each bias with the  $|P_{\text{BF}}|^2$  image by image processing. The registration consists of finding edges of both images (edge), using phase correlation of edges to find the relative shift [27], and translating the  $|P_{\text{DIC}}|^2$  image (imtransform) to eliminate the shift. To remove debris from images, we used morphological closure [28] (imclose) with a circular structuring element whose radius was set just larger than the largest debris observed in the image. Use of morphological processing rather than linear filtering allows satisfactory elimination of sharp intensity variations (introduced by debris) without blurring the edges of the BFP. From the edge of the  $|P_{\text{BF}}|^2$  image, we measure (in pixels) the diameter of the BFP with the morphological region measurement algorithm (regionprops). Note that in normalized units of  $\lambda/\text{NA}_{\text{obj}}$ , this diameter has a value of 2. The cleaned and registered  $|P_{\text{BF}}|^2$  and  $|P_{\text{DIC}}|^2$  are shown in Fig. 8(b); the associated image sequence (Media 4) shows the results of preprocessing at different bias settings.

### C. Obtaining Interference Fringes $|P_{\text{DIC}}|^2/|P_{\text{BF}}|^2$ and Estimating Shear

By dividing registered  $|P_{\text{DIC}}|^2$  images by  $|P_{\text{BF}}|^2$ , we obtain normalized fringes. We set all pixels outside the BFP to zero. The normalized fringes at different bias values are shown in Media 5, a snapshot of which at bias 0 is shown in Fig. 8(c). We extract line profiles from the center of  $|P_{\text{DIC}}|^2$ , whose length is 2 in normalized units as mentioned previously. This line profile is low pass filtered to suppress high-frequency noise and is fitted to Eq. (12) using the curve fitting toolbox of MATLAB using a nonlinear least square algorithm (fit). The algorithm is initialized with nominal bias used during acquisition. The parameters to be estimated are normalized shear ( $2\Delta_n$ ) and exact bias ( $2\phi$ ) from the experimental data. By using normalized fringes at different bias values, we obtain nearly the same estimate of the shear. The right panel of Media 5 shows the experimental and fitted profiles, as well as estimated shear and root mean square (rms) error between both profiles (which ranges from 0.02 to 0.05). The disagreements between the experimental and the fitted profiles are mainly due to the noise in the line profile extracted from the center of the BFP.

### D. Stitching the Fringes Observed at Different Bias Values to Improve Estimate of the Shear

To improve the error performance of the fitting procedure described above, we construct a longer fringe profile by averaging the pixels and “stitching” profiles obtained at different bias values. From each

of the normalized fringes, we extract a square inscribed in the BFP. The pixels in these squares are averaged perpendicular to the fringes to obtain a fringe profile with low noise. Fringes are stitched as follows:

- Convert sinusoidal fringes into rectangular profiles by thresholding all fringes with a common threshold computed by Otsu’s method [29] (graythresh).
- Use the thresholded “fringes” to calculate the amount by which the fringe shifts (in pixels) at consecutive bias values. Since we acquired fringes at the same bias interval, this shift should be the same between any two consecutive fringes. However, slight variation in shift was observed due to human error in adjusting the de Sénarmont compensation. We use regionprops to measure the shifts between two profiles. The calculated shift allows stitching together the original sinusoidal fringes obtained at different bias values.

This stitched fringe is fitted to Eq. (12) by the same method as in the above subsection to estimate the shear. With this approach, as shown in Fig. 8(d), the shear of the  $20 \times 0.75$  NA objective was measured to be  $0.91\lambda/\text{NA}_{\text{obj}}$ . With the same approach, the shear of the  $40 \times 0.9$  NA objective was estimated to be  $0.537\lambda/\text{NA}_{\text{obj}}$  as shown in Fig. 9. Shear of the  $40 \times 0.6$  NA objective was measured to be  $0.371\lambda/\text{NA}_{\text{obj}}$  as shown in Fig. 10. The root mean square errors in the curve fitting procedure for  $20 \times 0.75$  NA,  $40 \times 0.9$  NA, and  $40 \times 0.6$  NA were 0.015, 0.009, and 0.012, respectively, indicating that the measured data were in excellent agreement with the theoretical model and that the computational implementation estimated the parameters of the model with high accuracy.

### 7. Verification of Estimated Shear and Error Analysis

To verify our approach, we make use of *a priori* information that, in our setup, the angular shear of the OPrism obtained from different measurements must corroborate within the bounds of systemic differences. The benchmark for comparison is provided by the angular shear measured in Eq. (6) with the benchtop setup discussed in Subsection 3.A. The shears measured from coherent fringes (produced with benchtop setup), beads, and partially coherent

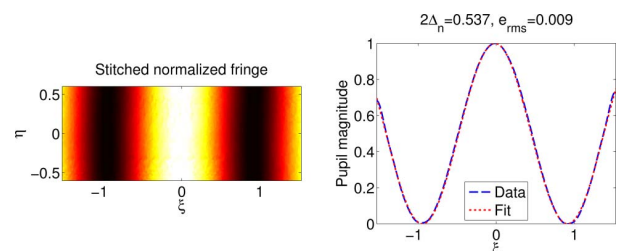


Fig. 9. (Color online) Estimation of shear introduced by OPrism when used with UplansAPO  $40 \times 0.9$  NA objective.



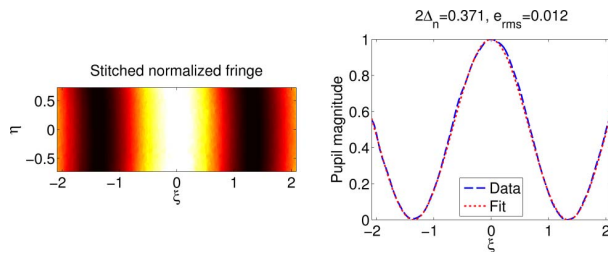


Fig. 10. (Color online) Estimation of shear introduced by OPrism when used with UPlanFl 40 × 0.6 NA objective.

fringes (produced with the microscope) are summarized in Table 1.

This comparison illustrates several interesting points. The maximum difference in angular shear estimated with three independent measurements performed with three objectives is 3%, confirming that our approach provides a consistent measurement of shear. As discussed in Appendix A, an ideal prism produces nearly the same fringe *in the plane of localization*, irrespective of the extent (spatial coherence) or spectral width (temporal coherence) of the source. However, the experimental system does produce slightly different fringes for different inclinations of the source [30]. Moreover, chromatic aberration of the objectives causes different shears at different wavelengths and slightly different shears across the objectives at the same wavelength.

The angular shear measured with coherent illumination at  $\lambda = 650$  nm and partially coherent illumination around  $\lambda = 550$  nm differ maximally by 9% among three objectives. This difference is due to the chromatic dispersion discussed above. Similar differences between shears measured at different wavelengths with help of 2FFCS have also been noted in [20]. Thus it is important to use quasi-monochromatic illumination and to measure the shear with partially coherent illumination for accurate calibration. We have computed partially coherent images [19] of an optical fiber under standard DIC and Köhler-DIC setups for a 20 × 0.75 NA objective using the shear as calibrated above and found the simulated images to be in good agreement with experimental images. The physical shears ( $2\Delta = 2\Delta_n\lambda/\text{NA}_{\text{obj}}$ ) at  $\lambda = 0.55 \mu\text{m}$  for our 20 × 0.75 NA, 40 × 0.9 NA, and 40 × 0.6 NA objectives are equal to 0.667, 0.33, and 0.34  $\mu\text{m}$ . We notice that the shear for a 20× objective is double that for a 40× objective. This is an expected result, since the angular shear,

$$\varepsilon = \frac{\Delta}{f_o} = \Delta \frac{f_l}{M}, \quad (13)$$

is constant for our setup, with a consequence that the spatial shear varies inversely with the magnification.

While the shear measured with our approach matches closely with measurement done by a benchtop setup and has allowed us to simulate partially coherent imaging accurately [19], phase-bead based measurement is 56% larger than the benchtop measurement. Taken together, these experimental results confirm that the bead-based measurement tends to overestimate the shear. Apart from effects of spatial and temporal coherence discussed above, there are sources of noise and systemic errors that affect the measurement of the shear. Next, we discuss these sources and how they have been accounted for in our measurement procedure.

#### A. Sources of Noise and Their Effects

- *Systemic errors:* We have found three systemic errors to be of significant impact: the variation in the BFP caused by the image of the filament, noise in the BFP images due to mottle, and misregistration of fringes imaged at different bias values due to an inclined rotatable analyzer. The effects and mitigation of these errors are discussed in detail in Section 6. Briefly, the mottle was removed by linear and morphological filtering, the bright-field BFP and BFP with fringes were registered with the phase correlation method, and their ratio was taken to eliminate the variations due to filament.

- *Quantization noise:* Methods based on a calibrated specimen require measurement of intensity distribution in the specimen space, which possesses high spatial frequencies. The acquisition of these high spatial frequencies and subsequent localization of peaks by data fitting is inherently prone to errors. On the other hand, the intensity distribution in the BFP is very smooth (as a result of the subresolution shear). Therefore it can be acquired with high fidelity and the results of data fitting are more accurate, because a sinusoid can be accurately estimated from very few points.

- *Dynamic range of useful signal and shot noise:* As seen from Fig. 5, images of beads have poor dynamic range and therefore required averaging of 100 images to overcome poor SNR due to shot noise. On the other hand, the fringes in the BFP occupy the entire dynamic range of the detector, and therefore their measurement is negligibly affected by shot

Table 1. Summary of Angular Half-Shear ( $\varepsilon$ ) and Spatial Half-Shear ( $\Delta$ ) Measured with Various Methods Presented in this Paper<sup>a</sup>

Shear Estimated Using	Benchtop Setup	20 × 0.75 NA		40 × 0.9 NA		20 × 0.6 NA	
	$\varepsilon(\text{rad})$	$\varepsilon(\text{rad})$	$\Delta(\mu\text{m})$	$\varepsilon(\text{rad})$	$\Delta(\mu\text{m})$	$\varepsilon(\text{rad})$	$\Delta(\mu\text{m})$
Coherent fringe (650 nm)	<b><math>3.46 \times 10^{-5}</math></b>		0.32		0.16		0.16
Partially coherent fringe (550 nm)		$3.707 \times 10^{-5}$	<b>0.335</b>	$3.646 \times 10^{-5}$	<b>0.165</b>	$3.77 \times 10^{-5}$	<b>0.17</b>
Peak distance in image of a bead (550 nm)						$5.4 \times 10^{-5}$	<b>0.245</b>

<sup>a</sup>Bold entries indicate the direct measurements. Other entries are computed using Eq. (13) from relevant measurements.

noise, except outside the BFP where the light intensity is nearly zero. In areas of low light, the ratio between the fringes and the bright-field BFP (used to correct for uneven illumination aperture) is erroneous if the registration between them is not correct. As illustrated in Fig. 5, the phase-correlation method provides quite accurate registration. Moreover, when obtaining an average fringe, which is fit to the model, we only use the intensity variation well within the BFP and avoid the contamination of accurate data by inaccurate data from low light regions. The *a priori* information that the fringe is of low spatial frequency also prevents the fitting procedure from being affected by sudden variations due to noise.

## 8. Discussion and Conclusion

In addition to the methods discussed in Sections 3 and 6, we also explored a potentially accurate method of measuring the shear using a subresolution fluorescent bead. This method relies on imaging of only one of the polarizations (ordinary or extraordinary) produced by the OPrism from unpolarized fluorescence emission. If the analyzer is placed after the OPrism and is aligned parallel to the ordinary or the extraordinary polarization, one can suppress the other polarization and obtain an image that is simply an Airy disk shifted by half the shear distance. By suppressing either polarization in turn, the peaks produced by both polarizations can be individually localized to a very high accuracy using methods developed for superresolution techniques such as PALM and STORM [31,32]. Nevertheless, we chose not to employ this method due to following practical problems.

- One needs to have an analyzer with extremely good extinction to remove the unwanted polarization. Otherwise, the localization of the peaks will be erroneous, especially when shears  $< 0.45\lambda/\text{NA}_{\text{obj}}$  are being measured. Although our analyzer has high extinction specification, the contribution from the unwanted polarization was significant enough (especially, at small shears) to affect the location of the peak.
- To suppress the unwanted polarizations in turn, one needs to rotate the analyzer by  $90^\circ$ . In doing this, the image of a fluorescent bead produced by individual polarization may become misregistered. In our setup, this occurs due to the inclined analyzer as discussed in Section 6. The slightest misregistration can introduce a large percentage error in the measured distance between peaks.

Section 5 shows that the model of partially coherent imaging in DIC facilitates measurement of shear and bias, which is used to devise the acquisition and image analysis algorithm of Section 6. The devised approach has been used to measure the shear of three different objectives and the bias of one objective as described in Sections 6 and 7. For image analysis and reconstruction only the shear produced

by the OPrism should be measured, since it is responsible for shearing interferometry. Nevertheless, the same procedure can be used to estimate the shear for the CPrism by inserting it between crossed polarizers (and removing the OPrism from the light path). We found that the shear employed for an Olympus UPlansapo  $20 \times 0.75$  NA objective is much larger than the usual recommendation that subresolution shear should be used. This points out the inherent trade-off involved in design of practical DIC systems when one is required to limit the total number of prisms used among different objectives.

We have shown in Section 7 that the accuracy of measurement of shear using our approach is better than 3%. If required, this accuracy can be improved by enhancing the image analysis algorithms for measuring the key parameters (such as diameter of the bright-field BFP, period of the fringe, and shift of the fringe with respect to the center of the BFP) with subpixel accuracy.

As observed in Appendix A and Section 7, in the absence of dispersion in the imaging light path, the angular shear and the spatial shear introduced by the OPrism for all wavelengths is the same. However, practical systems always have dispersion and some amount of chromatic aberrations. Depending on the amount of chromatic aberration introduced by the OPrism and the objective, one may need to measure the shear for each objective at the wavelength of operation. We recommend the use of a narrowband interference filter (i.e., quasi-monochromatic illumination) to record high-contrast interference fringes and to properly account for dependence of shear on wavelength of illumination. We have found that prisms from recent Olympus and Zeiss microscopes produce central achromatic fringe, which implies that the OPD between orthogonal polarizations at the center of the OPrism is zero. In such a case, the interference filter of 40 nm width was found to be sufficient. However, we found that Nikon Microphot SA performs interferometry with fringes that are chromatic, i.e., the OPrism produces a finite minimum OPD between split wavefronts. The CPrism in this microscope is designed to compensate for this OPD (and hence produces chromatic fringes as well) so that the total OPD in the absence of the specimen is zero. For prisms that employ chromatic fringes, one requires interference filters that are as narrow as 10 nm.

In conclusion, we have provided a useful description of properties of Nomarski prisms. We have shown that the peaks in the image of a small bead (transparent or fluorescent) are not necessarily located at the distance given by the shear, and hence measuring the shear as a distance between peaks leads to rather approximate results. We have demonstrated that measuring the period of the interference fringes relative to the size of the BFP provides an accurate method of calibrating shear of a partially-coherent DIC system. The bias can be estimated by measuring the shift of the fringe with respect

to the center of the BFP. The presented algorithm makes use of linear and morphological image-processing techniques to extract interference fringes from intensities recorded at the BFP. These interference fringes have been fitted to the model of the BFP to accurately estimate the shear and bias.

#### Appendix A: Effect of Spatial and Temporal Coherence on the Shear Produced by the Nomarski Prism

Since DIC is an *interferometer*, coherence of the source plays a vital role in its operation. Pioneering researchers [1,33] in shearing interferometry very well appreciated the coherence effects discussed here. However, these ideas do not appear to be mainstream within the DIC community—even though they are important. The following discussion also clarifies the choices made while developing acquisition methods presented in this paper.

When illuminated with unpolarized light or light polarized at an angle to the optic axes of the Nomarski prism, the prism acts as a birefringent beam splitter that introduces angular shear ( $2\varepsilon$ ) between two orthogonally polarized output beams. The polarizations of output beams are governed by the optic axes of two wedges of the prism. If the input light is unpolarized (i.e., without sufficient coherence between component polarizations), the output beams cannot produce detectable interference fringes. When the input is polarized (e.g., if the prism is placed between crossed or parallel polarizers), the output beams are derived from the same scalar field and hence interfere. Thus, to perform shearing interferometry, the Nomarski prism has to be illuminated with polarized light. Figures 11(a) and 11(b) show a Nomarski prism placed between crossed polarizers with its optic axes at  $45^\circ$  to the polarizers. The blue color represents a polarized wavefront, and green and yellow represent the orthogonally polarized wavefronts to which the prism has introduced angular shear. The relative distance between these two wavefronts represents the optical path difference (OPD) introduced due to the angular shear. These wavefronts are derived from the same scalar field and therefore combine in amplitude to form a wavefront whose polarization varies across the direction of the shear. As an example,

the OPDs of  $0$ ,  $\lambda/4$ ,  $\lambda/2$ , and  $\lambda$  between the green and yellow wavefronts give rise to linear (along the polarizer's axis), circular, linear (along the analyzer's axis), and linear (again along the polarizer's axis) polarizations. The wavefront with spatially varying polarization is passed through the analyzer, whose transmission axis is represented in red. The analyzer converts the spatial variation of polarization into sinusoidal variation of the intensity. Note that the fringe produced in this manner repeats when the OPD changes by  $\lambda$ . The period of the fringe is illustrated in Fig. 11(c) and noted as Eq. (1). The solid and dashed lines represent the wavefronts produced by light of wavelengths  $\lambda_1$  and  $\lambda_2$ , respectively. We assume that  $\lambda_2 > \lambda_1$ . Interference fringes produced by the Nomarski prism from a spatially coherent wavefront as illustrated in Fig. 11(a) can be observed anywhere in space as long as their intensities are detectable. Thus a spatially coherent source produces *nonlocalized* fringes ([34], subsection 7.5.3). As shown in Fig. 2, one can construct a benchtop setup with a coherent source to measure the shear of the prism from the period of the observed fringes.

Next, we consider effects of spatial coherence of the light on the fringe. By the van Cittert–Zernike theorem [34,35], the partially coherent field at a given plane can be represented as an *incoherent* sum of the plane waves coming from a finite numerical aperture. Out of this set of plane waves, Fig. 11(a) shows a normally incident plane wave, whereas Fig. 11(b) shows an obliquely incident plane wave. As illustrated in the figures, the fringes produced by individual plane waves are spatially displaced with respect to each other. Moreover, these fringes add in intensity over the entire space since the plane waves are mutually incoherent. The fringes are *aligned* only in the certain region of the space, where the optical path difference between the two split wavefronts (shown by green and yellow) is independent of the angle of illumination of the prism. As a result, fringe visibility diminishes over most of the space and remains significant only over a small region—a situation called *localization* of fringes ([36], chapter 5). OPrism and CPrism are designed such that the plane of localization of fringes produced by them

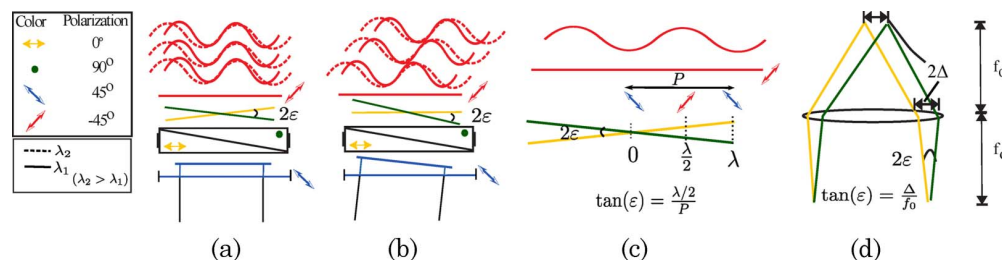


Fig. 11. (Color online) Schematic representation of the interference fringes produced by the Nomarski prism when illuminated by (a) normally incident plane wave and (b) oblique plane wave; (c) the relationship between the angular shear and the period of the fringe, and (d) the relationship between spatial shear ( $2\Delta$ ), angular shear ( $2\varepsilon$ ), and focal length of the lens ( $f_0$ ). Colors shown on the left are used to indicate polarization of light and the orientations of the optical axes of the optical components. Note that the relative distance between angularly-split wavefronts in (a)–(c) represents the relative optical path difference between them. Solid and dashed lines represent two different wavelengths.



coincide with the BFP and FFP, respectively, ensuring that interference contrast is high even when a partially coherent source is employed. Thus, for a properly designed DIC microscope, the fringes produced in the BFP by either a coherent or a partially coherent source are almost the same. When the prism is placed in the back focal plane of the objective, the spatial shear produced in the specimen plane depends on its focal length as illustrated in Fig. 11(d) and noted in Eq. (2). In the DIC setup, placing either the OPrism or the CPrism, but not both, between the polarizer and the analyzer produces the interference fringes. These interference fringes can be observed by looking at the objective back focal plane—either by removing the eyepiece or using a Bertrand lens.

Some comments about the effects of the temporal coherence (i.e., spectral extent) of the source are also in order. When white light is employed, the interference fringes produced by each component wavelength (e.g.,  $\lambda_1$  and  $\lambda_2$  in Fig. 11) have different periods. When multiple wavelengths are employed, only the central fringe, where peaks of fringes due to individual wavelengths align, is achromatic ([36], subsection 5.2). The subsequent fringes are chromatic and hence of lower visibility than the central fringe. Since the period of the fringe increases with wavelength [as implied by Eq. (1)], the physical shear is nearly independent of the wavelength [as implied by Eq. (2)] even when a source of broad bandwidth is used. Note that the dispersion by optical material used to manufacture the prism will affect the linear relationship between the wavelength and fringe period, causing variable angular and physical shears at different wavelengths.

S. B. Mehta thanks the  $\mu$ manager development team for providing help with development of the driver for the Olympus BX61 controller, Kou Shan Shan from National University of Singapore for useful discussion about acquisition of the fringes in the BFP, and Bai Jianhao from National University of Singapore for providing polystyrene beads. S. B. Mehta acknowledges support from Marine Biological Laboratory (MBL) for visiting research, and useful discussions with Rudolf Oldenbourg, Cellular Dynamics Program, MBL, regarding DIC configurations of Zeiss microscopes and the Nikon Microphot SA.

## References

1. G. Nomarski, "Interference polarizing device for study of phase objects," U.S. patent 2924142 (9 February 1960).
2. M. Pluta, *Advanced Light Microscopy. Vol. 2. Specialized Methods* (PWN-Polish Scientific, 1989).
3. C. J. Cogswell, N. I. Smith, K. G. Larkin, and P. Hariharan, "Quantitative DIC microscopy using a geometric phase shifter," *Proc. SPIE* **2984**, 72–81 (1997).
4. M. R. Arnison, K. G. Larkin, C. J. R. Sheppard, N. I. Smith, and C. J. Cogswell, "Linear phase imaging using differential interference contrast microscopy," *J. Microsc.* **214**, 7–12 (2004).
5. B. Kouskousis, D. J. Kitcher, S. Collins, A. Roberts, and G. W. Baxter, "Quantitative phase and refractive index analysis of optical fibers using differential interference contrast microscopy," *Appl. Opt.* **47**, 5182–5189 (2008).
6. C. Preza, S. V. King, J. Conchello, C. J. Cogswell, and T. Wilson, "Algorithms for extracting true phase from rotationally-diverse and phase-shifted DIC images," *Proc. SPIE* **6090**, 60900E (2006).
7. M. Shribak, J. La Fountain, D. Biggs, and S. Inoue, "Orientation-independent differential interference contrast microscopy and its combination with an orientation-independent polarization system," *J. Biomed. Opt.* **13**, 014011 (2008).
8. S. B. Mehta and C. J. R. Sheppard, "Partially coherent image formation in differential interference contrast (DIC) microscope," *Opt. Express* **16**, 19462–19479 (2008).
9. W. Galbraith, "The image of a point of light in differential interference contrast microscopy: computer simulation," *Microscopica acta* **85**, 233–254 (1982).
10. T. J. Holmes and W. J. Levy, "Signal-processing characteristics of differential-interference-contrast microscopy," *Appl. Opt.* **26**, 3929–3939 (1987).
11. E. B. van Munster, L. J. van Vilet, and J. A. Aten, "Reconstruction of optical path length distributions from images obtained by a wide-field differential interference contrast microscope," *J. Microsc.* **188**, 149–157 (1997).
12. P. Munro and P. Török, "Vectorial, high numerical aperture study of Nomarski's differential interference contrast microscope," *Opt. Express* **13**, 6833–6847 (2005).
13. H. H. Hopkins, "On the diffraction theory of optical images," *Proc. R. Soc. London Ser. A* **217**, 408–432 (1953).
14. T. Wilson and C. J. R. Sheppard, *Theory and Practice of Scanning Optical Microscope* (Academic, 1984).
15. C. J. R. Sheppard and T. Wilson, "Fourier imaging of phase information in scanning and conventional optical microscopes," *Phil. Trans. R. Soc. London Ser. A* **295**, 513–536 (1980).
16. C. Cogswell and C. Sheppard, "Confocal differential interference contrast (DIC) microscopy: including a theoretical analysis of conventional and confocal DIC imaging," *J. Microsc.* **165**, 81–101 (1992).
17. C. Preza, D. L. Snyder, and J. Conchello, "Theoretical development and experimental evaluation of imaging models for differential-interference-contrast microscopy," *J. Opt. Soc. Am. A* **16**, 2185–2199 (1999).
18. S. B. Mehta and C. J. R. Sheppard, "Phase-space representation of partially coherent imaging systems using the Cohen class distribution," *Opt. Lett.* **35**, 348–350 (2010).
19. S. B. Mehta and C. J. R. Sheppard, "Using the phase-space imager to analyze partially coherent imaging systems: bright-field, phase-contrast, differential interference contrast, differential phase contrast, and spiral phase contrast," *J. Mod. Opt.* (to be published).
20. C. B. Müller, K. Weiß, W. Richtering, A. Loman, and J. Enderlein, "Calibrating differential interference contrast microscopy with dual-focus fluorescence correlation spectroscopy," *Opt. Express* **16**, 4322–4329 (2008).
21. R. Danz, A. Vogelgsang, and R. Kathner, "PlasDIC—a useful modification of the differential interference contrast according to Smith/Nomarski in transmitted light arrangement," *Photonik* **1**, 42 (2004).
22. T. J. McIntyre, C. Maurer, S. Bernet, and M. Ritsch-Marte, "Differential interference contrast imaging using a spatial light modulator," *Opt. Lett.* **34**, 2988–2990 (2009).
23. M. Pluta, "Principles and basic properties," in *Advanced Light Microscopy* (PWN-Polish Scientific Publishers, 1988), Vol. 1.
24. P. Hariharan, "The Senarmont compensator: an early application of the geometric phase," *J. Mod. Opt.* **40**, 2061–2064 (1993).

25. J. W. Goodman, *Introduction to Fourier Optics*, 2nd ed. (McGraw-Hill, 1996).
26. K. J. Dana, "Three dimensional reconstruction of the tectorial membrane: an image processing method using Nomarski differential interference contrast microscopy," M.S. thesis (Massachusetts Institute of Technology, 1992).
27. C. D. Kuglin and D. C. Hines, "The phase correlation image alignment method," in *Proceedings of the International Conference on Cybernetics and Society* (IEEE, 1975), Vol. 4, pp. 163–165.
28. P. Soille, *Morphological Image Analysis: Principles and Applications* (Springer-Verlag, 2003).
29. N. Otsu, "A threshold selection method from gray-level histograms," *IEEE Trans. Syst. Man Cybern.* **9**, 62–66 (1979).
30. C. C. Montarou and T. K. Gaylord, "Analysis and design of modified Wollaston prisms," *Appl. Opt.* **38**, 6604–6616 (1999).
31. E. Betzig, G. H. Patterson, R. Sougrat, O. W. Lindwasser, S. Olenych, J. S. Bonifacino, M. W. Davidson, J. Lippincott-Schwartz, and H. F. Hess, "Imaging intracellular fluorescent proteins at nanometer resolution," *Science* **313**, 1642–1645 (2006).
32. M. J. Rust, M. Bates, and X. Zhuang, "Sub-diffraction-limit imaging by stochastic optical reconstruction microscopy (STORM)," *Nature Methods* **3**, 793 (2006).
33. M. Françon, *Optical Interferometry* (Academic, 1966).
34. M. Born and E. Wolf, *Principles of Optics: Electromagnetic Theory of Propagation, Interference and Diffraction of Light*, 7th ed. (Cambridge University Press, 1999).
35. H. H. Hopkins, "The concept of partial coherence in optics," *Proc. R. Soc. London Ser. A* **208**, 263–277 (1951).
36. M. Françon and S. Mallick, *Polarization Interferometers: Applications in Microscopy and Macroscopy* (Wiley-Interscience, 1971).



## 6.2 Phase reconstruction from DIC and AIDPC images

Although DIC and AIDPC provide a striking bas-relief visualization of the morphology of the specimen due to their sensitivity to the gradient of the specimen phase, the raw images are not amenable to computer-assisted processing. Segmentation of the features of interest out of the image is typically a first step in quantitative image analysis. The gradient of the OPL measured by DIC or AIDPC is not amenable to easy segmentation. Moreover, intensity recorded by the DIC microscope does not measure the gradient in a linear fashion. Consequently, phase-shifting is used to obtain an intensity image from DIC [Cogswell et al., 1997, Arnison et al., 2004, King et al., 2008] that linearly represents the gradient of the OPL. As discussed in sec. 3.2, DPC provides inherently linear measurement of the OPL-gradient. In this section, we describe algorithms that provide a quantitative representation of optical thickness (dry-mass for biological specimens and surface profile for reflective specimens) starting with high resolution measurements taken with DIC or DPC microscopes. Such measurements are useful for a number of biological studies that require long-term time-lapse imaging. Certain studies in cellular dynamics (such as cell division and cell motility) can especially benefit by instrumentation and analysis algorithms developed in this section.

At this point, it should be emphasized that the above assertion (viz., phase-shifting DIC and DPC linearly measure the OPL-gradient) is based on the assumption that the specimen is slowly varying with respect to the resolution of the imaging system.

The direct integration of the gradient image obtained with DIC or DPC gives rise to streaks in the image because the DC component of the phase distribution is lost in the direction of differentiation [Arnison et al., 2000]. To overcome this problem, the specimen gradient can be measured in two orthogonal directions. These two measurements provide the vector gradient field of the specimen phase, from which the phase can be retrieved by several approaches for integration. The problem of reconstructing a function from its vector gradient arises widely in computer vision [Agrawal et al., 2006] and phase unwrapping [Ghiglia and Pritt, 1998]. In our experiments, we use a direct integration approach based on division by a ‘spiral phase filter’ proposed by Arnison, Sheppard, and Larkin [Arnison et al., 2004, Larkin et al., 2001]. The same algorithm is known as Frankot-Chellappa

algorithm in computer vision [Agrawal et al., 2006].

To account for diffraction effects in the DIC microscope, a few researchers have attempted reconstruction of specimen phase by assuming coherent image formation [van Munster et al., 1997, Kagalwala and Kanade, 2003, Holmes and Levy, 1987, Shribak et al., 2008] in which the image intensity is obtained by convolution of the specimen transmission with a point spread-function. However, as shown in sec. 2.2, the notion of a point spread-function is not quite valid for polarization based shearing interferometers and in general, for partially coherent systems. Recently, Ishiwata [Ishiwata et al., 2006, 2008] has used the partially coherent model similar to that presented by Preza [Preza et al., 1999] to carry out reconstruction. As noted in Chapter 2, Preza’s model does not account for coherence effects of the condenser-side prism. The diversity of approximate imaging models and reconstruction approaches for DIC mentioned above highlight the fact that inversion of partially coherent imaging is a rather difficult task.

While we have developed an accurate model and simulation capability for forward imaging in partially coherent systems, we are yet to develop a reconstruction approach that exploits the model. In this section, we present a heuristic approach for high quality visualization of the specimen’s phase based on the DIC and AIDPC images. In our approach, we decompose the object as a sum of two spatially varying components, one component varying slowly with respect to resolution but possibly having large magnitude of phase variation (slowly varying specimen) and the other varying fast with respect to the resolution of the imaging system but having small magnitude of phase variation (weak specimen). In the following, we consider image formation with matched illumination.

Around the neighborhood (whose extent should relate to resolution of the imaging system) of each specimen point, the slowly varying component of the specimen refracts the light and causes loss of intensity due to vignetting of illumination. In other words, the slowly varying component moves the zero-order of illumination across the objective pupil. Since the illumination aperture is as large as imaging aperture, this refraction leads to loss of light (i.e., vignetting). The area of overlap of the condenser pupil and the objective pupil gives the strength with which the slowly varying component is imaged.

The weak component of the specimen on the other hand, diffracts the light in different

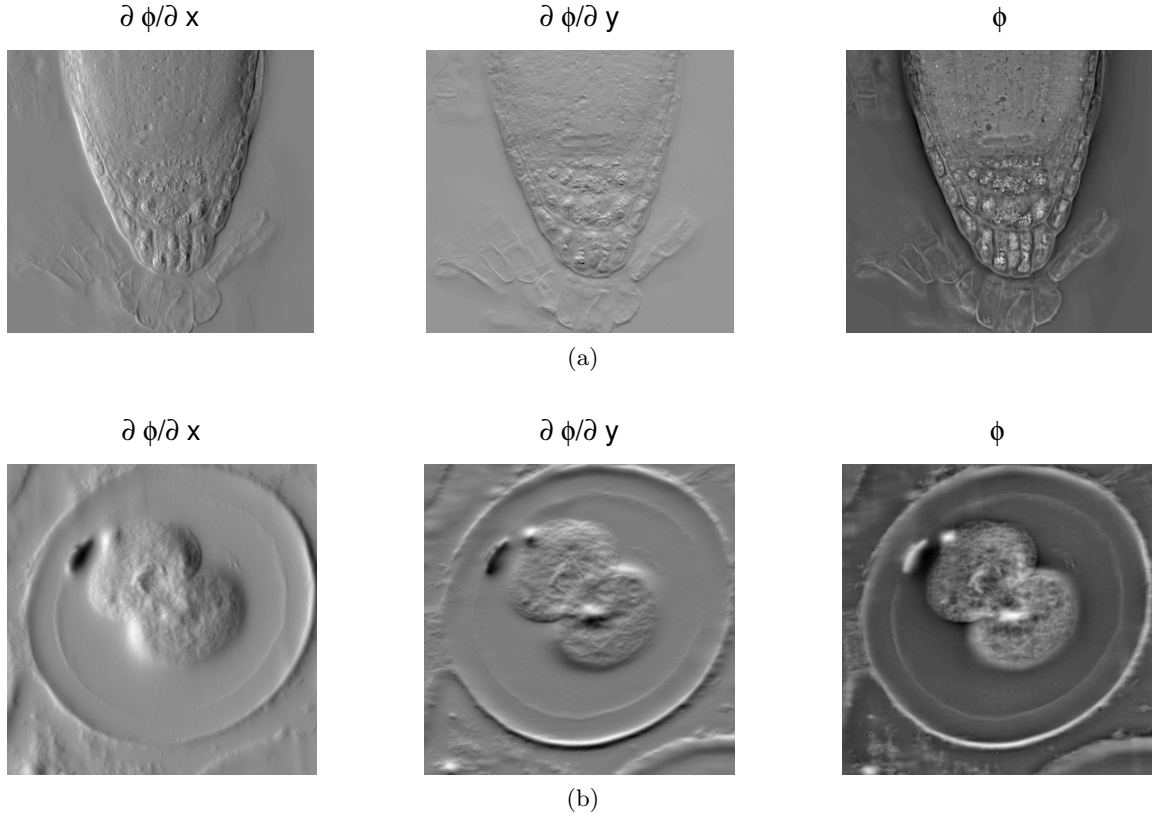


Figure 6.1: Direct reconstruction of specimen phase from (a) DIC and (b) AIDPC images using a combined spiral phase and deconvolution filter.

orders around the zero-order (as can be understood from fig. 1.3b). Since the size of the diffracted orders in the imaging back focal plane is the same as the zero-order, the strength with which the weak component is transmitted can be approximated by the area of overlap of the objective pupil - i.e., the optical transfer function of the wide-field microscope.

With phase-shifting DIC and AIDPC, we correct for the vignetting effect due to the slowly varying specimen phase. To incorporate the effect of fast varying but weak phase, we simply deconvolve the DIC and AIDPC images with the OTF of the wide-field setup.

The qualitative description above is in the same spirit as the PSI-kernel representation of the phase-space imager discussed in sec. 4.2.

Based on the above assumptions, we employ the following algorithm to retrieve phase information about the specimen.

1. Compute linear gradients of the specimen along  $X$  and  $Y$ , according to phase-shifting DIC or AIDPC.

2. Deconvolve each gradient image (via Wiener filtering using theoretically computed wide-field OTF). This step may be seen as boosting the higher spatial frequencies of the data acquired with the microscope.
3. Combine the gradients with spiral-phase integration to retrieve the phase map.

We combine the last two steps into one computational step by combining the spiral-phase filter with the Wiener filter that performs deconvolution. Thus, we obtain a direct inversion approach that provides high resolution visualization of the specimen's morphology that can be used for quantitative image analysis.

Figure 6.1 shows reconstructions achievable with our approach. Figure 6.1a shows the images of Arabidopsis (a plant) root acquired with DIC microscope. The gradients  $\partial\phi/\partial x$  and  $\partial\phi/\partial y$  were measured with the four-frame phase-shifting DIC algorithm. Since changing the direction of differentiation in DIC requires simultaneous rotation of the polarizers and prisms, we rotated the specimen manually. (b) shows the images of Ascaris (a type of ground-worm) cells acquired with AIDPC. The gradients  $\partial\phi/\partial x$  and  $\partial\phi/\partial y$  are obtained by rotating the condenser aperture stop rather than the specimen. Four blocks of paper were placed appropriately at four positions of the condenser turret and switched with a motorized condenser to acquire the necessary asymmetric illumination images.

During the retrieval process, we had to register the images acquired with DIC and AIDPC. When doing the registration, we realized that standard registration algorithms (as used previously by a few researchers [King et al., 2008]) are not applicable to these data. We therefore developed a fast and noise-robust algorithm that we describe next. The following section has been adapted from our conference paper [Mehta and Sheppard, 2009a].

### 6.2.1 Efficient and robust registration of phase-gradient data measured with DIC and AIDPC

One of the experimental difficulties in phase-retrieval process is to align phase-gradient images taken at different bias settings of DIC or with different directions of illumination in AIDPC. The mis-registration occurs due to mechanical movement during acquisition. A noise-proof method for solving this problem does not seem to be available in the litera-

ture. We propose a novel approach that extends the phase-correlation algorithm [Kuglin and Hines, 1975] to registration of phase-gradient images, acquired along the same or the orthogonal directions of differentiation.

Among automated image registration methods, phase correlation [Zitova and Flusser, 2003] is known to be robust against variety of noise sources, including additive noises and partial overlap. Phase-correlation relies on the shift theorem of the Fourier transform, and involves finding a positive correlation peak in the normalized cross-spectrum of the images to be registered. If  $I_t$  and  $I_r$  are target and reference images respectively, phase-correlation of  $I_t$  and  $I_r$  is computed as,

$$P(I_t, I_r) = \mathcal{F}^{-1} \left[ \frac{\mathcal{F}(I_t)\mathcal{F}^*(I_r)}{|\mathcal{F}(I_t)||\mathcal{F}(I_r)|} \right]. \quad (6.1)$$

The relative shift of  $I_t$  with respect to  $I_r$  is given by,  $(\Delta x, \Delta y) = \arg \max P(I_t, I_r)$ . Although, it has been used with DIC, it has been found to work in some cases [King et al., 2008] and not in other cases [Glasbey and Martin, 1996]. In our experience, the phase-correlation approach of eq. 6.1 does not usually work with DIC images. The reason for this is evident when we realize that *phase-correlation method is designed for registering two noisy and shifted measurements of the same two-dimensional function*. In the case of DIC or AIDPC, *we instead are registering two different functions, albeit related to the underlying phase of the specimen*.

As can be seen from the references, phase-retrieval in both DIC and AIDPC requires computation of a ratio of images that represents linear phase-gradient in the direction of the shear (in DIC) or in the direction of the asymmetry (in AIDPC). Linear-gradients computed in two orthogonal directions are used to retrieve an image proportional to phase using frequency domain non-directional integration algorithm called spiral phase integration.

In each direction, DIC requires registration of four images obtained at bias  $0, \pi/2, \pi$ , and  $-\pi/2$ ; termed  $I_0, I_{\pi/2}, I_\pi$ , and  $I_{-\pi/2}$ , respectively. AIDPC requires registration of only two images taken with the left-half of the illumination aperture ( $I_L$ ) and the right-half of the illumination aperture ( $I_R$ ).  $I_{\pi/2}$  and  $I_{-\pi/2}$  images of DIC measure phase-gradients with opposite contrast: so do  $I_L$  and  $I_R$  in AIDPC. To a first approximation, they represent

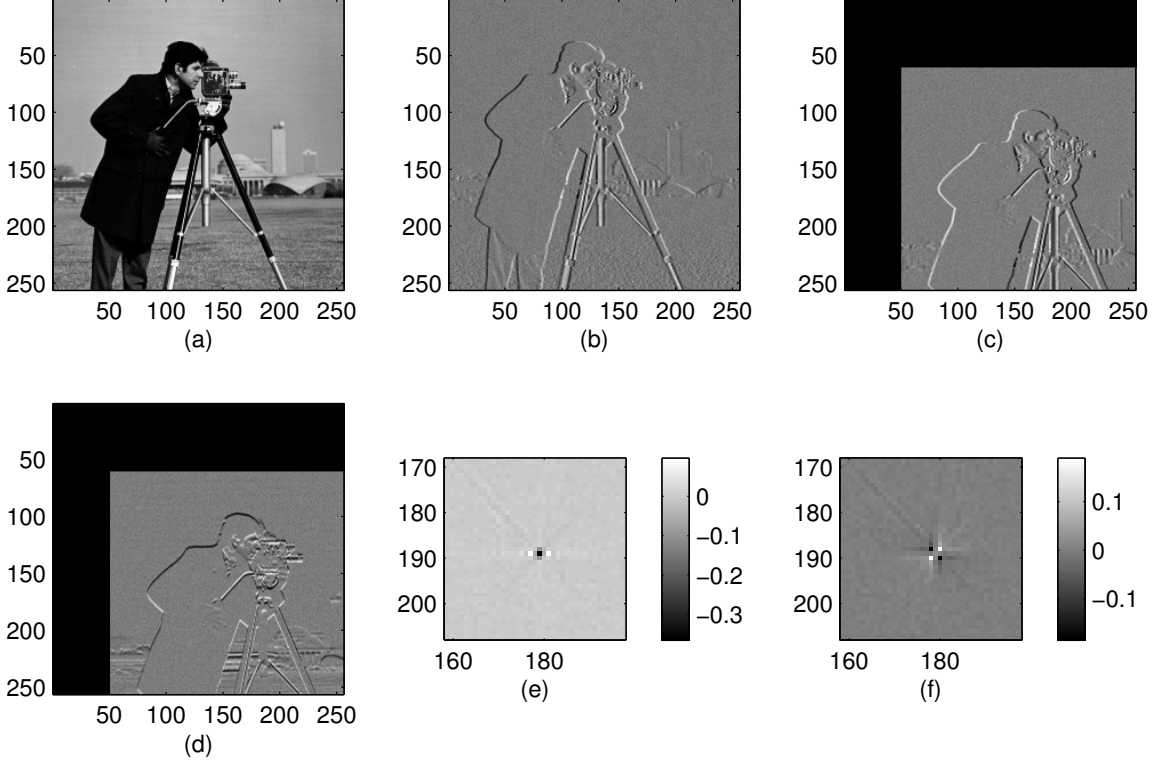


Figure 6.2: Simulation of phase-correlation of  $d\phi/dx$  with  $-d\phi/dx$  and  $d\phi/dy$ : (a) Original image of size 256X256, (b) gradient along  $X$ -direction, (c) gradient along  $-ve$   $X$ -direction shifted by  $(\Delta x, \Delta y) = (50, 60)$ , (d) gradient along  $Y$ -direction shifted by  $(\Delta x, \Delta y) = (50, 60)$ , (e) phase-correlation of (b & c), (f) phase-correlation of (b & d). Poisson noise with variance equal to the pixel-value was added to images (b, c, & d). Images (e & f) are zoomed to 40X40 pixels around the correlation peak. The negative correlation peak in (e) is situated at an offset (50,60) from the center pixel (129,129) of the image. The quad-peaks in (f) are centered around the same point.

$d\phi/dx$  and  $-d\phi/dx$ , mixed with amplitude information,  $\phi(x, y)$  being the phase information to be retrieved. In other words, they represent gradients of phase in opposite directions. Since they are the same function but with opposite sign, the phase-correlation will be *negative* where both images are in register. Therefore, by finding the position of *minima* of phase-correlation, we can find the relative shift.

Now, let us assume we need to register  $I_r = \frac{d\phi}{dx}(x, y)$ , and  $I_t = \frac{d\phi}{dy}(x + \Delta x, y + \Delta y)$ .

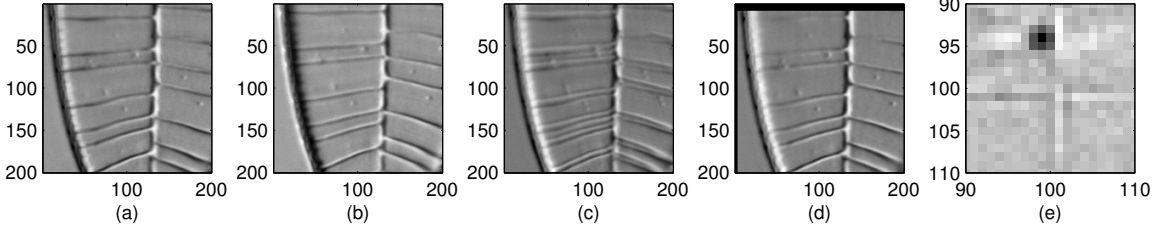


Figure 6.3: Registration of experimentally acquired DIC data with gradient phase-correlation algorithm: Images are cropped to the size of 200X200 pixels. (a) Bias  $\pi/2$ , (b) bias  $-\pi/2$ , (c) difference of (a & b) without registration shows duplication of features, (d) difference of (a & b) after registration produces an image with higher contrast, (e) Zoomed (20X20 pixels around center) phase-correlation map of (b) with respect to (a) shows the negative correlation peak at distance (-2,-7) from the center.

Computing normalized cross-spectrum and phase-correlation according to eq. 6.1,

$$\begin{aligned}
 P(I_t, I_r) &= \mathcal{F}^{-1} \left[ \frac{[i f_x \Phi(f_x, f_y) e^{i 2\pi(f_x \Delta x + f_y \Delta y)}][i f_y \Phi(f_x, f_y)]^*}{|f_x| |f_y| |\Phi(f_x, f_y)|^2} \right] \\
 &= \mathcal{F}^{-1} \left[ \text{sign}(f_x) \text{sign}(f_y) e^{i 2\pi(f_x \Delta x + f_y \Delta y)} \right] \\
 &= \frac{-1}{xy} \otimes \delta(x - \Delta x, y - \Delta y) = \frac{-1}{(x - \Delta x)(y - \Delta y)}. \quad (6.2)
 \end{aligned}$$

In the above,  $\Phi(f_x, f_y)$  is the Fourier spectrum of the phase  $\phi(x, y)$  and  $\text{sign}(f_x) = f_x/|f_x|$  is the signum function. It is seen that the phase-correlation in this case is a function that approaches positive and negative infinity around the point  $(\Delta x, \Delta y)$ . The phase-correlation appears as four peaks with positive and negative peaks placed diagonally with respect to each other.

Results of simulation that validate the above derivation are shown in fig. 6.2. Predictions from the above derivation are reproduced excellently in the discrete implementation of the algorithm. Experimental example of registration of DIC images taken with bias  $\pi/2$  and  $-\pi/2$  is shown in fig. 6.3.

The detection of the pattern of four peaks seen in the phase-correlation of  $d\phi/dx$  and  $d\phi/dy$  requires some effort to detect. These four peaks occur because of the  $\text{sign}(f_x)\text{sign}(f_y) = (f_x f_y / |f_x| |f_y|)$  term in eq. 6.2. We can eliminate that term and consequently, obtain a single peak, by taking an additional derivative of the recorded gradient images. It is easy to appreciate this argument when we do the same derivation as in eq. 6.2 for any of the following pair of images.

- $I_r = \frac{d^2\phi}{dydx}(x, y)$  obtained as  $Y$  derivative of the recorded  $d\phi/dx$  image and  $I_t = \frac{d^2\phi}{dxdy}(x + \Delta, y + \Delta)$  obtained as  $X$  derivative of the recorded  $d\phi/dy$  image.
- $I_r = \frac{d^2\phi}{dx^2}(x, y)$  obtained as  $X$  derivative of the recorded  $d\phi/dx$  image and  $I_t = \frac{d^2\phi}{dy^2}(x + \Delta, y + \Delta)$  obtained as  $Y$  derivative of the recorded  $d\phi/dy$  image.

The phase-correlation of both of the above pairs is a single peak corresponding to the shift to be detected.

Note that the rotational mis-registration of two gradient images in orthogonal directions can be corrected using an extension of phase-correlation that transforms angular shifts into translation [Zitova and Flusser, 2003].

## 6.3 Analysis of the dynamic beating of axoneme with dark-field microscope

### 6.3.1 Background and hypothesis

Flagellum and cilium are important cellular organelles responsible for a surprisingly diverse set of cellular mechanisms. Apart from their obvious role in movement of various cell types (such as sperm cells); they play an important role in ascertaining accurate positioning of cells during gastrulation [Supp et al., 1997], act as extra-cellular antennae for the cell [Christensen et al., 2007], and perform important functions across human organs [Badano et al., 2006]. The axoneme [Greek axōn, axis + nēma, thread] forms the ‘skeleton’ and the ‘motor’ of the flagella and cilia in eukaryotic cells. The axoneme is a near-resolution structure (of diameter 250nm) consisting of microtubules arranged in a highly conserved *9+2 structure*, which is illustrated in fig. 6.4. The axoneme chiefly consists of 9 microtubule doublets (fused microtubule singlets) arranged peripherally with 2 microtubule singlets at the center. The figure also shows the schematic of the components of axoneme other than microtubules. The dynein motor proteins located on outer-side and inner-side of the outer microtubule doublets interact with microtubules to give rise to motility.

It is natural to anticipate that the periodic beating of the flagellum (that contains only one axoneme) or cilium (that may contain multiple axonemes arranged in complex structure)



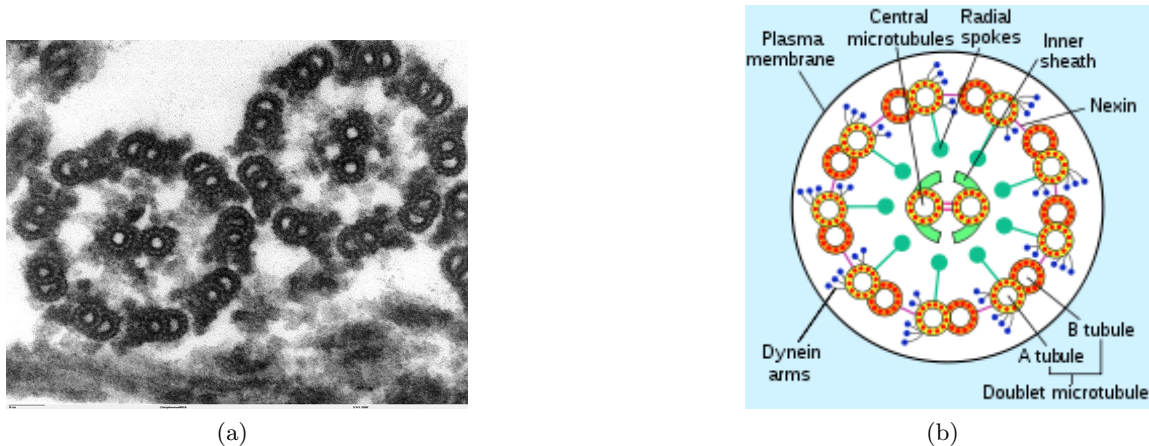


Figure 6.4: (a) An electron micro-graph showing the 9+2 arrangement of the microtubules within the axoneme from <http://en.wikipedia.org/wiki/Axoneme> and (b) a schematic representation of the structure of the axoneme from Figure 19.28 on page 819 of “Molecular Cell Biology, 4th edition, Lodish and Berk”.

is due to some periodic change in the structure of axoneme. However, the exact nature of the propagation of the structural change in axoneme remains elusive. In this section, we report our efforts at measuring the dynamic changes in structure of live specimens with a carefully constructed dark-field setup. This research is done in collaboration with Dr. Naoki Noda and Dr. Rudolf Oldenbourg at Cellular Dynamics Program of Marine Biological Laboratory (MBL) during my visit to MBL.

Several models have been proposed to account for how the structure of the axoneme changes to give rise to periodic bending of flagella or cilia. As discussed in the reviews by Porter and Sale [Porter and Sale, 2000] and Kamiya [Kamiya, 2002], the experimental results obtained so far indicate that the bending of the flagellum occurs due to sliding of the outer microtubule doublets located on opposite sides. The sliding of the doublets is caused by the movement of the inner dynein arm proteins in the presence of ATP. The inner dynein arm has been shown to be necessary and sufficient for producing flagellar waveforms, whereas the outer dynein arm provides the force required to overcome the viscous friction of the fluid surrounding the cell [Kamiya, 2002]. Moreover, with help of atomic force microscopy, it has been shown that the dynein movement leads to a change in the diameter of the axoneme [Sakakibara et al., 2004] of the order of 10nm. Thus, the dynein-microtubule interaction in the axoneme leads to large-scale bending in the plane containing the axoneme

and nanometer-scale vibrations in the plane normal to the axoneme.

To decipher how the above structural activity and consequently *the flagellar bend propagates along the length of the flagellum*, it is important to be able to visualize and quantify the propagation directly. However, to our knowledge, a live imaging method for quantitative analysis of how the microtubule-dynein interaction propagates through the flagellum has not been established. It is difficult, if not impossible, to label all of the dynein molecules within the flagellum with a fluorescent dye and examine the movement of dynein as the bend propagates. Thus, fluorescence based approaches are inadequate for studying the global propagation of structural changes and a label-free fast imaging approach is required to address this problem.

In an encouraging development, Oldenbourg has shown that quantitative imaging of birefringence (using the LC-Polscope [Oldenbourg, 2005]) with high-NA optics allows quantitative assessment of change in the density of microtubules [Oldenbourg et al., 1998]. Interestingly, birefringence profiles obtained with LC-Polscope show signatures of loss of key components of the axoneme assembly (observations from experiments carried out by Naoki Noda and Rudolf Oldenbourg, Marine Biological Laboratory, USA). The profile of measured birefringence changes when, for example, outer-arm dynein is extracted with biochemical treatment. Quantitative birefringence imaging thus can provide a mechanism of sensing the changes in axoneme structure. However, the speed of imaging (2 fps) that can be achieved with LC-Polscope is not adequate for imaging a beating axoneme. For live imaging of beating axoneme, dark-field microscopy has widely been used, because dark-field illumination eliminates non-scattering background and visualizes the near-resolution structures with high contrast.

Existing research has not paid attention to the *intensity profile in dark-field images* of the axoneme, perhaps because accurate computation of the image in dark-field microscope was difficult. Our phase-space imager model enables such computation [Mehta and Sheppard, 2010a,c]. We carried out simulations of the expected images of the axoneme as its diameter changes due to interaction of the outer microtubules and dynein arms. The simulations (presented next), reveal that when the diameter of the axoneme reduces, the intensity in the dark-field image increases (by a measurable factor) due to increased scattering of light.

This observation led us to a hypothesis that quantifying the temporal change in the intensity (of the dark-field image) along the length of the flagellum provides a quantitative measure of the propagation of structural change along the length of the flagellum. Based on this hypothesis, I have constructed an image analysis algorithm that extracts the propagation of the bend and the image intensity from time-lapse images of the axoneme. The presented analysis provides important clues about how the axoneme bend propagates and how the bend is controlled.

### 6.3.2 Simulated images of axoneme under dark-field microscope

For our experiments, we used Zeiss Plan-apochromat 63X 1.4NA objective with aperture iris and Zeiss ultra-condenser which provides maximum NA of 1.4 with oil immersion. To accurately simulate the transfer properties of our dark-field setup (based on Zeiss Axiovert 200M microscope), we measured the numerical apertures of the objective and the annular illumination ring. This ‘calibration’ was carried out by inserting the Bertrand lens in the optical path to image the objective back focal plane on the camera. After careful Köhler alignment of the microscope with oil immersed condenser and objective, we measured the numerical aperture of the dark-field ring to be  $1.2 - 1.3$ . We stopped down the objective iris to NA of 1 to obtain adequate rejection of background light, but good sensitivity to small changes in the structure of the axoneme. We used illumination wavelength of  $577\text{nm} \pm 20\text{nm}$  by placing an interference filter after the Mercury vapor light source X-Cite 120 from Exfo. We used Qimaging 2000RV camera to record the images.

First, we compare the supports (in the specimen plane) of mutual coherence of illumination due to the condenser annulus and the imaging PSF due to the objective with the dimensions of the axoneme. It is known from van Cittert-Zernike theorem [[Born and Wolf, 1999](#)] that the mutual coherence in the specimen plane due to incoherent illumination in the condenser front focal plane is given by Fourier transform of the intensity distribution in the condenser front focal plane. The top row of [fig. 6.5](#) shows the condenser annulus and the mutual coherence obtained as its Fourier transform. The bottom row shows the imaging pupil and the amplitude PSF obtained by Fourier transforming the imaging pupil. The mutual coherence is seen to be a slightly blurred version of the Bessel function of the

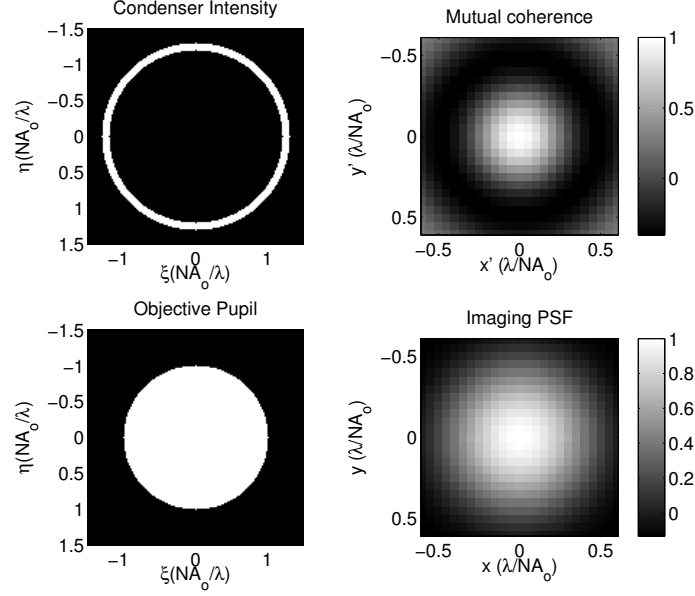


Figure 6.5: Comparison of the supports of the mutual coherence produced by the dark-field annulus (top row) and the point spread function of the imaging objective (bottom row). The pupil variables are expressed in units of  $\text{NA}_o/\lambda$ , whereas the spatial variables are expressed in the units of  $\lambda/\text{NA}_o$ . To signify that the mutual coherence is a function of the distance rather than position, we use  $(x', y')$  as variables over which mutual coherence is defined. The quantity in the right column is obtained as the Fourier transform of the quantity in the left column.

zeroth order,  $J_0(v)$  whereas the PSF is seen to be the jinc function  $J_1(v)/v$ , where  $v$  is the spatial co-ordinate in units of  $\lambda/\text{NA}_o$ . The first zero of the imaging PSF at  $0.61\lambda/\text{NA}_o$  corresponds to a distance of  $0.61 \times 0.577 = 0.352\mu\text{m}$  in our setup. The first zero of the mutual coherence function at  $0.38\lambda/\text{NA}_o$  corresponds to a distance of  $0.68 \times 0.577 = 0.22\mu\text{m}$  in our setup. We notice that over the radius of the axoneme,  $0.115\mu\text{m} = 0.2\lambda/\text{NA}_o$ , the mutual coherence function reduces to 0.6. Therefore, we may assume that the axoneme cross-section falls within the ‘coherence volume’ of the illumination, i.e., the light scattered by components in the axoneme structure is nearly coherent. Consequently, we assume the axoneme to be a cylinder of an effective uniform refractive index. By using dark-field illumination, we discard the unscattered light and increase the sensitivity to changes in the scattering properties of the axoneme.

We perform two simulations to determine if the intensity of the dark-field image should change for a small change in the axoneme’s structure. One detailed simulation accounts for

the 9+2 microtubule structure of the axoneme, whereas the other assumes the axoneme to be a cylinder of uniform index as discussed above. We determine relevant parameters from the cryo-electron tomography measurements performed by Nicastro et al. [Nicastro et al., 2006]. In resting state, the axoneme cross-section has a radius of approximately 115nm. Although fig. 6.4b suggests that axoneme cross-section is densely packed with proteins, in fact it is quite the opposite (personal communication with Daniela Nicastro, Brandeis University). Along the length of the axoneme, only the microtubules are continuously present. On the microtubule scaffold, different proteins occur at different intervals, e.g., dynein arms occur at 24nm interval. The axoneme structure has a global periodicity of 96nm. The space between the inner sheath (surrounding the pair of central microtubule) and the outer microtubules makes up roughly 50% of the volume occupied by axoneme. A tiny fraction of this space is occupied by radial spokes. Keeping above considerations in mind, it is safe to assume that the majority of light scattering comes from the 9+2 microtubule structure. With this assumption in mind, in fig. 6.6a we simulate the image of 9+2 structure under dark-field microscope, as the outer microtubules move away from the center.

Next we assume that the axoneme is a uniform cylinder. Let us denote the refractive index of protein by  $\eta_p$  and that of the embedding medium (water in our case) by  $\eta_e$ . If  $p$  is the fraction of the cross-section occupied by the proteins, we can estimate the effective refractive index of the axoneme assembly as,

$$\begin{aligned} n &= p\eta_p + (1 - p)\eta_e \\ &= \eta_e + p(\eta_p - \eta_e). \end{aligned} \tag{6.3}$$

The above equation assumes that the excess polarizability introduced within the embedding medium is proportional to the protein mass. The protein mass is conserved as the structure of axoneme changes. Therefore, when the axoneme contracts, the fraction of the cross-section occupied by the protein mass increases proportionally. In other words,  $p \times A = \text{const}$  where,  $A$  is the cross-section within which the protein mass is present.

Through a series of imbibition experiments, Sato, Ellis, and Inouè [Sato et al., 1975]

have determined that the refractive index of a single microtubule is 1.512. We assume that all protein components within the axoneme assembly have a refractive index of 1.512. We estimate that, within one repeat unit of length 96nm and diameter 115nm, 20% space is occupied by the proteins components, chiefly by microtubules. Thus, at any other radius,  $r$  the fraction of cross-section occupied by protein mass is  $p_r = 0.2(115^2/r^2)$ . Consequently, the effective refractive index of axoneme at cross-sectional radius  $r$  can be estimated as,

$$n_r = 1.33 + 0.2(1.512 - 1.33)\frac{115^2}{r^2} \quad (6.4)$$

Figure 6.6 shows simulated images of the axoneme with following assumptions for different radii ( $r = 105, 110, 115, 120, 125\text{nm}$ ) of the axoneme: (a) we account for only the 9+2 arrangement of microtubules and (b) we assume the axoneme to be uniform cylinder with RI computed as above. Media 6.6a and 6.6b show the computation of the images for all five radii. In both subfigures, the left plot shows the distribution of the refractive index across the cross-section of the axoneme, the middle plot shows the computed OPL at given wavelength as well as computed image intensity, and the right-most plot compares integrated image intensity for different radii of the axoneme. The computed images obtained with both models distinctly show that as the size of the axoneme increases, the intensity of the dark-field image reduces. The physical reason behind this effect is the reduced scattering at high angles as the refractive index profile of the axoneme smooths due to expansion.

In fig. 6.6, integrated intensity is computed because it is independent of defocus, unlike the peak intensity. Both simulations lead to the observation that the change in radius of the axoneme from 115nm to 110nm (as measured by Sakakibara et al. using AFM [Sakakibara et al., 2004]) leads to 4 – 5% increase in the dark-field intensity. In our experiments, we therefore use integrated intensity to monitor the progression of the dynein-microtubule activity. The small difference in integrated intensity for given cross-section can be accentuated by integration along the length of the axoneme. Since the axoneme structure varies slowly along the length, such an integration is not expected to lose important information.

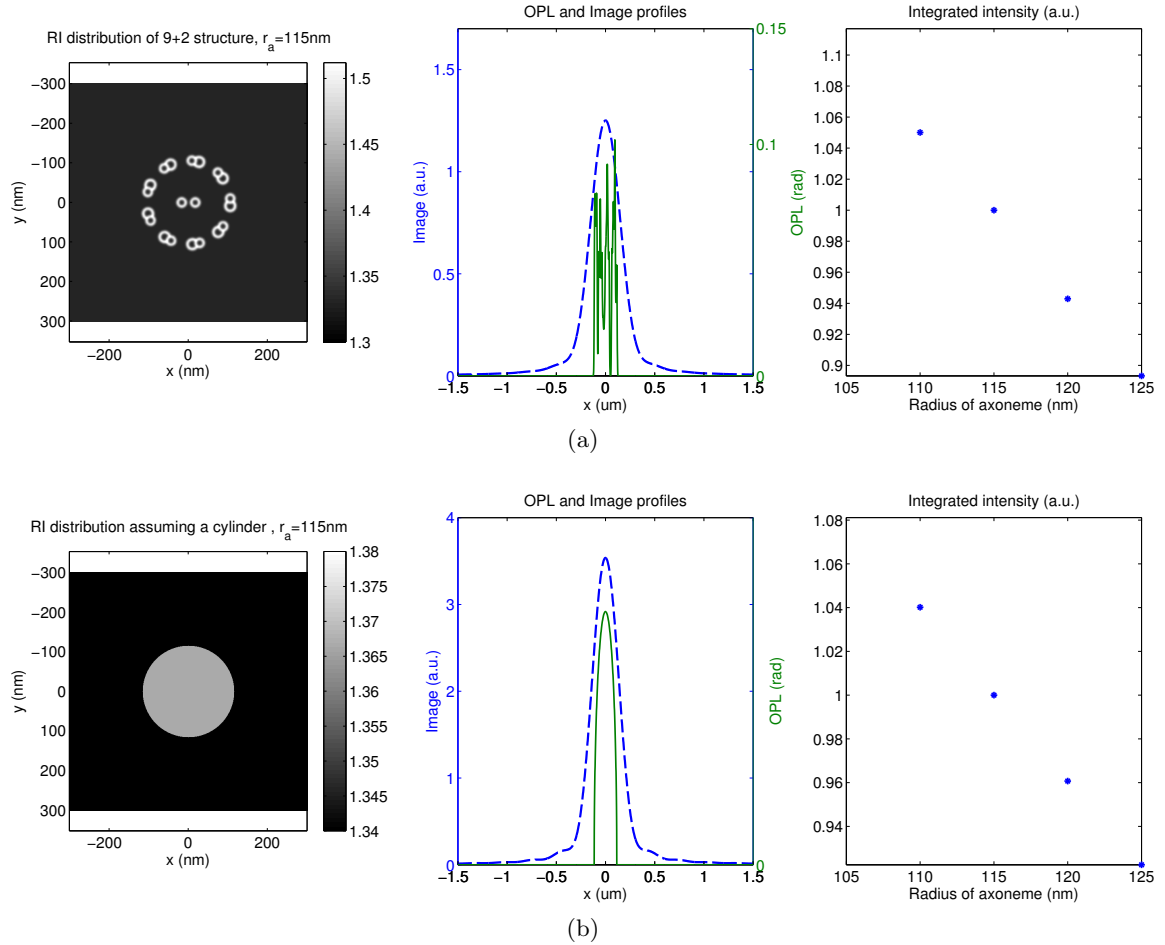


Figure 6.6: Computation of partially coherent dark-field images of the axoneme: Partially coherent image simulation shows that as the axoneme expands along its cross-section, the intensity of the image reduces: In (a) the axoneme is modeled with the 9+2 structure of microtubules and in (b) it is modeled as a cylinder of uniform RI. Media 6.6a and 6.6b shows the images computed for successively increasing distance between the outer microtubules. The specimen was illuminated with an annular aperture of NA 1.2 – 1.3 and imaging was performed with a Zeiss 63XO 1.4 NA objective with an adjustable aperture ring. The ring was adjusted to provide the imaging NA of 1 and configure a dark-field setup. These simulations were carried out in collaboration with Dr. Rudolf Oldenbourg, MBL, USA.

### 6.3.3 Imaging of live specimens

In this study, we used the demembranated flagellum of the sea-urchin sperm cell as a model to study axoneme's beating pattern. The sea-urchin sperm flagellum consists of the axoneme surrounded by thin membrane. Demembranating the flagellum exposes the axoneme, whose beating frequency can be controlled by controlling the concentration of ATP in the embedding medium.

The samples were prepared by Dr. Naoki Noda, MBL, USA. The demembranated axonemes were suspended in a solution containing ATP (reconstitution solution) and mounted between a coverglass and coverslip that were separated by 50 – 100 $\mu$ m thick miler spacer. The specimen was imaged on an inverted microscope.

Figure 6.7 and associated media 6.7 show an unprocessed (raw) time-sequence of a sperm cell whose flagellum is beating normally. The exposure time of the camera was 20 ms. From the media 6.7, we can distinctly perceive that the region of high intensity periodically moves towards the tail of the flagellum. The same figure compares the intensity line-profiles at two places on the sperm flagellum. While the image profiles are quite the same, their absolute values are not the same. This measurement matches the observations made from simulations of fig. 6.6.

The variations in intensity in raw dark-field images of fig. 6.6 are easy to notice, which could be attributed to three causes:

1. Frustrated total internal reflection at the interface of mineral oil and the reconstitution solution of axoneme: This possibility is ruled out since the maximum NA of illumination is 1.3, which is below the illumination angle required to cause the total internal reflection at the oil-water interface.
2. Defocus: The reduction in intensity of the flagellum's image may occur if the flagellum goes out of focus. When the flagellum is defocused, the peak intensity in the image reduces but the region over which the intensity is significant expands. Thus, the integration of the intensity provides a quantity that is independent of defocus.
3. Increased scattering power of the axoneme: If we notice that integrated intensity (in



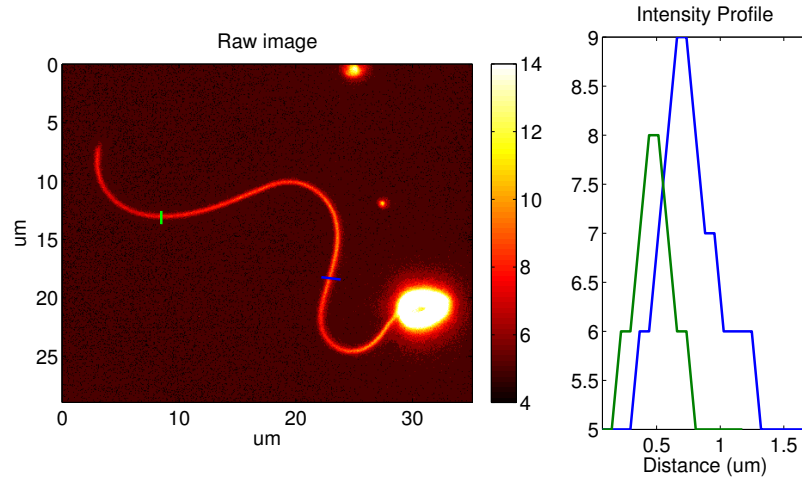


Figure 6.7: Raw image (left) and the contrast enhanced raw image (right) of the sea-urchin sperm with demembranated flagellum. Samples were prepared by Naoki Noda, MBL, USA, while imaging experiments were carried out collaboratively. Media 6.7 shows the time-lapse of raw images in which propagation of intensity is visible.

the direction perpendicular to the length of the axoneme) changes in an orderly fashion along the length of the flagellum, it very likely represents the changes in the scattering strength of the axoneme as the dynein arms interact with outer microtubules.

#### 6.3.4 Measurement of bend propagation and intensity propagation along the length of the axoneme

I developed the following three-step image analysis algorithm to correlate the propagation of the flagellar bend and the scattering strength:

1. Segment the head of the sperm and identify the orientation.
2. Similarly, segment the flagellum of the sperm. At each point on the flagellum, measure the angle (tangent) of the flagellum with reference to the angle of the head. This angle, called shear angle in axoneme community [Brokaw and Kamiya, 1987], is a direct measure of the sliding between microtubules.
3. At each point of the flagellum, compute the integrated intensity by summing the set of pixels perpendicular to the tangent of the flagellum at that point. The integrated intensity is the defocus-independent measure of the scattering strength of the axoneme.

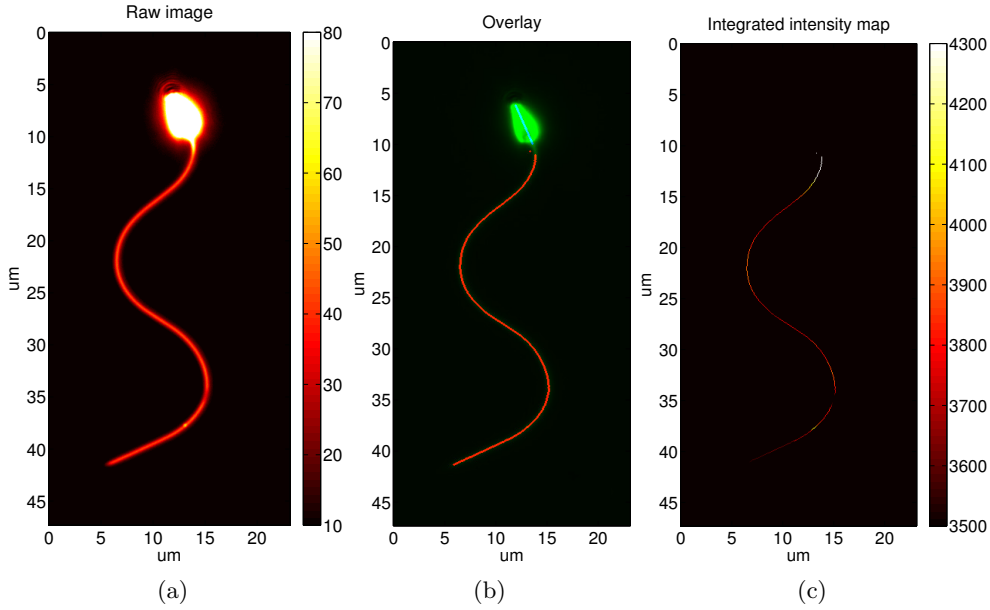


Figure 6.8: Control experiment to verify the insensitivity of our image analysis software with respect to defocus: (a) is the raw image of a non-beating axoneme taken from Z-stack shown in Media 6.8a. (b) is the overlay of segmented flagellum (green) and the head orientation line (blue) with the raw image (green). (c) is the integrated intensity along the segmented flagellum. Media 6.8b and 6.8c demonstrate that segmentation of flagellum, identification of head orientation line, and values of integrated intensity are independent of the defocus.

We first show two negative control experiments to demonstrate the efficacy of the image analysis algorithm. The first negative control is a Z-stack of the non-beating axoneme. Figure 6.8 and the associated media show that the estimation of the angle of the head, segmentation of the flagellum, as well as the values of integrated intensity are entirely independent of the focal position of the axoneme.

As the next negative control, we analyze time-lapse images of an axoneme which beats erratically and only near the head. Figure 6.9 shows the raw images, segmented head-orientation and the flagellum, as well as the integrated intensity. Media 6.9b and 6.9c demonstrate that only in the beating region (close to head) the integrated intensity changes. The integrated intensity at end of the segmented flagellum does not change due to lack of structural activity.

Having verified that the image analysis algorithm is independent of defocus and that the non-beating axoneme *does not show* propagation of the integrated intensity along the

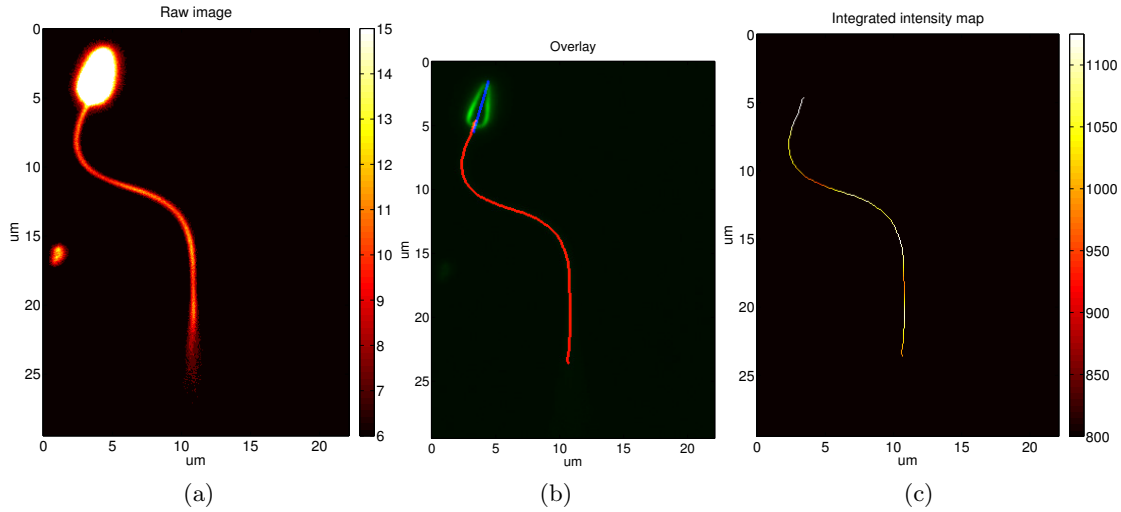


Figure 6.9: A negative control (erratically beating axoneme) shows the lack of propagation of the flagellar bend and integrated intensity: (a) is the raw image from a time-lapse shown in Media 6.9a. (b) is the overlay of segmented flagellum (green) and the head orientation line (blue) with the raw image (green). (c) is the integrated intensity along the segmented flagellum.

flagellum, we analyze the raw images of the specimen shown in fig. 6.7. Figure 6.10 shows the segmented head orientation and flagellum, integrated intensity, as well as a comparative plot of the integrated intensity and shear angle along the length of the flagellum. Note that the distance along the flagellum was measured starting from its tail and tracing the segmented flagellum towards the head. The media associated with fig. 6.10 show the above measurements at all time points. From media 6.10b, it can be observed that integrated intensity measured along the length of the flagellum appears to ‘flow’ towards the tail. A few useful observations can be made from the temporal change in the shear angle and the integrated intensity along the length of the flagellum as shown in media 6.10c. We can clearly notice the propagation of the flagellar shear angle from the head to the tail end. This behaviour strongly suggest initiation of the bending waveform at the head. We also notice that the integrated intensity propagates along the length of the flagellum and has higher spatial frequency than the shear angle profile. The higher rate of change of integrated intensity along the flagellar length may be hinting that the sliding of the microtubules is affected by the synchronous dynein-microtubule interaction at multiple locations on the flagellum.

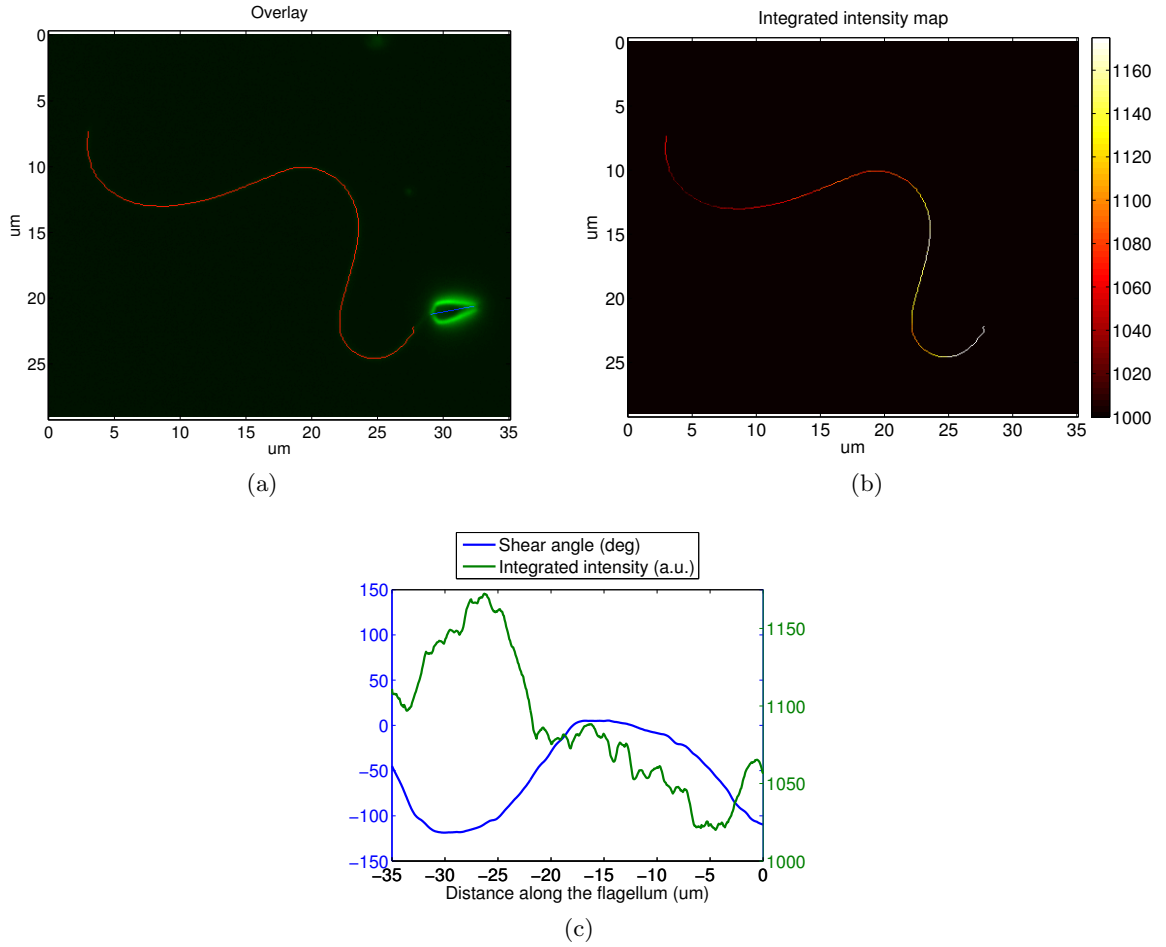


Figure 6.10: Analysis of the propagation of the bend and the scattering strength along the length of the beating axoneme: (a) Overlay of raw intensity (green), segmented flagellum (red), and measured orientation of head (blue). (b) Integrated intensity computed over the rectangle of size  $1 \times 5$  airy units, aligned perpendicular to the tangent of the flagellum at each point on the segmented flagellum. The airy unit is defined as  $0.61\lambda/\text{NA}_0$ . (c) Shear angle and the integrated intensity plotted along the flagellum. The distance along the flagellum is measured from the tail. Associated media 6.10a, 6.10b, and 6.10c show the temporal changes in above quantities.

## Chapter 7

# Conclusion

In conclusion, the following may be thought of as main contributions of the thesis to the fields of partially coherent imaging and quantitative phase microscopy of biological specimens.

1. Development and verification of an accurate image formation model for DIC that resolves some incorrect assumptions held in DIC community and leads to an accurate calibration algorithm.
2. New quantitative phase microscopy method of AIDPC that overcomes experimental artifacts of DIC and phase-contrast.
3. Development of the phase-space imager model of partially coherent imaging and using it to compare various phase microscopy methods.
4. Development of the image analysis algorithms for quantitative study of beating dynamics of axoneme and for reconstruction of the cellular morphology from DIC and AIDPC images.

In following sections, we summarize the results and discuss interesting directions of research that follow from the results. Both sections are divided in three parts by combining the discussion of the first two contributions noted above.

## 7.1 Summary of results

### 7.1.1 Partially coherent methods of quantitative phase microscopy

Due to practical advantages afforded by partially coherent illumination (as explained with fig. 1.3), there is a growing interest in using partially coherent illumination for quantitative imaging. These advantages have made DIC a method of choice for biological phase microscopy, and several approaches for performing quantitative analysis with DIC are emerging. It is important to have clear understanding of image formation in DIC to build useful quantitative systems and to develop reconstruction approaches. Towards this end, we have developed an accurate quantitative model [Mehta and Sheppard, 2008] that amends the incorrect assumption [Preza et al., 1999] about the coherence of illumination in DIC. The same model leads to a surprising result (observed experimentally and explained analytically in sec. 2.2) that the image of a point specimen *varies* with coherence of illumination. With this result, we correct another incorrect assumption [Galbraith, 1982, Preza et al., 1999] that one can define a point-spread function for a DIC microscope. Apart from above contributions, we have also developed an accurate calibration algorithm for DIC that measures the shear and bias by quantitatively analyzing the image intensity recorded in the objective back focal plane. The algorithm is simple to implement and does not require any sample [Mehta and Sheppard, 2010b].

While DIC possesses important practical advantages of depth-sectioning, its key shortcoming is the artifacts produced in the presence of birefringence. We have developed a partially coherent method of AIDPC that overcomes key practical artifacts of DIC (see fig. 3.1) and phase-contrast [Mehta and Sheppard, 2009b]. AIDPC provides more quantitative measure of phase-gradient than DIC does. However, AIDPC suffers from artifacts if there is a differential absorption across two asymmetric beams caused by the specimen. Moreover, the depth of focus of AIDPC is larger than that of DIC.

### 7.1.2 Phase-space representation of partially coherent imaging

The fact that both DIC and AIDPC provide similar phase-gradient images, but with entirely different optical arrangement may seem surprising at first. Similarly, different phase imag-

ing methods of phase-contrast [Zernike, 1955], hoffman modulation contrast [Hoffman and Gross, 1975], single-sideband edge enhancement [Ellis, 1981], spiral phase-contrast [Maurer et al., 2008] have been developed with different heuristic arguments.

For a long time, there has been a demand for developing a unified description of partially coherent phase imaging [Martin, 1966]. In areas such as optical lithography and X-ray microscopy, a more intuitive model for partially coherent image formation than the transmission cross-coefficient [Hopkins, 1953, Wong, 2001] model has been desirable.

We have discovered a long suspected phase-space ‘link’ to the transmission cross-coefficient model. Our model, called phase-space imager [Mehta and Sheppard, 2010a] (PSI) is physically meaningful and computationally efficient. It is elegant in the sense that it provides a phase-space equivalent of the point spread function or the optical transfer function as discussed in sec. 4.2.

The phase-space models prevalent in optics mainly rely on Wigner distribution or ambiguity function to describe propagation of partially coherent fields [Bastiaans, 2008]. However, PSI is a ‘system’ model that describes the input-output relationship of partially coherent imaging. The PSI distribution falls in a general Cohen class of phase-space distributions [Cohen, 1995].

The fact that the PSI describes ‘a physical process’ is interesting. In an intriguing comment, Cohen has stated that idealizations imposed on the Cohen class of distributions are severe enough to preclude their use for describing a physical bilinear process [Cohen, 1989]. So far, Cohen class distributions have mainly been the ‘constructions’ that facilitate processing of data and extraction of features [O’Neill and Williams, 1999, Wax and Thomas, 1996, Robles et al., 2009] rather than descriptions that capture the behaviour of a ‘physical’ process. Cohen class distributions have been developed [Wax and Thomas, 1996, Robles et al., 2009] for analysis of data acquired with temporally partially coherent methods such as OCT. Thus, PSI is one of the possibly few ‘physically meaningful’ phase-space distributions. We note that the ‘disadvantage’ that the PSI possesses on the account of being physical is that it is not frequency-shift covariant with respect to the specimen. The lack of frequency-shift covariance is physical too, because partially coherent image formation is not frequency-shift covariant due to presence of the condenser aperture as can be judged by from fig. 1.3b.

We have implemented an efficient MATLAB software for forward image formation in partially coherent systems. We have used this simulation capability to compare image formation in five interesting microscopy methods [Mehta and Sheppard, 2010c].

### 7.1.3 High-resolution quantitative analysis of cellular morphology

With our simulation capability, we discovered an interesting application of dark-field illumination to study of dynamic beating pattern of a molecular machine called the axoneme. The results are discussed in sec. 6.3. While dark-field has been used to ‘see’ the axoneme, we decided to pay attention to small changes in the intensity profile in the dark-field image as the structure of the axoneme changes. We developed an image analysis algorithm that accentuates this signal and provides a quantitative measurement of bending of the axoneme and the structural changes that cause the bending.

We have developed a fast and robust image registration approach applicable to gradient data as measured with DIC and AIDPC (sec. 6.2.1). Our approach extends the existing approaches of image registration that work with two measurements of the same function, rather than two gradients of the same function. With image registration and a fast reconstruction that incorporates heuristic deconvolution (sec. 6.2), we have been able to obtain high-resolution morphological images amenable to quantitative analysis. These algorithms should be widely useful in studies of dynamic cellular processes such as cell division and cell motility, where changes in cellular morphology are important. By the nature of being non-invasive, the above instrumentation and algorithms can allow long-term time-lapse imaging.

## 7.2 Future directions

Although we have made tangible progress in analytical, computational and experimental research related to partially coherent phase microscopy, there are many interesting directions that are yet to be pursued.



### 7.2.1 Partially coherent methods of quantitative phase microscopy

Although we have resolved key difficulties in describing image formation of DIC in-focus, we look forward to addressing a long-standing question of why DIC has good depth-sectioning [Inoué, 1996] and other methods (e.g. DPC) do not. To do so, we intend to employ our PSI model and compare image formation between DIC and DPC as we defocus the specimen.

There is a possibility that the low temporal coherence (large spectrum of illumination) has an important role to play in sectioning. In our approach, we account for spatial partial coherence, but assume quasi-monochromatic illumination. We note that OCT is an interesting sectioning method that is temporally partially coherent but uses ‘quasi-point’ illumination. Extending our approach to include temporal coherence will likely explain the sectioning properties of DIC and allow design of configurations that provide the desired sectioning and lateral resolution properties.

While we have studied in detail the DIC (which is an interferometer, or specifically, a shearing interferometer) and the DPC (which is non-interferometric method) methods, there are other interesting quantitative partially coherent phase methods. Recently, a few researchers have explored the use of phase-contrast for quantitative imaging [Fiolka et al., 2009, Wang et al., 2010] by changing the phase-shift employed in the back focal plane of the phase-contrast objective. These methods essentially do phase-shifting to measure the relative phase between direct light and diffracted light. Moreover, transport of intensity (TIE) [Paganin and Nugent, 1998, Nugent et al., 1996, 2008] is an interesting non-interferometric approach to quantitative phase imaging. Analyzing these ideas with our model and building upon their strengths are interesting directions to pursue.

### 7.2.2 Phase-space representation of partially coherent imaging

As has been hinted in sec. 7.1.2, PSI is an interesting and physically meaningful phase-space distribution. It is important to further establish its connections with the well-developed theory of Cohen class distributions. By answering comparative questions, such as what properties does PSI possess that the Wigner distribution does not, we aim to gain better

insight into how the specimen properties are affected by the partially coherent imaging system. The intuition derived from such studies will allow us to clarify the image formation in different partially coherent approaches noted above and build methods that provide higher-resolution and more quantitative measurements.

In the above endeavor, it is important to be able to simulate the image formation process. While our current implementation of phase-space computations is accurate and moderately fast, we aim to improve the speed of computation significantly. To this end, we aim to incorporate ideas from about the matrix representation of transmission cross coefficient model [Yamazoe et al., 2009a, Yamazoe, 2010] developed in the field of optical lithography, where fast partially coherent image computation is absolutely essential.

### 7.2.3 High-resolution quantitative analysis of cellular morphology

From the user’s perspective, the primary benefits of partially coherent microscopy methods are the high resolution, depth-sectioning, high signal-to-noise ratio and high light-throughput in comparison to coherent methods. However, the key problems that the user has with partially coherent methods is the difficulty of performing quantitative image analysis and absolute measurements.

We aim to develop a proper reconstruction/deconvolution approach for partially coherent methods. Interestingly, in X-ray microscopy there has been development of methods called ‘ptychography’ [Rodenburg, 2001]. Ptychography relies on similar principles as the scanning DPC and may be thought of as DPC’s generalization. The data acquired with ptychography has been expressed using Wigner distributions and approaches for its deconvolution have been proposed [Rodenburg and Bates, 1992, Chapman, 1997]. These ideas may lead us to an efficient and useful deconvolution procedure for partially coherent methods. By enabling better quantitative analysis of cellular morphology than has been possible, these developments may allow the researchers to address a wider range of biological questions without having to label their specimens.

# Bibliography

- A. Agrawal, R. Raskar, and R. Chellappa. What is the range of surface reconstructions from a gradient field? In *Computer Vision - ECCV 2006*, pages 578–591. 2006.
- R. D. Allen and N. S. Allen. Video-enhanced microscopy with a computer frame memory. *Journal of Microscopy*, 129(Pt 1):3–17, Jan. 1983.
- M. R. Arnison, C. J. Cogswell, N. I. Smith, P. W. Fekete, and K. G. Larkin. Using the hilbert transform for 3D visualization of differential interference contrast microscope images. *J. Microsc.*, 199(1):79–84, 2000.
- M. R. Arnison, K. G. Larkin, C. J. R. Sheppard, N. I. Smith, and C. J. Cogswell. Linear phase imaging using differential interference contrast microscopy. *J. Microsc.*, 214(1):7–12, Apr. 2004.
- D. Axelrod. Zero-cost modification of bright field microscopes for imaging phase gradient on cells: Schlieren optics. *Cell Biochemistry and Biophysics*, 3(2):167–173, 1981.
- J. L. Badano, N. Mitsuma, P. L. Beales, and N. Katsanis. The ciliopathies: an emerging class of human genetic disorders. *Annual Review of Genomics and Human Genetics*, 7:125–148, 2006.
- M. J. Bastiaans. Applications of the wigner distribution to partially coherent light beams. In A. T. Friberg and R. Dandliker, editors, *Advances in Information Optics and Photonics*, volume PM183, pages 27–56. SPIE Press, June 2008.
- M. J. Bastiaans. Wigner distribution in optics. In B. Hennelly, J. Ojeda-Castaeda, and M. Testorf, editors, *Phase Space Optics: Fundamentals and Applications*, pages 1–

44. McGraw-Hill, 2009. URL [http://www.sps.ele.tue.nl/members/m.j.bastiaans/pdfs/ps\\_book.pdf](http://www.sps.ele.tue.nl/members/m.j.bastiaans/pdfs/ps_book.pdf).
- M. Born and E. Wolf. *Principles of Optics: Electromagnetic Theory of Propagation, Interference and Diffraction of Light*. Cambridge University Press, Cambridge, 7th expanded edition, 1999.
- C. J. Brokaw and R. Kamiya. Bending patterns of chlamydomonas flagella: IV. mutants with defects in inner and outer dynein arms indicate differences in dynein arm function. *Cell motility and the cytoskeleton*, 8(1):68-75, 1987.
- H. N. Chapman. Phase-retrieval x-ray microscopy by wigner-distribution deconvolution: signal processing. *Scanning Microscopy*, 11:67-80, 1997.
- S. T. Christensen, L. B. Pedersen, L. Schneider, and P. Satir. Sensory cilia and integration of signal transduction in human health and disease. *Traffic*, 8(2):97-109, 2007.
- C. Cogswell and C. Sheppard. Confocal differential interference contrast(DIC) microscopy: including a theoretical analysis of conventional and confocal DIC imaging. *J. Microsc.*, 165:81-101, 1992.
- C. J. Cogswell, N. I. Smith, K. G. Larkin, and P. Hariharan. Quantitative DIC microscopy using a geometric phase shifter. In *Proceedings of SPIE*, volume 2984, page 72, 1997.
- L. Cohen. Generalized phase-space distribution functions. *Journal of Mathematical Physics*, 7:781, 1966.
- L. Cohen. Time-frequency distributions-a review. *Proceedings of the IEEE*, 77(7):941-981, 1989.
- L. Cohen. *Time-frequency analysis: theory and applications*. Prentice Hall, 1995.
- N. H. Dekkers and H. de Lang. Differential phase contrast in a STEM. *Optik*, 41(4):452-456, 1974.
- G. W. Ellis. Edge enhancement of phase phenomena, Mar. 1981. US Patent: 4255014.

- R. Fiolka, K. Wicker, R. Heintzmann, and A. Stemmer. Simplified approach to diffraction tomography in optical microscopy. *Optics Express*, 17(15):12407-12417, 2009.
- D. Gabor. A new microscopic principle. *Nature*, 161(4098):777-778, 1948.
- W. Galbraith. The image of a point of light in differential interference contrast microscopy: computer simulation. *Microscopica Acta*, 85(3):233-254, 1982.
- D. J. Gallant, B. Bouchet, and P. M. Baldwin. Microscopy of starch: evidence of a new level of granule organization. *Carbohydrate Polymers*, 32(3-4):177-191, Apr. 1997.
- D. C. Ghiglia and M. D. Pritt. *Two-dimensional phase unwrapping: theory, algorithms, and software*. Wiley New York, 1998.
- C. A. Glasbey and N. J. Martin. Multimodal microscopy by digital image processing. *J. Microsc.*, 181(3):225-237, 1996. doi: 10.1046/j.1365-2818.1996.91372.x. URL <http://dx.doi.org/10.1046/j.1365-2818.1996.91372.x>.
- D. Hamilton and C. Sheppard. Differential phase contrast in scanning optical microscopy. *J. Microsc.*, 133(1):27-39, 1984.
- D. Hamilton, C. Sheppard, and T. Wilson. Improved imaging of phase gradients in scanning optical microscopy. *Journal of microscopy*, 135(3):275-286, 1984.
- R. Hoffman and L. Gross. Modulation contrast microscope. *Applied Optics*, 14(5):1169-1176, May 1975.
- T. J. Holmes and W. J. Levy. Signal-processing characteristics of differential-interference-contrast microscopy. *Appl. Opt.*, 26(18):3929, 1987.
- H. H. Hopkins. On the diffraction theory of optical images. *Proc. R. Soc. Lond. A*, 217 (1130):408-432, May 1953.
- S. Inoué. Ultrathin optical sectioning and dynamic volume investigation with conventional light microscopy. In J. Stevens, L. Mills, and J. Trogadis, editors, *Three-Dimensional Confocal Microscopy: Volume Investigation of Biological Systems*, page 397-419. Academic Press, San Diego, USA, 1996.

- S. Inoué. Windows to dynamic fine structures, then and now. *FASEB J*, 13 Suppl 2: S185–S190, Dec. 1999.
- S. Inoué and K. R. Spring. *Video microscopy : the fundamentals*. Plenum Press, New York, 2nd edition, 1997.
- H. Ishiwata, M. Itoh, and T. Yatagai. A new method of three-dimensional measurement by differential interference contrast microscope. *Optics Communications*, 260(1):117–126, Apr. 2006.
- H. Ishiwata, M. Itoh, and T. Yatagai. A new analysis for extending the measurement range of the retardation-modulated differential interference contrast (RM-DIC) microscope. *Optics Communications*, 281(6):1412 – 1423, 2008.
- B. Kachar. Asymmetric illumination contrast: a method of image formation for video light microscopy. *Science*, 227(4688):766–768, Feb. 1985.
- F. Kagalwala and T. Kanade. Reconstructing specimens using DIC microscope images. *Systems, Man, and Cybernetics, Part B: Cybernetics, IEEE Transactions on*, 33(5):728–737, 2003.
- R. Kamiya. Functional diversity of axonemal dyneins as studied in chlamydomonas mutants. *International review of cytology*, 219:115-155, 2002.
- S. V. King, A. Libertun, R. Piestun, C. J. Cogswell, and C. Preza. Quantitative phase microscopy through differential interference imaging. *J. Biomed. Opt.*, 13(2):024020, 2008.
- S. S. Kou and C. J. Sheppard. Imaging in digital holographic microscopy. *Optics Express*, 15(21):13640-13648, 2007.
- S. S. Kou and C. J. R. Sheppard. Image formation in holographic tomography. *Optics letters*, 33(20):2362-2364, 2008.
- S. S. Kou and C. J. R. Sheppard. Image formation in holographic tomography: high-aperture imaging conditions. *Applied optics*, 48(34):168–175, 2009.

- \*S. S. Kou, \*S. B. Mehta, S. Rehman, and C. Sheppard. Image formation and analysis of coherent microscopy and beyond - towards better imaging and phase recovery. In P. Ferraro, A. Wax, and Z. Zalevsky, editors, *Coherent light microscopy for imaging and quantitative phase analysis*. Springer, To be published, Dec 2010. \*Equal contribution first authors.
- C. D. Kuglin and D. C. Hines. The phase correlation image alignment method. In *Proc. Int. Conf. on Cybernetics and Society*, volume 4, pages 163 – 165, 1975.
- K. G. Larkin, D. J. Bone, and M. A. Oldfield. Natural demodulation of two-dimensional fringe patterns. i. general background of the spiral phase quadrature transform. *Journal of the Optical Society of America A*, 18(8):1862–1870, 2001.
- D. L. Lessor, J. S. Hartman, and R. L. Gordon. Quantitative surface topography determination by nomarski reflection microscopy. i. theory. *Journal of the Optical Society of America*, 69(2):357–366, Feb. 1979.
- R. A. Lewis. Medical phase contrast x-ray imaging: current status and future prospects. *Physics in Medicine and Biology*, 49(16):3573–3583, 2004.
- A. W. Lohmann, M. Testorf, and J. Ojeda-Castaeda. Holography and the wigner function. In E. N. Leith and H. J. Caulfield, editors, *The art and science of holography: a tribute to Emmett Leith and Yuri Denisjuk*. SPIE Press, 2004.
- L. C. Martin. *The theory of the microscope*. American Elsevier Pub. Co., 1966.
- C. Maurer, A. Jesacher, S. Bernet, and M. Ritsch-Marte. Phase contrast microscopy with full numerical aperture illumination. *Opt. Express*, 16(24):19821–19829, 2008.
- S. B. Mehta and C. J. R. Sheppard. Partially coherent image formation in differential interference contrast (DIC) microscope. *Opt. Express*, 16(24):19462–19479, 2008. URL <http://www.opticsinfobase.org/oe/viewmedia.cfm?uri=oe-16-24-19462&seq=0>.
- S. B. Mehta and C. J. R. Sheppard. A new Phase-Correlation based gradient registration approach for Phase-Retrieval with DIC and DPC. In *OSA Technical Digest*, page SWA4, Signal Recovery and Synthesis, San Jose, USA, Oct. 2009a.



- S. B. Mehta and C. J. R. Sheppard. Quantitative phase-gradient imaging at high resolution with asymmetric illumination-based differential phase contrast. *Optics Letters*, 34(13):1924–1926, 2009b. URL <http://dx.doi.org/10.1364/OL.34.001924>.
- S. B. Mehta and C. J. R. Sheppard. Phase-space representation of partially coherent imaging systems using the cohen class distribution. *Optics Letters*, 35(3):348–350, Feb. 2010a. URL <http://www.opticsinfobase.org/abstract.cfm?URI=ol-35-3-348>.
- S. B. Mehta and C. J. R. Sheppard. Sample-less calibration of the differential interference contrast microscope. *Applied optics*, 49(15):2954–2968, 2010b. URL <http://www.opticsinfobase.org/abstract.cfm?URI=ao-49-15-2954>
- S. B. Mehta and C. J. R. Sheppard. Using the phase-space imager to analyze partially coherent imaging systems: brightfield, phase-contrast, differential interference contrast, differential phase contrast, and spiral phase contrast. *Journal of Modern Optics*, 57:718–739, 2010c. URL <http://www.informaworld.com/openurl?genre=article&issn=0950-0340&volume=57&issue=9&spage=718>.
- D. Nicastro, C. Schwartz, J. Pierson, R. Gaudette, M. E. Porter, and J. R. McIntosh. The molecular architecture of axonemes revealed by cryoelectron tomography. *Science*, 313(5789):944, 2006.
- G. Nomarski. Interference polarizing device for study of phase objects, Feb. 1960. U. S. Patent 2924142.
- G. Nomarski. New theory of image formation in differential interference microscopy (DIM). In *J. Opt. Soc. A*, volume 59 of 11, page 1524, 1969.
- K. A. Nugent, T. E. Gureyev, D. F. Cookson, D. Paganin, and Z. Barnea. Quantitative phase imaging using hard x rays. *Physical Review Letters*, 77(14):2961, 1996.
- K. A. Nugent, B. D. Arhatari, and A. G. Peele. A coherence approach to phase-contrast microscopy: Theory. *Ultramicroscopy*, 108(9):937–945, Aug. 2008.

- R. Oldenbourg. Polarization microscopy with the LC-Poloscope. In R. D. Goldman and D. L. Spector, editors, *Live cell imaging*, pages 205–37. CSHL Press, Cold Spring Harbor, NY, 2005.
- R. Oldenbourg, E. D. Salmon, and P. T. Tran. Birefringence of single and bundled microtubules. *Biophysical journal*, 74(1):645–654, 1998.
- A. Olivo and R. Speller. A coded-aperture technique allowing x-ray phase contrast imaging with conventional sources. *Applied Physics Letters*, 91:074106, 2007.
- J. C. O’Neill and W. J. Williams. Shift covariant time-frequency distributions of discrete signals. *IEEE Transactions on Signal Processing*, 47(1):133–146, 1999.
- D. Paganin and K. A. Nugent. Noninterferometric phase imaging with partially coherent light. *Physical Review Letters*, 80(12):2586, Mar. 1998.
- J. B. Pawley. *Handbook of Biological Confocal Microscopy*. Springer, 3rd ed. edition, June 2006.
- F. Pfeiffer, T. Weitkamp, O. Bunk, and C. David. Phase retrieval and differential phase-contrast imaging with low-brilliance x-ray sources. *Nat Phys*, 2(4):258–261, Apr. 2006.
- W. B. Piekos. Diffracted-light contrast enhancement: A re-examination of oblique illumination. *Microscopy Research and Technique*, 46(4-5):334–337, 1999.
- M. E. Porter and W. S. Sale. The 9+ 2 axoneme anchors multiple inner arm dyneins and a network of kinases and phosphatases that control motility. *The Journal of Cell Biology*, 151(5):F37, 2000.
- C. Preza. Rotational-diversity phase estimation from differential-interference-contrast microscopy images. *J. Opt. Soc. Am. A*, 17(3):415–424, 2000.
- C. Preza, D. L. Snyder, and J. Conchello. Theoretical development and experimental evaluation of imaging models for differential-interference-contrast microscopy. *J. Opt. Soc. Am. A*, 16(9):2185–2199, 1999.

- J. Ren, A. Kan, S. H. Leong, L. L. P. J. Ooi, K. Jeang, S. S. Chong, O. L. Kon, and C. G. L. Lee. FAT10 plays a role in the regulation of chromosomal stability. *J. Biol. Chem.*, 281(16):11413–11421, Apr. 2006.
- F. Robles, R. N. Graf, and A. Wax. Dual window method for processing spectroscopic optical coherence tomography signals with simultaneously high spectral and temporal resolution. *Optics Express*, 17(8):6799–6812, 2009.
- J. M. Rodenburg. A simple model of holography and some enhanced resolution methods in electron microscopy. *Ultramicroscopy*, 87(3):105–121, 2001.
- J. M. Rodenburg and R. H. T. Bates. The theory of super-resolution electron microscopy via wigner-distribution deconvolution. *Philosophical Transactions: Physical Sciences and Engineering*, 339(1655):521–553, 1992.
- H. M. Sakakibara, Y. Kunioka, T. Yamada, and S. Kamimura. Diameter oscillation of axonemes in sea-urchin sperm flagella. *Biophysical journal*, 86(1):346–352, 2004.
- H. Sato, G. W. Ellis, and S. Inou. Microtubular origin of mitotic spindle form birefringence. demonstration of the applicability of wiener’s equation. *Journal of Cell Biology*, 67(3):501, 1975.
- F. M. Schellenberg. *Resolution Enhancement Techniques in Optical Lithography*, volume MS 178 of *SPIE Milestone Series*. 2004.
- G. S. Settles. *Schlieren and shadowgraph techniques: visualizing phenomena in transparent media*. Springer, 2001.
- C. J. R. Sheppard and A. Choudhury. Image formation in the scanning microscope. *J. Mod. Opt.*, 24(10):1051–1073, 1977.
- C. J. R. Sheppard and T. Wilson. Fourier imaging of phase information in scanning and conventional optical microscopes. *Phil. Trans. Roy. Soc. London, Series A*, 295(1415):513–536, 1980.

- M. Shribak, J. LaFountain, D. Biggs, and S. Inoue. Orientation-independent differential interference contrast microscopy and its combination with an orientation-independent polarization system. *Journal of Biomedical Optics*, 13(1):014011–10, Jan. 2008.
- M. I. Shribak and R. Oldenbourg. Mapping polymer birefringence in 3D using a polarizing microscope with oblique illumination. In *Proceedings of the SPIE*, volume 5462, pages 57–67, Sept. 2004.
- W. Singer, M. Totzeck, and H. Gross. *Handbook of Optical Systems, vol 2, Physical Image Formation*. Wiley, New York, 2005.
- W. C. Stewart. On differential phase contrast with an extended illumination source. *Journal of the Optical Society of America*, 66(8):813–818, 1976.
- D. M. Supp, D. P. Witte, S. S. Potter, and M. Brueckner. Mutation of an axonemal dynein affects left-right asymmetry in inversus viscerum mice. *Nature*, 389(6654):963, 1997.
- M. E. Testorf, J. Ojeda-Castaeda, and A. W. Lohmann, editors. *Selected papers on phase-space optics*, volume MS181 of *SPIE Milestone series*. July 2006.
- E. B. van Munster, L. J. van Vliet, J. A. Aten, A. V. Priezhev, T. Asakura, and R. C. Leif. Quantitative interferometric imaging using a conventional differential interference contrast microscope. In *Optical Diagnostics of Biological Fluids and Advanced Techniques in Analytical Cytology*, volume 2982, pages 458–467, San Jose, CA, USA, May 1997. SPIE.
- S. Vertu, J. J. Delaunay, I. Yamada, and O. Haeberl. Diffraction microtomography with sample rotation: influence of a missing apple core in the recorded frequency space. *Central European Journal of Physics*, 7(1):22–31, 2009.
- J. Ville. Theory and applications of the notion of complex signal. 1958.
- O. von Hofsten, M. Bertilson, and U. Vogt. Theoretical development of a high-resolution differential-interference-contrast optic for x-ray microscopy. *Opt. Express*, 16(2):1132–1141, Jan. 2008.

- W. Wang, L. Meng, R. Hackett, and D. Keefe. Developmental ability of human oocytes with or without birefringent spindles imaged by polscope before insemination. *Hum. Reprod.*, 16(7):1464–1468, July 2001.
- Z. Wang, I. S. Chun, X. Li, Z. Ong, E. Pop, L. Millet, M. Gillette, and G. Popescu. Topography and refractometry of nanostructures using spatial light interference microscopy. *Optics Letters*, 35(2):208–210, Jan. 2010.
- A. Wax and J. E. Thomas. Optical heterodyne imaging and wigner phase space distributions. *Optics letters*, 21(18):1427–1429, 1996.
- E. Wigner. On the quantum correction for thermodynamic equilibrium. *Physical Review*, 40(5):749–759, 1932.
- T. Wilson and C. J. R. Sheppard. *Theory and Practice of Scanning Optical Microscope*. Academic Press, London, 1984.
- A. K. Wong. *Resolution Enhancement Techniques in Optical Lithography*. SPIE Publications, Mar. 2001.
- K. Yamazoe. Computation theory of partially coherent imaging by stacked pupil shift matrix. *Journal of the Optical Society of America A*, 25(12):3111–3119, Dec. 2008.
- K. Yamazoe. Two matrix approaches for aerial image formation obtained by extending and modifying the transmission cross coefficients. *Journal of the Optical Society of America A*, 27(6):1311–1321, June 2010.
- K. Yamazoe, Y. Sekine, and T. Honda. Aerial image back propagation with two-dimensional transmission cross coefficient. *Journal of Micro/Nanolithography, MEMS and MOEMS*, 8(3):031406–7, July 2009a.
- K. Yamazoe, Y. Sekine, and T. Honda. Fast computation of constructive and destructive interference areas in partially coherent imaging for resolution enhancement in optical microlithography. *Applied Optics*, 48(8):1419–1424, Mar. 2009b.
- F. Zernike. How I discovered phase contrast. *Science*, 121:345–349, Mar. 1955.

- B. Zitova and J. Flusser. Image registration methods: a survey. *Image and vision computing*, 21(11):977–1000, 2003.